

Flocculation dynamics of cohesive sediment

Flocculatie dynamica van cohesief sediment

Proefschrift

ter verkrijging van de graad van doctor
aan de Technische Universiteit Delft,
op gezag van de Rector Magnificus prof. dr. ir. J.T. Fokkema,
voorzitter van het College voor Promoties,
in het openbaar te verdediging op 12 september 2005 om 13:00 uur.

door

Federico MAGGI

Laureato in Ingegneria Civile al Politecnico di Torino,
geboren te Vercelli, Italië.

Delft, 2005

Dit Proefschrift is goedgekeurd door de promotor
Prof. dr. ir. J.A. Battjes

Samenstelling promotiecommissie

Rector Magnificus	voorzitter
Prof. dr. ir. J.A. Battjes	Technische Universiteit Delft, promotor
Dr. ir. J.C. Winterwerp	Technische Universiteit Delft, toegevoegd promotor
Prof. dr. J. Berlamont	Katholieke Universiteit Leuven
Prof. dr. K. Dyer	University of Plymouth
Prof. dr. ir. M.C.M. van Loosdrecht	Technische Universiteit Delft
Prof. dr. I.T. Young	Technische Universiteit Delft
Ir. W.G.M. van Kesteren	WL Waterloopkundig Laboratorium

This research is supported by the BEO programme of Delft University of Technology.

ISBN 90-9019613

Copyright ©2005, Federico Maggi.
Printed by PrintPartners Ipskamp B.V., The Netherlands.

All rights reserved. No part of this publication may be reproduced in any form, by print or photo print, microfilm or any other means, without written permission by the publishers.

This thesis is also published in the series 'Communications on Hydraulic and Geotechnical Engineering' of the Faculty of Civil Engineering and Geosciences, Delft University of Technology, as Report No. 05-1. ISSN 0169-6548.

*There is no pleasure more complex than that of
thought and we surrendered ourselves to it.*

Jorge Luis Borges

Labyrinths
Selected Stories & Other Writings

Edited by D.A. Yates and J.E. Irby (1962)

Abstract

Cohesive sediment suspended in natural waters is subject not only to transport and deposition processes but also to reactions of flocculation, *i.e.* aggregation of fine particles, and breakup of aggregates. Although aggregation and breakup occur at small and very small length scales compared to transport and deposition, flocculation can effectively have an impact on the large scale as well. Some phenomena that are correlated to (or find roots in) flocculation reactions are, for instance, coastal morphodynamics, pollutant and contaminant transport and deposition, and sedimentation in rivers, estuaries, lakes, canals, harbours and water basins in general. Water environments accommodate a variety of societal functions, like navigation and fish culture, provide the potable water supply and serve the industrial and waste water processes demand. At the same time, natural waters also bear several ecosystem functions that are essential for a healthy environment. The complicated balance between human need and ecosystem safeguard is one of the rationales for studying flocculation of suspended sediment in natural waters. The specific focus of this thesis is directed towards the genesis of flocs by flocculation of cohesive sediment and the behaviour of a population of flocs in aqueous environments.

Floc size distribution, floc structure and flocculation models are investigated in this thesis by means of three methods: experiments, mathematical analysis and numerical modeling.

The experimental activity has been carried out in the settling column of the Laboratory for Environmental Fluid Mechanics, aimed at collecting information on the population of flocs under different conditions of turbulence intensity. An optical system dedicated to collect images at scales comparable to the floc size has been designed and coupled to the settling column. This has enabled an innovative sight on the properties of a suspension of cohesive sediment, allowing the analysis of the floc size distribution and the structure of individual flocs.

The images collected with the optical recording system are elaborated and analysed numerically to assess the properties of sediment flocs. First, the data have been processed to extract black-and-white images of individual flocs. Second, flocs have been characterised by means of several quantities, amongst which the size, fractal dimensions and disorder function. Third, statistics of the population have been calculated. This has been repeated for different experimental conditions. The result is an overall portrait of the time evolution of the floc size distribution, and of the response of a population of flocs to the turbulence field produced in the column at various intensities. In general we observe that flocs grow in time from a (nearly) monodisperse suspension of primary particles, developing a population distributed over a wider range of sizes. On the one hand (the large length scales), the population evolution appears to adapt to the forcing, the process that is coupled to a decrease in spatial entropy of the system and a reshaping of the floc size distributions into a more complex population. On the other hand (the small length scales), floc growth is accompanied by a decrease in fractal dimension and, at the same time, by an increase in geometrical complexity, *i.e.* disorder.

The analysis of floc structure and floc size distribution from the experimental results has given an innovative pulse to the modelling of flocculation of cohesive sediment suspensions by means of a new population balance equation. First, the floc structure has been implemented through a fractal model. Second, the population balance equation has been implemented for a full population of flocs. Third, different mechanisms of aggregation and breakup have been examined. The floc size distribution has been then compared with the

experimental ones to evaluate the predictive skills of the model. The analysis of the results shows that the implementation of floc structure and kinematic processes at population scales enables a proper prediction capability of the model.

The major innovative aspects of the present study are the characterisation of the geometrical structure of the flocs and the interaction among fractal aggregates within a population. This is the source of several considerations on the dynamics of cohesive sediment in particular and flocculating systems in general. However, this could not have been achieved without the experimental data obtained from the settling column, unique with respect to the length and time scales involved, the control parameters and the measuring techniques.

Prefazione

Il sedimento coesivo presente in corpi acquei naturali è soggetto non solo a processi di trasporto o deposizione ma anche a flocculazione, cioè aggregazione e frammentazione del particellato stesso. Nonostante la flocculazione sia un processo che ricorre a scale caratteristiche relativamente piccole rispetto a quelle di trasporto e deposizione, questa può avere un impatto percettibile anche su scale più ampie. Alcuni fenomeni che sono correlati alla flocculazione di sedimenti coesivi, o che in essa trovano origine, sono, per esempio, la morfodinamica delle zone costiere, il trasporto e la deposizione di contaminanti e inquinanti, la sedimentazione in fiumi, estuari, laghi, canali, porti o bacini idrici in generale. Gli ambienti acquei svolgono una varietà di funzioni correlate con la normale attività umana, come ad esempio la navigazione e l'acquacoltura, e forniscono acqua ad uso potabile e industriale. Allo stesso tempo, però, i corpi acquei contribuiscono a mantenere in mutuo equilibrio l'ambiente naturale con la flora e la fauna. La complessa interazione tra bisogni umani e salvaguardia ambientale è uno dei motivi che ci spinge a studiare la flocculazione di sedimenti coesivi in sospensione in ambienti acquei naturali.

Gli aspetti principali di questa tesi di dottorato di ricerca riguardano la genesi di fiocchi di sedimento cohesivo causato dalla flocculazione, la loro struttura geometrica, la loro organizzazione all'interno di una popolazione e la presentazione di un modello per la previsione della distribuzione di probabilità dei loro diametri. Tre metodi sono state seguiti: sperimentale, analitico e numerico.

L'attività sperimentale è stata svolta nella colonna di sedimentazione costruita nel Laboratorio di Fluidodinamica Ambientale nell'ambito di questo dottorato. Un particolare sistema di registrazione ottico è stato disegnato e accoppiato alla colonna per il tracciamento delle traiettorie dei fiocchi e la misurazione delle loro proprietà geometriche, permettendo di svolgere una ricerca innovativa su proprietà e comportamenti di sedimenti coesivi in sospensione, durante la fase di flocculazione.

Le immagini raccolte durante le sperimentazione sono state successivamente elaborate per estrarre, individualmente, le immagini di fiocchi. Da queste, successivamente, è stato calcolato il diametro, le dimensioni frattali, la funzione disordine, e molte altre quantità. Di queste è stata effettuata sia un'analisi statistica che di correlazione per diverse condizioni sperimentali. Ciò ha permesso di ottenere una rappresentazione della risposta di una popolazione di fiocchi nella loro evoluzione temporale e per diverse intensità di turbolenza generate nella colonna. In generale, i fiocchi si formano a partire da blocchi elementari, cioè le particelle primarie, sviluppando, progressivamente nel tempo, una popolazione molto variegata in quanto a forme e dimensioni. La popolazione sviluppa, nella sua evoluzione temporale, una struttura complessa di individui con proprietà molto distribuite. Allo stesso modo, la crescita dei fiocchi sembra essere marcata da una diminuzione della dimensione frattale e da un aumento di disordine nella loro organizzazione geometrica interna.

L'analisi della struttura dei fiocchi e lo studio della distribuzione dei loro diametri ottenuta dagli esperimenti ha permesso di dare un impulso alla modellazione del fenomeno di flocculazione di particelle di sedimento coesivo. Per prima cosa, l'approccio frattale è stato impiegato per descrivere le proprietà geometriche dei fiocchi. Quindi, un nuovo modello è stato proposto per un'intera popolazione di fiocchi frattali interagenti tra loro. Per finire, vari meccanismi di aggregazione e frammentazione sono stati esaminati, e l'evoluzione temporale della distribuzione di probabilità dei fiocchi è stata confrontata con quella sperimentale. L'analisi di sensitività ha permesso di stabilire che l'implementazione di processi semi-stocastici di aggregazione e frammentazione, e della struttura statisticamente auto

simile dei fiocchi ha effettivamente dato risultati soddisfacenti nella previsione.

Gli aspetti innovativi di questo studio sono la caratterizzazione della struttura geometrica di aggregati frattali, e la loro interazione all'interno di una popolazione. Ciò è stato anche fonte di molte considerazioni riguardo la dinamica di sedimenti coesivi specificatamente, e di sistemi particellati in generale. L'intero studio qui descritto si è basato su dati sperimentali raccolti per la prima volta nella nuova colonna di sedimentazione, unica in quanto riguarda le scale spaziali e temporali coinvolte, la possibilità di controllo e monitoraggio del sistema e le tecniche di misurazione.

Samenvatting

Het in natuurlijke wateren zwevende cohesieve sediment wordt niet alleen onderworpen aan processen van transport en afzetting, maar ook flocculatie, dat wil zeggen aggregatie van fijne deeltjes en opbreken van grote aggregaten. Hoewel aggregatie en opbreken in vergelijking tot transport en afzetting optreden op kleine en zeer kleine lengteschalen, kan flocculatie ook op de grote schaal invloed hebben. Enkele verschijnselen die gecorreleerd zijn met (of hun wortels vinden in) flocculatiereacties zijn, bijvoorbeeld, kustmorfodynamica, transport en afzetting van verontreinigingen en vervuilingen, en sedimentatie in stuwmeren, rivieren, estuaria, meren, kanalen en havens. Watermilieus herbergen een verscheidenheid aan maatschappelijke functies, zoals scheepvaart, viskwekerij, drinkwatervoorziening en het voorzien in de vraag naar industrie- en afvalwaterprocessen. Tegelijkertijd dragen natuurlijke wateren ook verscheidene ecosysteemfuncties die wezenlijk zijn voor een gezond milieu. De ingewikkelde balans tussen menselijke behoeften en ecosysteembescherming is een van de beweegredenen om flocculatie van zwevend sediment in natuurlijke wateren te bestuderen. Dit proefschrift is daarom gericht op de genese van vlokken door flocculatie van cohesief sediment en het gedrag van een populatie van vlokken in watermilieus.

De vloggrootteverdeling, vlokstructuur en flocculatiemodellen worden in dit proefschrift door middel van drie methoden onderzocht: laboratorium experimenten, wiskundige analyse en numerieke modellering.

De experimentele activiteit is uitgevoerd in de sedimentatiekolom van het Laboratorium voor Vloeistofmechanica en is gericht op het inwinnen van informatie over de populatie van vlokken onder verschillende condities van turbulentie intensiteit. Een optisch systeem toegespitst op het inwinnen van beelden op schalen vergelijkbaar met de vloggrootte is ontworpen en gekoppeld aan de sedimentatiekolom. Dit heeft een innovatief zicht mogelijk gemaakt op de eigenschappen van een suspensie van cohesief sediment, door een analyse mogelijk te maken van de vloggrootteverdeling en de structuur van afzonderlijke vlokken.

De met het optische opnamesysteem ingewonnen beelden zijn numeriek uitgewerkt en geanalyseerd om de eigenschappen van de sedimentvlokken te bepalen. Ten eerste zijn de gegevens bewerkt om daaruit zwartwit beelden van afzonderlijke vlokken te halen. Ten tweede zijn vlokken gekarakteriseerd door middel van verscheidene grootheden, waaronder de grootte, de fractale dimensie en de wanordefunctie. Ten derde zijn statistische kengetallen van de populatie berekend. Deze methode is voor verschillende experimentele omstandigheden herhaald. Het resultaat is een totaalportret van de evolutie van de vloggrootteverdeling in de tijd en van de respons van een populatie vlokken op het turbulentievel dat in de kolom met verschillende intensiteiten geproduceerd is. In het algemeen nemen we waar dat de vlokken in de tijd groeien vanuit een (vrijwel) monodisperse suspensie van primaire deeltjes, waarbij zich een populatie ontwikkelt die verdeeld is over een wijder bereik van afmetingen. Aan de ene kant (de grote lengteschalen) blijkt de populatieevolutie zich aan te passen aan de forcering, het proces dat gekoppeld is aan een afname van de ruimtelijke entropie van het systeem en een hervorming van de vloggrootteverdelingen tot een complexere populatie. Aan de andere kant (de kleine lengteschalen) gaat de vloggroei vergezeld met een afname van de fractale dimensie en, tegelijkertijd, een toename van de geometrische complexiteit, dat wil zeggen wanorde.

De analyse van vlokstructuur en vloggrootteverdeling uit de experimentele resultaten heeft een innovatieve stoot gegeven aan het modelleren van flocculatie van suspensies van cohesief sediment door middel van een nieuwe populatiebalansvergelijking. Ten eerste is vlokstructuur geïmplementeerd met een fractaal model. Ten tweede is de populatiebal-

ansvergelijking voor een volledige populatie van vlokken geïmplementeerd. Ten derde zijn verschillende mechanismen van aggregatie en opbreken onderzocht. De vlogrootteverdeling is vervolgens vergeleken met de experimentele verdelingen om conclusies te trekken en de voorspelkracht van het model te beoordelen. Deze vergelijkende analyse en een gevoeligheidsanalyse van de resultaten laten zien dat de implementatie van vlokstructuur en kinematische processen op populatieschalen een juist voorspelvermogen van het model mogelijk maakt.

De voornaamste innovatieve aspecten van de voorliggende studie zijn de karakterisering van de geometrische structuur van de vlokken en de wisselwerking tussen fractale aggregaten binnen een populatie. Dit is de bron van verscheidene beschouwingen over de dynamica van cohesief sediment in het bijzonder en flocculerende systemen in het algemeen. Dit zou echter niet mogelijk zijn geweest zonder de met de sedimentatiekolom verkregen experimentele gegevens, uniek wat betreft de betrokken lengte- en tijdschalen, de instelparameters en de meettechnieken.

Contents

1	Introduction	1
1.1	Cohesive sediment and its behaviour	1
1.2	Floc size distribution and floc structure	2
1.3	Objectives	3
1.4	Outline	3
2	Suspensions of cohesive sediment	5
2.1	Cohesive sediment suspensions in natural waters	5
2.1.1	Non-organic and organic constituents	5
2.1.2	Electro-chemical properties of cohesive minerals	6
2.1.3	Effect of salinity and acidity on cohesion	6
2.2	Cohesive suspensions and flocculation	7
2.2.1	Aggregation mechanisms	7
2.2.2	Breakup mechanisms	9
2.3	Turbulence and flocculation	11
2.3.1	Interaction between turbulence structures and cohesive sediment	11
2.3.2	Rate of shear and flocculation	12
2.4	Description of the aggregate structure	13
2.4.1	Size	13
2.4.2	Fractal description	14
2.4.3	Porosity	15
2.4.4	Primary particle number in a floc and excess density	15
2.5	Approach to modelling of flocculation	16
2.5.1	Population balance equations	16
2.5.2	Floc growth	17
2.6	Discussion	19
2.6.1	On the small scales: flocs as growing individuals	19
2.6.2	On the large scales: populations of interacting individuals	19
2.6.3	A comprehensive view	20
3	Phenomenological description and characterisation of flocculating systems	21
3.1	Phenomenology of flocculation at large scales	21
3.1.1	Spatial entropy and organisation in flocculating systems	21
3.1.2	Far-from-equilibrium dynamics in flocculating systems	23
3.1.3	Feedback loops in flocculating systems	24
3.1.4	A step towards self-organisation in flocculating systems	25
3.2	Phenomenology of flocculation at small scales	27

3.2.1	Spatial organisation of floc geometry	29
3.2.2	Fractal dimensions	29
3.2.3	Generalised dimensionality and multifractality	30
3.2.4	Multifractal spectrum and mass density organisation of mud flocs .	31
3.3	Summary	33
4	Experimental facility: the settling column	35
4.1	Targets and design criteria	35
4.2	Conceptual design of the settling column	35
4.3	Scheme structure and functioning	37
4.4	The climatized room	38
4.5	The sedimentation column and the grid	38
4.6	The sediment injection system	38
4.7	The measuring section	41
4.8	The optical system	42
5	Analysis of the experimental floc size distribution	45
5.1	Introduction	45
5.2	Time evolution of the floc size distribution	46
5.2.1	Description of the experiment	46
5.2.2	t -dependence of the FSD	47
5.3	Floc size distribution and rate of turbulent shear	49
5.3.1	Description of the experiment	49
5.3.2	G -dependence of the FSD	50
5.4	Statistical (information) entropy	52
5.5	Self-organised criticality	53
5.6	Discussion	54
5.6.1	Flocculation and equilibrium	54
5.6.2	Self-similarity and autonomy	55
5.7	Conclusions	55
6	Analysis of the geometrical structure of flocs	57
6.1	Introduction	57
6.2	Index of disorder and boundary structures	57
6.3	Mass-density organisation of the flocs: multifractality	59
6.4	Multifractality: from projected to real aggregates	61
6.5	The three-dimensional capacity dimension	62
6.6	Discussion	65
6.6.1	Disorder and multifractality	65
6.6.2	A comprehensive representation of growth and equilibrium dynamics of flocculation at large and small scales	66
6.6.3	Generalised geometrical representation of growth processes in the (ℓ, d_0)-plane	68
6.7	Conclusions	69

7	Population balance equation for cohesive sediment flocs	71
7.1	Introduction	71
7.2	Population balance equation	72
7.3	Characteristics of the model	74
7.4	Properties of the model	75
7.4.1	Method of integration	75
7.4.2	Derivation of the floc size distribution	76
7.4.3	Calibration of the parameters	76
7.4.4	Calibration of the model	76
7.5	Results	78
7.5.1	Modelling flocculation in the settling column	78
7.5.2	Effect of mass concentration c	78
7.5.3	Effect of shear rate G	79
7.6	Sensitivity analysis	82
7.6.1	Initial conditions	83
7.6.2	Collision efficiency	83
7.6.3	Breakup distribution function	84
7.6.4	Capacity dimension	85
7.7	Discussion	86
7.7.1	Overview of the results	86
7.7.2	Mono- and non-monotonicity	88
7.7.3	Self-organised criticality in the population balance equation	91
7.8	Conclusions	92
8	Conclusions and recommendations	95
8.1	Achievements of the research	95
8.2	Application, users and other domains of applicability	96
8.3	Future improvements	97
8.4	Concluding comment	98
A	Characterisation and classification of fractal sets	101
A.1	Characterisation of fractal sets	101
A.2	Classification of fractal sets	104
B	Detailed description of the column design: computation and experiment	107
B.1	Determination of the column length	107
B.2	Determination of required amount of sediment	107
B.3	Determination of the buffer volume	108
B.4	Experimental design of the grid	110
B.5	Calibration of the grid	112
B.6	Recirculation velocity in the buffer tank	114
B.7	Sediment migration from the buffer tank into the column	115
B.8	Relaxation time in the buffer tank	116
B.9	Gallery	117

C Projections of compact fractal measures	119
C.1 Test set	119
C.2 Correlation analysis between $d_0(S_2)$ and $d_0(S_3)$	120
C.3 Perimeter of fractal sets	120
C.4 Semi-empirical relation for $d_P(S_2)$ and $d_0(S_3)$	123
C.5 Validation to DLA and CCA aggregates	125
Bibliography	129
List of symbols	135
List of acronyms	136
Acknowledgments	139

Chapter 1

Introduction

The quality of natural water environments is inseparable from the cohesive particle matter therein suspended. Open water systems and reservoir in natural environments always carry sediment in the form of organic and/or inorganic compounds. These are not inert, rather they are subject to biologically-, chemically- and physically-driven processes, causing complicated behaviour. The suspended matter manifests variations during its evolution from a non-flocculated to a flocculated state. Dispersed cohesive particles aggregate with other particles, bacteria and algae, incorporating contaminants and gas bubbles. In other words, they flocculate, resulting in aggregates characterised by a wide variability in size, relative density and settling velocity, among others.

1.1 Cohesive sediment and its behaviour

Cohesive sediment consists predominantly of clayey particulate matter that is subject to aggregation, breakup, deposition and erosion processes, Figure 1.1. Turbulent mixing of the fluid causes the suspended aggregates to come in contact, inducing further aggregation and causing the growth of large aggregates. Simultaneously, the forcing by the fluid disrupts those aggregates that cannot withstand the shear stresses. The frequency with which particles collide, grow and break up depends largely on the intensity of turbulent quantities (fluctuating velocity, rate of shear) and, secondarily, on gravity. Flocs fall by settling and may accumulate on the bed. Large flocs settle faster than small flocs, consequently the bed structure shows a stratification of fine sediments upon rough layers made of larger clusters. When turbulent fluctuations are sufficiently intense, light aggregates forming part of the bed net are lifted up and eroded from the interface bed/water. Hence, those aggregates take part in the flocculation reactions again.

The dynamical behaviour of a suspension of clay minerals is strongly marked by their capability to form aggregates distributed over a wide range of sizes. This capability is an intrinsic characteristic of cohesive sediment, although also the medium plays a fundamental role. The floc size distribution is fundamental to characterise a cohesive suspension because is correlated to the residence time of the sediment in the water column, as the settling velocity scales with a power of the floc size. Specifically, two phenomena are correlated to the floc size distribution: sediment transport and sediment deposition. Large-scales phenomena of transport and sedimentation of cohesive sediment should be explored in the light of the underlying small-scale processes, *i.e.* the flocculation reactions. Sediment balance equations used nowadays to estimate sediment advection and deposition should account

for the properties of the aggregates. However, this task would require a better knowledge of the processes that contribute in shaping both the flocs (as growing individuals) and the population of flocs (as a system). This doctoral thesis is therefore focussed on the dynamical patterns (time evolution) and structural properties (floc geometry) of a population of interacting aggregates, with an overall aim of serving the understanding of the small-scales processes of sediment dynamics.

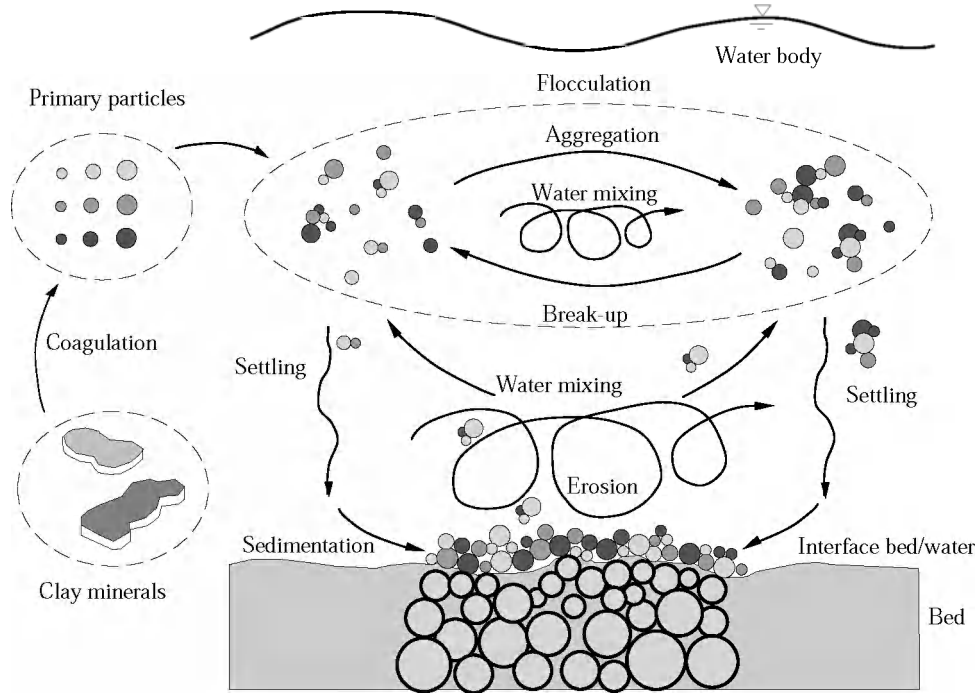


Figure 1.1: Cycle of deposition and resuspension of cohesive sediment involved in particle aggregation and breakup.

1.2 Floc size distribution and floc structure

The mechanisms of floc growth do not yield flocs with identical characteristics, although those mechanisms apply unconditionally (in a statistical sense) to any floc in a suspension.

Flocculation produces a population consisting of different "individuals". Normally, a population is characterised by quantities such as the size distribution; the statistical description of the floc size gives a portrait of the structure of the population, e.g. which type of individuals (*i.e.* which floc size) is dominant with respect to others. The floc size distribution, therefore, is an indicator of the response of the aggregates to the forcing, to the presence of other aggregates and to the constitutive properties of the minerals. The shape of the floc size distribution typically has one or two peaks (Van Leussen, 1994). However, the mechanisms governing the shape of the floc size distribution are not understood rich yet. On the one hand, exogenous factors (physico-chemical properties of the medium and hydro-climatic action) influence the shaping of the floc size distribution (Wells & Goldberg, 1993). On the other hand, also endogenous factors (sedimentological properties and autonomous dynamical behaviours) can have a role in the genesis of the population of aggregates. A comparative investigation of the time evolution and steady state of the

floc size distribution for different environmental forcing is expected to bring light to the dynamics of flocculation processes.

Particulate systems consisting of a collection of massive cohesive particles interacting with each other show intriguing behaviour. For instance, large flocs generally have higher settling velocity than small flocs. However, it is observed *in situ* that, for flocs with similar size, the settling velocity may vary widely because of differences in relative density (Manning & Dyer, 2002). This implies that the properties of size and porosity do not correlate always, meaning that the causes of the different behaviours lie in the geometrical structure of the flocs. The genesis of flocs is marked by the emergence of complex geometrical features: when two particles approach and merge, and this repeats several times, the resulting aggregate displays a porous and cluster structure which is far from the one of the primary particles, and that resemble itself (in a self-similar or fractal fashion) to some extent of length scales (Kranenburg, 1994). Floc genesis is, in terms of physics, the result of stochastic processes of aggregation and breakup amongst primary particles and higher order aggregates, while floc's structure can be described, in terms of geometry, with scaling laws.

1.3 Objectives

The first objective of this thesis is to acquire experimental data of the time evolution of the floc size distribution, and of the changes of the floc size distribution for different shear rates. This task is carried out through settling column observations. Furthermore, a statistical analysis is performed to characterise the dynamics of the population of cohesive sediment flocs.

The second objective is to enhance the understanding of floc morphodynamics during flocculation. This task is carried out by means of analysis of experimental data and numerical modelling to detect dominant scaling laws in the structure of the flocs.

The third objective is to model flocculation. This study is based on mathematical modelling through a population balance equation which comprises the achievements of the previous objective.

1.4 Outline

A literature survey is presented in Chapter 2, where the state-of-the-art knowledge of cohesive sediment flocculation is explored together with approaches to describe the geometrical properties of the aggregates and models used to predict the floc size distribution. An approach to the phenomenology of flocculation is elaborated in Chapter 3, and the quantities required to improve the characterisation of floc structure and population dynamics are introduced. Next, in Chapter 4, the settling column used for our experiments is described. The analysis of the floc size distribution is tackled in Chapter 5 with respect to the time evolution and response to various turbulent shear rates. Floc structure is analysed in Chapter 6 with the aim of describing the complicated mass-density organisation of the flocs. The major findings attained in Chapters 5 and 6 are next implemented in a new population balance equation in Chapter 7. We conclude, in Chapter 8, with a summary of the major achievements of this doctoral investigation, giving suggestions and recommendations to continue this research and guide the users of the models.

Chapter 2

Suspensions of cohesive sediment

This chapter introduces the properties and behaviours of cohesive sediment in suspension, with a survey of the current literature dealing with flocculation processes and floc characterisation. A broad research has been pursued about flocculation processes of cohesive particles, but we analyse and extrapolate only that which concerns our main objectives.

2.1 Cohesive sediment suspensions in natural waters

Many natural sites worldwide are marked by the presence of cohesive sediment at large scales, either as deposit or in suspension. Cohesive sediment or mud appears as a mixture of organic and non-organic compounds, silt, sand, water and gas. The composition of mud can vary largely from rivers to estuaries or coastal zones (Van Ledden, 2003), and also seasonally and with water depth. Clays are the smallest solid constituents of mud and they are responsible for cohesion properties together with organic bounds, whereas silt and sand particles have no effect on cohesion. Clays consist of small board-shaped particles of sizes between 0.1 and 5 μm (McAnally, 1999) that form larger (primary) particles by coagulation. These particles have sizes between approximately 5 and 20 μm , with generally face-to-face connected minerals. Unlike edge-to-edge or face-to-edge, this type of connection gives them massive structures and high resilience. Primary particles, next, form larger aggregates sometimes up to sizes of about 1 mm, characterised by filamentous and clustered structures. Cohesive suspensions are subject to flocculation processes, *i.e.* aggregation and breakup, which is the subject of this thesis.

2.1.1 Non-organic and organic constituents

The non-organic share of natural cohesive sediment consists predominantly of various clay minerals, polymers and, depending on the ambient conditions, films of metals or other chemicals. Amongst the clays, the most common are kaolinite, illite, montmorillonite and chlorite minerals, all characterised by different equivalent diameter (Van Leussen, 1994; McAnally, 1999).

Cohesive sediment contains also organic and chemical compounds including algae, fungi, bacteria, polysaccharides, polymers, faecal pellets, nutrients, animal parts and animal waste products. These cover the particles with mucous filaments, altering the particles' physico-chemical bonds holding them together (Mehta, 1991; Manning & Dyer, 1999; Mikes *et al.*, 2002).

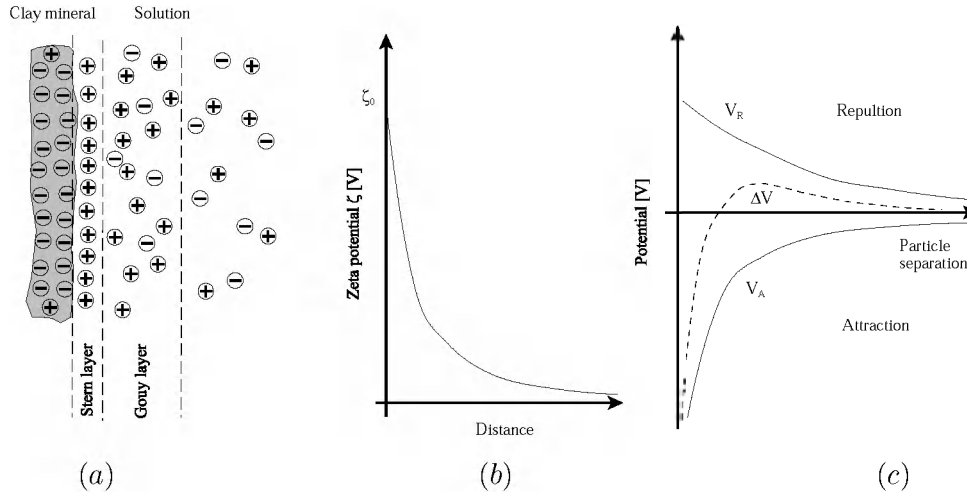


Figure 2.1: (a) schematic representation of the electric double layer surrounding the particles. (b) qualitative representation of the ζ -potential as a function of the distance from the surface of the particle. (c) potential energy corresponding to the double layer interaction for two approaching particles, where V_R and V_A are the potential energies associated with repulsion and attraction respectively, with ΔV the electrical barrier (Valioulis, 1983).

2.1.2 Electro-chemical properties of cohesive minerals

The cohesion of fine clays is due to their electro-chemical properties. Fine clay particles are negatively charged at their face and they may be surrounded by a cloud of cations, whose concentration is very high in the Stern layer, immediately adjacent to the particle surface, and decreases in the outer Gouy layer; these together form the so-called diffusive *double layer*, Figure 2.1 (a). The double layer is characterised by the ζ -potential ζ_0 at the water/particle interface, which decreases proportionally to the ion concentration, Figure 2.1 (b). The thickness of the double layer can vary largely for different minerals and ion concentration in the medium, and also according to the balance between attractive electrical forces and diffusion within the medium (Van Leussen, 1994). The interaction between two approaching particles is governed by the interaction of their double layer, Figure 2.1 (c): a first repulsive electrical force tends to separate the particles; if this is overcome at a certain distance, then collision may occur and the particles may be kept attached to each other by attractive forces.

2.1.3 Effect of salinity and acidity on cohesion

The energy of the electrical barrier can vary widely as a function of ion concentration. The presence of salt in natural water produces free ions and cations that cause a decrease of the energy barrier, and ultimately an elimination for mid to high salt concentrations. An average salinity of 2‰ is suggested in Drake (1976) for increasing minerals cohesion and allowing aggregation, while Van Leussen (1994) and McAnally (1999) suggest different salt concentrations for different minerals, such as 0.6‰ for kaolinite, 1.1‰ for illite and 2.4‰ for montmorillonite. However, it appears more clearly in Vane & Zang (1997) that the ζ -potential (therefore the cohesion) of kaolinite mineral can be related to salt concentration, Figure 2.2 (a).

An analogous mechanism of double layer compression and consequent decrease in ζ -potential occurs in acid waters. Analyses of the ζ -potential of different types of kaolinite

reported in Vane & Zang (1997) and Yukselen & Kaya (2003) have shown that a decrease in pH , *i.e.* increasing acidity, weakens the ζ -potential of the minerals up to a full elimination for $pH \simeq 2$, Figure 2.2 (b).

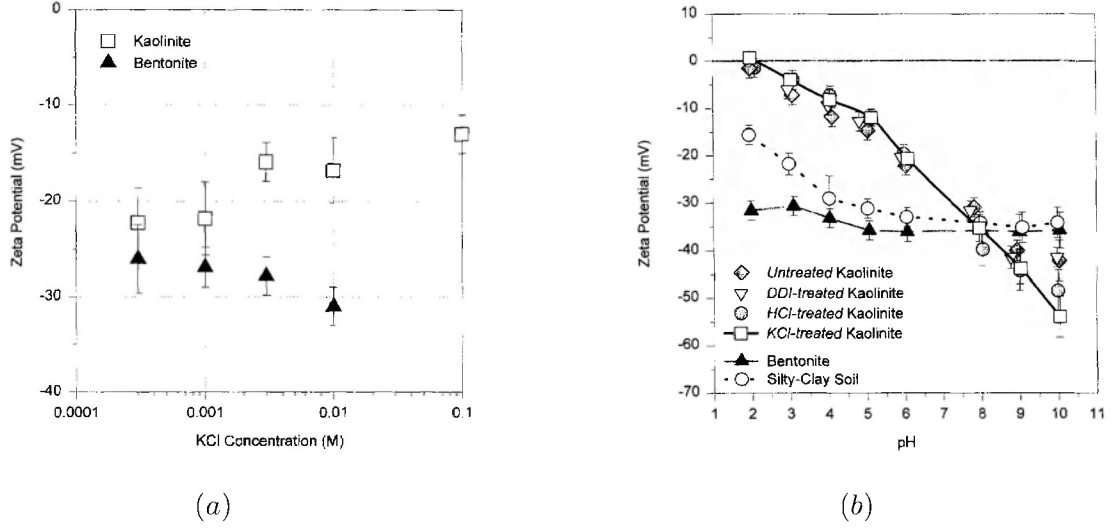


Figure 2.2: (a) representation of the ζ -potential of kaolinite mineral as a function of potassium chloride (KCl) concentration at $pH = 6$ (Vane & Zang, 1997). (b) representations of the ζ -potential as a function of pH due to acid chloride (HCl) (Vane & Zang, 1997).

2.2 Cohesive suspensions and flocculation

Flocculation is the phenomenon by which a cohesive suspension produces flocs from a dispersion of particles. Flocculation is due to *aggregation* and *breakup* processes that, respectively, cause and limit floc growth.

2.2.1 Aggregation mechanisms

The most important mechanism for particle aggregation is the collision amongst particles, which can be described by means of a *collision function* Λ . The mechanisms of collision between two flocs of sizes L_i and L_j are *Brownian motion*, *laminar and turbulent shear*, and *differential settling* (Saffman & Turner, 1956; Broadway, 1978; Hunt, 1980; McCave, 1984; Tsai & Hwang, 1995, *etc.*):

$$\text{Brownian motion} \quad \Lambda_{i,j}^{(BM)} = \frac{2}{3} \frac{KT}{\mu} \frac{(L_i + L_j)^2}{L_i L_j}, \quad (2.1)$$

$$\text{Shear} \quad \Lambda_{i,j}^{(S)} = \frac{\Gamma}{6} (L_i + L_j)^3, \quad (2.2)$$

$$\text{Differential settling} \quad \Lambda_{i,j}^{(DS)} = \frac{\pi}{4} (L_i + L_j)^2 |w_i - w_j|, \quad (2.3)$$

where T is the absolute temperature, μ is the dynamic viscosity of the surrounding fluid, K is the Boltzmann constant, Γ is either $\Gamma = \partial U / \partial z$ for laminar shear in the direction z normal to the mean flow or $\Gamma = G$ for turbulent shear (Section 2.3.1), and w_i and w_j are the

settling velocities. The total collision frequency $\Lambda_{i,j}$ can be derived as linear superposition of the aforementioned terms:

$$\Lambda_{i,j} = \Lambda_{i,j}^{(BM)} + \Lambda_{i,j}^{(TS)} + \Lambda_{i,j}^{(DS)}, \quad (2.4)$$

where $\Lambda_{i,j}^{(TS)}$ corresponds to $\Lambda_{i,j}^{(S)}$ in the case of turbulent flow ($\Gamma = G$). Figure 2.3 shows that $\Lambda_{i,j}^{(TS)}$ and $\Lambda_{i,j}^{(DS)}$ are the most important mechanisms for interparticle collision, while $\Lambda_{i,j}^{(BM)}$ can be considered a negligible factor, especially in estuary and sea waters (Van Leussen, 1994; Winterwerp, 1999). If we focus on $\Lambda_{i,j}^{(TS)}$ and $\Lambda_{i,j}^{(DS)}$ we note that the first

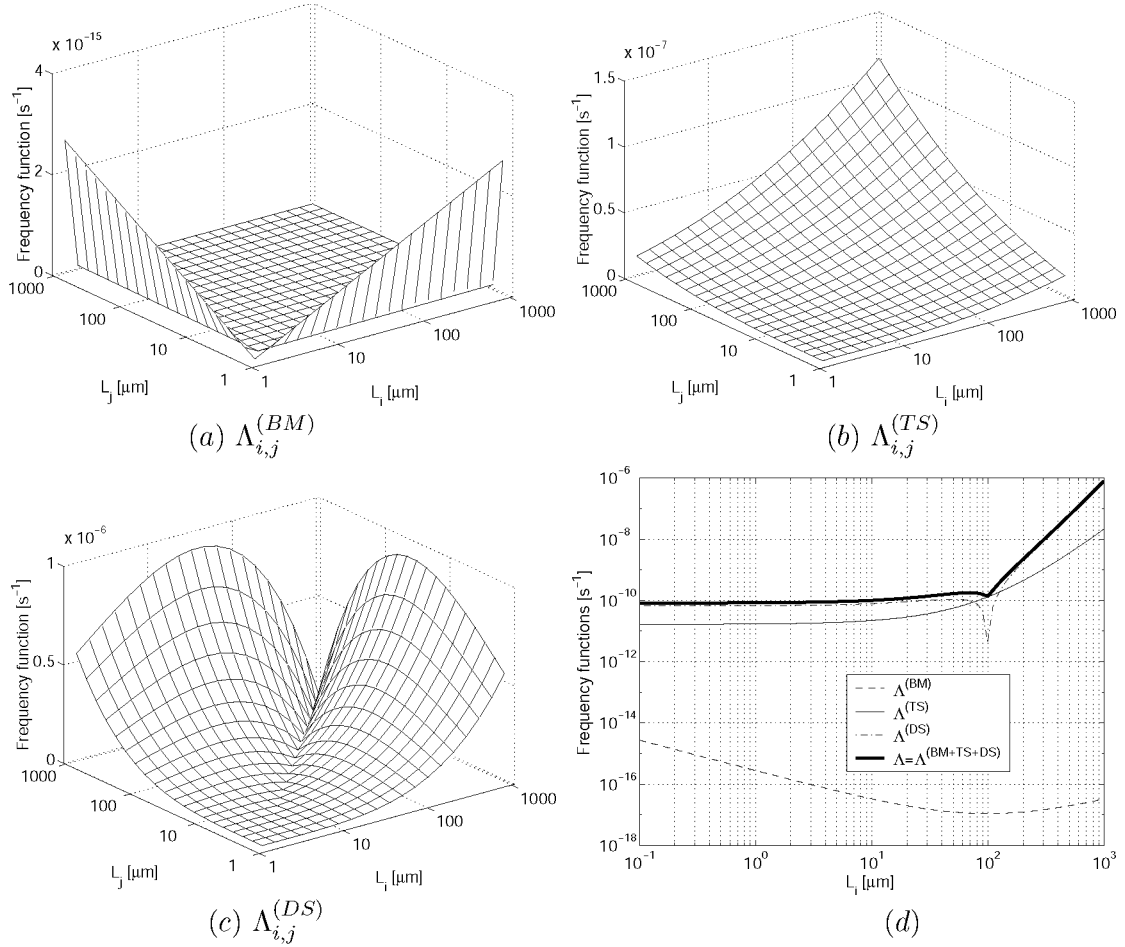


Figure 2.3: (a), (b) and (c) collision frequencies $\Lambda_{i,j}^{(BM)}$, $\Lambda_{i,j}^{(TS)}$ and $\Lambda_{i,j}^{(DS)}$ computed as function of floc size L_i and L_j . (d) cross-section of these functions for $L_j = 100 \mu\text{m}$, with Boltzmann constant $K = 1.381 \cdot 10^{-23} \text{ J} \cdot \text{K}^{-1}$, absolute temperature $T = 293 \text{ K}$, gravity acceleration $g = 9.81 \text{ m} \cdot \text{s}^{-2}$, dynamic viscosity $\mu = 1.02 \cdot 10^{-3} \text{ kg} \cdot \text{m}^{-1} \text{s}^{-1}$, kinematic viscosity $\nu = 10^{-6} \text{ m}^2 \text{s}^{-1}$, turbulent shear rate $G = 100 \text{ s}^{-1}$, $\rho_s = 2500 \text{ kg} \cdot \text{m}^{-3}$ and $\rho_w = 1020 \text{ kg} \cdot \text{m}^{-3}$ (Maggi, 2002).

increases with particle sizes while the second reaches a maximum for a certain relative difference $|L_i^2 - L_j^2|$, and $\Lambda_{i,j}^{(TS)} \rightarrow 0$ when $L_i \approx L_j$. Consequently, $\Lambda_{i,j}^{(DS)}$ can be more important than $\Lambda_{i,j}^{(TS)}$ for increasing $|L_i^2 - L_j^2|$ and for low values of G . However, Stolzenbach & Elimelech (1993) investigated the collision process between two approaching particles with different Reynolds number and size in still water, showing that the hydrodynamic interaction decreases dramatically the probability of collision as $|L_i^2 - L_j^2|$ increases, the

effect that is not taken into account in Eq. (2.3). For this reason, $\Lambda_{i,j}^{(DS)}$ probably has a lower order of magnitude compared to $\Lambda_{i,j}^{(TS)}$, also for small G .

Collision itself, however, does not suffice for aggregation; the effective adherence of two aggregates is described in terms of *collision efficiency* (or sticking probability), *i.e.* the likelihood for two aggregates to adhere and glue together after collision. The collision efficiency is normally written in the form of an empirical coefficient. Van Leussen (1994) and Winterwerp (1999) made use of an efficiency parameter α_c related to the physico-chemical properties of the sediment and the water, to the organic compounds in the sediment (coatings, polysaccharides, *etc.*), and to floc shape and structure. For particles moving by Brownian diffusion (random walk) Valioulis (1983) showed that: (1) hydrodynamic forces dominate the collision process as the Van der Waals forces become of shorter range; (2) hydrodynamic effects also decrease the collision efficiency (this effect is more pronounced for particles of different sizes); (3) the collision efficiency accounting for Van der Waals forces depends on the relative and absolute size of the interacting particles and is proportional to the value of the Hamaker constant (Hamaker, 1937). Following the last indication, the collision efficiency $\alpha_{i,j}$ for two particles of sizes L_i and L_j can be approximated as in Pruppacher & Klett (1978):

$$\alpha_{i,j}^{(1)} = \frac{(L_i/L_j)^2}{2(1 + L_i/L_j)^2}, \quad (2.5)$$

stating that $\alpha_{i,j}$ increases when the ratio L_i/L_j becomes larger. A similar formulation for $\alpha_{i,j}$ was proposed in Friedlander (1957, 1965):

$$\alpha_{i,j}^{(2)} = 1 - \frac{3}{2(1 + L_i/L_j)} + \frac{1}{2(1 + L_i/L_j)^3}. \quad (2.6)$$

The mechanism of aggregation is finally written as the product of the collision efficiency $\alpha_{i,j}$ and collision frequency $\Lambda_{i,j}$.

A further mechanism of floc genesis in natural waters, not related to collision, is due to the biological activity of fish and filter feeders, and goes under the name of *biogenic aggregation*. The frequency $\Lambda_{i,j}^{(B)}$ associated with active particle catching and production by animals is written as:

$$\Lambda_{i,j}^{(B)} = A^{(B)}U\alpha_{i,j}^{(B)}, \quad (2.7)$$

where an organism j is assumed to filter a certain volume of water $V = A^{(B)}U$, where $A^{(B)}$ is the area of water swept at speed U , and $\alpha_{i,j}^{(B)}$ is a capture efficiency depending on the type of organism j , the particle size L_i and the perceived food value $f^{(B)}$. A numerical evaluation of the term $\Lambda_{i,j}^{(B)}$ in McCave (1984) shows that, although relevant in the near-surface and near-bed zones, this contribution can be neglected in the water column.

2.2.2 Breakup mechanisms

Breakup (or disaggregation) occurs to flocs that cannot withstand external forcing, either from the surrounding flow or from collision with other aggregates. Breakup can be described by means of a *breakup frequency* expressing the rate of disruption of flocs, usually divided into *linear* and *nonlinear*. The former ($B_i^{(S)}$) is induced by turbulent shear (Pandya & Spielman, 1982; Spicer & Pratsinis, 1996a), while the latter ($B_{i,\forall j}^{(C)}$) is due to collision

with other aggregates (Serra & Casamitjana, 1998a):

$$\text{Linear} \quad B_i^{(S)} = EG^b \cdot L_i, \quad (2.8)$$

$$\text{Nonlinear} \quad B_{i,\forall}^{(C)} = \sum_{j=1}^N \kappa \Lambda_{i,j} n_j, \quad (2.9)$$

where b and E are empirical quantities. Flesch *et al.* (1999) found values $b = 1.6$ and $E \approx 7 \cdot 10^{-4} \text{ s}^{b-1} \text{m}^{-1}$ by fitting the data of Oles (1992). Serra & Casamitjana (1998b) found $b = 1.65$ for low values of volumetric concentration ϕ , while for $\phi > 6 \cdot 10^{-5}$ the exponent b would increase. In the nonlinear breakup rate, $\Lambda_{i,j}$ is the collision frequency function of Eq. (2.4), κ is the probability of disaggregation by collision and n_j is the number concentration of flocs of given size. The values of κ are not well known at present: it has been argued theoretically to be generally very small, and appreciable only for high and very high volume concentration (Serra & Casamitjana, 1998a).

In analogy to Eq. (2.4), the total breakup frequency can be computed as linear superposition of Eqs. (2.8) and (2.9):

$$B_i = B_i^{(S)} + B_{i,\forall}^{(C)}. \quad (2.10)$$

B_i is expected to increase with G and L , as large flocs are usually observed to be weaker than small ones (Spicer & Pratsinis, 1996b; Serra & Casamitjana, 1998b). Furthermore, B_i increases with volumetric concentration ϕ as the number of collisions and rate of nonlinear breakup increase with ϕ (Serra & Casamitjana, 1998a). Shear breakup has been estimated to be a second-order process within the water column far from a boundary, because a floc is free to rotate according to the surface forcing (Lick and Lick, 1988). Shear and normal forcing may become a dominant mechanism in the near-bed zone, where a brief contact with the bed can greatly increase stresses within the aggregate bulk (Mehta & Partheniades, 1975). More effective in floc breakup seems to be the elongational flow in turbulent mixing, which causes normal and shear stresses on the floc surface (Higashitani & Iimura, 1998). In addition, Lick and Lick (1988) have argued that collision among aggregates (nonlinear breakup) can play a role in the breakup process, but McAnally (1999) suggests nonlinear breakup to occur more frequently in three-body collision. The hydrodynamic interaction of a three-body collision is schematised in Clercx & Schram (1992) as a sequence of two two-body collisions, enabling to consider three-body collision as implicitly accounted for in case of time intervals larger than the breakup time scale.

Higashitani & Iimura (1998) and Higashitani *et al.* (2001) studied the breakup of two-dimensional (2D) and three-dimensional (3D) aggregates exposed to shear flow consisting of 100 mono-distributed primary particles interacting by visco-elastic forces (rheological model). The numerical results showed that: (1) the average number of primary particles in broken fragments is related to the intensity of the shear stresses; (2) aggregates with the same porosity are fragmented in the same fashion; (3) elongational flows are more effective than shear flows in breaking up aggregates; (4) the breakup time scale is very small, approximately 10^{-6} s .

Another quantity necessary to characterise breakup is the *breakup distribution function*, that defines the size distribution of the resulting aggregates. Breakup of a floc produces a number of smaller flocs. At present, scientific literature lacks in experimental investigations on the effective floc breakup dynamics. Only theoretical and numerical works have been reported in literature. For instance, the hypothesis of Friedlander considers a totally

reversible process of breakup for which a floc resulting from aggregation of any two smaller aggregates would return the previous aggregates. Spicer & Pratsinis (1996a) have put forth three different hypotheses for the distribution function $\gamma_{i,j}$ of the aggregates i resulting from floc j : binary, ternary and Gaussian. The first one expresses that only two daughter aggregates are formed with identical mass, equal to $1/2$ of the mother's mass M_f . Ternary breakup produces two flocs with $1/4 M_f$ and one floc with $1/2 M_f$. Finally, Gaussian breakup produces a full spectrum of flocs with a Gaussian mass distribution. Also the numerical results from Higashitani and Iimura mentioned before suggest that a distribution function is more likely to occur in floc breakup rather than a simple binary breakup. Recently, an investigation of fragmentation processes in particulate material has shown that a power-law distribution characterises the resulting fragments (Wittel *et al.*, 2004) but no such relation has been investigated in cohesive suspensions. The mentioned mechanisms may have an impact on the stochastic process of redistribution of particles with different sizes and on the restructuring process of floc structure.

2.3 Turbulence and flocculation

Cohesive sediment in a turbulent flow is subject to *flocculation*. In the following sections, a brief theoretical introduction to turbulence is given in order to characterise turbulence length scales and define the rate of turbulent shear, the quantity which will serve the flocculation model discussed in Chapter 7.

2.3.1 Interaction between turbulence structures and cohesive sediment

Local instantaneous velocities u of a fluid in turbulent motion have a mean component U and a fluctuating component u' . The fluctuating component can be isolated by means of Reynolds decomposition as $u' = u - U$, and it can be characterised by the *autocorrelation function* γ_{τ_d} :

$$\gamma_{\tau_d} = \overline{u'(t)u'(t^*)} = \overline{u'(t^*)u'(t)}. \quad (2.11)$$

where $u(t)$ and $u(t^*)$ are the velocities separated by a time lag $\tau_d = t - t^*$. The autocorrelation function γ_{τ_d} can be normalised with the second order moment $\overline{u'^2}$, which is constant for the stationary variable u' :

$$\frac{\gamma_{\tau_d}}{\overline{u'^2}} = \frac{\overline{u'(t)u'(t^*)}}{\overline{u'^2}} = \rho_{\tau_d}.$$

The area \mathfrak{S} defined by the autocorrelogram ρ_{τ_d} in the (τ_d, ρ) -plane is the *integral time scale* :

$$\mathfrak{S} = \int_0^{+\infty} \rho_{\tau_d} d\tau_d, \quad (2.12)$$

which is a measure of the time interval beyond which $u(t)$ is not self-correlated anymore. It can be interpreted as the largest time scale in a turbulent flow or, correspondingly, related to the size of the largest eddy, *i.e.* equivalent to the depth or width of the flow. The integral scale \mathfrak{S} does not play a central role in flocculation as the interaction water/sediment at large length scales is represented essentially by transport (advection and diffusion) (Parker *et al.*, 1972; McCave, 1984).

More relevant to the flocculation processes is the *Taylor microscale* λ , that is obtained from the zero-centered second derivative of $\rho(\tau_d)$:

$$\left. \frac{d^2 \rho_{\tau_d}}{d\tau_d^2} \right|_{\tau_d=0} = -\frac{2}{\lambda^2}.$$

The Taylor microscale λ is representative of the energy transfer from large to small scales. The process of energy transfer (or energy cascade) is expressed by the energy dissipation rate per unit mass ε . For large Reynolds numbers, the structure of turbulence tends to be approximately isotropic, and ε can be approximated as (Tennekes & Lumley, 1973):

$$\varepsilon = 15 \frac{\nu u^{*2}}{\lambda^2}, \quad (2.13)$$

where u^* is the isotropic fluctuating velocity scale and ν is the kinematic viscosity of the fluid. The rate of turbulent shear is defined within this context as:

$$G = \sqrt{\frac{\varepsilon}{\nu}}, \quad (2.14)$$

with $G \propto u^*/\lambda$ from Eq. (2.13), *i.e.* neglecting the factor $\sqrt{1/15}$. Eq. (2.14) expresses the turbulence-induced contribution to the frequency of collision $\Lambda_{i,j}^{(S)}$ in flocculating particles, Section 2.2.1.

The Taylor microscale λ is not the smallest length scale occurring in turbulence. At very small length scales, viscosity becomes effective in smoothing out velocity fluctuations, hence preventing the generation of infinitely small scales by dissipating small-scale energy into heat. The smallest scale of motion automatically adjusts itself to the value of the viscosity. Relating viscosity ν and energy dissipation rate ε , we can write the *Kolmogorov microscales* of length η_k , time τ_k and velocity v_k :

$$\eta_k = (\nu^3/\varepsilon)^{\frac{1}{4}}, \quad \tau_k = (\nu/\varepsilon)^{\frac{1}{2}}, \quad v_k = (\nu\varepsilon)^{\frac{1}{4}}, \quad (2.15)$$

where η_k is the size of the smallest eddies. The small length scales are relevant for the forcing on the aggregates' surface and for bringing aggregates distant from one another to collision. Flocculation is predominantly caused by turbulent mixing. The rate of turbulent shear G is also expressed as $G = \nu/\eta_k^2$, showing that active interaction between fluid and aggregates in flocculation phenomena occurs at small and very small (Taylor-to-Kolmogorov) scales, and such that $G = \tau_k^{-1}$. Turbulent mixing induces aggregation and, at the same time, subjects aggregates to higher shear stresses, hence causing breakup if $L \approx \eta_k$. For $L > \eta_k$ there may be floc surface erosion (McCave, 1984); however, experimental investigations (Mikes *et al.*, 2002) and numerical simulations (Higashitani & Iimura, 1998; Higashitani *et al.*, 2001) have hardly found aggregates with $L > \eta_k$. Thus, floc surface erosion is unlikely to occur and will be omitted in this thesis.

2.3.2 Rate of shear and flocculation

Clay minerals are very sensitive to the electrochemical double layer forces. The primary particles are, therefore, rather stable against turbulence action, *i.e.* they do not break up. Low-to-mid values of shear rate ($G \approx 10 \div 100 \text{ s}^{-1}$) aids flocculation reactions, increasing

collision among the particles and producing flocs. In contrast, large flocs are strongly affected by higher turbulent shear ($G > 100 \text{ s}^{-1}$) because the internal bonds are weaker than those of the primary particles. This explains the sensitiveness of the modal floc size to G , as observed in several experimental campaigns and numerical simulations (Parker *et al.*, 1972; Dyer, 1989). In Figure 2.4 it is qualitatively suggested that the modal floc size reaches a maximum at a given G^* for limited residence time. The effect of G is however wider, affecting the full shape of the floc size distribution: very high and very small G are in general correlated to left-skewed floc size distributions, whereas $G \approx G^*$ result in right-skewed floc size distributions (Auger, 2004).

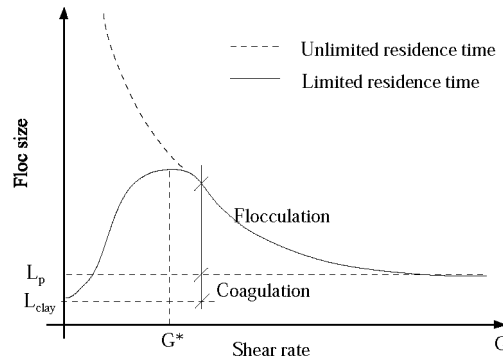


Figure 2.4: Qualitative representation of the modal floc size \tilde{L} against G for limited and unlimited residence time (Winterwerp, 1999).

2.4 Description of the aggregate structure

The structure of an aggregate is the result of flocculation processes, torquing and deformation due to turbulence and collision with other aggregates, consolidation, *etc.* At the same time, floc structure governs the response to different forcing and to the interaction with other aggregates, as floc strength depends on the size, shape, compactness, *etc.* In the next sections we survey the quantities that can be used to characterise the floc structure.

2.4.1 Size

Although natural flocs are rather irregular, a correlation between floc shape and forming mechanisms has been found. For example, elongated and chain-like large flocs are produced in low shear conditions, often present in deep-ocean waters (Wells & Goldberg, 1993). Aggregates formed by differential settling in laboratory experiments appear crescent-shaped in 2D photos (Lick *et al.*, 1993), while spherically-shaped small flocs are typical of high shear rates in estuaries (Van Leussen, 1994).

A number of studies have been presented in the literature to characterise the shape of flocs. Amongst them, we only mention a *static structure factor* which takes into account the compactness of the network of primary particles and the interparticle distance. Gmachowski (1996) suggests that the value of the static structure factor can change slightly, affecting the hydraulic flow through the aggregates, hence their settling velocity. A parallel study of a combination of several structural parameters of an aggregate was carried out by Serra & Casamitjana (1998a), confirming Gmachowski's results. However, no experimental

evidence has been found by the author in the literature that flocculation would be affected by fluid flow through the flocs. Rather, flow around a floc can be effective in increasing drag forces due to surface roughness.

The size L is more significant to characterise the suspended aggregates, despite the problem in defining the linear size (or diameter or length scale) of aggregates appearing randomly-shaped. Currently no unique or generally accepted standard definition of floc size exists among scientists dealing with cohesive sediment. The most common definitions of size are the gyration diameter, the hydraulic diameter, the diameter of the circumscribing sphere, the Feret diameter, or some geometric average of sizes measured in different directions. Associating, for instance, a sphere or a cube with a randomly-structured body is an equally arbitrary choice; whatever a floc looks like, it is neither a sphere nor a cube. However, choosing to describe a floc with a sphere or a cube can have important numerical consequences. An analysis in Maggi (2002) shows that the use of the gyration radius as well as other size estimators for the computation of fractal attributes does not satisfy geometrical limits, and does not return the effective fractal dimensions of test bodies. This means that some coefficients would be required, and that they should be calibrated. A convenient way to circumvent this was the use of the size of the smallest square $\subset \mathbb{R}^2$ or cube $\subset \mathbb{R}^3$ enveloping a floc. Tests performed on objects with known fractal dimensions show that this definition of size does not require coefficients and always gives the expected fractal dimensions. When working on 2D images, the size L of the smallest square circumscribing the aggregate will be used as the floc linear size in view of the theoretical and computational analyses of the fractal properties in the following chapters. This size L is then used to derive the dimensionless size ℓ' :

$$\ell' = L/L_p, \quad (2.16)$$

of an aggregate, where L_p is the average primary particle size.

2.4.2 Fractal description

The recursive building of cohesive sediment flocs suggests that floc growth occurs by multiplicative steps, as proposed in Kranenburg (1994). This gives a conceptual framework to describe floc structure as sketched in Figure 2.5, where several orders of aggregation are represented according to Krone (1963) and Van Leussen (1994). For this reason, the fractal approach has found application in describing aggregates as fractal structures, such that the floc mass M_f scales as a power of its dimensionless size ℓ' : $M_f \propto \ell'^{d_C}$. The exponent d_C is the capacity dimension (or *Hausdorff-Besicovitch dimension*, Vicsek, 1992):

$$d_C = \frac{\log[N_p]}{\log[\ell']}, \quad (2.17)$$

with N_p the number of primary particles. The capacity dimension d_C is a measure of how the constituting particles fill the embedding space, *i.e.* the Euclidian space which envelops an aggregate. An estimation of d_C based on the settling velocity of estuarine flocs in the water column shows that $d_C : 1.7 \lesssim d_C \lesssim 2.3$ (Winterwerp, 1999).

The *perimeter-based* fractal dimension d_P is also used to characterise the aggregates (Spicer & Pratsinis, 1996b; Meakin, 1998):

$$d_P = 2 \frac{\log[P]}{\log[A]}, \quad (2.18)$$

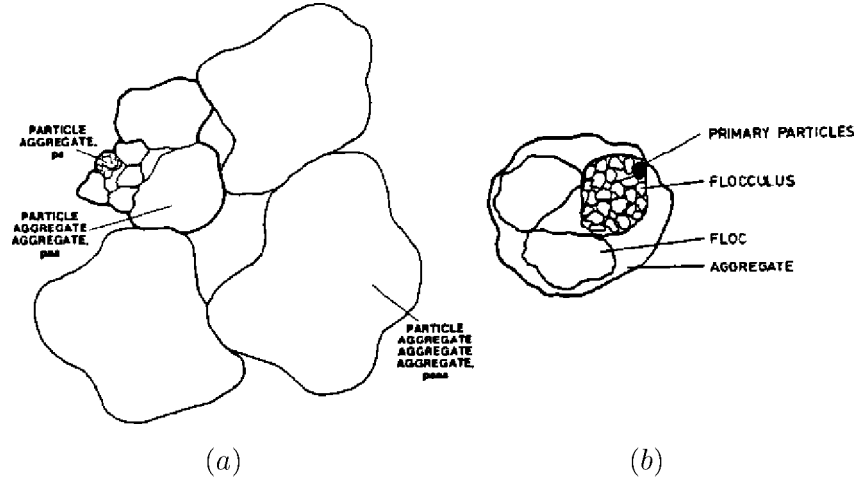


Figure 2.5: Aggregate description according to (a) Krone (1963) and (b) Van Leussen (1994).

where P and A represent the dimensionless perimeter and area of the projected image of a floc in \mathbb{R}^2 , such that $1 \leq d_P \leq 2$ ¹. De Boer *et al.* (2000) noted that flocs in streams have lower values of d_P upstream and during snowmelt rather than downstream. Analogously, Spicer & Pratsinis (1996b) reported that large flocs are in general more segmented than small flocs.

The use of the fractal approach, especially of d_C , may overcome the use of other generic shape and structure factors mentioned in Section 2.4.1, as the compactness properties of the net structure (space filling ability, density, *etc.*) can be scaled through d_C .

2.4.3 Porosity

The pore system in a floc is strongly related to the space-filling ability of the floc matrix, hence to the fractal dimension d_C . An aggregate is assumed to be characterised by a uniform effective internal permeability corresponding to its average porosity. By definition, an aggregate of fractal dimension $d_C = 3$ constitutes a massive (Euclidian), non porous space-filling structure, while an aggregate with $d_C < 3$ has a weaker space filling ability, which results in larger porosity (Gmachowski, 1996). When the porosity is higher than zero, water is incorporated inside the floc structure.

2.4.4 Primary particle number in a floc and excess density

An estimation of the number N_p of primary particles within a floc can be obtained from the definition of capacity dimension of Eq. (2.17):

$$N_p = \left(\frac{L}{L_p} \right)^{d_C} = \ell^{d_C}. \quad (2.19)$$

The excess density of a floc with respect to water can be determined as (Gmachowski, 1996; Serra & Casamitjana, 1998b; Kranenburg, 1994; Winterwerp, 1999):

$$\rho_{r,f} = (\rho_s - \rho_w) \ell^{3-d_C}, \quad (2.20)$$

¹The perimeter-based fractal dimension $d_P = 1$ corresponds to lowly-segmented, regular shapes, while $d_P = 2$ corresponds to highly-segmented, irregular shapes.

with ρ_s and ρ_w the sediment and water density respectively.

2.5 Approach to modelling of flocculation

Population dynamics describes the changes in the number and composition of individuals within a generalised population, and the factors that influence those changes. Several approaches, based on the so-called *population balance equations*, have been proposed for cohesive sediment: some authors have used numerical (Monte Carlo) simulations (Vicsek, 1992), while others have used Eulerian formulations (Friedlander, 1977; O'Melia, 1980, 1986; Winterwerp, 1999, 2002), and Lagrangian formulations (Smoluchowski, 1917; Lick and Lick, 1988; Winterwerp, 1998). In parallel to the population dynamics, also the growth of individual flocs can be modelled (Vicsek, 1992; Meakin, 1998; Winterwerp, 1998).

2.5.1 Population balance equations

Most of the models proposed in literature make use of the number concentration n of aggregates per unit volume, although the bulk volumetric concentration ϕ and the mass concentrations c are important in practice. Under certain assumptions, n , c and ϕ are related to each other through the floc size L by simple algebraic equations (Kranenburg, 1994; Winterwerp, 1999).

The first fundamental work concerning aggregation processes was carried out by Smoluchowski (1917), who derived the time variation of the number concentration n of a mono-disperse system as a function of the rate of shear G , a rate of growth Λ^* , and a volumetric concentration ϕ . A limitation was that flocculation was not associated with any aggregation and breakup mechanism explicitly and it did not imply any mass balance and floc property, as the aggregates in the control volume were simply characterised by n . Only after several years Smoluchowski's equation was extended to a discrete floc size distribution where a number of processes were modelled explicitly. A generalised population balance equation comprises, for each size class n_k , the following contributions:

$$\frac{\partial n_k}{\partial t} + \mathcal{A} = \mathcal{G}_A - \mathcal{L}_A + \mathcal{G}_B - \mathcal{L}_B + \mathcal{G}_C - \mathcal{L}_C + \mathcal{G}_W - \mathcal{L}_W + \mathcal{D} \pm \mathcal{P}, \quad (2.21)$$

where \mathcal{A} is an advection term, \mathcal{G}_A is the gain in number concentration n_k due to aggregation of smaller flocs and \mathcal{L}_A is the loss in n_k due to aggregation with other particles. Similarly, \mathcal{G}_B is the gain in n_k caused by shear (linear) breakup of larger flocs and \mathcal{L}_B is the loss due to breakup of flocs belonging to class k . Again, \mathcal{G}_C is the gain for collision (nonlinear) breakup process while \mathcal{L}_C is the corresponding loss. The terms \mathcal{G}_W and \mathcal{L}_W are the gain and loss of flocs in n_k due to settling, \mathcal{D} takes into account turbulence and Brownian diffusivity while \mathcal{P} represents a term of production of particles due to chemical and/or biological activity.

However, not all the terms in Eq. (2.21) are always present in the population balance equations proposed in literature. For instance, Friedlander (1977) accounts for aggregation (\mathcal{G}_A , \mathcal{L}_A), breakup (\mathcal{G}_B , \mathcal{L}_B) estimated on the basis of floc strength according to Jeffrey (1992), Brownian and turbulent diffusivity (\mathcal{D}), and particle removal by settling (\mathcal{G}_W , \mathcal{L}_W). In Friedlander's model, each collision is assumed to result in aggregation, and breakup is only due to shear (linear breakup) with a binary distribution function. More important, flocs are treated as regular (Eulerian) spheres, *i.e.* fractal description of flocs is not adopted.

A similar model proposed in O'Melia (1980, 1986) describes the rate at which the particle number concentration n_k of floc size L_k changes with time by means of aggregation (\mathcal{G}_A , \mathcal{L}_A), accounted for by a collision function of the form of Eq. (2.4), and a collision efficiency parameter α reflecting the particle's stability and surface chemistry, Section 2.2. Horizontal advection (\mathcal{A}) and settling (\mathcal{G}_W , \mathcal{L}_W) are also accounted for, together with a rate of floc production or disruption (\mathcal{P}) by biological presence and chemical agents. Remarkably, breakup is ignored in O'Melia's equation, and aggregates are Eulerian spheres.

Similar discrete models with some conceptual improvements and/or simplifications have been proposed in a number of papers (Hunt, 1980; Farley & Morel, 1986; Krishnappan, 1989; Lick *et al.*, 1993; Lee *et al.*, 1997; Serra & Casamitjana, 1998a). Amongst these, the population equation proposed by Lick and Lick (1988) accounts for aggregation as in the previous formulations, but breakup is given by linear (\mathcal{G}_B , \mathcal{L}_B) and nonlinear (\mathcal{G}_C , \mathcal{L}_C) contributions, assuming that breakup redistributes the resulting fragments through a breakup distribution function, Section 2.2.2. This model neglects advection, diffusion and settling terms (differing from Friedlander's and O'Melia's equation), and flocs are described as porous spheres, but no fractal description does appear explicitly.

An approach similar to Smoluchowski's model is proposed in Winterwerp (1998) in which the fractal description of the aggregates is taken into account explicitly:

$$\frac{\partial N}{\partial t} + \frac{\partial}{\partial x_i} \left\{ \left[u_i - \delta_{i3} \frac{(1-\phi)(1-\phi_p)}{(1-2.5\phi)} w_{s,r} \right] N \right\} - \frac{\partial}{\partial x_i} \left[(\varepsilon_M + \Gamma_T) \frac{\partial N}{\partial x_i} \right] = -k'_A(1-\phi_*)GL^3N^2 + k_B G^{q+1}(L-L_p)^p L^{2q} N, \quad (2.22)$$

where ϕ and ϕ_p are the volumetric concentration of the suspension and primary particles, $\phi_* = \min\{1, \phi\}$, ε_M is the molecular diffusion coefficient for mud flocs, Γ_T is the eddy diffusivity, and $p = 1/2$ is a parameter derived from the balance between shear stresses and floc strength, and $q = 3 - d_C$ (Winterwerp, 1998). Eq. (2.22) describes the time evolution of the number concentration N in a 3D domain, where aggregation, breakup, advection and hindered settling are accounted for. The parameters for aggregation and breakup k'_A and k_B are defined as follows:

$$k'_A = \frac{3}{2} \alpha_c \pi e_d \quad \text{and} \quad k_B = a_{eb} L_p^{-p} \left(\frac{\mu}{F_y} \right)^q, \quad (2.23)$$

where α_c is discussed in Section 2.2.1, e_d is a diffusion efficiency, a_{eb} is a breakup efficiency and F_y is the floc strength.

In Chapter 7 we return to some of the concepts and formulations presented here, and we propose a modified Smoluchowski equation implementing floc properties.

2.5.2 Floc growth

It is possible to identify a number of growth regimes involving particulate systems, amongst which the most significant are Diffusion-Limited Aggregation (DLA) and Cluster-Cluster Aggregation (CCA), Vicsek (1992) and Meakin (1998). One of the techniques to investigate particulate systems comes from computational physics and consists of Monte Carlo simulations. Although this is not directly connected to flocculation of cohesive sediments, important behaviours have been highlighted, especially concerning fractal growth processes.

DLA takes into account the binding of particles which get in contact by diffusive motion (random walks), stick irreversibly to an initial fixed particle and, eventually, form one large

aggregate. For high sticking probability, aggregation results in characteristic flocs as shown in Figure 2.6 (a). CCA is the growth of interacting aggregates by diffusion in a control volume. The system is in general initialised with a random spatial distribution of non-aggregated particles that collide and result in a population of aggregates. These may themselves join further, resulting in extensive cluster-to-cluster connected aggregates. The mean cluster size increases in time and, in principle, all the particles become part of one large cluster after a sufficiently long period, Figure 2.6 (b). Also in this case, the collision

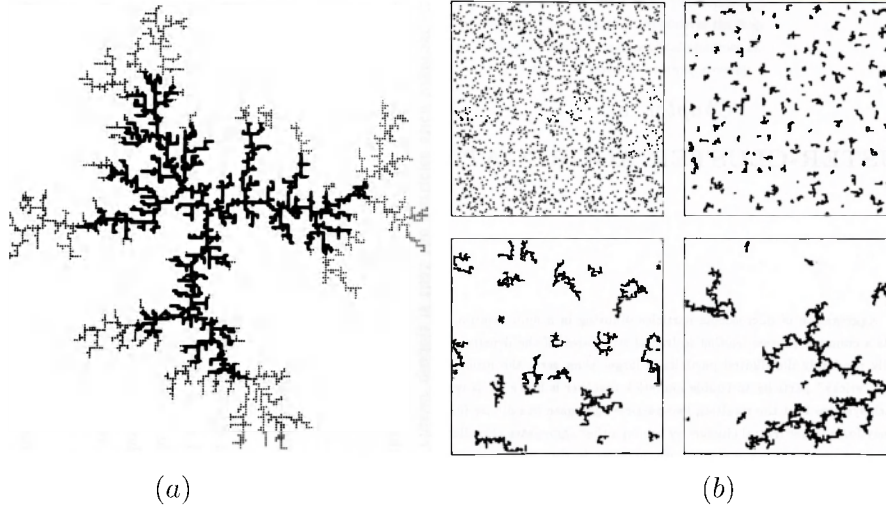


Figure 2.6: 2D DLA (a) and CCA (b) aggregates produced on a discrete Lattice-Boltzmann domain.

efficiency is high, but different rules can be implemented such that several reaction modes can be simulated. One of the most important achievements of these approaches to floc growth is that scaling behaviours can be detected. In particular, aggregates in \mathbb{R}^3 produced by DLA have $d_C \approx 2.5$, while aggregates produced by CCA have $d_C \approx 1.8$ (Vicsek, 1992). Real mud flocs are observed to have, in average, capacity dimension $d_C \approx 2$, Section 2.4.2, and they are formed similarly to CCA processes. Yet, the capacity dimension of real flocs can change by deformation of floc structure.

Other paths can be followed to model floc growth. For example, the Lagrangian time evolution of the modal floc size of sediment in estuaries and sea waters is proposed in Winterwerp (1998), according to the following generalised formulation:

$$\frac{dL}{dt} = k_A G L^{4-d_C} - k_B G^{q+1} L^{2q+1} (L - L_p)^p, \quad (2.24)$$

with:

$$k_A = k'_A \frac{L_p^{d_C-3}}{d_C f_s \rho_s}, \quad k_B = k'_B \frac{L_p^{-q}}{d_C} \left(\frac{\mu}{F_y} \right)^q, \quad (2.25)$$

where k_A and k_B are the dimensional aggregation and breakup parameters, where q and p are given in Section 2.5.1. This equation accounts for aggregation and breakup solely, which are modelled in a parametric manner. The aggregation rate depends on a floc shape factor and sediment density while breakup considers floc strength, Section 2.2.2. Both aggregation and breakup parameters are functions of the fractal dimension.

2.6 Discussion

This chapter is concluded with a discussion on a few open questions on specific features of flocculating systems. With respect to the objectives stated in Chapter 1, two main aspects require further study: the first is the behaviour of reorganisation displayed by fractal units within a population evolving from a non-flocculated towards a flocculated state, while the second concerns the extent to which the fractal structure of mud flocs is related to the formative mechanisms. It is evident that these aspects need to be treated together to some degree.

2.6.1 On the small scales: flocs as growing individuals

In recent years, the fractal approach has shown the capability to characterise floc properties over a wide spectrum of features. The first proposition in fractal theory is the scale-invariance, or *self-similarity*, of geometrical quantities. This means that the capacity dimension d_C is a "static" property, constant over all scales. According to Wiesner (1992), Vicsek (1992) and Meakin (1998), the value of d_C would depend on the particular regime of growth (DLA, CCA, Section 2.5.2). Recently Chakraborti *et al.* (2003), Stone & Krishnappan (2003) and Gardner *et al.* (1998) have observed in laboratory experiments that the average $\overline{d_C}$ decreases in time during flocculation. As this behaviour is not understood, it might be assumed that d_C varies with local turbulence scales and primary particle presence in the control volume, or that, perhaps, variations in d_C are intrinsic to flocculation dynamics, therefore autonomous. Indeed, flocculation is driven by *stochastic* processes which form *randomly* structured flocs. The floc structure can further change in time in a random way due to the readjustment of the primary particles to the forcing. The floc structure can therefore be inferred to be irregular and not fully self-similar. Consequently, we may anticipate that the capacity dimension of a population of fractal flocs is not a *universal* (or system) constant but a quantity that changes locally because of (or determines locally) the evolution of the aggregates in the system itself. For this, d_C may be statistically distributed as well as any other random variable or, for instance, be correlated to L .

Quantities which are sensitive to variations in capacity dimension are, in particular, floc permeability and porosity (Gmachowski, 1996), capture (aggregation) efficiency (Winterwerp, 1999), floc strength (Kranenburg, 1994), distribution of aggregates resulting from linear and nonlinear breakup (Higashitani & Iimura, 1998) and settling velocity (Winterwerp, 1998). For this reason, determining the capacity dimension becomes underpinning for a proper modelling of floc morphodynamics within a population balance equation. To this purpose, the concept of self-similarity in the fractal theory sets a starting point to fully describe floc geometry. However, the generalised dimensionality (multifractal spectrum or spectrum of fractal dimensions) and entropy functions will be used as more advanced tools to evaluate the "degree of self-similarity" of real mud flocs. This analysis, pursued in Chapter 3, will provide new information to phenomenologically describe the mechanisms of aggregation and breakup, and implement them in a mathematical model.

2.6.2 On the large scales: populations of interacting individuals

Population balance equations formulated in the past have been able to characterise, describe and predict the behaviour of cohesive sediment only partly. Although, on the one hand, the larger part of population balance equations do consider a full spectrum of floc

sizes, the major ill-posed aspect is that floc properties are not incorporated, as only spherical aggregates are considered. On the other hand, fractal properties have been neatly measured in both laboratory and *in situ*. These have been accounted for in Winterwerp's Lagrangian and Eulerian formulations, but not within a population of aggregates, Section 2.5.1. The two formulations (population balance equation and the fractal approach in Winterwerp's Lagrangian equation) seem to be complementary and the possibility to merge the two approaches would lead to a more complete formulation of the flocculation processes. Therefore, the basis for implementing a new population balance equation is to account for a *population* of *fractal* individuals organised over different sizes. This is elaborated in Chapter 7.

2.6.3 A comprehensive view

One of the major issues which has to be highlighted is the kinematics (how) and the dynamics (time evolution) of a population of interacting *fractal units*.

Within this context, the suspended particle matter cannot simply be characterised by mean quantities (e.g. concentration or floc size) but local, individual quantities are required as well (e.g. fractal dimensions, entropy distribution, mass-density distribution of individual aggregates and organisation of the full system). Small particles form aggregates. Aggregates hence constitute a population, whereas the large number of interactions causes the population to evolve into dominant and weak individuals, whose properties emerge progressively and are not present in the primary units. This aspect is fundamental in the behaviour of cohesive particle systems because, apparently, some large-scale manifestations show up independently from the outside world. In other words, part of the complex manifestation of the suspended particle matter at population and floc scales is inseparable from the "particle nature" of those systems (*i.e.* detectable only when a large number of particles may interact) and, to a given extent, independent from the nature of the system itself (*i.e.* some particular dynamical features are universal).

New approaches in the theory of nonlinear complex systems seem to be able to provide a phenomenological characterisation of the governing processes (Maturana & Varela, 1972; Nicolis & Prigogine, 1974; Vicsek, 1992; Argyris *et al.*, 1994; Meakin, 1998). For instance, self-organising (self-adjusting) systems have been studied in different fields of science with application to multi-disperse systems and population dynamics. The concept of self-organisation might also give a measure of the deterministic patterns present in the dynamics of such systems, aiding the traditional approach to flocculation equations. Following this direction, a platform to analyse flocculation as mentioned in Sections 2.6.2 and 2.6.1 is set up in Chapter 3.

Chapter 3

Phenomenological description and characterisation of flocculating systems

Flocculation processes in aquatic suspensions of cohesive sediment particles govern the small-scale structural properties of individual flocs as well as the large-scale character of populations of these. In this section, we explore the meaning of the attribute *large* and *small* when referring to the scales. Further, we discuss some properties of the system at these scales and the extent to which they are correlated.

3.1 Phenomenology of flocculation at large scales

The phenomenon of flocculation of cohesive sediment is part of several processes that occur at a broad range of time and length scales, therefore correlated, for instance, to geophysical formation of the sediment, climate variation, biological activity, human activity, *etc.* Flocculation occurs when cohesive particles in a medium aggregate and break up. However, this is not enough to describe flocculation phenomenologically; as discussed in Chapter 2, aggregation occurs because of temperature, mixing or gravity. Similarly, breakup occurs when shear stresses exceed floc strength. Still, this is not enough. To elucidate the nature of flocculation, the suspended sediment is reduced to its elementary constituents, *i.e.* the primary particles. Next, we elaborate, conceptually, the type of manifestations that emerge from such an elementary system, and we relate these to the associated dynamical equilibrium by means of simple concepts.

3.1.1 Spatial entropy and organisation in flocculating systems

The Floc Size Distribution (FSD) changes shape during flocculation, and the modal floc size \tilde{L} shifts from the size of the primary particles L_p towards dominant aggregate sizes, Figure 3.1. This re-shaping is a consequence of the transformation of a large set of primary particles into a smaller set of larger aggregates. Let us explore such a transformation, and its implication, from the point of view of the (large) system scales.

Consider a closed domain in which a set of $N \gg 1$ particles can move freely by random walks, and where only energy transfer (no mass transfer) is allowed, Figure 3.2. The state

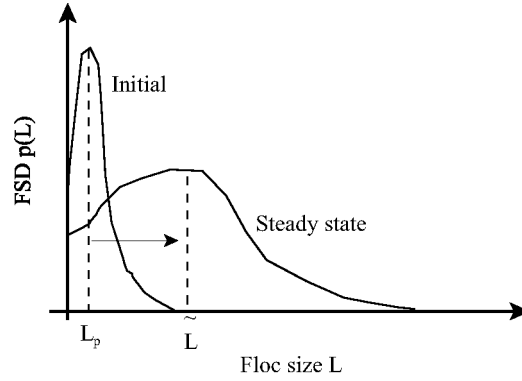


Figure 3.1: Qualitative floc size distributions for an initial (non-flocculated) and steady state (flocculated) population of cohesive sediment flocs.

of the system can be characterised by means of the total particle distance H :

$$H(t) = \sum_{i=1}^{N-1} \sum_{j=i+1}^N d(\mathbf{p}_i, \mathbf{p}_j, t), \quad (3.1)$$

where $d(\mathbf{p}_i, \mathbf{p}_j, t)$ is the distance between any two particles i and j at positions \mathbf{p}_i and \mathbf{p}_j at time t . Consider first particles that collide elastically (case C1) and preserve their kinetic energy (fully conservative system). Since there is no aggregation, the system does not change its structure in time, therefore $H_{C1}(t_\infty) = H(t_0) = \text{const } \forall t$ except for small oscillations due to random displacement of the particles, Figure 3.2 (a).

Let us now introduce cohesive properties (case C2) such that each collision results in particle aggregation and that aggregates larger than a critical size L_c break up into the original primary particles. In a short time this (dissipative) system will display a size distribution with a number of fractal aggregates $N_a < N$. $H_{C2}(t)$ has an asymptotic limit at $H_{C2}(t_\infty) \leq H_{C1}(t_\infty) = H(t_0)$, Figure 3.2 (b).

Penultimately, consider the case that aggregates cannot breakup (case C3), *i.e.* one large fractal aggregate will grow catching all the primary particles, Figure 3.2 (c). This implies $H_{C3}(t_\infty) \leq H_{C2}(t_\infty)$, because now $N_a = 1 \ll N$.

Finally, consider the primary particles to result in the nucleation of a unique crystal (case C4), *i.e.* particles stick if and only if collision occurs at a precise location and configuration of the neighbour particles. This system will manifest a fully-dense Euclidian structure, with $H_{C4}(t_\infty) \leq H_{C3}(t_\infty)$, because all the particles are collected in the most dense structure, Figure 3.2 (d).

The quantity H is a measure of the spatial distribution of the particles, therefore it is a measure of the large-scale organisation (and, in some geometrical sense, of the *spatial* disorder or entropy) of the system. For the scheme in Figure 3.2 we write $H(t_0) \geq H_{C1}(t_\infty) \geq H_{C2}(t_\infty) \geq H_{C3}(t_\infty) \geq H_{C4}(t_\infty)$, as the disorder decreases for increasing level of organisation. Under certain conditions some systems may show Euclidian organisation (crystal), that is the highest level of order (C4). In most cases the spatial organisation is less regular (C2 and C3), *i.e.* fractal-organised, or even fully disordered, like in gases (C1).

The conceptualisation of flocculation in terms of geometric organisation does not suffice for a full and precise characterisation of the system. Therefore, the quantity H , although scaling to some extent with a geometrical entropy, cannot be used alone as *the* entropy of the system. For example, consider the particles to be the white boxes of a chessboard;

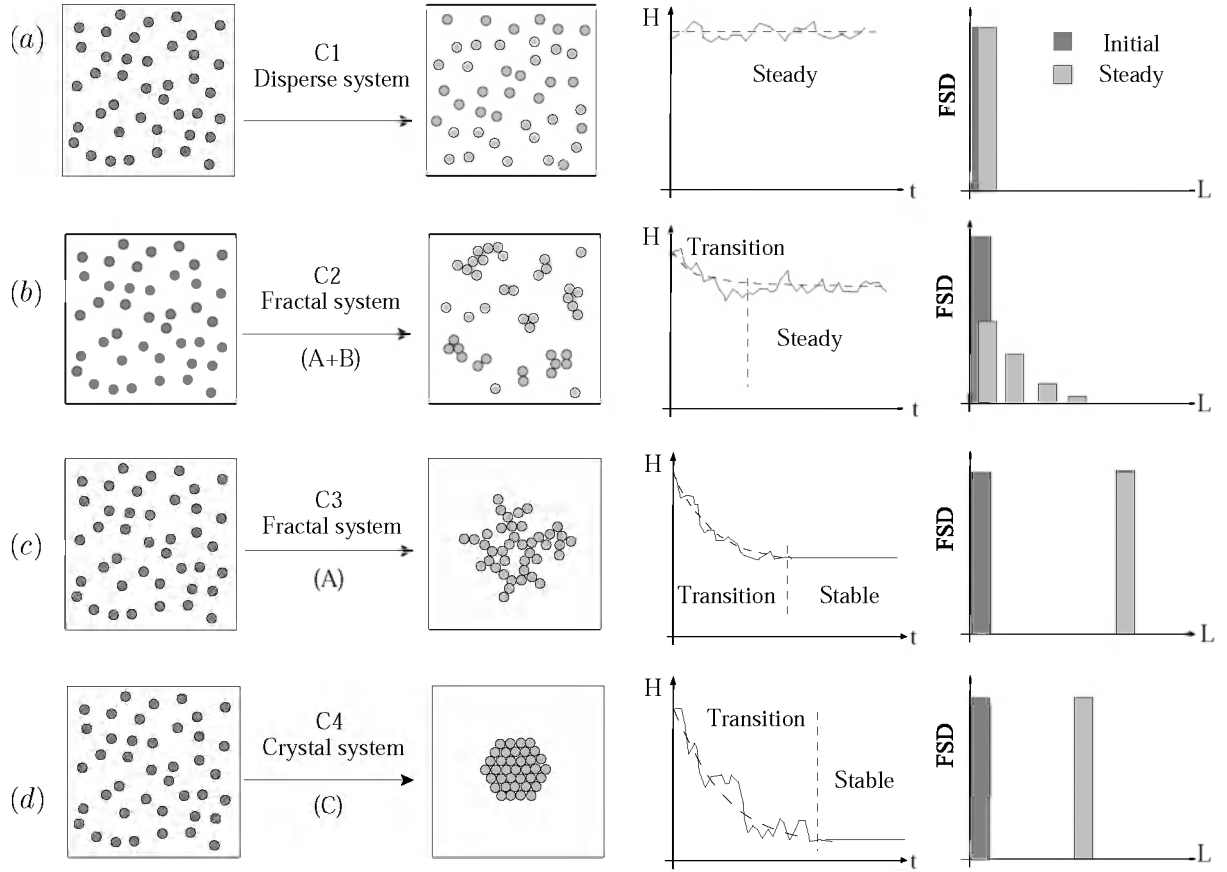


Figure 3.2: Various organisation levels in an evolving particle system. System C1 is not subject to any aggregation and breakup process; system C2 is subject to both aggregation and breakup ($A+B$); system C3 is subject to aggregation (A) solely; system C4 is subject to crystallisation (C). The evolution is here characterised by means of the total particle distance H and by the floc size distribution FSD .

in this case H is maximum, but no disorder appears in a chessboard-like particle spatial organisation, because this represents the most organised and spread (homogeneous) configuration of particles. Though, if we neglect extreme cases that are not likely in natural conditions (aggregates in a real suspension do not distribute in a 3D chessboard-like matrix or, at least, the chances for that are exceedingly small), then H can be seen as indicator of the spatial order of the system within a given domain. A more specific analysis of the entropy variation within a flocculating system is reported in Hermanowicz (2004), where a decrease in entropy is shown to be consequent to both geometric and chemical contributions. A similar approach was already attempted by R. Krone, who measured the temperature of an isolated flocculating sludge suspension. He observed a decrease in temperature, meaning that the thermodynamic entropy was decreasing during coagulation (Krone, unpublished work; Winterwerp, personal communication).

3.1.2 Far-from-equilibrium dynamics in flocculating systems

In terms of equilibrium dynamics, system C1 does not show structural changes in the absence of damping processes and cohesion properties, except for statistical fluctuations of H which have no counterpart in the population organisation. Both systems C3 and

C4 (only aggregation and crystallisation) reach a *stable equilibrium*, as reactions no longer occur for $t \rightarrow \infty$. System C2 approaches, differently, a *steady* (statistically stationary) state. The state is stationary because aggregation and breakup attain a balance, and it is statistically steady because only noisy (random) fluctuations are responsible for changes in the FSD. These fluctuations are caused by stochastic processes of aggregation and breakup, that are continuous in time and hold also for $t \rightarrow \infty$. In the real world, aggregation and breakup are powered by a supply of energy from outside the system, the energy which is dissipated in collision, deformation, breakup, *etc.* This dynamical state is called *far-from-equilibrium* state (Nicolis & Prigogine, 1974)¹. The distance from the equilibrium can be quantified, for the example in Figure 3.2, by the quantity H (Nicolis & Prigogine, 1974), which is assumed proportional to the entropy content (or at least to part of it - the geometric share) of the system and reciprocal to the exergy² (Hermanowicz, 2004; Dincer & Cengel, 2001). Basically, dissipative systems evolving far from an equilibrium display a decrease in entropy (or disorder), corresponding to an increase in organisation, that can be maintained only through a continuous supply of energy (Collier & Hooker, 1999; Kay, 2002).

3.1.3 Feedback loops in flocculating systems

Flocculation can be conceptually depicted by C2-systems, since flocs may grow to a critical size (the maximum stable floc size - normally not larger than the Kolmogorov length scale, Section 2.3.1), beyond which they are not stable. Aggregation and breakup are *stochastic processes* that reach a statistical balance at the *far-from-equilibrium* (statistically stationary) *steady* state.

To show the extent to which stochastic processes and far-from-equilibrium dynamics are linked to each other, the mechanism of feedback loop is introduced. To this end, consider the number of aggregations N_{Agg} and disaggregations N_{Bre} in a population of flocs at number concentration n and mean floc size \bar{L} . Assume as an example that $N_{Agg} \propto n^2$ and $N_{Bre} \propto \bar{L}$. As aggregation proceeds, the number of aggregates n decreases, therefore the number of aggregations N_{Agg} decreases too, whereas the average floc size \bar{L} increases. At the same time, breakup becomes more likely, therefore N_{Bre} increases and the number of aggregates n increases too, while the average floc size \bar{L} decreases. Figure 3.3 shows the correlation (positive and negative, respectively marked by a sign + and -) among the quantities N_{Agg} , N_{Bre} , n and \bar{L} . In this panel, a feedback loop is represented by a closed cycle of correlations. A feedback loop is positive if the product of signs in a closed cycle is positive, whereas is negative otherwise. Positivity and negativity must be identically satisfied along different arcs connecting the same quantities (Richardson, 1992, cit. in Capra, 1996, pag. 73). In particular, we observe that the loop ($N_{Agg} \rightleftharpoons N_{Bre}$) has a positive feedback, meaning that aggregation and breakup are *self-reinforcing* processes. However, aggregation and breakup do not cause the system to "explode" because they are essentially the opposite of one another, *i.e.* *competing*. Self-reinforcing and competing processes act in

¹From here we will refer to the far-from-equilibrium statistically stationary state with the term "steady state"

²In thermodynamical terms, the exergy Ex is expressed as $Ex = (En - En_0) - T_0(K - K_0) + p_0(V - V_0)$, where En is the enthalpy, T is the temperature, K is the entropy, p is the pressure, V is the volume, and the subscript ₀ denotes a reference value with respect to the ongoing process. Other terms can be included in this expression, like chemical potential or any other form of energy. However, within this context we only refer to the concept, with no specific attention to the terms involved.

the same way as *self-balancing* processes, that are typical in negative feedback loops. Figure 3.4 shows schematically that aggregation and breakup can reach a *statistical* equilibrium, effectively due to this negative feedback loop. A *stable* equilibrium is therefore possible when either only aggregation (for instance the system in Figure 3.2 (c)) or only breakup hold within the system. However, in reality aggregation and breakup are *always* coupled. Further, both depend on G (Eqs. (2.2) and (2.8)), therefore on the energy dissipation rate ε of Eq. (2.13). The far-from-equilibrium state in flocculating systems is a particular dynamical state of balance of self-balancing (competing and reinforcing) processes, that is possible only through energy supply. We can now better mark the significance of the energy dissipation and supply to the two self-balancing stochastic processes of aggregation and breakup in relation to the far-from-equilibrium dynamics of flocculating systems, and how the feedback loop has a role in maintaining the system state.

In the far-from-equilibrium state the system fluctuates around a dynamical equilibrium. If we consider the number concentration n (which scales to some extent with the total particle distance H), the far-from-equilibrium steady state can be represented by a statistical fluctuation of n around a steady \bar{n} , Figure 3.4. Also the FSD, therefore, should oscillate around a steady distribution, but this is expected not to be easy to detect experimentally.

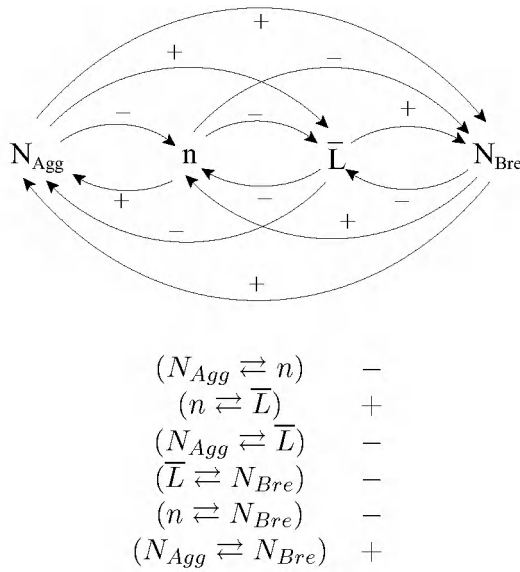


Figure 3.3: Feedback loops between aggregation and breakup processes. The feedback is positive, i.e. self-reinforcing, but aggregation and breakup have opposite effects on the population characteristics. Therefore they result in a self-balancing action, as in a negative feedback.

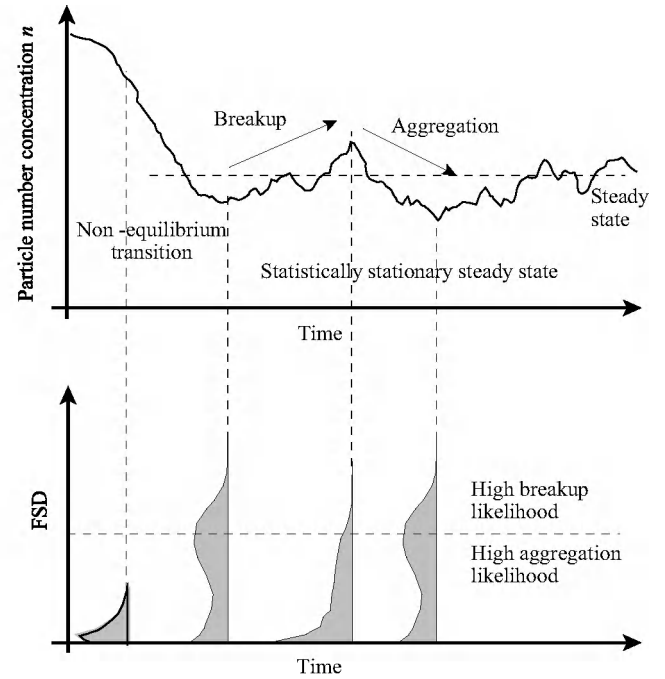


Figure 3.4: Indicative representation of the variability of particle number concentration n around a steady value \bar{n} due to a feedback between aggregation and breakup (top panel). This is also represented by means of the FSD (bottom panel).

3.1.4 A step towards self-organisation in flocculating systems

The types of feedback mechanisms described in Section 3.1.3 have been investigated extensively by Maturana & Varela (1972), showing that in living and non-living systems they

are linked to forms of self-organisation (or autopoiesis). Nicolis & Prigogine (1974) investigated the spontaneous onset of organisation in far-from-equilibrium chemical reactions, while Vicsek (1992), Meakin (1998) and Stanley & Barabási (1995) observed organised manifestations in particulate systems. Many other examples of coherent manifestations in complex systems are given in Novak (2000). These studies address to the so-called *Self-Organised Criticality* (SOC), as proposed originally in Bak (1990, 1996). SOC applies to open and dissipative systems consisting of units that can interact with the others through internal forces, and under external forces as well. Self-organization refers to the ability of systems away from the equilibrium to develop coherent structures or patterns that exhibit properties of equilibrium at a critical point. The structure is somehow maintained by itself autonomously, regardless of any "fine tuning" by external forces. Criticality refers to a system that is at (or is approaching) a point at which its behaviour will change abruptly; this point is often regarded as a phase transition.

The sandpile system is very much a studied self-organising system at critical point (Buchholtz & Pöschel, 1996; Casartelli & Zerbini, 2000; Ahluwalia & Ananthakrishna, 2001). Imagine to drop sand grains from a fixed point onto a plane; soon a pile will accumulate. The structure of the system (the pile) will be conic, at all sizes. This is due to the fact that avalanches will originate at the top of the pile, redistributing the grains in such a way as to give again (or to maintain) the pile with a similar conic shape. An avalanche will occur every once in a while but with no apparent possibility to predict the time of its occurrence and its size (*i.e.* the number of grains involved). An analogous picture can be adopted, metaphorically, to explain how SOC applies to flocculating cohesive systems. Consider flocs to be the analogue of a sandpile, floc growth the analogue of one-by-one grain accumulation on top of the pile and the sandpile shape the analogue of the floc size distribution. Self-organised criticality appears in that large flocs suddenly break up because their structure is at a critical point of a balance between resilience and shear stresses, in the same way as a sandpile caves in restoring its typical conic structure due to instabilities on the pile's surface. Also in the case of flocs, we do not know exactly when breakup will occur, to which of the flocs within a population, and neither how the sizes of the daughter flocs will be distributed. Anyhow, when breakup will happen, the population (in the sense of its structure, or its FSD) will readjust itself to "critical equilibrium", *i.e.* the far-from-equilibrium steady FSD.

Most of the scientific literature seems to agree, after some decades of theoretical and experimental research, on the necessity to accord far-from-equilibrium dynamics, fractals (and chaos) and self-organisation with some universal physical principles. For many reasons that we omit here, see for instance Novak (2000) and Badii & Politi (1997), the concepts of self-organisation, far-from-equilibrium dynamics and self-similarity have been included into what is nowadays called *complexity*. Although no clear or formal definition does exist of necessary conditions under which SOC behavior arises, one of the most common ways to characterise complexity, in the form of SOC, is to detect a typical $1/f$ noise (called also flickering or pink noise with frequency f) in some underlying processes (Bak *et al.*, 1987). The $1/f$ noise, later generalised into the $1/f^a$ noise (Bak, 1990), is actually a power-law relationship between observed quantities, stating that no characteristic time or length scales are associated with a particular process, named also scale-free behaviour³.

³A typical example characterised by $1/f$ noise is seismic activity, for which it is not possible to detect the time scale of an event in relation to its intensity (Olami *et al.*, 1992). Another example is avalanches (the case of sandpile described before).

The concept of $1/f$ -noise can be applied to a population of cohesive sediment flocs as follows: if the probability $p(\ell)$ of finding a floc of dimensionless size ℓ can be written as a power-law distribution:

$$p(\ell) \propto \ell^a, \quad (3.2)$$

with $a \approx -1$ then the population is likely to show complexity in the form of self-organised criticality. Shiner (2000) in particular suggests that Eq. (3.2) can be also written as:

$$p(r) \propto r^a, \quad (3.3)$$

with $a \approx -1$, where the floc size occurring most frequently has rank $r = 1$; the second most frequent has rank $r = 2$; *etc*⁴.

In Chapter 5 we will explore whether the suspended sediment flocs observed with PIV technique in our settling column are distributed in size with a such power-law or rank power-law.

3.2 Phenomenology of flocculation at small scales

Clay minerals are regularly shaped crystals, likewise forming fairly regular stack primary particles. These further flocculate into larger aggregates that, unlike the previous, usually have either round or filamentous- and clustered-like shapes, Figure 3.5. The mechanisms of floc structuring have been discussed in Chapter 2 but much literature has been devoted to study similar fractal structures as a result of far-from-equilibrium dynamics, especially in DLA and CCA mechanisms defined in Chapter 2 (Gleiser & Howell, 2003; Hentschel *et al.*, 2004). Within this context, specific characteristics can be detected also in the morphodynamics of individual aggregates.

If we look again at Figure 3.5, we recognise that a transition from ordered elements (the minerals) to less ordered structures (primary particles) and, eventually, to disordered clusters (aggregates) characterises, phenomenologically, the evolution of growing flocs. The way in which flocs grow depends largely on the interaction with other aggregates, and with the environment. At present, scientific literature lacks *direct* experimental evidence (for instance optical recordings) of both aggregation and breakup. Despite this, several experiments have allowed analysis of the structural properties of cohesive sediment (Van Leussen, 1994; Manning & Dyer, 2002; Maggi *et al.*, 2003), all recognising their fractal nature. The analysis of floc structure can give insight in the processes that have formed flocs, as floc geometry is a sort of memory of accretion experienced by any individual floc in time.

The approach adopted in this thesis to analyse floc structure is aimed at finding dominant scaling laws, and at characterising the kinematics of aggregation and breakup. Let us consider a set $\Omega_{d_E} \subset \mathbb{R}^{d_E}$ of size L , with d_E the Euclidian (or embedding) dimension. If we cover Ω_{d_E} with a set $\{\omega\}$ of equal d_E -dimensional hypercubes of arbitrary size ϵ then we obtain an ω -covering (mapping) of Ω_{d_E} with resolution:

$$\ell = L/\epsilon, \quad (3.4)$$

⁴From here we refer to rank- or r -ordered probabilities $p(r)$.

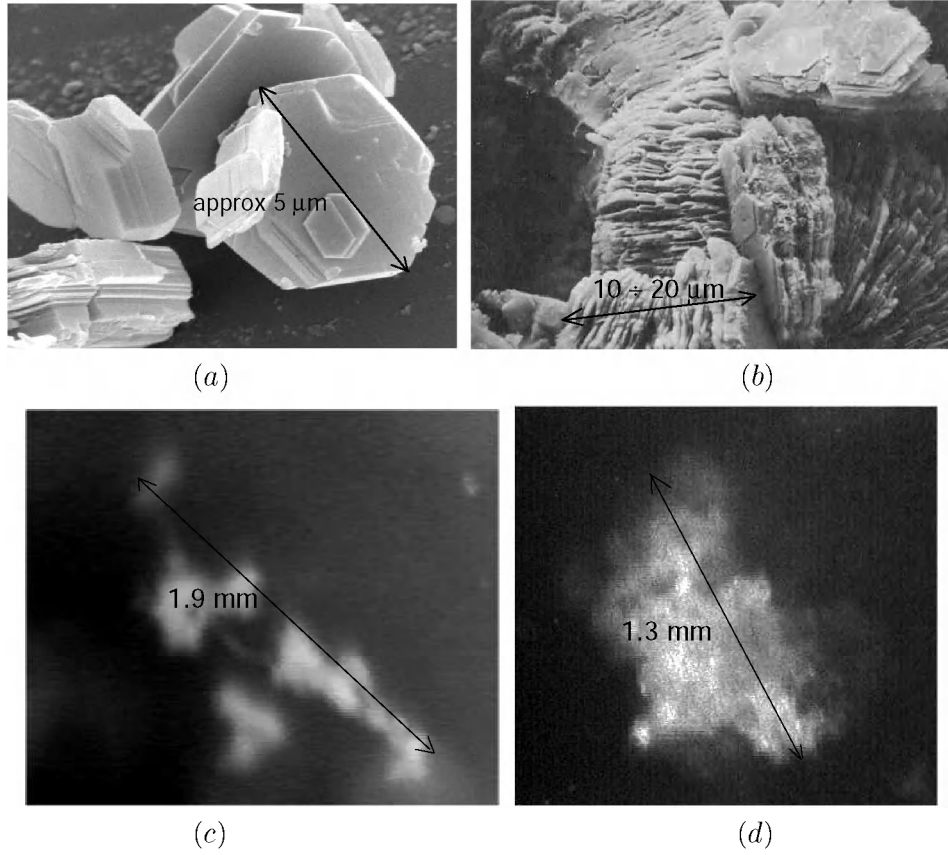


Figure 3.5: Examples of (a) clay (kaolinite) mineral, (b) primary particles, and (c) and (d) mud flocs. Here an increasing complexity of the geometrical structure can be observed in the transition from the elementary minerals to the primary particles and, finally, to flocs. Picture (a) kindly provided by Andrew Manning.

where ℓ is a dimensionless length scale of Ω_{d_E} and the linear size L is defined in Section 2.4.1 as the size of the smallest hypercube enveloping Ω_{d_E} . We name:

$$N_{\Omega} \quad : \quad \text{the number of points of } \Omega_{d_E} \quad (3.5)$$

$$N_{\omega}(\epsilon) = \ell^{d_E} \quad : \quad \text{the total number of boxes in } \{\omega\} \quad (3.6)$$

$$N(\epsilon) \quad : \quad \text{the number of boxes in } \{\omega\} \text{ occupied by } \Omega, \quad (3.7)$$

$$N_{\Omega,i}(\epsilon) \quad : \quad \text{the number of points of } \Omega \text{ within box } \omega_i. \quad (3.8)$$

The theory in the following sections deals with d_E -dimensional sets in a general form. However, it is clear that real mud flocs are embedded in $d_E = 3$ Euclidian spaces. Yet, most of the times we will refer to 2D discrete embedding spaces, as we next will mainly elaborate digital images. Therefore, when explicitly referring to digital images ($d_E = 2$), the one-pixel box is the smallest ω that can be used in this mathematical frame, while the ℓ -pixel box is the largest one. Furthermore, in Section 4.8 we show that, based on optical arrangements of the measuring system, the size of the smallest box used in the analysis of the floc structure can be associated with the size of the primary particle.

3.2.1 Spatial organisation of floc geometry

The entropy of a system gives an indication of its complexity because it is related to the probability to find recursive patterns; the higher the probability for a given pattern the lower the entropy. Non-homogeneity can be characterised by the variety of patterns and substructures irregularly distributed within the floc structure.

To this end, we compute the entropy function and disorder index (Maggi *et al.*, 2003). Consider an ω -covering of $\Omega_2 \subseteq \mathbb{R}^2$. If N_m is the number of boxes with identical $N_{\Omega,i}(\epsilon)$ (say pattern) then $p_m(\epsilon) = N_m/N(\epsilon)$ is the probability to find a pattern $N_{\Omega,i}(\epsilon)$ within Ω_2 . The corresponding entropy function $S(\epsilon)$ is (Chhabra & Jensen, 1989):

$$S(\epsilon) = - \sum_{m=1}^{N_{dp}} p_m(\epsilon) \ln[p_m(\epsilon)], \quad (3.9)$$

with $N_{dp} \leq N(\epsilon)$ the number of different patterns $N_{\Omega,i}(\epsilon)$ found in the ω -covering. $S(\epsilon) = 0$ for both $\epsilon = 1$ and $\epsilon = L$, while $S(\epsilon) \geq 0$ for $1 < \epsilon < L$, with a maximum S' at a given $\epsilon = \epsilon'$. We call $S' = S(\epsilon')$ the *specific entropy* of Ω_2 , since S' is associated with one value of ϵ . In analogy with S' we compute the *maximum specific entropy* $S'_{max} = 2 \ln[\epsilon']$ corresponding to the equiprobability to find *any* possible pattern (white-noise) in the ω' -covering, *i.e.* $p_m(\epsilon') = 1/N_{dp} = 1/\epsilon'^2$. Since the number of *observed* patterns is less than or equal to the *possible* number of patterns ($S' \leq S'_{max}$), we can write the disorder index Υ' (Shiner, 2000):

$$\Upsilon' = \frac{S'}{S'_{max}}, \quad \text{such that} \quad 0 \leq \Upsilon' \leq 1. \quad (3.10)$$

Υ' measures the level of disorder of Ω_2 . $\Upsilon' = 1$ corresponds to maximum disorder (or complexity), while $\Upsilon' = 0$ means that Ω_2 possesses a fully recurrent mass organisation (without pattern variability). In practice, complex structures can show regularities which are repeated in a (fully or statistically) self-similar way.

3.2.2 Fractal dimensions

The capacity dimension introduced in Eq. (2.17), Section 2.4.2, originates from the Hausdorff-Besicovitch dimension, the detailed definition of which can be found for instance in Turner *et al.* (1998). However, both definitions (Eq. (2.17) and Hausdorff-Besicovitch) do not provide a practical approach to measure the fractality of mud flocs from experimental optical recordings. The former because it supposes the primary particles to be monodisperse (L_p is unique), and the latter because of the need to find the optimal ω -covering to be applied to Ω . Therefore, the capacity dimension of Eq. (2.17) has been adapted to digital elaboration by replacing L/L_p with $\ell(\epsilon) = L/\epsilon$ of Eq. (3.4) and N_p with $N(\epsilon)$ as follows:

$$d_C = \frac{\ln N(\epsilon)}{\ln \ell(\epsilon)}. \quad (3.11)$$

Eq. (3.11) can be computed via *box-counting* techniques (Argyris *et al.*, 1994; Turner *et al.*, 1998). The capacity dimension is not the only fractal dimension of interest. A different (probabilistic) fractal dimension is the *information dimension* d_I (Balatoni & Rényi, 1956):

$$d_I = \lim_{\epsilon \rightarrow 0} \frac{I(\epsilon)}{\ln \epsilon}, \quad (3.12)$$

with $I(\ell)$ the Shannon information function (Shannon, 1948):

$$I(\epsilon) = -K \sum_{i=1}^{N(\epsilon)} p_i(\epsilon) \ln p_i(\epsilon), \quad (3.13)$$

where K is a constant and $p_i(\epsilon)$ is the probability that ω_i is occupied by the fractal⁵. Another fractal dimension is the *correlation dimension* d_K (Grassberger & Procaccia, 1983):

$$d_K = \lim_{r \rightarrow 0} \frac{\ln C(r)}{\ln r}, \quad (3.14)$$

where $C(r)$ expresses the spatial correlation of two generic points at locations \mathbf{p}_i and \mathbf{p}_j , and is called the *correlation integral* of the fractal:

$$C(r) = \frac{1}{N_\Omega^2} \sum_{j=1}^{N_\Omega-1} \sum_{i=j+1}^{N_\Omega} H(r - |\mathbf{p}_i - \mathbf{p}_j|), \quad (3.15)$$

with H the Heaviside step function, *i.e.* $H(x) = 0$ for $x \leq 0$ and $H(x) = 1$ for $x > 0$. The parameter r is a critical Euclidian distance used to correlate two points with distance $|\mathbf{p}_i - \mathbf{p}_j| > r$.

3.2.3 Generalised dimensionality and multifractality

The fractal dimensions defined in Eqs. (3.11), (3.12) and (3.14) have been investigated in detail leading to the concept of *generalised dimensionality* d_q (Hentschel & Procaccia, 1983). Consider an ω -covering of Ω ; then $p_i(\epsilon) = N_{\Omega,i}(\epsilon)/N_\Omega$ determines the probability of a measuring point lying in ω_i . By using a q -order information function I_q (Balatoni & Rényi, 1956):

$$I_q(\epsilon) = -\frac{1}{1-q} \ln \sum_{i=1}^{N_\omega(\epsilon)} [p_i(\epsilon)]^q, \quad (3.16)$$

the q -order generalised dimensionality d_q (with $q \in \mathbb{R}$) is:

$$d_q = \lim_{\epsilon \rightarrow 0} \frac{I_q(\epsilon)}{\ln \epsilon} = -\frac{1}{1-q} \lim_{\epsilon \rightarrow 0} \frac{\ln \sum_{i=1}^{N_\omega} [p_i(\epsilon)]^q}{\ln \epsilon}. \quad (3.17)$$

The fractal dimensionions d_I , d_C and d_K are special cases of d_q (Argyris *et al.*, 1994):

$$d_q = \begin{cases} d_0 = d_C & \text{capacity dimension, if } q = 0, \\ d_1 = d_I & \text{information dimension, if } q = 1, \\ d_2 = d_K & \text{correlation dimension, if } q = 2. \end{cases} \quad \text{with } d_2 \leq d_1 \leq d_0 \leq d_E \quad (3.18)$$

The generalised dimensionality d_q expresses that fractals may show a spectrum of fractal dimensions as a function of q . The presence of an infinite number of fractal dimensions

⁵The information function $I(\epsilon)$ represents a measure of the possible number of realisations that the system can have. Consider an ordered set of n numbers $\{x_1, x_2, \dots, x_n\}$ with $x_i = c \ \forall i$. Imagine now to select $n^* \leq n$ adjacent numbers; the number of different patterns N_{dp} in the sequence is $N_{dp} = 1$ because all the $n - n^* + 1$ subsets show the same sequence. In this case, the information gain I is zero because the probability $p_j = 1/(n - n^* + 1)$. If the set $\{x_1, x_2, \dots, x_n\}$ is composed of random numbers then $N_{dp} > 1$ and $I > 0$ consequently.

can be associated with the presence of an infinite number of different fractals, each with a different fractal dimension (Meakin, 1998). This has yielded the theory of *multifractal sets*, stating that multifractals are combinations of many *monofractal sets*. Conceptually, mono- and multifractality can be described as follows. For monofractals, a generalised probability of a measure P within an ω -covering scales with ϵ as $P = P_i \sim \epsilon^{d_f}$, where $d_f = \text{const} \forall i$ is a fractal dimension. For multifractals, in contrast, the generalised probability P within any box ω_i scales as $P = P_i \sim \epsilon^{\alpha_i}$, with α_i the Lipschitz-Holder exponent or *singularity strength* (Halsey *et al.*, 1986a,b). The number $N(\alpha)$ of boxes, where P_i has singularity strength between α_i and $\alpha_i + d\alpha$, scales as $N(\alpha_i) \sim \epsilon^{-f(\alpha_i)}$. Here $f(\alpha)$ is called the *spectrum of fractal dimensions* (or multifractal spectrum) of the family of boxes with singularity α , and it is equivalent to d_q . The spectrum $f(\alpha)$ is a continuous function of α and, usually, with a maximum at $df(\alpha)/d\alpha = 0$. In particular, the generalised dimensionality d_q of monofractals collapses to $d_q = \text{const} = d_0 \leq d_E \forall q \in (-\infty, +\infty)$. In contrast, for multifractals, $d_q \neq \text{const} \leq d_E \forall q \in (-\infty, +\infty)$.

3.2.4 Multifractal spectrum and mass density organisation of mud flocs

Chhabra & Jensen (1989) proposed an efficient technique to compute the spectrum of fractal dimensions f . Applying an ω -covering to $\Omega_2 \subseteq \mathbb{R}^2$, we compute the probability $p_i(\epsilon) = N_{\Omega,i}(\epsilon)/N_{\Omega}$ and we define a q -order family of normalised probabilities $\mu(q, \epsilon)$:

$$\mu_i(q, \epsilon) = \frac{[p_i(\epsilon)]^q}{\sum_{i=1}^{N(\epsilon)} [p_i(\epsilon)]^q}, \quad \text{such that} \quad \sum_{i=1}^{N(\epsilon)} \mu_i(q, \epsilon) = 1. \quad (3.19)$$

The exponent $q \in \mathbb{R}$ is a weighting moment (or family order) which strengthens high mass-concentration regions if $q > 1$. It strengthens low mass-concentration regions if $q < 1$, and it replicates the original measure if $q = 1$. The multifractal spectrum $f(q)$ is:

$$f(q) = \lim_{\epsilon \rightarrow 0} \frac{\sum_{i=1}^{N(\epsilon)} \mu_i(q, \epsilon) \cdot \ln [\mu_i(q, \epsilon)]}{\ln \epsilon}, \quad (3.20)$$

The average value $\alpha(q)$ of the singularity strength α_i in the ω -covering is:

$$\alpha(q) = \lim_{\epsilon \rightarrow 0} \frac{\sum_{i=1}^{N(\epsilon)} \mu_i(q, \epsilon) \cdot \ln [p_i(\epsilon)]}{\ln \epsilon}. \quad (3.21)$$

Particular interest is addressed to the measure $p_i(\epsilon)^q$, which scales as:

$$\sum_{i=1}^{N(\epsilon)} p_i(\epsilon)^q \sim \epsilon^{\tau(q)} \quad \text{with} \quad \tau(q) = (q-1)d_q, \quad (3.22)$$

where $\tau(q)$ is the q -order *mass-correlation exponent* (Halsey *et al.*, 1986b). $\tau(q)$ and $f(q)$ are related to each other by Legendre transformation (Meakin, 1998):

$$f(\alpha(q)) = q\alpha(q) - \tau(q), \quad \alpha(q) = \frac{d\tau(q)}{dq}. \quad (3.23)$$

From a numerical analysis in Maggi (2002) the quantities $f(q)$, $\alpha(q)$ and $\tau(q)$ can be used to detect the geometrical nature of sets (intended as physical bodies), as elucidated in the following four cases.

For Euclidian sets with $d_0 \equiv d_E$ (e.g. a square in \mathbb{R}^2 or a segment in \mathbb{R}^1), where d_E is the embedding dimension, the corresponding multifractal spectrum is $f(q) = \text{const} = d_0 \forall q$ in the (f, q) -representation, and collapses into a unique point at $\alpha = 0$ in a (f, α) -representation. These sets are characterised by $\alpha(q) = d\tau(q)/dq = \text{const} = 0 \forall q$, meaning that the mass-correlation exponent is $\tau(q) = \text{const} = 0 \forall q$.

For Euclidian sets with $d_0 < d_E$ (e.g. a segment in \mathbb{R}^2), again the multifractal spectrum is $f(q) = \text{const} = d_0 \forall q$ in the (f, q) -representation, collapsing into one point at singularity strength $\alpha(q) = d\tau(q)/dq = \text{const} = \alpha^* > 0$ in a (f, α) -representation. The mass-correlation exponent is therefore $\tau(q) \neq 0$, with slope $d\tau(q)/dq = \alpha(q) = \text{const} = \alpha^*$ and curvature $d^2\tau(q)/dq^2 = 0$.

Fully self-similar (monofractal) sets with $d_0 < d_E$ (e.g. Sierpinski carpet) are characterised by $f(q) = \text{const} = d_0 \forall q$ and $\forall \alpha(q)$ in both the (f, q) - and (f, α) -representation. Also in this case the mass-correlation exponent has a constant slope $d\tau(q)/dq = \alpha(q) = \text{const} > 0 \forall q$ with zero curvature $d^2\tau(q)/dq^2 = 0$.

Statistically self-similar (multifractal) sets with $d_0 < d_E$ (e.g. random fractals) are characterised by $f(q) \neq \text{const}$ in the (f, q) - and (f, α) -representation. Further, $d\tau(q)/dq = \alpha(q) \neq \text{const}$, meaning that the mass-correlation exponent $\tau(q)$ does not have a constant slope. Therefore $d^2\tau(q)/dq^2 \neq 0$, implying that different slopes are associated to different scaling laws in the mass-density distribution.

Table 3.1 summarises these four typologies of sets associated with the multifractal spectrum, singularity strength and mass-correlation exponent. From this we underline that Euclidian and fully self-similar sets are characterized by:

$$d_{-\infty} = \dots = d_0 = d_1 = d_2 = \dots = d_{+\infty}, \quad (3.24)$$

whereas statistically self-similar sets are characterized by:

$$d_{-\infty} < \dots < d_0 > d_1 > d_2 > \dots > d_{+\infty}. \quad (3.25)$$

The aforementioned notions are fundamental for characterizing the properties of real aggregates. In addition, the reader is referred to the examples given in Appendix A.1.

Set property		$f(q)$	$\tau(q)$	$\alpha(q) = d\tau(q)/dq$	$d^2\tau(q)/dq^2$
Euclidian	$(d_0 \equiv d_E)$	$\text{const} = d_0$	$\text{const} = 0$	$\text{const} = 0$	$\text{const} = 0$
Euclidian	$(d_0 < d_E)$	$\text{const} = d_0$	$\neq \text{const}$	$\text{const} > 0$	$\text{const} = 0$
Fully self-similar	$(d_0 < d_E)$	$\text{const} = d_0$	$\neq \text{const}$	$\text{const} > 0$	$\text{const} = 0$
Statistically self-similar	$(d_0 < d_E)$	$\neq \text{const}$	$\neq \text{const}$	$\neq \text{const} > 0$	$\neq \text{const}$

Table 3.1: Summary of the properties of the multifractal spectrum $f(q)$, mass-correlation exponent $\tau(q)$ and singularity strength $\alpha(q)$ with respect to different properties of the sets.

Fractal geometry has found wide application in describing aggregates as self-similar structures characterised by a capacity dimension d_C . However, the concept of self-similarity, further widened by the formalism of generalised dimensionality d_q and multifractality, has given the tools to characterise fractal structures as follows. *Fully self-similar* fractals are exactly and deterministically identical at different scales, while *statistically self-similar*

fractals look much the same at different scales but, in reality, are not precisely identical. The extent to which a geometric structure is irregular and non-homogeneous (*i.e.* statistically self-similar or multifractal) rather than regular and homogeneous (*i.e.* fully self-similar or monofractal) is measured through the spectrum of fractal dimensions $f(q)$, the singularity strength $\alpha(q)$ and the mass-correlation exponent $\tau(q)$. Dominant scaling in floc geometry can be established from a combined analysis of f , α and τ . This, especially, suits well to our need to characterise the shape and the mass-density organisation of cohesive sediment flocs and to evaluate whether, and to which extent, there are irregularities. The reader is further referred to Appendix A.2 for a classification of the properties of self-similarity, homogeneity, and mono- and multifractality of fractal sets on the basis of the mentioned quantities applied to examples.

3.3 Summary

It is useful to summarise some concepts that are important within the phenomenological framework described in this chapter.

In nature, driving forces change all the time, as a result of which the composition of a population of flocs (its FSD) changes. Here, for clarity of arguments, we discuss the evolution of a population consisting of identical primary particles. At a system level (large scale), a population of flocs is inferred to evolve from a non-flocculated to a flocculated (equilibrium-like) state, Section 3.1.1. More specifically, the latter can be described as a far-from-equilibrium steady state that corresponds to a lower level of entropy or disorder, as conceptualised in Section 3.1.1 and 3.1.2. The dynamics of flocculation has been linked to self-balancing-equivalent (competing and self-reinforcing) feedback interactions between aggregation and breakup processes, Section 3.1.3. The fact that particulate systems far from equilibrium can be sources of negative entropy in the presence of negative feedback has led us to consider flocculating systems as possibly marked by self-organisation properties. As it is not proven to the author's knowledge whether self-organisation effectively governs flocculation of cohesive sediment particles, the concepts and ideas exposed in Section 3.2 will be applied to the floc size distribution, as this can be used to detect self-organised criticality. This study is therefore aimed at broadening the current knowledge of the statistical properties of size distributions of cohesive flocs. If evidences of SOC are found in the form of power-law relationships, then we have made a step further into the understanding of the processes of flocculation of cohesive sediment.

For the study of flocculation at floc level (small scale), we have introduced the theoretical tools that allow to detect the quantity of randomness and determinism in the floc structure and to characterise their irregularities with scaling laws. First, the entropy and disorder index, Section 3.2.1, can show if and how disordered and repetitive mass-density patterns develop during floc growth. This, in other words, allows to detect how floc growth is accompanied by a disordered expansion of the structure. Second, irregular mass-density organisation of floc structure can be characterised and scaled fully by computing the multifractal spectrum, Section 3.2.4. In particular, monofractal structures have a fully self-similar organisation, characterised by a monoscaling geometry and low level of entropy, while multifractal structures are statistically self-similar, and are characterised by a multiscaling geometry with high level of entropy.

The issues discussed in Section 3.1 lead us to look at cohesive sediment flocs as a population that evolves at a far-from-equilibrium state towards a less (spatially) disordered

geometrical state, continuously in time and in a feedback system with self-organisation properties. The issues discussed in Section 3.2, in contrast, lead us to look at flocs as structures that grow and break up continuously in time and that, from regular blocks, form more complex structures with fractal properties and disordered mass-density distribution. The questions are: to which extent are the processes at these scales autonomous, and to which extent can the external conditions (energy dissipation) effectively influence the evolution of a flocculating system; to which extent does development of order at large scales occur at the expenses of development of geometrical complexity at small scales; how should the mechanisms of aggregation and breakup be implemented in a population balance equation in the light of this phenomenological characterisation. We will address these questions on the basis of our experimental results from the settling column.

Chapter 4

Experimental facility: the settling column

The understanding of the dynamics of flocculation of cohesive sediment calls for a dedicated settling column to generate the aggregation and breakup processes of sediment flocs. Such a settling column was designed and manufactured at Delft University of Technology from 2000 to 2003, and it has been one of the major tasks for the study reported in this thesis; the work included several computations, designs, tests, modifications of the components, *etc.* This chapter describes the settling column, especially the design criteria, its structure, geometry, functioning, control systems and measuring techniques.

4.1 Targets and design criteria

Investigation of flocculation, of settling and bed formation were the three main issues considered in the design of the settling column. This doctoral thesis is focussed on flocculation processes (*e.g.* aggregation and breakup), while settling and bed formation will be the subject of future research.

The fundamental functioning criteria to be fulfilled by the column design were: (1) the conditions of concentrations and turbulent shear rates in the column had to replicate the hydrodynamic and sedimentological characteristics met in estuaries and coastal zones; (2) the conditions in the column had to allow the evolution of flocculation towards an equilibrium floc size distribution; (3) the column had to be constructed such that advanced measuring techniques could be applied.

4.2 Conceptual design of the settling column

The issues mentioned in the previous section have been taken into account and elaborated into a conceptual design of the column with the aim to assess the dimensions of the facility, the time scales of the flocculation reactions and the sedimentation processes in the settling column. Simple numerical computations enabled to establish characteristic quantities and to draw a first schematic picture of the structure and functioning of the column.

The sedimentation column embeds the control volume in which flocculation and settling take place, this therefore being the active core of the facility. Flocculation is induced by turbulence and depends on the concentration and residence time of the flocs in the

turbulence field, *i.e.* in the water column. Therefore, the first step in the design of the facility was the assessment of the column height, for homogeneous turbulent mixing conditions.

The height of the column is assessed as follows. Sediment concentrations and turbulent shear rate in the range $c = (0.05, 1)$ g/l and turbulent shear rates $G = (1, 100)$ s⁻¹ are normally found in natural waters. These sedimentological and hydrodynamic conditions served the computation of the equilibrium flocs size $L_e(c, G)$ and settling velocity $w_e(c, G)$ by means of the flocculation model of Eq. (2.24) (Winterwerp, 1998). In this model, the flocculation time t_f scales as $t_f \propto 1/(cG)$, while the residence time $t_{rc}(c, G)$ in the column scales as $t_{rc} \propto H_c/w_e(c, G)$. For the chosen ranges of c and G , we could predict an equilibrium floc size $L_e = (10^{-5}, 10^{-3})$ m, a settling velocity at equilibrium $w_e = (5 \cdot 10^{-5}, 4 \cdot 10^{-3})$ ms⁻¹, and a flocculation time $t_f = (2 \cdot 10^2, 3 \cdot 10^4)$ s. At equilibrium, t_f should be smaller than t_{rc} ; a height $H_c = 4$ m was estimated to satisfy the requirement $t_f < t_{rc}$ for a wide variety of conditions. Furthermore, $H_c = 4$ m would be physically representative of natural depths, and the residence time t_{rc} is in the range $t_{rc} = (10^3, 10^5)$ s, Appendix B.1 (see Section 4.5).

Due to the height of the column, convective currents can form as a result of temperature gradients in vertical direction. A temperature difference of about 10÷15 °C was measured from the ceiling to the floor of the laboratory, where the column was to be erected. This would result in convection velocities exceeding largely the settling velocity of the sediment in the column. A climatized room was therefore designed to keep the temperature as uniform as possible (see Section 4.4).

Within the column, a homogeneous and isotropic turbulence field should be generated. Tests by Rouse (1938) and Dobbins (1944) with non-cohesive materials have shown that a homogeneous and isotropic turbulent field can be generated with a grid. Nowadays, homogeneous and isotropic turbulence is often generated by placing a grid in the flow. In the settling column, turbulence is produced by oscillating the grid over the full column height. Early experience by Van Leussen (1994) showed that an axially oscillating grid matched well specific requirements of turbulence properties. The specific design of the grid was investigated by means of pilot experiments, without numerical computations (see Section 4.5).

The settling column was designed for a continuous supply of sediment, rather than a recirculation flow. Consequently, a sediment injection system was required to maintain a chosen test concentration c_d at any chosen shear rate G . To this end, a storage tank with volume $V_s = 100$ l was used. Given the residence time $t_{rc}(c, G)$ in the column, the total amount of dry sediment mass M_r required for the anticipated test conditions could be established, Appendix B.2. The storage tank was then connected to a pump to inject the sediment into the column. However, sediment could not be injected directly, because of variability in sediment concentration and formation of dense clouds of sediment in the column. A buffer tank was therefore coupled to the storage tank and injection system, and mounted on top of the settling column. Analytical computation was performed to assess the sensitiveness of the required buffer tank dimensions to different concentrations c_d , turbulent shear rates G and fluctuations in the sediment injection as a function of its volume V_b , Appendix B.3. This allowed to establish an optimal buffer volume of $V_b = 0.1$ m³. The transition time and the residence time were also computed once V_b was determined, Appendix B.3 (see Section 4.6).

Settling flocs had to be recorded in a measuring section (see Section 4.7) specifically

designed to apply PIV (Particle Image Velocimetry) techniques. The measuring section mounted underneath the column was provided with a window to enable camera focussing to the measuring volume. Within the measuring section a separation chamber with a small entrance at its top was constructed. Flocs could settle into this separation chamber, unaffected by the large-scale circulation generated by the grid and by the suspension settling in the column. For details on the design and functioning of the separation chamber, the reader is referred to (Jouan, 2004).

Finally, due to the continuous sediment supply, a discharge outlet was foreseen.

4.3 Scheme structure and functioning

The settling column resulting from the conceptual design consists of the following elements: (1) a *climatised room* to isolate the facility from ambient temperature gradients; (2) a *sediment injection system* that provides the settling column with a controlled flux of sediment; (3) a *column* made from a cylindrical perspex tube in which flocculation is induced by an oscillating grid; (4) a *measuring section* where optical recordings of the flocs are collected, and the sediment is finally deposited; (5) an *overflow tank* to discharge extra flow from the control volume. A schematised view of the column (excluding the climatised room) is shown in Figure 4.1.

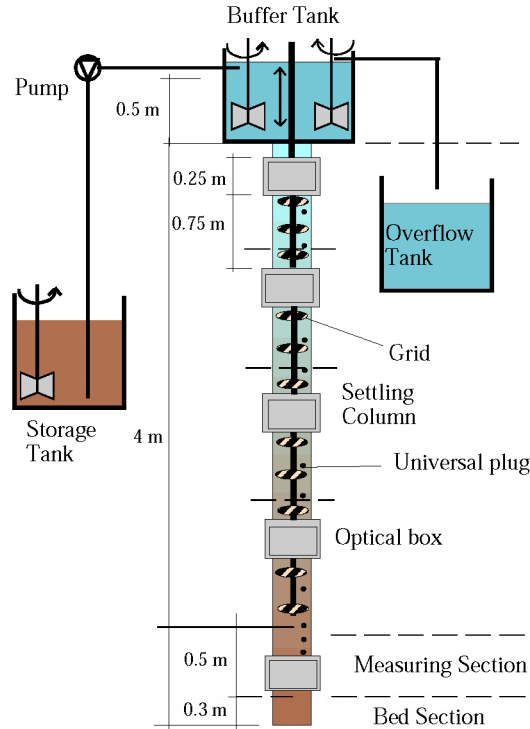


Figure 4.1: (a) Sketch of the settling column.

A mud suspension at high concentration c_s is prepared and continuously mixed in the storage tank. This suspension is injected into the buffer tank mounted on top of the settling tube. Sediment injection is controlled to maintain the concentration c_d in the column. The buffer tank dilutes the storage tank suspension at concentration c_s down to $c_d < c_s$, while two counter-rotating vanes produce a recirculating flow that distributes the particles

uniformly before entering the column. In the settling column, homogeneous and isotropic turbulence from an axially oscillating grid induces flocculation. Flocculated aggregates pass through the turbulence field in the column, then reach the measuring section underneath the column, where they are monitored with PIV techniques, and eventually settle in the bed section, on the bottom. The settling column is placed inside a climatized room that minimises temperature gradients and convective flows.

Specific description of each component is presented in the following sections.

4.4 The climatized room

The entire settling column is housed inside a room of about 6 m height that avoids external temperature gradients and maintains its internal temperature nearly uniform by a forced circulation flow. Temperature difference in vertical direction is ± 0.1 °C.

4.5 The sedimentation column and the grid

The column houses the grid and is the section within which flocculation and sedimentation take place, Figure 4.2 (a) and (b). The sedimentation column consists of two perspex pipes 2 m high and 0.3 m in diameter connected to each other, resulting in a column 4 m high. The column is provided with several plugs along the axial direction that allow the insertion of measuring probes. Furthermore, several optical boxes are built for performing either LDA (Laser Doppler Anemometry) or PIV measurements.

The grid was designed by means of a series of experiments on test sections measuring the isotropy and homogeneity of the turbulence field, eventually resulting in the final design of the grid, Appendix B.4. This grid is made from square cross-section bars of 0.8 cm size, that form a square configuration extending over a circular area of 22 cm diameter, leaving 2 cm clearance from the column wall, Figure 4.2 (c) and (d). The grids are mounted in four posts 1 m long at a spacing of 7.5 cm, Figure 4.2 (e). These grid sections can be mounted in the column in various combinations to yield grid lengths of 1÷4 m, thus varying the residence time of the sediment in the turbulence field. The grid is suspended from a driving system that forces the grid to move up and down to a maximum stroke $A_g = 8.4$ cm and maximum frequency $f_g = 1$ Hz. The hydrodynamical behaviour of the full-length grid was measured to calibrate the turbulent shear rate G *versus* the grid frequency f_g (Figure 4.3), as detailed in Appendix B.5.

The basement of the column is further provided with an air-spring system aimed at isolating the full experimental structure from vibrations generated by the driving system of the grid.

4.6 The sediment injection system

The sediment injection system consists of a storage tank, a peristaltic pump, an OSLIM (Optical Silt Measuring probe) and a buffer tank, Figure 4.4 (a).

A storage tank with a capacity of 100 l is equipped with a rotating propeller to keep a given amount of sediment in suspension. The storage tank is connected to a peristaltic pump that is used to inject the suspension at concentration c_s into the buffer tank. The

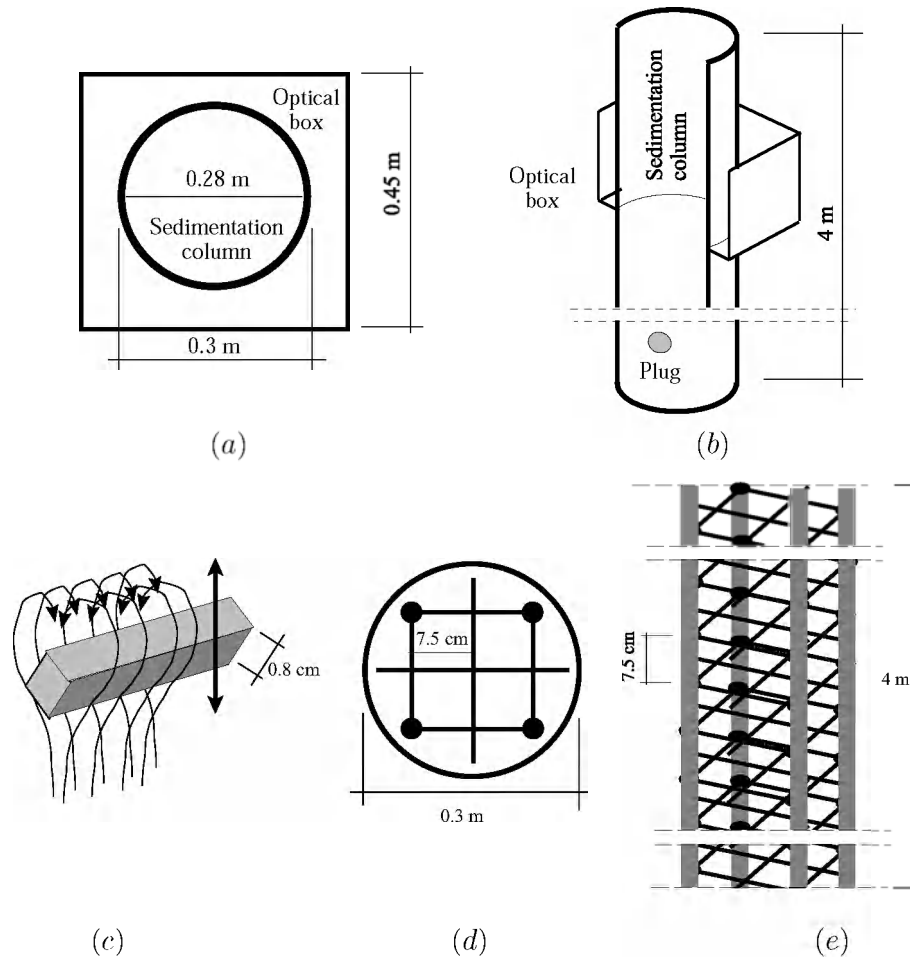


Figure 4.2: (a) top-view and (b) 3D sketch of the sedimentation column. The optical box, filled with water, enables undistorted optical recording. (c) elementary bar used for the grid mesh, (d) grid configuration and (e) grid structure. See gallery in Appendix B.9.

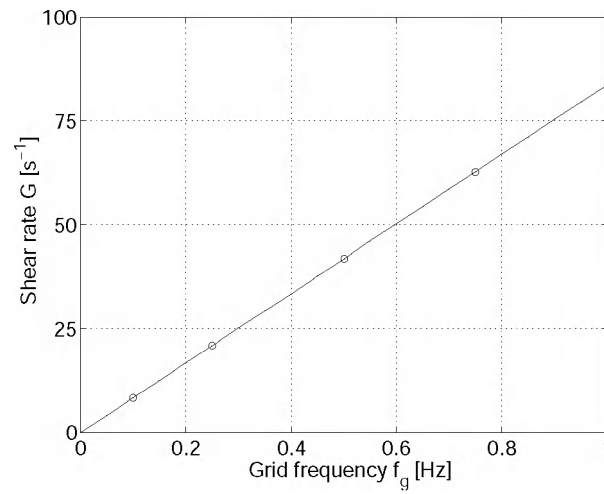


Figure 4.3: Calibration curve of the turbulent shear rate G as a function of grid frequency f_g .

concentration c in the buffer tank is measured real-time with an OSLIM system sampling the suspension with a recirculating flow.

The sediment pump is switched on if the measured concentration is $c < c_d - 0.015$ g/l, whereas it is turned off if $c > c_d + 0.015$ g/l, where c_d is the *a priori* chosen target concentration. In this way the sediment supply is controlled and the concentration in the column can be kept practically constant in time at any c_d and G , without hand tuning or calibration of the sediment pump rate. To reduce wear of moving parts of the peristaltic pump, it was preferable to inject a highly-concentrated sediment suspension at low rate. Each test was carried out with a batch of sediment/water mixture, which is stirred in the storage tank, preventing variability in the physico-chemical behaviour and properties of the suspension. However, because of the high concentration in the injection system, and because the sediment pump is periodically switched on/off during an experiment, the sediment is deposited in the tubes before reaching the buffer tank. To circumvent sedimentation within the system, a shunt was installed recirculating the flow with a centrifugal pump.

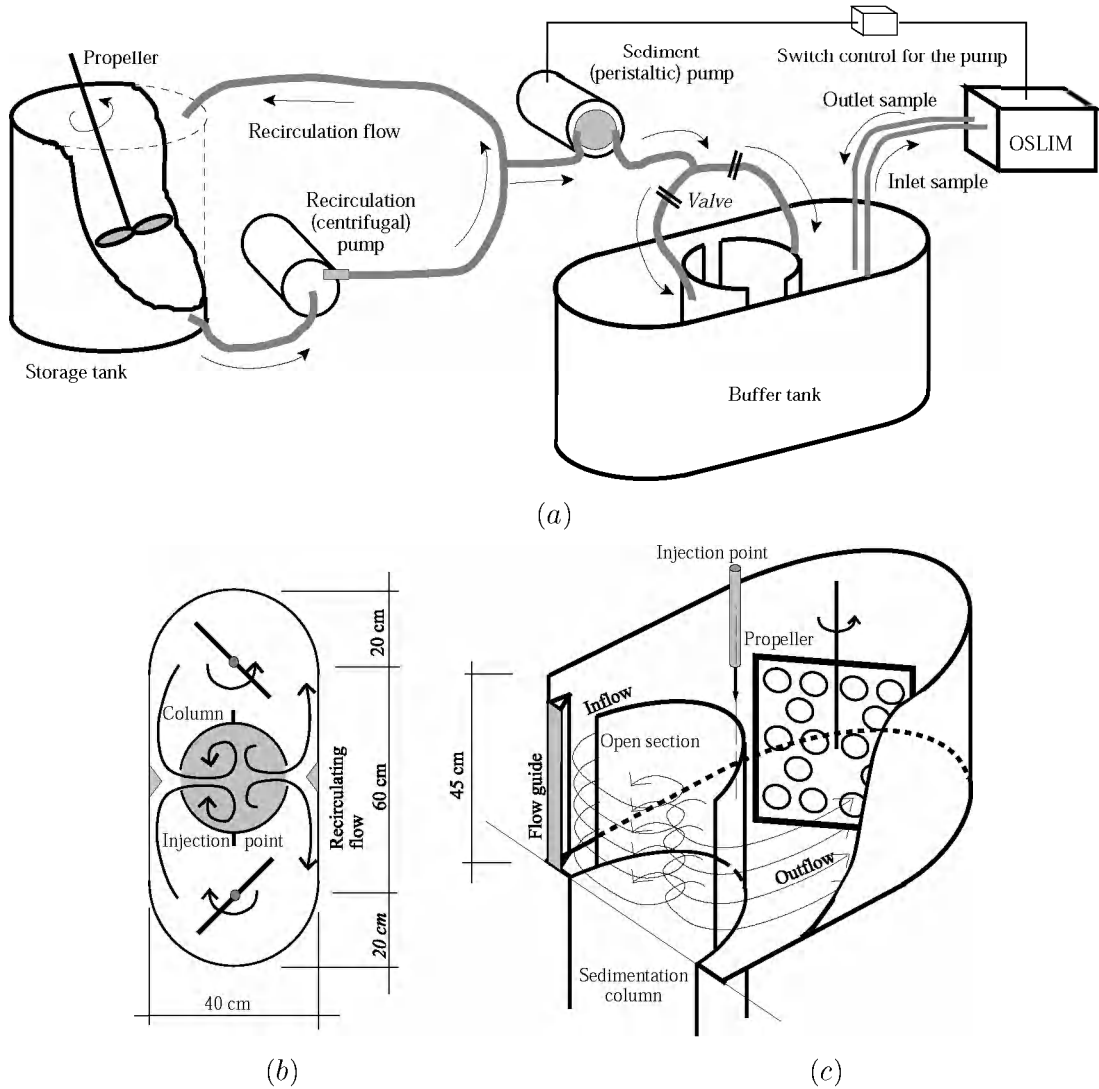


Figure 4.4: Sketch of the sediment injection system. (b) top-view and (c) 3D sketch of the buffer tank. See gallery in Appendix B.9.

The buffer tank is symmetric, 1 m large, 0.4 m wide and 0.45 m high, with a volume of $V_b = 0.12 \text{ m}^3$. The tank is mounted around the upper 0.4 m of the settling column. This upper part is provided with two narrow open sections leaving free passage to the motion of the fluid. Moreover, the column divides the buffer tank into two subvolumes in which the suspension is stirred by means of two flat vanes. There are two injection points for the suspension coming from the storage tank, Figure 4.4 (b) and (c).

Several qualitative and quantitative tests have been performed to determine the hydrodynamic behaviour of the buffer tank by operating on the rotational speed of the propellers. The first experiment was aimed at investigating the extent to which the mixing system affected the hydrodynamics within the buffer tank, especially important for avoiding to drive the sediment to preferential paths, Appendix B.6. It appeared that propeller frequencies $f_p < 0.1 \text{ Hz}$ could not be used during the experiments because these caused non-homogeneities in the mixing. A second (qualitative) test on the buffer was aimed at evaluating the properties of sediment diffusion in the upper part of the column, showing that particles were diffused homogeneously at the top section of the column, with no preferential sedimentation at mid-frequencies, Appendix B.7. The last set of measurements was aimed at estimating the residence time t_{rbe} (the characteristic time the sediment stays in the buffer tank) as a function of f_p . This experiment consisted in applying a series of injections of sediment at high concentration and various f_p . The decay in concentration was recorded after each pulse and the residence time t_{rbe} was retrieved. The results showed that t_{rbe} was increasing for increasing propeller frequency, Appendix B.8. To summarise, the propeller system was observed to work generally well at high frequencies, enabling proper sediment mixing, homogeneous sediment distribution in the column, and low sedimentation rate in the buffer.

4.7 The measuring section

The measuring section is designed for optical measurements of settling flocs. For this reason, the development of the measuring section was carried out by investigating its hydrodynamic behaviour in presence of the turbulent field from the column, and by using optical devices of the PIV system. In this section we describe only the functioning and geometry of the measuring section; further description on tests and improvements can be found in Jouan (2004). The measuring section is a perspex pipe 0.5 m high connected to the lower part of the column, Figure 4.5. Flocs are collected in the so-called floc collector, which separates a small fraction of flocs from the main suspension addressing them to the separation chamber. Herein, floc properties are measured unaffected by large-scale water circulation in the column. Flocs are illuminated by a laser beam through a flat transparent window on the side, and recorded by the digital camera of the PIV system through a second window. An hydraulic system was designed to clean the separation chamber by pumping clear water into it and discharging turbid water from it, at the same rate.

This description refers to the final configuration of the measuring section, after a number of trials and optimisations. Due to the iterative nature of this, the experiments described in the following Chapter 5 were not carried out with the same measuring section, but two different configurations were used, see Sections 5.2.1 and 5.3.1.

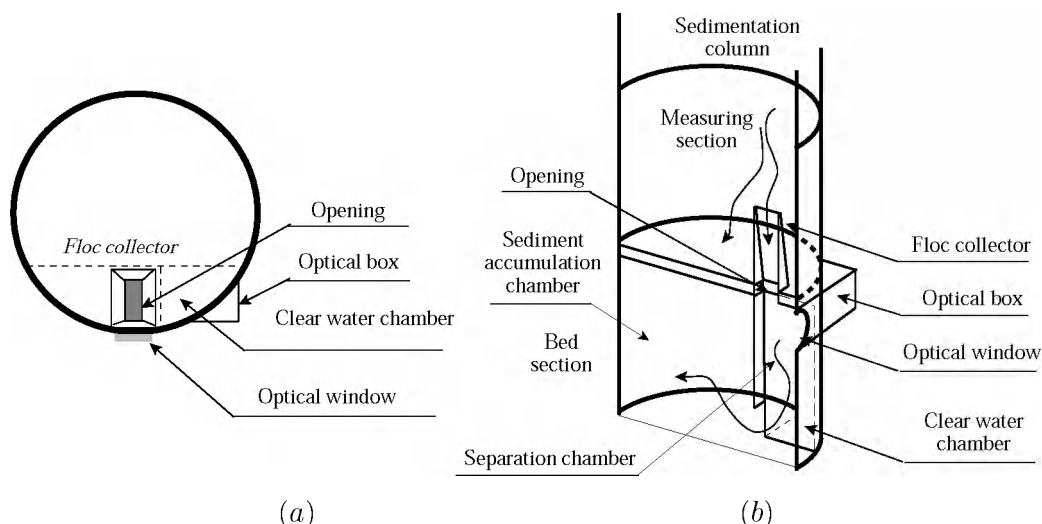


Figure 4.5: (a) top-view and (b) 3D view of the measuring section. See gallery in Appendix B.9.

4.8 The optical system

Particle Image Velocimetry (PIV) has been used in our facility with the purpose to visualise floc structure and motion. Conceptually, the PIV system consists of a light source that illuminates settling flocs; part of the light scattered by the flocs is captured by a camera and recorded in digital format, Figure 4.6.

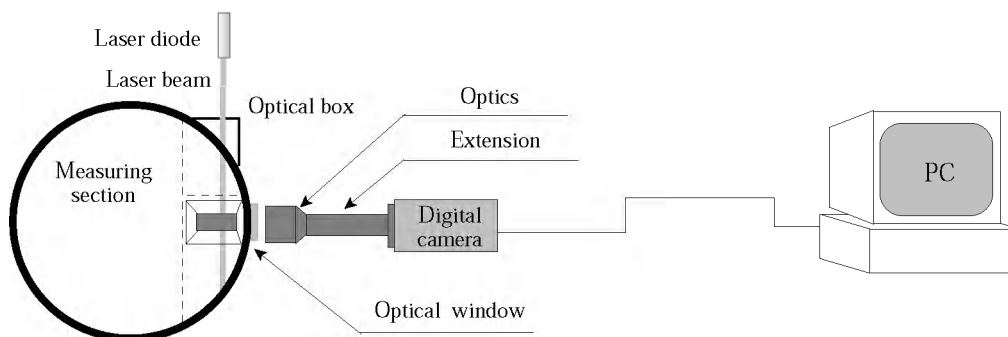


Figure 4.6: Sketch of the optical system mounted next to the measuring section for carrying out PIV measurements.

The floc size distribution and individual geometrical properties of flocs are retrieved from these digital images. All these quantities are recorded in time to allow interpretation of flocculation processes in terms of population dynamics.

The PIV technique was adapted to geometrical constraints of the facility through a series of numerical computations and pilot tests, fulfilling the following requirements: (1) the optical system had to be able to grab at least two frames of each of the fastest settling flocs in order to perform post-processing; (2) the resolution had to be high enough to represent accurately the spectrum of floc sizes and for detecting the geometry of flocs (pixel size \leq primary particle size); the images had to be qualitatively appreciable (focus, intensity, contrast, *etc.*).

An experiment run in our laboratory by Dr. T. Schuid recorded the particle size distri-

bution of kaolinite minerals used in the column, Figure 4.7. The data were recorded with a particle counter MET-ONE PCX (laser blocking technique), with kaolinite concentration 0.028g/l in a recirculating water flow system. From this, the mode size was detected in the range of $5 \div 7 \mu\text{m}$. Next, a numerical computation was carried out to preview the

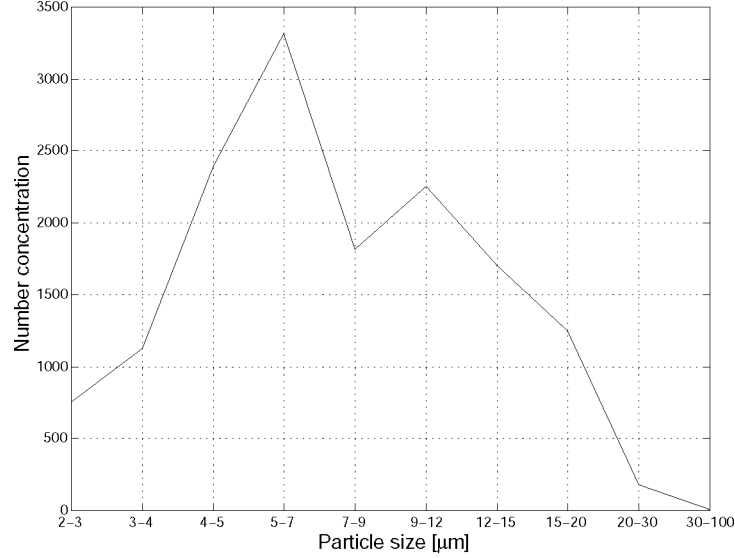


Figure 4.7: Size distribution of kaolinite mineral/primary particles used in the settling column.

floc size range likely to appear in the column due to flocculation (Auger, 2004). Focal distance, window size and resolution were then estimated on the basis of lens properties, camera frequency and resolution. Subsequently, several pilot tests were performed in order to qualitatively evaluate image focus, illumination and contrast. Two different configurations were tested: one with a camera of 720-by-512 pixel coupled with a 50 mm lens and an extension of 22 cm, and a second one with a camera of 1008-by-1008 pixel coupled with a 50 mm lens and an extension of 6.5 cm. The former configuration allowed to obtain a resolution of $4.16 \mu\text{m}/\text{pixel}$, whereas the latter allowed a resolution of $6.42 \mu\text{m}/\text{pixel}$. The laser generator was identical for both systems. Specific arrangements of the PIV system and post-processing techniques are briefly described in Section 5. These two optical configurations are used in the experiments described in Chapter 5.

The PIV optics have been set up such as to approximately detect the mode size in Figure 4.7. Kaolinite mineral is made of crystals with no porosity, and no surface or mass fractal properties. It is therefore sufficient to observe the mineral with one pixel. Also the primary particles are massive bodies, despite their surface can be described as fractal. However, following the definitions of dimensionless size ℓ' in Eq. (2.16) and ℓ in Eq. (3.4), we can approximate the primary particle size L_p with the pixel size ϵ . In this way one primary particle will result in a massive body (*i.e.* one single pixel) to the detector. This setting, on the one hand, preserves the substantial geometrical information, as kaolinite crystals and primary particles have effectively fractal dimension $d_0 = 3$ and $d_0 \approx 3$. On the other hand, this setting enables to use the camera resolution at best.

Chapter 5

Analysis of the experimental floc size distribution

This chapter describes flocculation at large scales on the basis of data collected in the settling column and the concepts elaborated in Chapter 3. Little literature is available to characterise (or to describe) flocculation dynamics in term of self-similarity, entropy, and organisation. This study is therefore focussed on detecting the large-scales structural properties of populations of flocs of cohesive sediment during their time evolution towards equilibrium, and for different regimes of turbulent shear rate under this perspective.

5.1 Introduction

The population dynamics is characterised by means of the Floc Size Distribution (FSD). From the analysis of the FSD four issues are addressed in this investigation. First, it is very common in laboratory as well as field measurements that the FSD appears non-monotonic with a peak centered about the 100-200 μm size range and, more rarely, with a peak also about the primary particle size. The FSD will therefore be characterised in terms of its (mono- and non-monotonic) shape. Second, the response of a population of flocs at equilibrium is analysed for different turbulent shear rates G in the settling column. Third, the quantity of order (information) of the FSDs at different times t and shear rates G is computed in the form of entropy, as introduced in Chapter 3. In this way a link between the (complexity of the) structure of the population will be established with respect to t and G . Fourth, the FSD will be analysed to discern whether scale-free characteristics, typical of Self-Organised Criticality (SOC), emerge in the population structure; if self-organisation is effectively present then a power-law in the FSD should appear as the population grows in time or adapts to the forcing.

This investigation is based on two separate experimental sessions carried out in the settling column: the first is aimed at the time evolution (t -dependence) of the floc size distribution at constant shear rate; the second is aimed at the response of the FSD to different shear rates (G -dependence). The suspension in the settling column can reach a uniform sediment concentration through two different regimes: *static* and *dynamic*. In the static regime, sediment is injected with a stationary grid; as it is not mixed throughout the column, the concentration profile shows a steep gradient before becoming uniform and equal to the desired concentration c_d , Figure 5.1 (a). Next, the experiment is started by moving the grid at time $t = 0$, which is the reference for all experiment. In the dynamic

regime sediment is mixed by the grid also during injection and the concentration profile appears nearly uniform, increasing in time until the desired value c_d is reached, Figure 5.1 (b). The first experiment (t -dependence of the FSD) is carried out in the dynamic regime, while the second experiment (G -dependence of the FSD) is run in the static regime.

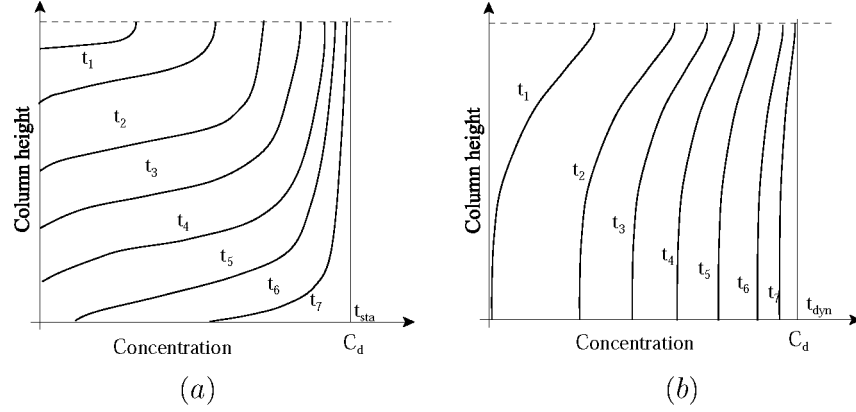


Figure 5.1: Qualitative time variation of the concentration profile in time for (a) static and (b) dynamic regime, where t_{sta} and t_{dyn} are the corresponding times to reach uniform sediment concentration in the column.

The interpretation of the results presented here, and the theoretical tools introduced in Chapter 3, will help us to draw an overall picture of the time evolution and equilibrium dynamics of flocculation on the large scales.

5.2 Time evolution of the floc size distribution

5.2.1 Description of the experiment

In this experiment the sediment is gently injected in clear water and with an equilibrium turbulent field (dynamic regime). As the concentration increases in time, also the flocculation reactions take place more frequently, the frequency being proportional to the sediment concentration. Therefore, the population observed in the measuring section is expected to show small flocs at the beginning of the experiment, and larger flocs when the concentration becomes uniform.

Kaolinite was used in the experiment with mineral size between 3 and 5 μm , and density $\rho_s \approx 2650 \text{ kg/m}^3$. The suspension in the storage tank was prepared at approximately $c_s = 15 \text{ g/l}$, while the desired sediment concentration in the column was set at $c_d = 0.5 \text{ g/l}$, in slightly salt water at salinity $s = 5 \text{ ppt}$. The temperature in the climatized room was set at $T = 18 \text{ }^\circ\text{C}$, while the grid was deployed with a displacement amplitude of 84 mm at a frequency $f_g = 0.5 \text{ Hz}$, corresponding to a turbulent shear rate of about $G = 18 \text{ s}^{-1}$. The experiment started at time $t = 0$ with an equilibrium turbulent field without sediment.

The PIV system used for this series of experiments consisted of a laser diode and a low-resolution digital camera that recorded 8-bit gray-scale digital images with a resolution of 720-by-512 pixel. An extension of 22 cm applied between the camera chip and the lens allowed an observation window of about 3-by-2 mm size with a lens of 50 mm, thus obtaining 4.16 $\mu\text{m/pixel}$ resolution (the primary particle size is $\approx 5 \mu\text{m}$). Single-frame

images were recorded at 25 Hz and organised in series of 7 minutes every 3 hours, eight times a day for 7 days, thus yielding a total of 577,500 images stored on digital tapes.

The images were transferred to PC and converted to black-and-white with the algorithm proposed in Maggi & Winterwerp (2003). 2D images (optical projections) of individual flocs $\Omega_2 \subseteq \mathbb{R}^2$ were extracted one-by-one from the black-and-white full-view images, and framed into the smallest square. The size L of this square was taken as the aggregate size, and normalised with the pixel size $\epsilon = 4.16 \mu\text{m}$ to obtain the dimensionless aggregate size $\ell = L/\epsilon$.

5.2.2 t -dependence of the FSD

Although a large number of frames were collected in the settling column, only few could be used to compute the FSDs. This was due to a stable vortex caused by the asymmetric geometry of the prototype separation chamber mounted in the measuring section, in which the samples were collected. The vortex caused the flocs to pass through the measuring window too fast to have good quality images. Because of this, flocs could be measured properly only a few times during the experiment, and only the frames at times $t = \{0, 3, 120, 162, 165\}$ h were processed to calculate the FSDs¹. Frames at time $t = 0$ h, in particular, were recorded in a separate test, without the column of sedimentation, by injecting the sediment directly in the measuring section. The data at time $t = 0$ describe the non-flocculated Suspended Particle Matter (SPM) injected in the buffer tank, and are the reference for investigating the SPM at times $t = \{3, 120, 162, 165\}$ h during flocculation in the full-scale facility.

The FSDs measured at times $t = \{0, 3, 120, 162, 165\}$ h are represented in Figure 5.2 in the form of probability $p(L)$ to find flocs of size L belonging to the geometrical series of classes $[L_i, L_i + \Delta L_i)$, $\Delta L_i \propto \epsilon 2^i \mu\text{m}$ being the class size and i the class number. The

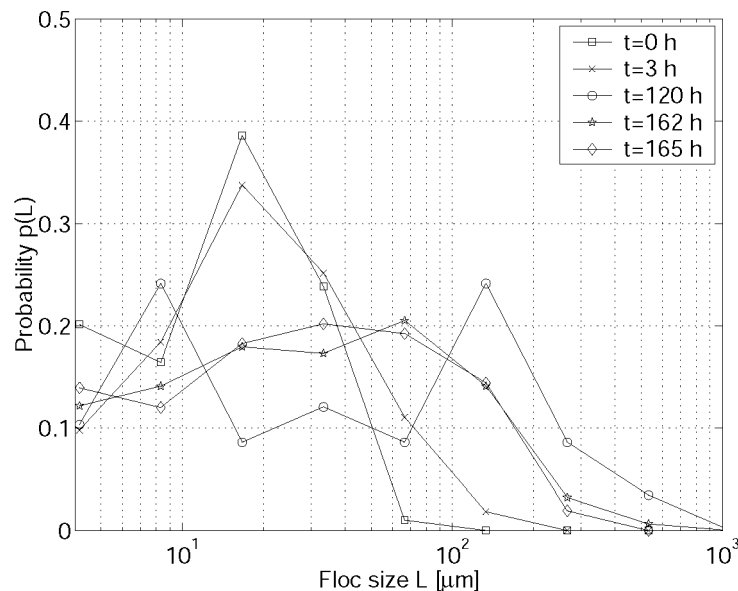


Figure 5.2: FSDs of kaolinite flocs at experimental times $t = \{0, 3, 120, 162, 165\}$ h for $G = 18 \text{ s}^{-1}$. See also Table 5.1.

¹The experiment was not repeated, but it gave important inputs on how to modify the geometry of the measuring section, the work that was done across 2003 and 2004.

data indicate that the majority of the flocs are, as expected, small initially and become larger in time. The modal floc size \tilde{L} is about $16.6 \div 20 \mu\text{m}$ at $t = 0 \text{ h}$ and $t = 3 \text{ h}$, then it increases to more than $100 \mu\text{m}$ at time $t = 162 \text{ h}$ and $t = 165 \text{ h}$. The FSDs $p_{t162}(L)$ and $p_{t165}(L)$ appear non-monotonic and almost similar, without strong variability. Unlike $p_{t0}(L)$, $p_{t3}(L)$, $p_{t162}(L)$ and $p_{t165}(L)$, the FSD $p_{t120}(L)$ has three peaks, with mode $\tilde{L}_{120} \approx 120 \mu\text{m}$ larger than for the FSD $p_{t162}(L)$, Table 5.1. However, $p_{t120}(L)$ comprises too few floc samples to properly represent the floc population at $t = 120 \text{ h}$.

Experimental time	t	[h]	0	3	120	162	165
Number of flocs			298	163	58	156	208
Mean	\bar{L}	$[\mu\text{m}]$	21.7	34.0	120.6	71.8	65.5
Mode ^(a)	\tilde{L}	$[\mu\text{m}]$	102.2	25.7	25.7	25.7	25.7
Mode ^(b)	\tilde{L}	$[\mu\text{m}]$	20.8	16.6	133.1	116.4	108.1
Std	σ_L	$[\mu\text{m}]$	14.9	31.4	150.9	86.6	72.5
State			NE	NE	SS	SS	SS

^(a) evaluated from the FSD.

^(b) evaluated from the sample.

Table 5.1: Statistics of the FSDs of Figure 5.2. NE stays for non-equilibrium, while SS stays for steady.

In the light of the mentioned lack of data, the effective time evolution could not be recorded properly. From our preliminary computations, a flocculation time scale $t_f \approx 0.5 \text{ h}$ and a residence time in the column $t_{rc} \approx 2 \text{ h}$ were predicted for constant concentration $c_d = 0.5 \text{ g/l}$ and shear rate $G = 18 \text{ s}^{-1}$, while measurements of the sediment concentration c along the column showed that $c = c_d = \text{const}$ only after time $t_{dyn} \approx 24 \text{ h}$, with aggregation and breakup rates homogeneously distributed in the water column, Table 5.2. We infer that

Sediment concentration	c	$[\text{gl}^{-1}]$	0.5	0.5	0.5	0.5	0.5	0.5
Shear rate	G	$[\text{s}^{-1}]$	0	5	10	18	20	40
Residence time in the column	t_{rc}	[h]	-	1.2	1.8	2.2	2.4	3.2
Residence time in the buffer tank	t_{rb}	[h]	6.3	6.3	6.3	6.3	6.3	6.3
Flocculation time	t_f	[h]	∞	1.9	1.0	0.53	0.476	0.2
Transition time in the settling column (dynamic regime)	t_{dyn}	[h]	24	24	24	24	24	24
Transition time in the settling column (static regime)	t_{sta}	[h]	10	10	10	10	10	10

Table 5.2: Time scales related to the functioning of the facility. The computation of t_{rc} and t_f is based on the flocculation model in Eq. (2.24) (Winterwerp, 1999).

the flocculation time scale t_f is much larger than the predicted value of $t_f \approx 0.5 \text{ h}$, because the concentration increases slowly in the column. From this, we infer that flocculation at times $t < t_f + t_{dyn} \approx 25 \text{ h}$ is not at equilibrium, while for times $t > t_f + t_{dyn} \approx 25$

h flocculation can be considered in equilibrium. For this reason, we are confident that the FSD at time $t = 0$ h represents the initial *non-flocculated* SPM, the FSD at time $t = 3$ h represents a *flocculating* SPM, while FSDs at times $t = \{120, 162, 165\}$ h represent *flocculated* SPM. Excluding $p_{t120}(L)$ from this analysis, we argue that the FSDs $p_{t0}(L)$ and $p_{t3}(L)$ belong to the non-equilibrium transition, whereas the FSDs $p_{t162}(L)$ and $p_{t165}(L)$ belong to the steady state. An interpretation of the flocculation processes in time can be drawn despite the lack of data for the mid-time FSDs, thus making not necessary to repeat the experiment. The data drawn in Figure 5.2 allow in fact to detect the effect of the major process (flocculation) occurring to the suspension, because the initial and final states of the system show an evident difference. In particular: (1) kaolinite minerals are predominantly subject to processes of aggregation (rather than breakup) from time $t = 0$ h to a time $t_{tr} \approx 25$ h, that is denoted as the non-equilibrium transition time; (2) the evolution of the population reaches a steady state characterized by a balance between aggregation and breakup. The time evolution of the FSD of the population is marked by a shift of the mode from $\tilde{L} \approx 17 \mu\text{m}$ to $\tilde{L} \approx 67 \mu\text{m}$, and by a widening of $p(L)$ from $\sigma_L = 31.4 \mu\text{m}$ to $\sigma_L = 73.5 \mu\text{m}$. The population at steady state can be inferred to be statistically stationary, according to Sections 3.1.1 and 3.1.3, as aggregation and breakup processes are stochastically balanced.

Changes in $p(L)$ are indicators of the growth processes of the population. In this particular experiment with controlled sediment type and concentration, temperature and turbulence, all FSDs are non-monotonic with one maximum (excluding p_{t120}). Yet, the probability $p(L = L_p)$ of the first class of the FSDs in Figure 5.2 (the smallest flocs) may not be accurate because the optical system and post-processing techniques have the tendency to underestimate the concentration of aggregates whose size compares to the pixel size ($\epsilon = 4.16 \mu\text{m}$), *i.e.* the primary particles approximately ($L_p \approx 5 \mu\text{m}$) (Maggi & Winterwerp, 2003). This is caused by the low energy scattered by the smallest particles, resulting in low-contrast pixels with respect to the surrounding background noise². This lets us argue that the FSDs may have a peak also at L_p , and not only at large floc sizes.

5.3 Floc size distribution and rate of turbulent shear

5.3.1 Description of the experiment

In this experiment the floc size distribution a suspension of kaolinite mineral is studied with respect to the turbulent field generated by the grid at different shear rates G . The sediment is gently injected in clear water and with no turbulent field (static regime). When the sediment concentration is nearly uniform and constant in time along the column, the grid oscillation is started.

A different supply of kaolinite was used in this experiment with respect to the previous one. A comparison of the sedimentation curve of the two different kaolinites showed that kaolinite from the second stock was a bit less reactive than from the first one. This

²Based on a qualitative comparison between raw and filtered images, $p(L = L_p)$ might be approximately 20÷40% higher than in Figure 5.2. Surprisingly, the literature does not devote attention to this aspect, even when similar techniques have been used. However, a smallest reference floc size is needed, preferably the actual primary particle size. As this floc size probably cannot be measured, the pixel size is used instead in the remainder of the thesis.

motivated a slight correction by adding few moles of chloride acid (HCl) to decrease the electrical barrier. The quantity of acid was calibrated against the sedimentation curves. A decrease in pH from 8 to 6.7 allowed to obtain substantially similar sedimentation curves (not shown here). The pH in the settling column was thereby decreased to 6.7.

The kaolinite suspension in the storage tank was prepared at approximately $c_s = 35$ g/l, while the desired sediment concentration in the column was set at $c_d = 0.5$ g/l. The temperature in the climatised room was set at $T = 18$ °C, while the grid was deployed with a displacement amplitude of 84 mm and various frequencies f_g corresponding to $G = \{0, 5, 10, 20, 40\}$ s⁻¹. The time scale t_{sta} for the column to reach a uniform sediment concentration profile in the static regime was $t_{sta} \approx 10$ h, and the flocculation time scale t_f varied in $t_f = (0.5, \infty)$ h, Table 5.2. The shear rate G was changed once every 12 hours to do a series of measurements, also when $G = 0$ s⁻¹ and $t_f \rightarrow \infty$.

The PIV system used for this experiment consisted of a laser diode and a high-resolution digital camera that recorded 8-bit gray-scale digital images of 1008-by-1008 pixel size. An extension of 6.5 cm applied between the camera chip and the lenses allowed an observation window of about 6-by-6 mm with a 50 mm lens, thus obtaining 6.42 μm /pixel resolution. The measurements consisted of 3 series of recordings for each value of G , with a time lag of 3 hours³. Each series was organised in 80 blocks, each one consisting in 2 seconds of recording and 3 seconds of pause in order to renew the population in the camera view. The 2 seconds recordings allowed us to collect 30 single-frame images at 15 Hz frequency, which were stored directly on the hard-drive of the PC controlling this PIV system.

Gray-scale images recorded during the experiment were converted to black-and-white with the algorithm proposed in Auger (2004), and processed in the same way as described in Section 5.2, to obtain the size L of individual flocs.

The measuring section used in the experiment described in Section 5.2 was improved to obtain better quality images and increase the number of flocs to be analysed. Consequently, this experiment could rely on a larger data set, yielding better statistics.

5.3.2 G -dependence of the FSD

The floc size distributions given in Figure 5.3 have been recorded in the measuring section of the column at $G = \{0, 5, 10, 20, 40\}$ s⁻¹. The data in Figure 5.3 show that the turbulent shear rate has an impact on the sediment suspension: increases in G correspond to a shift of \tilde{L} towards smaller aggregates, Table 5.3.

Turbulence shear rate	G	[s ⁻¹]	0	5	10	20	40
Number of flocs			872	527	624	458	500
Mean	\bar{L}	[μm]	88.6	44.8	42.7	38.8	35.5
Mode ^(a)	\tilde{L}	[μm]	102.2	25.7	25.7	25.7	25.7
Mode ^(b)	$\tilde{\tilde{L}}$	[μm]	32.1	32.1	32.1	25.7	25.7
Std	σ_L	[μm]	63.6	40.8	44.3	38.36	34.1
State			-	SS	SS	SS	SS

^(a) evaluated from the FSD.

^(b) evaluated from the sample.

Table 5.3: Statistics of the FSDs of Figure 5.3. SS indicates steady state conditions.

³For instance, with $G = \text{const}$ for time $t \in [0, 12]$ h, three series were recorded at times $t = \{6, 9, 12\}$ h.

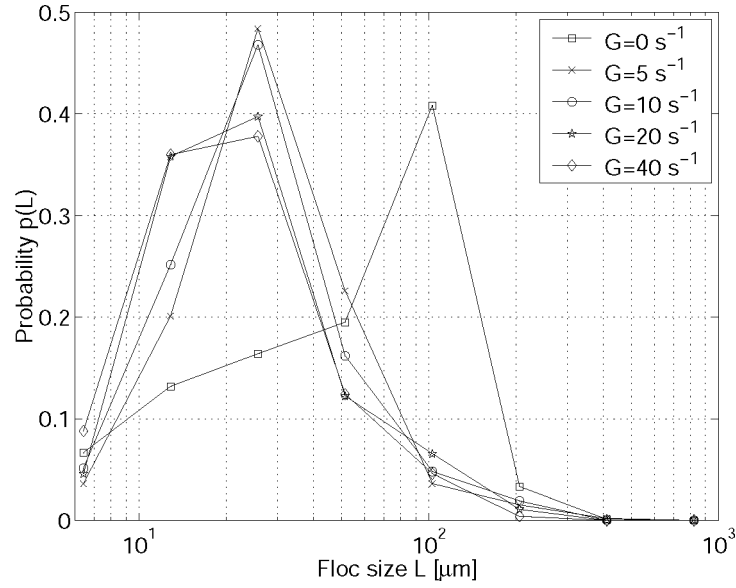


Figure 5.3: FSDs of kaolinite flocs for shear rates $G = \{0, 5, 10, 20, 40\} \text{ s}^{-1}$.

Figure 5.4 shows that the mean floc size \bar{L} decreases with G from $\bar{L} \approx 90 \text{ } \mu\text{m}$ at $G = 0 \text{ s}^{-1}$ to $\bar{L} \approx 35 \text{ } \mu\text{m}$ at $G = 40 \text{ s}^{-1}$. Furthermore, Figure 5.4 shows that the average floc size is much smaller than the Kolmogorov length scale η_k estimated as in Eq. (2.15).

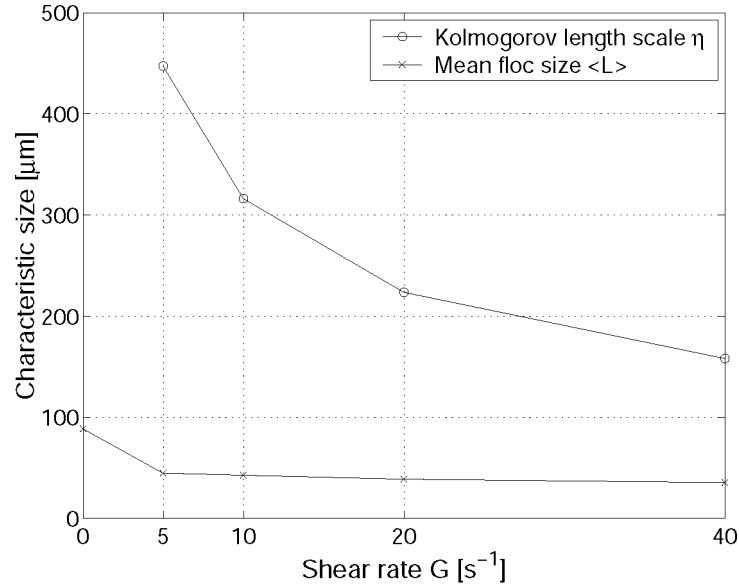


Figure 5.4: Representation of the average floc size \bar{L} and Kolmogorov length scale η_k estimated according to Eq. (2.15) as a function of turbulent shear rates $G = \{0, 5, 10, 20, 40\} \text{ h}$.

A particular note is required for the FSD $p_{G0}(L)$ measured with $G = 0 \text{ s}^{-1}$. In the frame of turbulence-induced flocculation, flocs should not form if $G = 0$ because $t_f \rightarrow \infty$, hence something else is promoting flocculation in the column. The propellers in the buffer tank are a source of mixing, therefore the sediment may be subject to turbulence-induced flocculation during the time they reside in the buffer tank. Another possibility is that large flocs in $p_{G0}(L)$ are the result of differential settling. A third reason for a high probability

density of large aggregates may be due to the use of chloride acid: as the strength of the electrical barrier decreases by lowering the pH , the collision efficiency can become higher (perhaps close to 1), thus causing large aggregates to grow even for low frequency of collision.

5.4 Statistical (information) entropy

The probabilities $p(L)$ plotted in Figures 5.2 and 5.3 can be used to compute the entropy $S = -\sum p(L) \ln[p(L)]$ of the population of flocs according to Eq. (3.9), Section 3.2.1.

Note that in Section 3.1.1, the concepts of entropy and organisation have been introduced with respect to the large-scale *spatial* structure of the system within its domain. There, we have argued that the spatial entropy decreases as a consequence of flocculation, and the works by Hermanowicz (about geometric entropy) and Krone (about thermodynamic entropy) have been quoted in Chapter 3. However, the entropy S computed in this section does not refer to the spatial organisation or to the temperature variations in the systems, but to the organisation of the sizes of the flocs within the population. Following the definition of the information function I of Eq. (3.13) in Section 3.2.2, it is possible to observe that $I \propto S$, regardless of what the probability p is associated with. Therefore, theoretically, S computed for $p(L)$ gives a measure of the quantity of information needed to describe the stochastic distribution of flocs with respect to their sizes.

The entropy S computed at times $t = \{0, 3, 162, 165\}$ h, Table 5.4, shows that the population increases its level of complexity as it proceeds towards the steady state. This

Experimental time	t	$[h]$	0	3	120	162	165
Number of flocs			298	163	58	156	208
Information entropy	S		1.375	1.569	-	1.888	1.835
State			NE	NE	SS	SS	SS
Turbulence shear rate	G	$[s^{-1}]$	0	5	10	20	40
Number of flocs			872	527	624	458	500
Information entropy	S		1.549	1.325	1.372	1.361	1.372
State			-	SS	SS	SS	SS

Table 5.4: Information entropy of the t -dependent and G -dependent FSDs for $c_d = 0.5$ g/l. NE and SS indicate non-equilibrium and steady state respectively.

is due to an increasing number of large aggregates within the population. The fact that the entropy S increases as flocculation proceeds means that the population is progressively increasing its maximum floc size and complexity. Physically, the system displays a wider set of *different* individuals. A similar interpretation holds for the entropy S computed for the equilibrium FSDs at shear $G = \{0, 5, 10, 20, 40\}$ s^{-1} , Table 5.4. In this case we note that S tends to decrease for increasing G at low shear rates, as a higher shear causes large flocs to break up. This corresponds to a decrease in complexity of the population in terms of floc size description.

5.5 Self-organised criticality

Indication (but not proof) of self-organised criticality may be found in the scale-free behaviour of the floc size distribution, Section 3.1.4.

The FSDs of Figures 5.2 and 5.3 do not display any apparent exponential relationship between L and $p(L)$; the data point of the FSDs at time $t = \{0, 3, 162, 165\}$ h and shear rate $G = \{0, 5, 10, 20, 30\}$ s⁻¹ are therefore sorted by rank r as explained in Section 3.1.4. In order to have more classes than in the data shown in Figures 5.2 and 5.3, the probabilities $p(L)$ are computed for 200 classes evenly spaced ($[L_i, L_i + \Delta L_i)$, where $\Delta L_i = \text{const } \forall i$)⁴.

The resulting t -dependent r -ordered probabilities $p(r)$ are given in Figure 5.5 (a). Neglecting values $p(r) \leq 5 \cdot 10^{-2}$, as being too small to describe the population significantly and because they are distorted by statistical sampling, we recognise two different slopes. One corresponds to the FSDs $p_{t0}(r)$ and $p_{t3}(r)$ in the non-equilibrium state (marked as NE) and, a second one, to the FSDs $p_{t162}(r)$ and $p_{t165}(r)$ in the steady state (marked as SS). The corresponding power regressions $y = bx^a$ have slopes $a_{NE} = -0.37$, which differs much from the theoretical value $a \approx -1$ associated with self-organised criticality, and $a_{SS} = -0.93$, which is remarkably close to -1 . From the time evolution of the FSD we deduce that values $-1 < a < 0$ can be associated with non-equilibrium populations in the course of evolution, and that values $a = -1$ can be associated with FSDs at steady states.

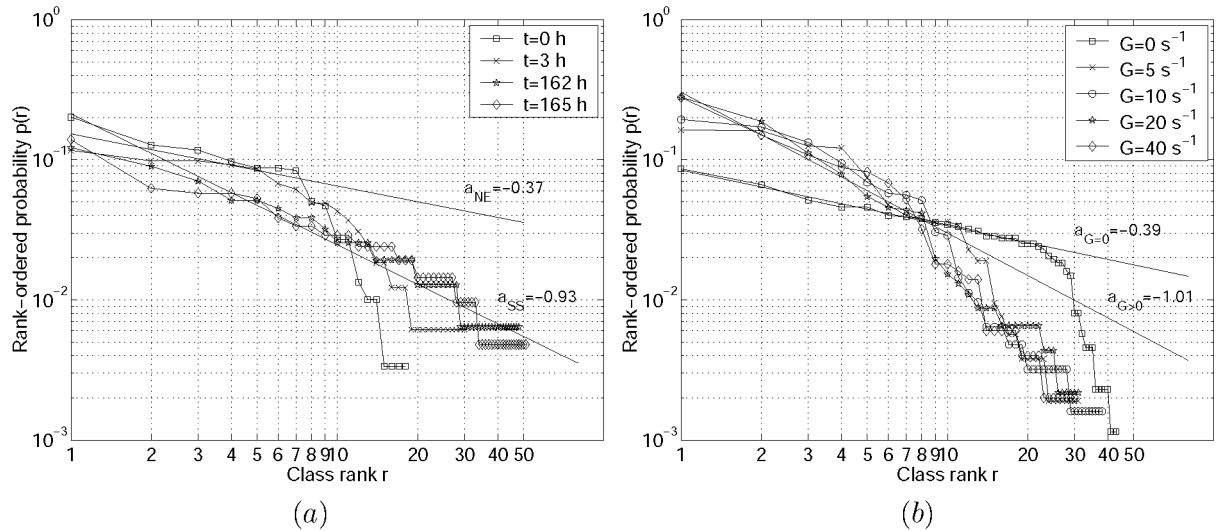


Figure 5.5: Rank-ordered FSDs of kaolinite flocs for (a) experimental times $t = \{0, 3, 162, 165\}$ h and (b) shear rates $G = \{0, 5, 10, 20, 40\}$ s⁻¹. The straight lines represent the power regressions $y = bx^a$, with slope a .

The r -ordered G -dependent FSDs have been analysed analogously. Probabilities $p(r) \leq 5 \cdot 10^{-2}$ are neglected also in this case, Figure 5.5 (b). Again, we observe that two dominant power-law scaling are present with two different slopes: the first $a_{G=0} = -0.39$ for $G = 0$ s⁻¹, and the second $a_{G>0} = -1.01$ for shears $G = \{5, 10, 20, 40\}$ s⁻¹. Two aspects must be noted. The first is that a slope $a \approx -1$ is present in the equilibrium FSDs independently from the forcing G applied to the suspended aggregates, see also constant entropy S in Table 5.4. This, again, can be considered as an indication of self-organised criticality. The second is that $a_{G=0} > -1$ differs largely from the slope of the other FSDs. This can be

⁴The r -ordered probabilities $p(r)$ are still such that $\sum p(r) = 1$.

attributed again to the processes of flocculation occurring in the settling column in the absence of a turbulent field, Section 5.3.2. According to the interpretation given to a , the FSD $p_{G0}(r)$ is at non-equilibrium⁵.

5.6 Discussion

5.6.1 Flocculation and equilibrium

The results in Figure 5.5 do not yield a straightforward interpretation; careful reasoning is needed. Phenomenologically, we can interpret these results as follows. Take into consideration the initial monodisperse system of case C2 of Figure 3.2: here the power scaling $p(r) \propto r^a$ does not hold as it collapses to a singularity point corresponding to $a = 0$ and $p(r) = 1$, with rank $r = 1$ solely (equivalent to $p(L_p) = 1$, *i.e.* monodisperse population). If the system is multidisperse, then a size distribution of primary particle would lead to an r -ordered initial distribution with $a \neq 0$. Therefore, the non-flocculated SPM of dispersed real sediment in the non-equilibrium is characterised by $-1 \ll a \approx 0$. The number of flocculated aggregates is zero or nearly zero and the information entropy is the lowest. As flocculation takes place, the population starts to develop its structure, which becomes increasingly complex as aggregation and breakup go on. During this phase, the exponent a can be inferred to depart from zero with $a : -1 < a < 0$, and the structure of the population can be thought of as "under construction", as aggregation and breakup are not in balance. Here, the number of larger aggregates is progressively increasing together with the information entropy, Table 5.4. Only after a certain time, the population's structure is wholly formed and the exponent a approaches the value $a \approx -1$. This can be associated with FSDs at steady state and with the maximum information entropy at equilibrium. A similar evolution of the parameter a can be defined for a non-equilibrium SPM, where the initial condition is not represented by a non-flocculated population but rather by a population saturated by large aggregates.

Our interest goes to the particular case of equilibrium expressed by $a = -1$. This may be an indication that the floc population at steady state lies at a criticality point at which any event of aggregation and breakup causes the population to redistribute its individuals in such a way as to *replicate* its structure (its FSD), like in the case of the sand pile described in Section 3.1.4. Self-organised criticality (structure replication) does not occur in populations with $-1 < a < 0$, as an event of aggregation is not equally balanced by an event of breakup. Although the large amount of data collected worldwide on the FSD of suspended sediment in both laboratory and field, it is not known from the literature whether such rank power scaling with $a = -1$ has been observed earlier. In addition, the extent to which natural conditions allow equilibrium in the FSD of suspended sediment aggregates is not known, because of the large number of factors that influence the sediment's fate at so different time and length scales. As an exercise, assume the r -ordered probability $p(r)$ to scale universally as a power of r with $a = -1$ if and only if at equilibrium. Then, a power-law of the form $p(r) = b \cdot r^{-1}$ would appear fruitful to

⁵Till now we have only referred to non-equilibrium population in terms of non-flocculated dispersed SPM. However, we do not have to exclude that a non-equilibrium state occurs for other cases as well: imagine that the SPM is initially all grouped into a single large floc like the one in Figure 3.2, Section 3.1.1. If breakup is allowed then it will disintegrate into smaller flocs, meaning that the initial system is at non-equilibrium.

establish whether the SPM is at equilibrium without assessing the full time history of the population: the parameter b is in this case determined as:

$$b = p(r = 1) = p(L = \tilde{L}). \quad (5.1)$$

Application to field data would give an immediate indication of the *status* of the suspended sediment, allowing to predict whether changes in the SPM are likely to occur in the short-term. Further data should be analysed to validate this assumption on the power scaling at criticality point, preferably from *in situ* and laboratory observations.

5.6.2 Self-similarity and autonomy

This analysis allows us to develop further some simple concepts on the equilibrium dynamics and structural properties of a suspension of cohesive sediment at equilibrium. The r -ordered probability density of the floc size distribution observed in time and for different turbulent shear rate appears essentially t - and G -invariant. This raises the following question: is there any autonomous behaviour in the distribution of floc sizes of interacting particles? Early studies by Schumann (1940) about suspensions of fog droplets, and more recent studies by Lehtinen & Zachariah (2001) about aerosols, showed that the normalised size distribution possesses some sort of invariance, sometimes called also self-similarity, like in Thomas *et al.* (1999). According to the author, the term self-similar is not appropriate here, as self-similarity implies similar (affine) shape at different length scales: this is not the case for floc size distributions, because these are normally non-monotonically shaped with one maximum, and not an infinity of (relative) maxima. Rather, it is more appropriate to call this *shape-invariance*, or *shape-preservation* (Lehtinen & Zachariah, 2001). However, a major point must be mentioned: such shape-invariance is a geometrical property expressing that the FSD is invariant with regard to the boundary conditions. As any FSD analysed in these two experiments (t - and G -dependence) show identical power-law distribution $p(r)$ at equilibrium (with $a = -1$) then we can infer that *autonomy* is the property that better describes this behaviour.

As self-organised criticality is characterised by power-law distributions with $a = -1$, we have added a property for which a system at SOC state is autonomous from the external forcing, in the sense that $a = -1$ could be a characteristic constant of the system. This particular behaviour might be linked to a far-from-equilibrium steady state, governed by negative feedbacks of processes (aggregation and break) continuous in time, as discussed in Chapter 3. If the paradigm of self-organised criticality holds, it is likely to be correlated to far-from-equilibrium dynamics. However, to the author's knowledge, no formal definition or written theory is known that comprises these aspects in a comprehensive framework on the dynamics of particulate systems. This motivates the author to consider this as a possible future path to improve our knowledge of flocculating systems.

5.7 Conclusions

The floc size distribution of cohesive sediment suspensions possesses many characteristics that can be used to bring light on to the flocculation processes.

First, the time evolution of the FSD indicates that a suspension of kaolinite flocs subject to flocculation processes reaches a steady state from a non-flocculated state. This affects

the average floc size and, above all, the modal floc size, as recognised elsewhere in the literature and in the data presented here.

Second, flocculation is accompanied by an increase in information entropy of the sizes of the flocs in the population. The evolution towards steady state implies floc growth, the population becoming more complex. If we associate this with the progressive decrease in total particle distance H of Section 3.1.1, then the population of flocs becomes less disordered spatially and more complex in terms of size distribution.

Third, the suspended particle matter is affected by the turbulent shear rate, as observed from the relationship between the mean floc size \bar{L} and G . However, the population's structure, *i.e.* how it is organised, appears invariant and described by a rank power-law $p(r) \propto r^a$ with $a = -1$, at any equilibrium state.

Fourth, the equilibrium dynamics of a population of flocs is marked by a progressive transition towards a criticality point characterised by the exponent $a = -1$. This value is associated with self-organised criticality, meaning that the population might experience an equilibrium for which its structure, or its floc size distribution, remains statistically stationary independently from turbulent shear and time. This behaviour has been called autonomy; it can be associated with the far-from-equilibrium state of the system, and the negative feedback that contributes to the complex behaviour of flocculating systems, Section 3.1.3.

The measurements performed in the column, and the settling column itself, give an innovative view of the flocculation process of cohesive sediment, due to the time and length scales involved. Despite this, a number of limitations exist. First, we do not possess a wide data set; this does limit our capability to study flocculation for specific physical, chemical and sedimentological aspects. For example, the lack of floc samples in the non-equilibrium state does not allow to track the time evolution of the floc size distribution with a high time resolution. Second, the optical system, the resolution of the digital camera and the post processing technique for data analysis do not allow to quantify accurately the presence of very small flocs and primary particles. This means that the observed floc size distributions might have two peaks, one at the small floc sizes. Third, we have seen in Section 5.3 that the floc size distribution at $G = 0 \text{ s}^{-1}$ shows a problematic interpretation. However, the available data have allowed to draw a number of conclusions that enhance our understanding of flocculation.

Chapter 6

Analysis of the geometrical structure of flocs

The structural properties of flocs are analysed in this chapter as a result of the large-scales processes. This is carried out on the basis of optical recordings collected in the settling column. The analysis of the floc structure is limited to two dimensions but, thanks to the mathematical tools developed for this analysis, we will be able to infer three-dimensional structure properties of cohesive sediment flocs and elaborate on a detailed characterisation of their growth dynamics.

6.1 Introduction

This chapter is focussed on three aspects. First, though the primary particles are nearly monodisperse in size and shape (Figure 3.5 (b)), the flocs' shape normally appears rather irregular (Figure 3.5 (c) and (d)). Flocs' shape will therefore be characterised by means of the entropy function S and index of disorder Υ' (*i.e.* the normalised form of the spatial entropy function of Section 3.2.1) as a function of L . Second, aggregates have been fruitfully described as *self-similar* structures with a capacity dimension $d_C = d_0 = \text{const}$ for each aggregate within the same population. Despite this, recent investigations have shown that d_0 changes in time during flocculation (Chakraborti *et al.*, 2003), therefore $d_0 \neq \text{const}$. For this reason, we will elaborate in detail the concept of self-similarity by means of the multifractal spectrum to detect whether one or more scaling exponents (or fractal dimensions) are needed to describe their geometry. Third, the multifractal spectrum will give the possibility to establish a method to extract the 3D capacity dimension of the aggregates from their optical projections and to elaborate further the relationship between d_0 and the dimensionless floc size ℓ .

This investigation is based on optical data collected in the settling column, discussed in Chapter 5. The interpretation of the results presented here, and the theoretical tools introduced in Section 3.2, will guide us to draw a specific picture of the growth process of aggregates at small scales.

6.2 Index of disorder and boundary structures

The spatial entropy function $S(\epsilon)$ of 2D projected floc shapes $\Omega_2 \subseteq \mathbb{N}^2$ is computed according to the theory in Section 3.2.1 and applied to the steady state population of flocs at

time $t = 165$ h described in Section 5.2. Figure 6.1 (a) shows the entropy $S(\epsilon)$ as a function of the normalised box size $0 < \epsilon/L \leq 1$ of the ω -covering and floc size L ¹. We observe that $S(\epsilon) = 0 \forall \epsilon \in (0, 1]$ when flocs are very small. Starting from $L \simeq 10 \mu\text{m}$, the entropy function is not constant but increases progressively with increasing L , showing a typical Gaussian-like shape, with a maximum $\sup\{S(\epsilon)\} = S'$ for a certain value $\epsilon = \epsilon'$. However, this representation of the entropy does not give us a clear view of the total amount of disorder relative to a reference; to this end the disorder index $\Upsilon' = S'/S'_{max}$ is computed according to Eq. (3.10). The values of Υ' are shown in Figure 6.1 (b), from which we deduce that $0 < \Upsilon' \ll 1$ describes small flocs with a highly homogeneous mass distribution, similar to Euclidian (fully-massive, fully-regular) shapes. In contrast, $\Upsilon' \approx 0.5$ suggests that large flocs lie mid-way between regular and white-noise-like (fully random with no spatial correlations) shapes, being rather complex and less homogeneous.

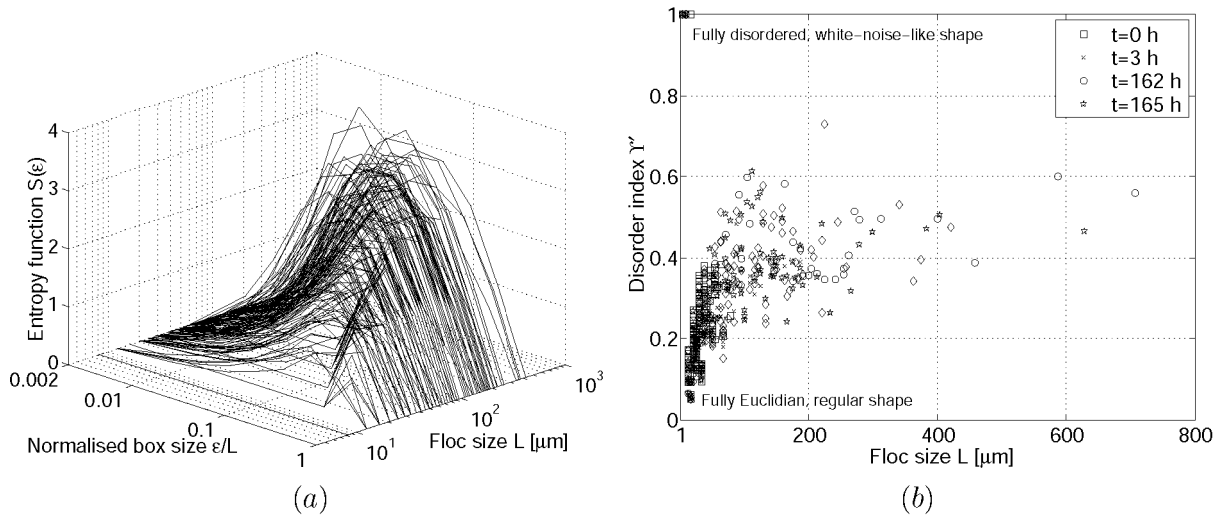


Figure 6.1: (a) representation of the entropy function $S(\epsilon)$ of flocs at time $t = 165$ h (steady state population) as a function of normalised box size ϵ/L and floc size L . (b) representation of the disorder index Υ' of flocs at time times $t = \{0, 3, 162, 165\}$ h as a function of L .

The data in Figure 6.1 are based on 2D projected shapes of flocs; this requires a few more words to understand the significance of these results. Consider the 2D projection of an irregular 3D body with uniform (*i.e.* of all scales) and non-homogeneous (*i.e.* unevenly distributed in space) porosity: the result is the shadow of the object, that is irregular along the perimeter and possibly with no, or very little, porosity (voids) within the area. The entropy function $S(\epsilon)$ detects the irregularities appearing essentially on the border, therefore Υ' refers to the floc roughness. Hence, the length scales of the surface roughness can be characterised by means of ϵ' because it corresponds to the ω -covering that detects the largest variety of patterns (on the border). Figure 6.2 shows that, in general, the size ϵ' of surface structures increases linearly with L : $\epsilon' \propto L$. The data align to the straight lines with regular slopes because of the box sizes ϵ of the ω -covering chosen for this computation. Suppose a continuous, instead of discrete, variation of ϵ ; then the data would be scattered (distributed), rather than clustered. Because of this, it is reasonable to consider $\epsilon' = \rho L$,

¹As digital images (*i.e.* discrete and $\subseteq \mathbb{N}^2$) are analysed, the finest ω -covering corresponds to $\epsilon = 1$ pixel. The resolution is such that 1 pixel is $4.16 \mu\text{m}$ size (Section 5.2), hence approximating the primary particle size, that is about $5 \mu\text{m}$. The dimensional floc size L is computed by the product $L = \ell \cdot \epsilon$, see also Section 3.2.

with $\varrho : 1/2 < \varrho < 1/8$ roughly. This result is an indication that floc growth is accompanied by development of structures growing linearly with L and with a distribution. This may be linked to particle diffusion and aggregation processes of DLA and CCA examined in Section 2.5.2, or correlated to the spectrum of frequencies and length scales associated with a turbulence field.

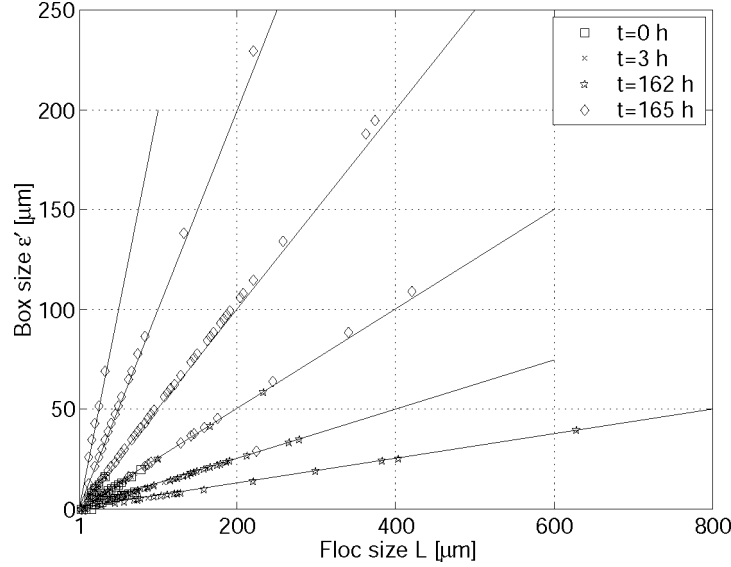


Figure 6.2: Representation of the box size ϵ' of the ω -covering corresponding to S' as a function of L . ϵ' indicates the length scales of the maximum disorder associated with surface structures.

6.3 Mass-density organisation of the flocs: multifractality

A distribution in length scales ϵ' of the peripheral structures on the flocs in Section 6.2, makes us foresee that the geometry of the flocs is not built up in a regular manner during growth. Said regularity can be better characterised in terms of scaling laws by means of the multifractal spectrum, as this is able to detect non-homogeneous organisation in mass-density. The spectrum of fractal dimensions $f(q)$, the singularity strength $\alpha(q)$ and the mass-correlation exponent $\tau(q)$ are computed for the population of flocs at time $t = 165$ h. The reader is therefore referred to the theory and method of computation in Sections 3.2.2, 3.2.3 and 3.2.4.

The multifractal spectrum $f(q)$ and singularity strength $\alpha(q)$ are represented as functions of the family order q and floc size L in Figure 6.3 (a) and (b). From these plots we observe that the majority of the aggregates have $f(q) \neq \text{const}$ and $\alpha(q) \neq \text{const}$. However, a certain number of aggregates in the range of small-to-mid sizes have $f(q) = \text{const} \leq 2$, and part of these have $\alpha(q) = 0$. This means that small and very small aggregates can be described as either Euclidian ($f(q) = 2$) or fully self-similar ($f(q) = \text{const} < 2$) bodies, while the majority shows statistically self-similar geometry ($f(q) \neq \text{const}$). Upon combination of $f(q)$ and $\alpha(q)$ we obtain the curves in Figure 6.3 (c). This representation, enables a better view of the fractal attributes of the aggregates as a function of L . Euclidian and fully self-similar aggregates are represented by the dots in Figure 6.3 (c) (in the

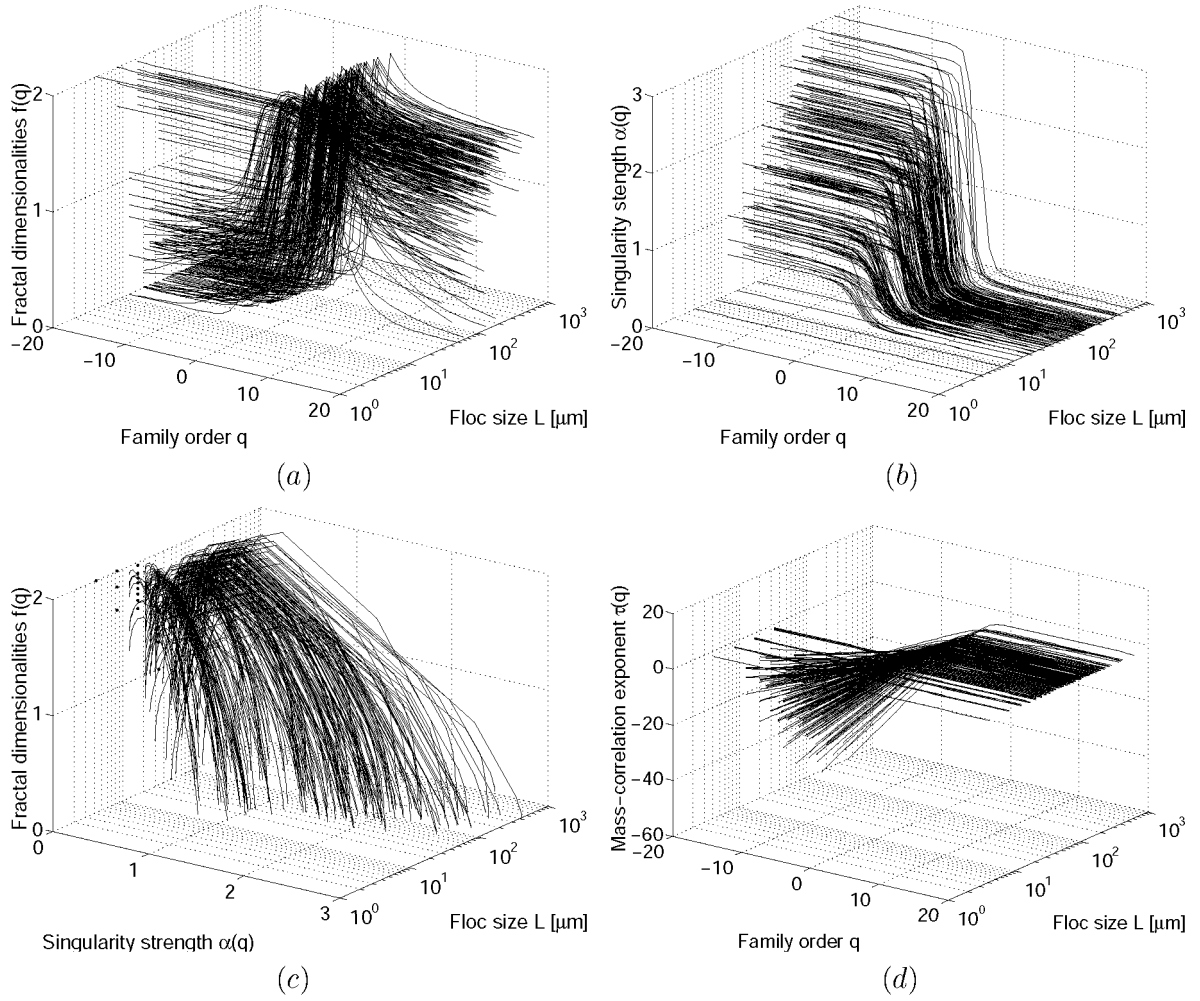


Figure 6.3: (a) multifractal spectra $f(q)$ as a function of family order q and floc size L . (b) singularity strengths $\alpha(q)$ as a function of family order q and floc size L . (c) multifractal spectra $f(q)$ as a function of singularity strength $\alpha(q)$ and floc size L . (d) mass-correlation exponents $\tau(q)$ as a function of family order q and floc size L . All data are computed for a floc population at time $t = 165$ h.

plane $\alpha = 0$ and $\alpha > 0$ respectively, see also Appendix A.1), while statistically self-similar ones are represented by the solid lines. In particular, growth of aggregates is accompanied by a progressive development of multifractal geometry. Small aggregates are characterized by a spectrum corresponding to a singularity point; the larger an aggregate the wider the singularity strength α and the lower the dimensions $f(q)$. Finally, the mass-correlation exponent $\tau(q)$ is represented in Figure 6.3 (d) as a function of q and L . Some small aggregates have $\tau(q) = \text{const}$ while, for larger sizes, aggregates are characterised by $\tau(q) \neq \text{const}$. This means that the mass-density distribution of small, fully self-similar flocs can be described by a unique scaling exponent, which is related to the slope of $\tau(q)$. Unlike small flocs, large flocs are statistically self-similar, with multiscaling geometries. These aggregates require more than one scaling exponent to describe their mass-density distribution. These exponents are related to the two dominant slopes of the mass-correlation exponent τ , for $q < 0$ and $q > 0$ respectively.

6.4 Multifractality: from projected to real aggregates

The multifractal property of 2D images of flocs $\Omega_2 \subseteq \mathbb{N}^2$ does not imply straightforward that real flocs $\Omega_3 \subseteq \mathbb{R}^3$ are multifractals. According to Falconer (1990), the linear transformation of projection $\mathcal{P} : \mathbb{R}^m \rightarrow \mathbb{R}^n$ of a fractal set $\Omega_m \subseteq \mathbb{R}^m$ of generalised dimensionality $d_q(\Omega_m)$ into $\Omega_n \subseteq \mathbb{R}^n$ with $m > n$, yields:

$$d_q(\Omega_n = \mathcal{P}(\Omega_m)) = \min\{n, d_q(\Omega_m)\}. \quad (6.1)$$

If $d_q(\Omega_m) > n$, then the projection Ω_n has dimensionality $d_q(\Omega_n) = n$, otherwise $d_q(\Omega_n) = d_q(\Omega_m)$. When the projection Ω_n has the same dimensionality as the projected set Ω_m ($d_q(\Omega_n) = d_q(\Omega_m) < n$), then \mathcal{P} is called a *dimension-preserving* transformation. Hunt & Kaloshin (1997) have proven analytically that Eq. (6.1) is dimension preserving only for $q \in (1, 2]$, hence for the information and correlation dimensions d_1 and d_2 . Formally, we write:

$$d_q(\Omega_n) \begin{cases} = d_q(\Omega_m) & \text{for } q \in (1, 2] \wedge d_q(\Omega_m) \in [0, n), \\ = n & \text{for } q \in (1, 2] \wedge d_q(\Omega_m) \in [n, m], \\ \text{undet.} & \text{otherwise,} \end{cases} \quad (6.2)$$

with $\Omega_n = \mathcal{P}(\Omega_m)$. Next, consider the inverse transformation $\mathcal{P}^{-1} : \mathbb{R}^n \rightarrow \mathbb{R}^m$ of the set $\Omega_n \subseteq \mathbb{R}^n$ into $\Omega_m \subseteq \mathbb{R}^m$, with $n < m$. This is dimension preserving if and only if $q \in (1, 2]$, and we write:

$$d_q(\Omega_m) \begin{cases} = d_q(\Omega_n) & \text{for } q \in (1, 2] \wedge d_q(\Omega_n) \in [0, n), \\ \text{undet.} & \text{otherwise,} \end{cases} \quad (6.3)$$

with $\Omega_m = \mathcal{P}^{-1}(\Omega_n)$. Equation (6.3) can be used to determine the infinitive number of fractal dimensions $d_q \in [d_2, d_1)$ (*i.e.* for $q \in (1, 2]$) of the set $\Omega_m \subseteq \mathbb{R}^m$ from its lower-dimensional projection $\Omega_n \subseteq \mathbb{R}^n$. In essence, consider the optical linear transformation $\mathcal{P} : \mathbb{R}^3 \rightarrow \mathbb{N}^2$ applied by the PIV system in recording 2D digital images $\Omega_2 \subseteq \mathbb{N}^2 \subseteq \mathbb{R}^2$ from real aggregates $\Omega_3 \subseteq \mathbb{R}^3$. Furthermore, consider the inverse transformation $\mathcal{P}^{-1} : \mathbb{N}^2 \rightarrow \mathbb{R}^3$, and the cases of $q \rightarrow 1$ for d_1 , and $q = 2$ for d_2 ; given $m = 3$ and $n = 2$, Eq. (6.3) becomes:

$$d_1(\Omega_3) = d_1(\Omega_2) \quad \text{for } q \rightarrow 1 \wedge d_1(\Omega_2) < 2, \quad (6.4a)$$

$$d_2(\Omega_3) = d_2(\Omega_2) \quad \text{for } q = 2 \wedge d_2(\Omega_2) < 2. \quad (6.4b)$$

If we consider the multifractal spectra $f \equiv d_q$ of the sets Ω_2 in Figure 6.3 (b) we observe that, except for small and very small flocs, $f \neq \text{const}$ with:

$$f(q = 2) < f(q = 1) < f(q = 0) < 2,$$

meaning that:

$$d_2(\Omega_2) < d_1(\Omega_2) < d_0(\Omega_2) < 2. \quad (6.5)$$

This relationship is well depicted in Figure 6.4 for the information and correlation dimensions d_1 and d_2 of experimental data. Upon substitution of Eqs. (6.4) into Eq. (6.5), we obtain the following inequality for the sets Ω_3 :

$$d_2(\Omega_3) < d_1(\Omega_3) \leq \underline{d_0(\Omega_3)} \leq 3, \quad (6.6)$$

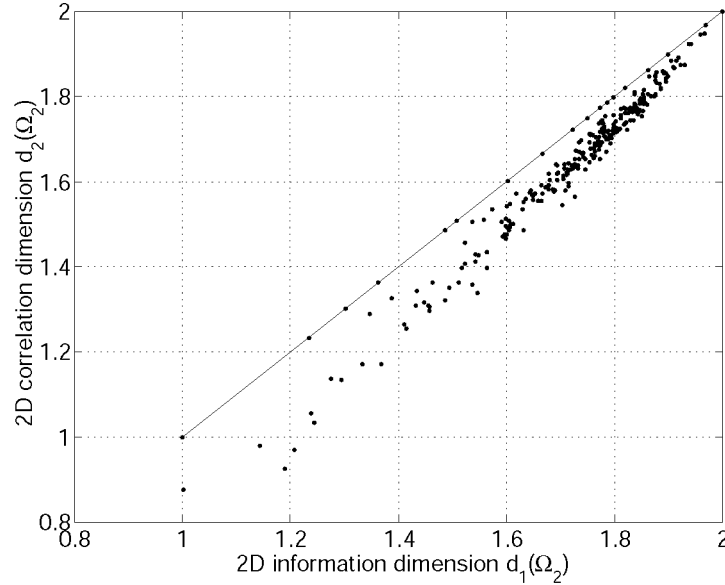


Figure 6.4: Relationship between information and correlation dimensions d_1 and d_2 of 2D optical projections Ω_2 of kaolinite aggregates observed in the column. These are Euclidian when $d_2 = d_1 = 2$, fully self-similar when $d_2 = d_1 < 2$ (straight line) and statistically self-similar when $d_2 < d_1 < 2$.

where $\overline{d_0(\Omega_3)}$ is unknown because of $q = 0$ in Eq. (6.3).

According to the classification given in Table 3.1, multifractality occurs when $d_q \neq \text{const}$, Eq. (3.25). Therefore, the kaolinite aggregates observed in our settling column are quantitatively statistically self-similar because Eq. (3.25) holds for at least $q \rightarrow 1$ and $q = 2$.

6.5 The three-dimensional capacity dimension

Having shown that flocs are statistically self-similar bodies, rather than fully-self-similar, we now focus on the 3D capacity dimension $d_0(\Omega_3)$. In studying the three-dimensional organisation of sediment flocs we come across two fundamental aspects.

The first is that the capacity dimension is normally assumed to be constant, characterising each aggregate within the same population. However, recent investigations have shown that the average $\overline{d_0(\Omega_3)}$ in a population of aggregates changes in time during aggregation (Chakraborti *et al.*, 2003). This has a profound consequence on the extent to which the concept of self-similarity applies to the mass organisation of the aggregates. Specifically, a changing capacity dimension may confirm that the structure of real flocs is not fully but statistically self-similar, as theoretically argued in Section 6.4.

The second aspect is the computability of $d_0(\Omega_3)$: flocs are multifractal in the 3D domain as shown in Eq. (6.6). However, the only dimension that is useful in scaling floc density, porosity, settling velocity, *etc.*, is the capacity dimension $d_C \equiv d_0$. Because $\mathcal{P} : \Omega_3 \rightarrow \Omega_2$ is not dimension-preserving for $q = 0$, we know that:

$$d_0(\Omega_2) \neq \min\{2, d_0(\Omega_3)\}, \quad (6.7)$$

and in particular that:

$$d_0(\Omega_3 = \mathcal{P}(\Omega_3)) \neq d_0(\Omega_2), \quad (6.8)$$

even when $d_0(\Omega_2) < 2$. Moreover, Eq. (6.1) holds for indefinitely extensive fractals and no precise distinction has been made for *compact* (finite and closed) fractals, such as images of aggregates.

Because of these two aspects, the 3D capacity dimension $d_0(\Omega_3)$ is assessed from the 2D image according to the following equation (Maggi & Winterwerp, 2004a):

$$d_0(\Omega_3) = \sqrt{\frac{a(\ell)}{d_P(\Omega_2) - b(\ell)}} \quad \text{for } d_P(\Omega_2) < 2, \quad (6.9)$$

where $d_P(\Omega_2) = 2 \cdot \log(P)/\log(A)$ is the perimeter-based fractal dimension (Spicer & Pratsinis, 1996b; Meakin, 1998), with P and A the dimensionless perimeter and area of Ω_2 respectively. The functions $a(\ell)$ and $b(\ell)$ are known for any $\ell = L/\epsilon$:

$$a(\ell) = 9 \left(z(\ell) - \frac{2[k(\ell)]^2 - 9z(\ell)}{[k(\ell)]^2 - 9} \right), \quad b(\ell) = \frac{2[k(\ell)]^2 - 9z(\ell)}{[k(\ell)]^2 - 9}, \quad (6.10)$$

where:

$$k(\ell) = z(\ell)[z(\ell) - 1] + 1, \quad z(\ell) = d_P \frac{\log[4\ell - 4]}{\log[\ell]}. \quad (6.11)$$

The derivation of Eq. (6.9) is shown in detail in Appendix C. Furthermore, Eq. (6.9) assumes that the information of the 3D structure is preserved *on the contour* of the 2D shapes Ω_2 resulting from the projection \mathcal{P} , as mentioned in Section 6.2. The validation of such an assumption is given in Appendix C where Eq. (6.9) has been validated for Diffusion-Limited Aggregates and Cluster-Cluster Aggregates.

Results of the computation of $d_0(\Omega_3)$ suggested in Eq. (6.9) for non-equilibrium and steady state floc populations at times $t = \{0, 3, 120, 162, 165\}$ h, are presented *versus* ℓ in Figure 6.5. From this we observe the following aspects.

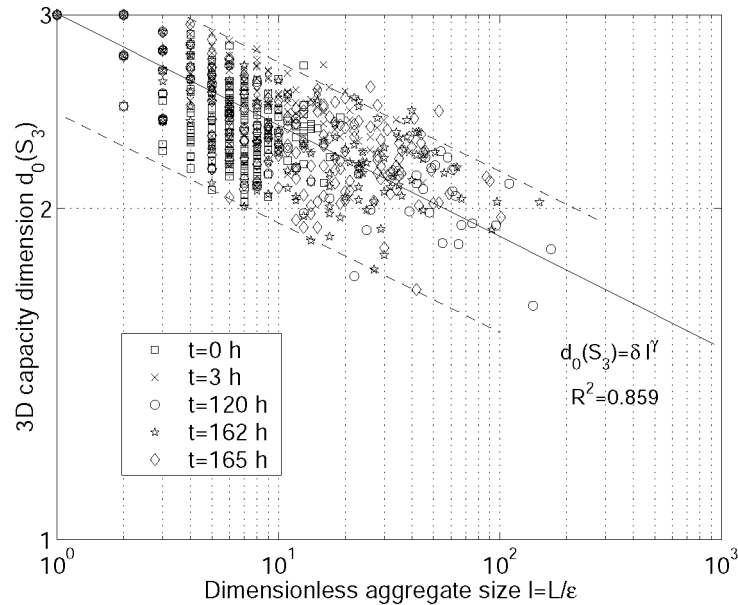


Figure 6.5: Relationship between the dimensionless aggregate size ℓ and the 3D capacity dimension $d_0(\Omega_3)$. In addition, the power-law $d_0(\Omega_3) = \delta \ell^\gamma$ is plotted for $\delta = 3$ and $\gamma = -0.1$, with $R^2 = 0.859$, for the populations of flocs at times $t = \{0, 3, 120, 162, 165\}$ h.

First, the size evolution of kaolinite flocs is characterised by a decrease in 3D capacity dimension $d_0(\Omega_3)$ with increasing dimensionless size ℓ . Small aggregates (close to the primary particle size) have higher capacity dimension than large aggregates. Hence, growing aggregates display a progressive increase in clustered- or filamentous-like structures, as discussed in Section 6.2.

Second, the size evolution of $d_0(\Omega_3)$ in Figure 6.5 may be approximated with a power-law of the form:

$$d_0(\Omega_3) = \delta \ell^\gamma, \quad (6.12)$$

where the values of δ and γ are derived by fitting Eq. (6.12) to the data at different experimental times. We observe in Table 6.1 that δ and γ appear more or less invariant ($\delta \approx 3.3$ and $\gamma \approx -0.09$) for both the non-equilibrium and the steady state. We can

Time	t	$[h]$	0	3	120	162	165
δ			3.43	3.38	3.41	3.36	3.36
γ			-0.11	-0.08	-0.10	-0.09	-0.09
R^2			0.85	0.83	0.91	0.86	0.86
State			NE	NE	SS	SS	SS

Table 6.1: Values of the parameters δ and γ of Eq. (6.12) resulting from least squares fitting of data at times $t = \{0, 3, 120, 162, 165\}$ h. NE and SS refer to non-equilibrium and steady state respectively.

reasonably approximate the data by $\delta = 3$ and $\gamma = -0.1$; in this case the correlation coefficient with measured data is $R^2 = 0.859$. Under this assumption, an aggregate of size $L = \epsilon$ (i.e. $\ell = 1$, the primary particle), measured with pixels of size $\epsilon = 4.16 \mu\text{m}$, yields:

$$d_0(\Omega_3) = 3 \cdot \left(\frac{L}{\epsilon}\right)^{-0.1} = 3, \quad (6.13)$$

which agrees with a physical representation, as kaolinite primary particles are very massive at sizes $L \approx 5 \mu\text{m}$, Figure 3.5 (b). The capacity dimension $d_0(\Omega_3)$ of aggregates of sizes $L > \epsilon$ is determined by the power γ , as it controls the slope of $d_0(\Omega_3)$ in the double logarithmic (ℓ, d_0) -plane.

Third, the data in Figure 6.5 span a band indicatively drawn by two parallel dashed lines. The width of this band reflects the variability of d_0 for an aggregate of given size ℓ . To characterise how the estimated capacity dimension $d_0^*(\Omega_3)$ is distributed around the power law of Eq. (6.12) in this band, we compute the variation $d_0'(\Omega_3)$ of the full data set at times $t = \{0, 3, 120, 162, 165\}$ h as:

$$d_0'(\Omega_3) = d_0^*(\Omega_3) - \delta \ell^\gamma. \quad (6.14)$$

The quantity $d_0'(\Omega_3)$ falls within the interval $[-0.5, 0.5]$, Figure 6.6 (a), which means that the capacity dimension d_0 of the aggregates does not exceed $\delta \ell^\gamma \pm 0.5$. Figure 6.6 (b) shows the probability distribution $p(d_0')$ of $d_0'(\Omega_3)$ around $\delta \ell^\gamma$ for different ranges of ℓ . The probabilities appear centered about $d_0'(\Omega_3) = 0$ and are more or less Gaussian distributed, hence suggesting a stochastic nature of aggregation and breakup.

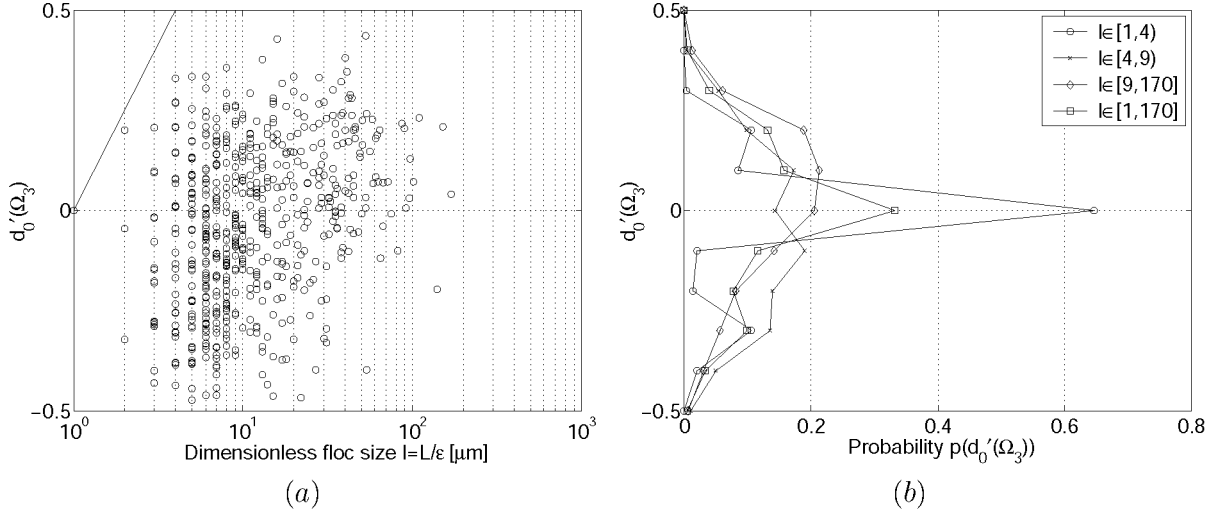


Figure 6.6: (a) representation of the fluctuating component $d'_0(\Omega_3)$ of the capacity dimension $d_0(\Omega_3)$ of flocs recorded at times $t = \{0, 3, 120, 162, 165\} h$ (Section 5.2) obtained from the decomposition in Eq. (6.14). (b) probability distribution of $d'_0(\Omega_3)$ around $\delta\ell^\gamma$ for different ranges of ℓ .

6.6 Discussion

This discussion is directed to integrate in a comprehensive frame the experimental results of flocculation processes both on the large and the small scales. This results in a theory for growth dynamics with generalised applicability to particulate systems.

6.6.1 Disorder and multifractality

The interpretation of the results in the previous sections motivates three main considerations. First, growth of individual aggregates is marked by a gradual development of structures progressively disordered at the contour of the projected images of flocs. These structures display a certain amount of randomness and determinism at the same time (rather balanced for large flocs - $\Upsilon' \approx 0.5$). Second, the fractal description of the aggregates used till now was based on the assumption of full self-similarity, whereas the multifractal spectrum shows that a *continuum* of fractal dimensions is needed to describe the complicated geometry of the flocs. Moreover, multifractality, theoretically, holds also for real 3D aggregates. Further to this analysis, we have deduced a method to assess the 3D capacity dimension of growing aggregates, which appear to follow the power-law $d_0(\Omega_3) = \delta\ell^\gamma$. The last issue, in particular, can be directly linked to the development of multifractality. As all these quantities describe floc growth from neighbouring domains, a relationship between the disorder index Υ' and the 3D capacity dimension $d_0(\Omega_3)$ can be expected. The scatter plot in Figure 6.7 shows that high-dimensional aggregates have low level of disorder, while mid-dimensional aggregates may have higher level of disorder, with an upper bound. This can be expressed by the following inequality:

$$\Upsilon' \leq -\frac{1}{2}d_0(\Omega_3) + \frac{3}{2}. \quad (6.15)$$

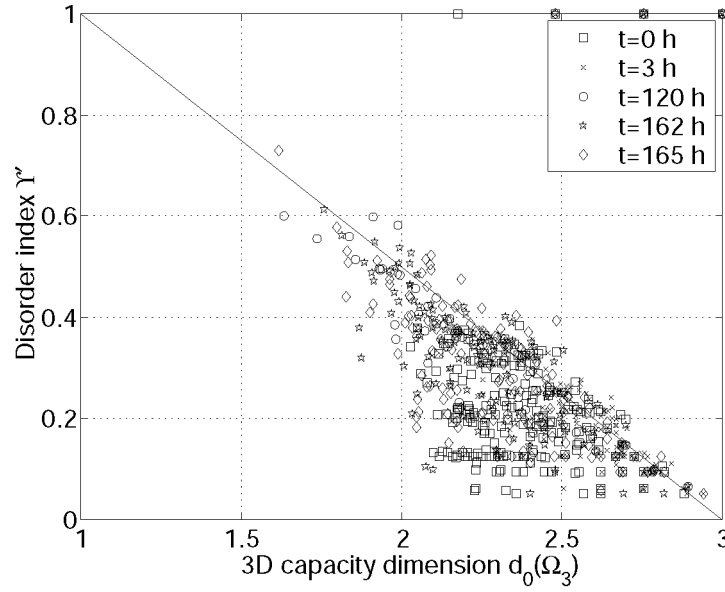


Figure 6.7: Relationship between the 3D capacity dimension estimated from Eq. (6.9) and the index of disorder Υ' .

6.6.2 A comprehensive representation of growth and equilibrium dynamics of flocculation at large and small scales

The evolution of the multifractal geometry of the aggregates analysed in this chapter can be represented together with the transition from non-equilibrium to steady state of the population of flocs observed in Chapter 5. The aim is to connect the small (floc) scales to the large (population) scales in a comprehensive picture describing particular aspects involved in flocculation, as depicted in Figure 6.8.

Consider first the floc scales and the (ℓ, d_0) -plane. The growth dynamics of flocs is marked by the sequence of points B , where $B(t)$ represents the capacity dimension $d_0 = \delta \hat{\ell}^\gamma$ of the aggregate with largest size $\hat{\ell}(t)$ at time $t \in [t_0, t_{tr}]$. The non-equilibrium is characterised by a transition of $B(t)$ from point $A \equiv B(t_0)$ towards point $C \equiv B(t_{tr})$ following a path departing from self-similarity by an angle φ . Point $A \equiv B(t_0)$ represents a system consisting of fully massive (Euclidian) primary particles with capacity dimension $d_0(\Omega_3) = 3$, hence with no fractal or multifractal properties, and it can be associated to instability of the system due to the high reactivity of the primary particles. The aggregates' growth proceeds progressively as $\hat{\ell}(t)$ increases and $B(t)$ moves according to $\delta \ell^\gamma$ towards C , hence with a decreasing capacity dimension and increasing disorder. During the non-equilibrium, aggregation is dominant over breakup; we can conceptually represent aggregation and breakup processes as two arrows that "pull" point B towards C and A respectively, where the difference in length of the arrows is a measure of the distance from the balance between aggregation and breakup. Conceptually, the two arrows have equal lengths (*i.e.* they are in balance) at point C . The decrease in d_0 for increasing $\hat{\ell}(t)$ is correspondingly accompanied by an increasing disorder and multifractal geometry of individual aggregates as shown in the (Υ', d_0) -plane. This (non-equilibrium) transition ends when $B(t)$ reaches the steady state point C . Despite this, individual flocs are not at stable (static) equilibrium, *i.e.* aggregation and breakup do not cease. Rather, aggregation and breakup are continuously fed by the energy supply from the turbulent field (far-from-equilibrium state). Therefore, small

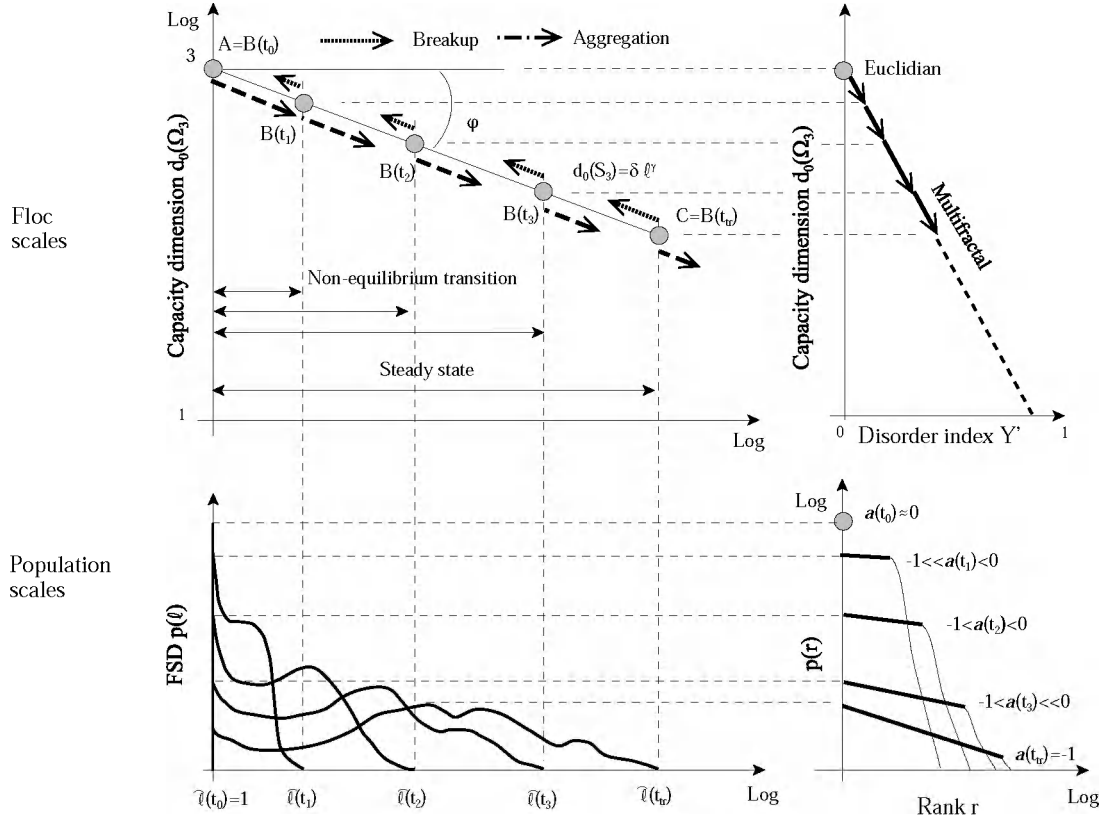


Figure 6.8: Representation of growth and equilibrium dynamics of flocculation: the small scales are represented by the individual geometrical properties of disorder Υ' and self-similarity $d_0(\Omega_3)$ of flocs, while the large scales are represented by the structure of the floc size distribution $p(\ell)$ and $p(r)$. This sketch is based on the results elaborated in Chapter 5 and 6.

aggregates continuously flocculate into larger flocs limited in size by $\widehat{\ell}(t_{tr})$, and breakup process forms flocs with dimensionless size ℓ distributed within the range $[1, \widehat{\ell}(t_{tr})]$. At this state, the population is fully developed, and the majority of flocs are characterised by statistical self-similarity, with disordered geometry.

Consider next the population scales and the $(\ell, p(\ell))$ -plane in Figure 6.8. We use the maximum dimensionless floc size $\widehat{\ell}(t)$ as a marker to describe the time evolution of the floc size distribution, corresponding to the sequence of points $B(t)$ in the (ℓ, d_0) -plane. Then, we can draw the following picture. The non-equilibrium is characterised by a progressive widening of $p(\ell)$ from the initial conditions (where the population consists of primary particles only, with $\ell = \ell(t_0) = 1$) to the steady state (where the population is fully developed with $\ell \in [1, \widehat{\ell}(t_{tr})]$). The floc size $\widehat{\ell}(t)$ reaches a stationary point $\widehat{\ell}(t_{tr})$ corresponding to point C in the (ℓ, d_0) -plane. However, an interesting property of the population organisation is not revealed by the floc size distribution $p(\ell)$ itself, but by the rank-ordered probability $p(r)$. During this transition, the population structure (the FSD) is not fully formed, and $p(r)$ is characterised by a power-law with exponent $a(t_0 < t < t_{tr}) > -1$. When the population reaches an equilibrium between aggregation and breakup the structure of the population can be described by a power-law with exponent $a(t > t_f) = -1$, that is invariant with respect to the shear rate G .

6.6.3 Generalised geometrical representation of growth processes in the (ℓ, d_0) -plane

The representation of the growth process of aggregates in the (ℓ, d_0) -plane gives interesting insight for its capability to describe also other types of growth patterns in particulate systems in general. Five cases of growth G1-G5 can be described by means of the power-law relationship between ℓ and d_0 of Eq. (6.12), depending on the specific value of the parameters γ and δ .

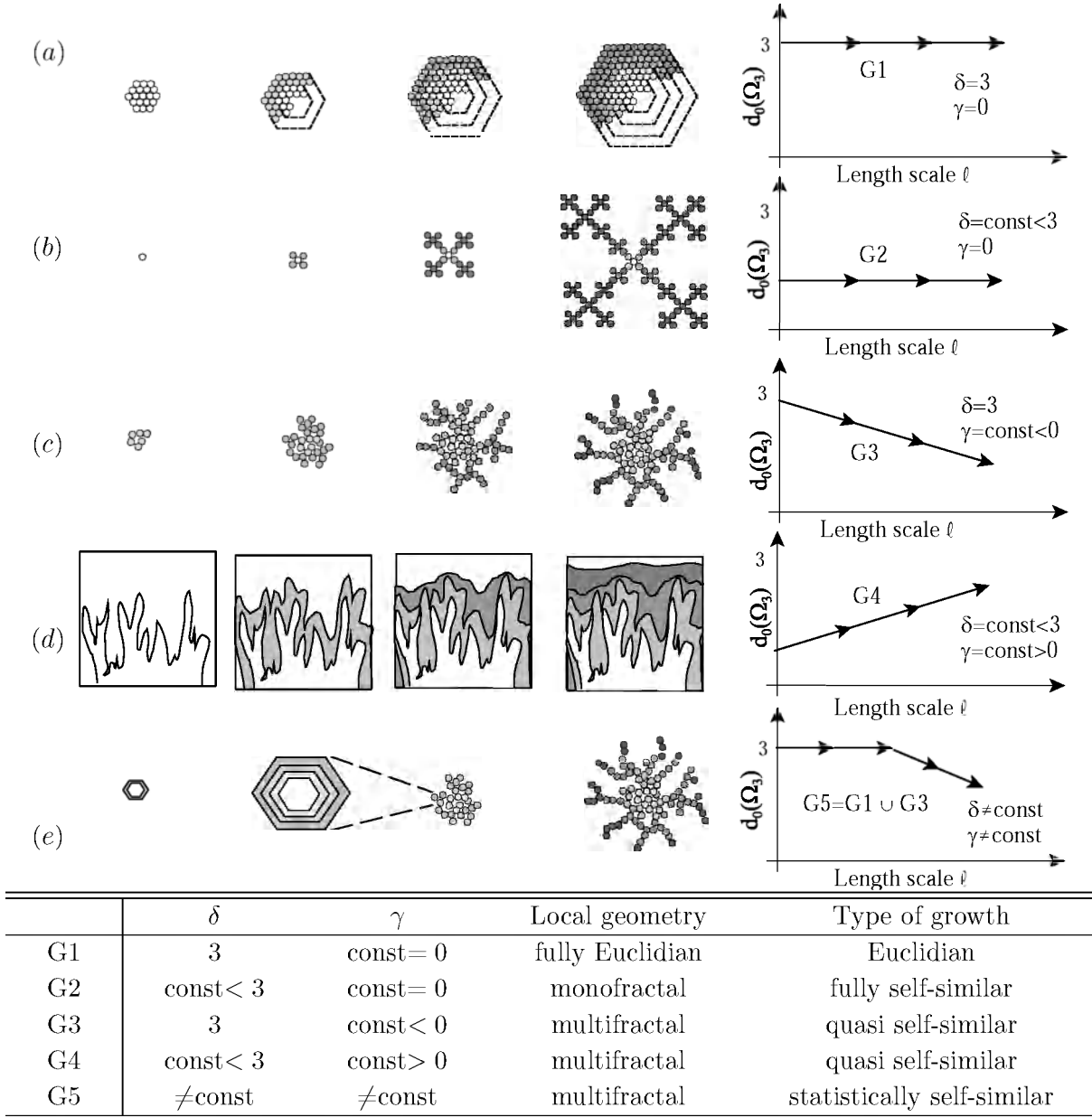


Figure 6.9: Classification of the types of growth patterns in the (ℓ, d_0) -plane. Each of them is correlated to local geometrical properties, i.e. the geometrical properties of Euclidian, mono- and multifractality. The table summarise the values of the parameters δ and γ of the power law of Eq. (6.8) associated to the growth patterns represented in the (ℓ, d_0) -plane

In the case of $\delta = 3$ and $\gamma = 0$, Eq. (6.12) becomes $d_0 = \text{const} = 3$, representing the accretion of fully Euclidian bodies, like crystals (growth pattern G1), Figure 6.9 (a). When

$\delta < 3$ and $\gamma = 0$, Eq. (6.12) becomes $d_0 = \text{const} = \delta$, which describes the growth process of monofractal theoretical bodies (growth pattern G2), Figure 6.9 (b). When $\delta = 3$ and $\gamma < 0$ Eq. (6.12) represents the growth of multifractal bodies, like in the case of real aggregates (growth pattern G3), Figure 6.9. If $\delta < 3$ and $\gamma < 0$, the growth pattern expressed by Eq. (6.12) is similar to G3, where the primary particles are not fully massive and Euclidian but fractal. If $\delta < 3$ and $\gamma > 0$, Eq. (6.12) describes the growth of multifractal bodies which tend towards an Euclidian structure, like in the case of ballistic deposition, surface growth or roughness coarsening (growth pattern G4), Figure 6.9 (d). Beside patterns G1, G2, G3 and G4, representing growths in a uniform regime, a fifth case of growth G5 is represented by a non-uniform regime, *i.e.* by a combination of the previous growth patterns. The example drawn in Figure 6.9 (e) represents the growth of crystals in its first track with a pattern of type G1; beyond a certain length scale, the growth pattern turns from G1 into G3 as for multifractal aggregates. If the reader refers back to Figure 3.5, then it is possible to observe a resemblance (at least phenomenological) of the constituting minerals forming the primary particles first, and the flocs next. In the case of Figure 6.9 (e) the length scale ℓ ranges from 10^{-10} m (molecular - during crystal nucleation) to $10^{-6} \div 10^{-3}$ m (micro-aggregate to milli-aggregate - during flocculation). The change in slope γ from G1 to G3 corresponds therefore to a phase transition in the growth process occurring at about the primary particle size $L_p \approx 10^{-6}$. The power law in Eq. (6.12) is therefore capable to characterise not only flocculation of cohesive minerals but also, to some phenomenological extent, the antecedent growth of the minerals that next undergo flocculation reactions.

6.7 Conclusions

To summarise, four fundamental aspects from the interpretation of the results collected till now deserve to be mentioned.

First, flocs consist of geometrically regular blocks (the primary particles) as those shown in Section 3.2. The process of growth causes the assembly of primary particles in a rather disordered fashion. The quantity of disorder increases with aggregates size, as shown by the entropy function and disorder index in Section 6.2.

Second, growth is accompanied by the development of structures which, at least in their projections, may be characterised by a distribution of length scales at any floc size. The multifractal spectrum expresses the specific value and number of fractal dimensions required to fully scale these structures. From the analysis in Section 6.3 we infer that growing aggregates show a gradual increase of the number of scaling exponents, *i.e.* of fractal dimensionalities f . According to theory, monofractal sets are exactly and deterministically identical at different scales, with a unique fractal dimension (the capacity dimension d_0), while multifractals look much the same at different scales but are not precisely identical (showing a full spectrum of fractal dimensions). Because of this, we have inferred that cohesive sediment flocs have multifractal mass-density organisation. A theoretical analysis of the information and correlation dimension in two dimensions has further shown that real sediment flocs possess multifractal (multiscaling) geometry also in three dimensions.

Third, the analysis of the three-dimensional capacity dimension has revealed that d_0 changes (decreases) during flocculation, confirming the observations of Chakraborti *et al.* (2003). This can be explained by multiscaling growth dynamics, which may be responsible for the development of clustered and disordered structures within the floc mass. In particular, monoscaling geometry means that aggregation and breakup processes occur

with pure multiplicative steps, while multiscaling geometry means that aggregation and breakup occur irregularly, and with stochastic fluctuations. The multifractal structure of observed aggregates lead us to infer that particle aggregation can occur between any floc of any size and that floc breakup produces a certain number of aggregates distributed in size. Moreover, multifractality in the growth process appears to be rather deterministically accompanied by a power-law decrease in $d_0(\Omega_3)$ with increasing ℓ . Analysis of this power-law in Section 6.5 shows that $d_0(\Omega_3)$ is ℓ -dependent and t -independent because the parameters γ and δ in Eq. (6.12) are essentially constant in time during both the non-equilibrium transition and the steady state, and independently from ℓ . In the light of these characteristics of Eq. (6.12), and on the basis of the multiscaling description of growth dynamics in a sediment population, we can conclude that aggregation and breakup do not occur with fully self-similar steps. The measure of the distance (deviation) from full self-similarity is given by the exponent γ or, correspondingly, by the slope $\varphi = \arctan(\gamma)$ of the power-law of Eq. (6.12).

Fourth, a phenomenological description and theoretical elaboration of the results obtained in this chapter and Chapter 5 has been implemented in Section 6.6.2 to find the link between the small and the large length scales, introduced in Chapter 3. The time evolution of the floc size distribution is effectively characterised by a non-equilibrium transition and by a steady state. The first is marked by a rank power-law distribution with exponent $a > -1$, and the steady state by $a = -1$. This transition on the large scales corresponds to a transition on the small-scale geometrical structure of the flocs, becoming increasingly complex and characterised by an increasing number of fractal dimensions. In other words, changes of the population's structure are reflected in changes of the capacity dimension of growing flocs (or, growth of flocs changes the population's structure). The capability to track several statistical and geometrical properties at so different length scales in flocculating systems has given a further input to classify growth processes within a generalised paradigm, as discussed in Section 6.6.3. In particular, the power-law of Eq. (6.12) is capable to describe growth processes on the large scales (Euclidian, fully self-similar, quasi self-similar and statistically self-similar) and on the small scales (Euclidian, monofractal and multifractal). If we recall the concepts of equilibrium analysed in Chapter 3, then we can refer to flocculation at steady state as a far-from-equilibrium statistically stationary process. Far-from-equilibrium dynamics are responsible for the attainment of a criticality state of self-organisation in the structure of the population, and for the formation of multifractal (multiple scaling) floc structures.

Chapter 7

Population balance equation for cohesive sediment flocs

This chapter describes a study of cohesive sediment flocs based on population dynamics. A population balance equation is proposed to model flocculation in the real world. It is derived from existing models, like those introduced in Chapter 2, but we implement some of the newly found properties and behaviour observed in the experiments in Chapter 5 about aggregation and breakup processes, and in Chapter 6 on floc structure. The results from this population equation are compared with experimental results obtained in the settling column and in similar numerical and experimental works presented in the literature.

7.1 Introduction

The objective of this chapter is to formulate a Population Balance Equation (PBE) to model flocculation of cohesive sediment. The main properties that we aim at are structured on two levels. First, cohesive sediment aggregates should be described as irregular rather than Euclidian bodies: a physically sound foundation of the PBE should consider the multifractal and (disordered) non-homogeneous mass-density distribution of the aggregates. Second, the mechanisms of aggregation and breakup among fractal aggregates should address the small-scales particle interaction, as these processes are responsible for the local growth of individual aggregates. For example, it is still unknown whether aggregates of a given size react effectively with aggregates of any other size or only with preferential ones, and which floc size distribution and geometrical properties the aggregates have following floc breakup. For this reason a number of aggregation and breakup mechanisms are considered in this PBE.

The conceptual survey of population balance equations resumed in Section 2.5 is extended in Section 7.7 to analyse the properties of three PBEs from the literature. However, those population balance equations do not account for the multifractal properties of the flocs. The population balance equation newly derived in Section 7.2 uses a different approach and structure in order to include the effect of multifractality. Following this path, the characteristics of the flocs and the kinematic processes are implemented in a parameterised way. The results of the model are compared with the experimental results with respect to shape, time evolution, autonomy and response of the floc size distribution, as discussed in Chapter 5.

7.2 Population balance equation

With reference to Eq. (2.21), the discrete Lagrangian PBE proposed in this thesis to express the time evolution of a population of cohesive flocs is the following:

$$\frac{dn_k}{dt} = \underbrace{\sum_{i=1}^{\hat{N}_p-1} \sum_{\substack{j=i+1 \\ j+i=k}}^{\hat{N}_p} \alpha_{i,j} \Lambda_{i,j} n_i n_j}_{\mathcal{G}_A} - \underbrace{n_k \sum_{j=1}^{\hat{N}_p} \alpha_{k,j} \Lambda_{k,j} n_j}_{\mathcal{L}_A} + \underbrace{\sum_{j=k+1}^{\hat{N}_p} \gamma_{j,k} B_j n_j}_{\mathcal{G}_B} - \underbrace{B_k n_k}_{\mathcal{L}_B} . \quad (7.1)$$

Equation (7.1) describes the time variation of the number concentration n_k of flocs that contain $N_p = k$ primary particles, where \hat{N}_p is the upper class number. The variation is modelled as a function of aggregation and breakup solely, with \mathcal{G}_A the gain in class k of aggregates with i and j primary particles such that $k = i + j$, \mathcal{L}_A the loss in class k due to aggregation with other flocs, \mathcal{G}_B the gain in class k due to breakup of aggregates with $j > k$ primary particles and \mathcal{L}_B the loss in class k due to breakup. Different from the literature surveyed in Chapter 2, advection, settling and variation in sediment concentration are not accounted for. The analysis of the floc size distribution in Chapter 5, and the multiscale geometry of the flocs found in Chapter 6, suggest that particle aggregation may occur between any two flocs of any size. For this reason, aggregation (\mathcal{G}_A and \mathcal{L}_A) is modelled as the product of a collision efficiency $\alpha_{i,j}$ and a collision frequency function $\Lambda_{i,j}$, Section 2.2.1:

$$\alpha_{i,j} = \text{parameter of the model}, \quad (7.2)$$

$$\Lambda_{i,j} = \Lambda_{i,j}^{(S)} = \frac{G}{6} (L_i + L_j)^3, \quad (7.3)$$

where $\Lambda_{i,j}^{(S)}$ is the turbulence-induced contribution to $\Lambda_{i,j}$. Differential settling ($\Lambda_{i,j}^{(DS)}$), Brownian motion ($\Lambda_{i,j}^{(BM)}$) and biogenic aggregation ($\Lambda_{i,j}^{(B)}$) are neglected. The gain in class k due to breakup of larger aggregates (\mathcal{G}_B) is modelled in a generalised way as the product of a breakup frequency function B_j and a binomial breakup distribution function $\gamma_{j,k}^{(Nom)}$ of daughters k resulting from the aggregate j , Section 2.2.2:

$$B_j = B_j^{(S)} = k'_b e_b G \left(\frac{L_j - L_p}{L_p} \right)^p \left(\frac{\mu G}{F_y / L_j^2} \right)^q, \quad (7.4)$$

$$\gamma_{j,k} = \gamma_{j,k}^{(Nom)} = \frac{\binom{j}{k}}{\sum_{k=1}^j \binom{j}{k}}, \quad (7.5)$$

where $B_j^{(S)}$ is the breakup frequency due to turbulent shear stresses. The loss in class k due to breakup (\mathcal{L}_B) is modelled with Eq. (7.4), but it does not involve a distribution function. Nonlinear breakup (two-body collision $B_{i,j}^{(C)}$, Section 2.2.2) is neglected because we consider low volume concentrations ϕ . Equation (7.4) was derived in Winterwerp (1998) from the ratio between turbulent stresses τ_t and floc strength τ_y . As it accounts for fragmentation of fractal flocs, it is used instead of Eq. (2.8), which considers Euclidian spheres only. In

particular, $k'_b \approx (10^{-3} \div 10^{-4}) \text{ s}^{0.5} \text{ m}^{-1}$ is an empirical parameter, $e_b = 2 \cdot 10^{-5}$ is an efficiency parameter for breakup and $F_y \approx 10^{-10} \text{ Pa}$ is the estimated floc strength (Winterwerp, 1999). As the equilibrium floc size L_e was found to scale with the Kolmogorov length scale η_k (Winterwerp, 1998), the exponent q was found $q = 1/2$, while $p = 3 - d_0$, with d_0 the capacity dimension of the floc. Eq. (7.4) can therefore be rewritten as:

$$B_i^{(S)} = E \sqrt{\frac{\mu}{F_y}} G^{3/2} L_i \left(\frac{L_i - L_p}{L_p} \right)^{3-d_0}, \text{ with } E = \text{parameter of the model.} \quad (7.6)$$

This equation possesses a structure similar to Eq. (2.8) written as $B_i^{(S)} = EG^b L_i$, with $E = k'_b e_b$ a single parameter comprising e_b and k'_b which allows calibration of the breakup algorithm. Moreover, the dimensionless factor $[(L_i - L_p)/L_p]^{1-d_0}$ incorporates the fractal description of the flocs, stating that an increase of d_0 lowers the rate of fragmentation, as flocs become more compact. Different distribution functions were hypothesised in Section 2.2.2, because the effective size distribution in floc breakup is not known. Breakup into a certain number of daughter flocs is generally modelled as a stochastic process. Since a large number of breakup events N_{Bre} occurs in a suspension, we can apply the Central Limit Theorem, according to which the probability resulting from the sum of the floc size distribution of a large number (theoretically $\rightarrow \infty$) of independent events of breakup is normally distributed. For this reason, the general form of this population balance equation considers a normal breakup distribution function approximated by a binomial discretisation, Eq. (7.5).

The population balance in Eq. (7.1) is coupled to the following equation:

$$d_{0,k} = \delta \ell^\gamma = \delta \left(\frac{L_k}{L_p} \right)^\gamma, \quad (7.7)$$

which stems from the power-law relationship between the dimensionless floc size ℓ and the capacity dimension d_0 found in Section 6.5. We remark that the PBE in Eq. (7.1) is not based on the floc size L but on the number of primary particles N_p within a floc. However, aggregation and breakup processes are modelled as functions of L , therefore the size L of growing flocs within the population is to be retrieved from Eq. (7.7). The fractal approach allows to write the number of primary particles $N_{p,k}$ in a floc belonging to class k as:

$$k = N_{p,k} = (L_k/L_p)^{d_0}, \quad (7.8)$$

with L_k unknown. Hence, substituting Eq. (7.7) into Eq. (7.8) we obtain the transcendental function:

$$k = (L_k/L_p)^{\delta(L_k/L_p)^\gamma}. \quad (7.9)$$

The sizes $L = L_k$ computed by solving this equation are then used to compute the quantities $\Lambda_{i,j}^{(S)}$ and $B_i^{(S)}$ to model two-body collision and floc breakup. The value added by Eq. (7.7) to the population balance equation is that to allow to describe flocs as multifractal units with disordered mass-density distributions because it expresses the quasi self-similar growth dynamics of type $G3$ in the (ℓ, d_0) -plane, Figure 6.9, Section 6.6.3.

Finally, the population balance in Eq. (7.1) does not consider production and drainage of the suspended matter in and from the control volume. This means that mass conservation is implicitly accounted for as follows:

$$c = \sum_{k=1}^{\hat{N}_p} n_k M_{f,k} = \text{const}, \quad (7.10)$$

where c is the mass concentration and, given L_p and the sediment density ρ_s , the mass $M_{f,k}$ of a floc belonging to class k is modelled as:

$$M_{f,k} = kL_p^3\rho_s, \quad (7.11)$$

assuming cubical primary particles.

7.3 Characteristics of the model

The model of Eq. (7.1) can be related to the population balance in Eq. (2.22) proposed in Winterwerp (1998), which considers the variation of the total particle number concentration N of aggregates in a suspension as a function of aggregation and breakup, neglecting advection, settling and turbulent diffusivity:

$$\frac{dN}{dt} = -k'_A GL^3 N^2 + k_B G^{q+1} (L - L_p)^p L^{2q} N.$$

If we further consider $q = 1/2$ and $p = 3 - d_0$ then we obtain:

$$\frac{dN}{dt} = - \underbrace{k'_A (1 - \phi_*) GL^3 N^2}_{\mathcal{L}_A^*} + \underbrace{k_B G^{3/2} (L - L_p)^{3-d_0} L N}_{\mathcal{G}_B^*}, \quad (7.12)$$

with \mathcal{L}_A the loss in total particle number concentration N due to aggregation, and \mathcal{G}_B the gain in N due to floc breakup. Inspection of Eq. (7.12) shows that \mathcal{L}_A^* and \mathcal{G}_B^* scale with the dimensional factors G , L and N as:

$$\mathcal{L}_A^* \propto GL^3 N^2, \quad (7.13a)$$

$$\mathcal{G}_B^* \propto G^{3/2} L \left(\frac{L - L_p}{L_p} \right)^{3-d_0} N. \quad (7.13b)$$

Similarly, the population balance in Eq. (7.1) accounts for loss by aggregation (\mathcal{L}_A) and gain by breakup (\mathcal{G}_B) in the same way as Eq. (7.12), and they scale as:

$$\mathcal{L}_A \propto G(L_i + L_j)^3 n_k n_j, \quad (7.14a)$$

$$\mathcal{G}_B \propto G^{3/2} L_j \left(\frac{L_j - L_p}{L_p} \right)^{3-d_0} n_j. \quad (7.14b)$$

By comparison of Eqs. (7.13) and (7.14) we note that \mathcal{L}_A and \mathcal{G}_B in the population balance of Eq. (7.1) are the analogue of \mathcal{L}_A^* and \mathcal{G}_B^* in Eq. (7.12), but extended to a population of aggregates that are described by the number concentration n_k over k classes, rather than by their total number concentration N . The fact that the population is organised into classes makes it necessary to account for mass-transfer terms \mathcal{G}_A and \mathcal{L}_B that are not present in Eq. (7.12).

The model in Eq. (7.1) possesses characteristics that are not present in the PBEs introduced in Section 2.5.1, as it is structured into classes corresponding to the number N_p of primary particles constituting the aggregates, that are finite and $\subset \mathbb{N}$, rather than their size L . However, the growth dynamics Eq. (7.7) relating ℓ , N_p and d_0 (quasi self-similar growth dynamics) enables to compute the size L of aggregates belonging to any class k , *i.e.* for any number of primary particle $N_p = k$, given δ and γ .

The class-to-class mass transfer in Eq. (7.1) occurs by fixed quantities, *i.e.* by a certain number of flocs, and each floc is accounted for by its number of primary particles. Because of the structure of this PBE, full mass conservation holds because the total number of primary particles within the control volume is preserved.

Eq. (7.1) models aggregation and breakup in a generalised form. This allows to study different mechanisms of particle collisions (due to Brownian motion, differential settling, turbulent and laminar shear) and different mechanisms of breakup (due to shear and collision with other aggregates, and with different distribution functions). Furthermore, a variety of (local) growth dynamics can be replicated amongst the aggregates by tuning the parameters δ and γ of Eq. (7.7), as depicted in Figure 6.9.

In the population balance of Eq. (7.1) aggregation is modelled in a *deterministic* way, while breakup is modelled in a *stochastic* way. For this reason, Eq. (7.1) can be referred as to a *semi-stochastic* model of flocculation processes. In addition, Eq. (7.7) expresses that flocs grow with statistically self-similar properties, and is used as a floc structure equation to determine the size of a floc given its number N_p of primary particles.

The population balance in Eq. (7.1) is a system of differential equations of the first order, nonlinear in n_k within the term \mathcal{L}_A . Analytical solution cannot be found straightforward, and we have to rely on numerical solutions of the system. The parameters $\alpha_{i,j}$ and E are calibrated against real measurements.

7.4 Properties of the model

Some specific aspects of the model are discussed in view of the numerical simulations described in the following Sections 7.5 and 7.6.

7.4.1 Method of integration

The method of integration of Eq. (7.1) consists of computing the discretised form $\Delta n_k / \Delta t$ of dn_k / dt . The variation Δn_k in concentration in class k is computed as a function of the particle concentration $\{n(t_1)\}$ for each class k at a given time t_1 :

$$\Delta n_k = f[\{n(t_1)\}] \cdot \Delta t,$$

This variation is then used to compute the number concentration $\{n(t_2)\}$ of each class at time $t_2 = t_1 + \Delta t$ as follows:

$$n_k(t_2) = n_k(t_1) + \Delta n_k.$$

This procedure is then repeated to compute the next variation $\Delta\{n\}$ and the concentration number $\{n(t_3)\}$ with $t_3 = t_2 + \Delta t$.

In this method, Δn_k is applied directly to its corresponding class k . For instance, consider in Eq. (7.1) only the gain \mathcal{G}_A in class k due to aggregation of flocs from classes i and j . The number concentration $n_k(t_1)$ is upgraded to $n_k(t_2)$, with $\Delta n_k = \mathcal{G}_{A,k}$. Analogously, the number concentrations $n_i(t_2)$ and $n_j(t_2)$ are upgraded as follows:

$$\begin{aligned} n_i(t_2) &= n_i(t_1) - \Delta n_k, \\ n_j(t_2) &= n_j(t_1) - \Delta n_k, \end{aligned}$$

where $\mathcal{L}_{A,i} = \mathcal{L}_{A,j} = -\Delta n_k$ corresponds to loss by aggregation \mathcal{L}_A in classes i and j .

The integration time step Δt is constant during a run. As aggregation and breakup are continuous-in-time processes, the steady state solution might be, consequently, sensitive to Δt (Mietta, 2004). If we take into account that the rates of aggregation and breakup scale as G and $G^{3/2}$ respectively, and that Δt should be smaller than the physical time scales of aggregation and breakup, then Δt is taken as $\Delta t \propto 1/G$. In particular, $\Delta t = 0.5$ s for $G = 5$ s⁻¹ and $\Delta t = 0.2$ s for $G > 5$ s⁻¹ (Mietta, 2004).

Finding the solution of the population equation numerically takes a long time; for this reason, a convergence criterion is used to detect the proximity to steady state. The relative variation K of primary particle-based number concentration $\{n\}$ at time t is computed as:

$$K = \frac{\sum_{i=1}^{\hat{N}_p} [n_i(t) - n_i(t - \Delta t)]}{\sum_{i=1}^{\hat{N}_p} n_i(t - \Delta t)}, \quad (7.15)$$

where $n_i(t)$ and $n_i(t - \Delta t)$ are the number concentrations of class i at times t and $t - \Delta t$, with Δt the integration time step. K is compared with an arbitrary tolerance TOL : if $K \leq TOL$ for a certain number of times then the solution is considered steady.

7.4.2 Derivation of the floc size distribution

The primary particle-based number concentration $\{n\}$ of the population balance in Eq. (7.1) cannot be compared straightforward to real suspended matter data, as this normally relies on the measurement of the floc *size* distribution. To this end, each n_k in Eq. (7.1) is associated with a floc size $L_k = f(k)$ computed through Eq. (7.9). Next, the FSD in the form of probability $p(L)$ is computed for a number of classes $n_c = 9 \ll \hat{N}_p$ in the same way as described in Chapter 5.

7.4.3 Calibration of the parameters

The collision efficiency $\alpha_{i,j}$ and the breakup parameter E in Eqs. (7.2) and (7.6) are calibrated by minimising the error:

$$Err = \sum_{i=1}^{n_c} |p_i^*(L) - p_i(L)|, \quad (7.16)$$

where $p_i^*(L)$ and $p_i(L)$ are respectively the computed and experimental FSD at steady state. The two-dimensional minimisation is performed with the Downhill Simplex Method (Press, 1999), starting from initial conditions corresponding to a fully dispersed system. This minimisation is iterative, meaning that dn_k/dt is computed until steady state ($dn_k/dt \approx 0$), then the error Err of Eq. (7.16) is used to upgrade the parameters $\alpha_{i,j}$ and E by $\Delta\alpha_{i,j}$ and ΔE . Next, another simulation (that is another iteration in the minimisation process) is launched and the steady state FSD $p_i^*(L)$ is computed anew and compared with the experimental FSD $p_i(L)$ (Mietta, 2004). The minimisation stops when $\Delta\alpha_{i,j} \rightarrow 0$ and $\Delta E \rightarrow 0$.

7.4.4 Calibration of the model

The experimental results described in Chapter 5 consist of the steady state FSD for five different values of the shear rate $G = \{0, 5, 10, 20, 40\}$ s⁻¹. The FSD for $G = 0$ s⁻¹ cannot

be used as the PBE considers turbulence as the only cause of flocculation. The FSDs for $G = \{10, 40\} \text{ s}^{-1}$ are used as calibration set, while the FSDs for $G = \{5, 20\} \text{ s}^{-1}$ constitute the validation set. The calibration of $\alpha_{i,j}$ and E , therefore, is done minimising the sum of the errors found throughout the two FSDs of the calibration set. The specific settings of the model are reported in Table 7.1.

Primary particle size	L_p	$[\mu\text{m}]$	6.4		
Mass concentration	c	$[\text{gl}^{-1}]$	0.5		
Initial distribution	n_k	$[\text{m}^{-3}]$	Mass concentrated in class $k = 1$		
Collision frequency	$\Lambda_{i,j}$	$[\text{s}^{-1}]$	$\Lambda_{i,j}^{(S)}$	Eq. (7.3)	
Breakup rate	B_i	$[\text{s}^{-1}]$	$B_i^{(S)}$	Eq. (7.4)	
Breakup distribution function	$\gamma_{i,j}$		$\gamma_{i,j}^{(Nom)}$	Eq. (7.5)	
Capacity dimension	d_0		δl^γ		
Time step	$\Delta t(G)$	$[\text{s}]$	0.5	for	$G = 10 \text{ s}^{-1}$
			0.2	for	$G = 40 \text{ s}^{-1}$
Error	Err		0.31	for	$G = 10 \text{ s}^{-1}$
			0.30	for	$G = 40 \text{ s}^{-1}$
Optimum collision efficiency	α_{opt}		0.642		
Optimum breakup efficiency	E_{opt}		$2.63 \cdot 10^{-4}$		

Table 7.1: Settings of the model of Eq. (7.1) for the calibration, and values of the optimal parameters α_{opt} and E_{opt} .

The optimum values α_{opt} and E_{opt} compare well, with data from the literature (Mietta, 2004). The FSDs resulting from calibration are shown in Figure 7.1, while the relative errors are resumed in Table 7.1.

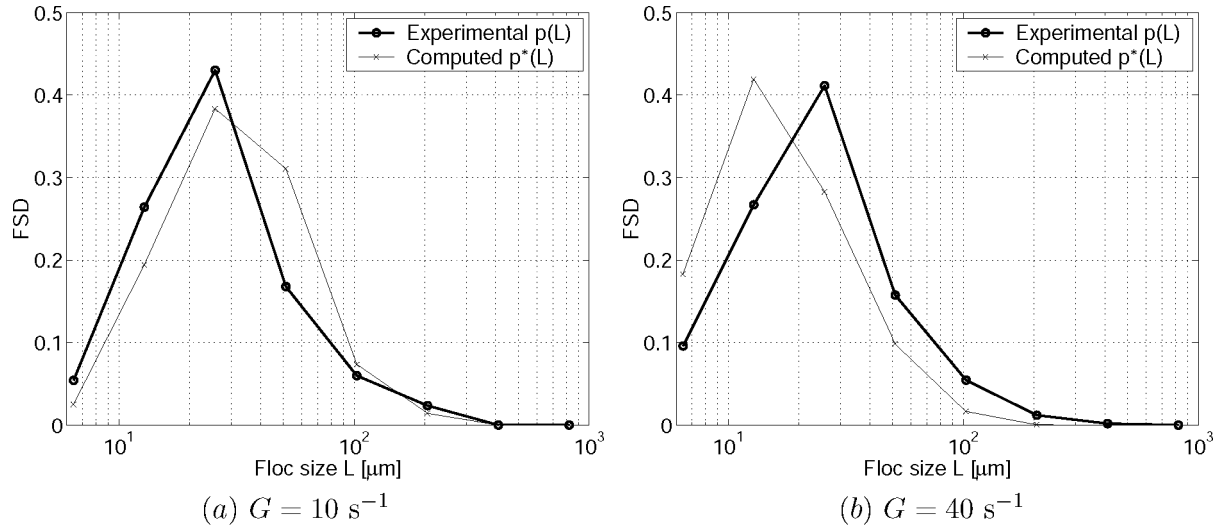


Figure 7.1: Experimental FSDs $p(L)$ and computed FSDs $p^*(L)$ resulting from the calibration of the model with $G = \{10, 40\} \text{ s}^{-1}$ at steady state, starting from fully disperse system. The errors are $Err = 0.31$ for $G = 10 \text{ s}^{-1}$ and $Err = 0.30$ for $G = 40 \text{ s}^{-1}$.

We note that the FSDs obtained by calibration, although displaying errors quantitatively similar in value, show two different characteristics, overestimating the mean floc size

for $G = 10 \text{ s}^{-1}$ and underestimating the mean floc size for $G = 40 \text{ s}^{-1}$.

7.5 Results

7.5.1 Modelling flocculation in the settling column

The population balance in Eq. (7.1) is used to predict the steady state FSD in the settling column for $G = \{5, 20\} \text{ s}^{-1}$. The FSD for $G = 20 \text{ s}^{-1}$ corresponds to the case of *interpolation* between the calibration values $G = \{10, 40\} \text{ s}^{-1}$, while $G = 5 \text{ s}^{-1}$ corresponds to *extrapolation*; in this way a proper evaluation of the predictive skills of the model is possible. These numerical simulations have been performed with the model settings listed in Table 7.1, with parameters α_{opt} and E_{opt} obtained from the calibration. The computed FSDs $p^*(L)$ in Figure 7.2 replicate the shape of the experimental FSDs $p(L)$ reasonably well, but with errors $Err = 0.43$ for $G = 5 \text{ s}^{-1}$ and $Err = 0.22$ for $G = 20 \text{ s}^{-1}$.

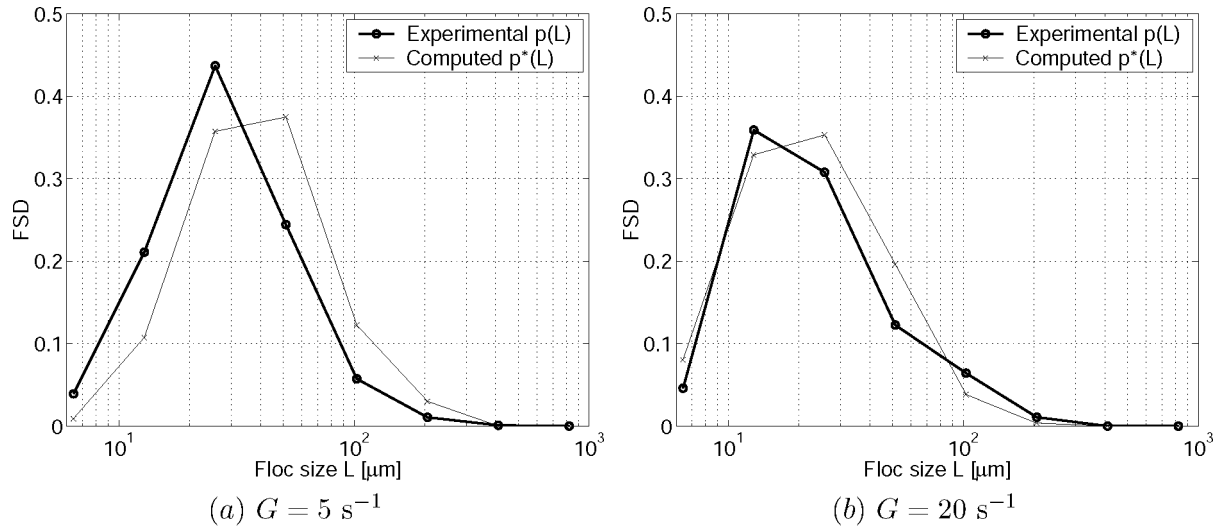


Figure 7.2: Comparison between experimental and computed steady state FSDs $p(L)$ and $p^*(L)$ for (a) $G = 5 \text{ s}^{-1}$ and (b) $G = 20 \text{ s}^{-1}$. The errors are $Err = 0.43$ for $G = 5 \text{ s}^{-1}$ and $Err = 0.22$ for $G = 20 \text{ s}^{-1}$.

The higher accuracy (smaller Err) at $G = 20 \text{ s}^{-1}$ with respect to $G = 5 \text{ s}^{-1}$ is somehow expected, because the calibration has been done with $G = \{10, 40\} \text{ s}^{-1}$. However, we note that the overall shape of the FSD is qualitatively well predicted, with the left and right tails of $p(L)$ and $p^*(L)$ in close vicinity in both interpolation and extrapolation.

As already mentioned, we do not command a large data set to explore widely the predictive skills of the model in Eq. (7.1). Nevertheless, we can do some simple, clarifying simulations and comparisons with other experimental and theoretical results.

7.5.2 Effect of mass concentration c

The rates of flocculation reactions are directly related to the SPM concentration in the water column. Similarly to what was already observed in Section 3.1.3 about negative feedback loops, the number of aggregation events N_{Agg} scales with the particle concentration n as $N_{Agg} \propto n^2$, while the number of breakup events N_{Bre} scales as $N_{Bre} \propto n$.

Therefore, at least theoretically, flocculation dynamics should be speeded up or it should result in larger flocs through an increase of the solid phase concentration. An interesting issue is therefore to investigate whether the model predicts flocculation dynamics properly for different mass concentrations c . The settings of the model are the same of Table 7.1, but with $c = \{0.2, 0.5, 1, 1.5, 2\} \text{ g l}^{-1}$, and $\alpha_{i,j} = \alpha_{opt}$ and $E = E_{opt}$.

The steady state FSDs thus computed are shown in Figure 7.3 (a), where we note that their shape is sensitive to the mass concentration c . Increases in c correspond to a progressive increase in probability density of large aggregates, as expected from the theory. This means that increases in c correspond also to an increase of mean and modal floc size \bar{L} and \tilde{L} , as shown in Figure 7.3 (b). According to Dyer (1989), for low shear stresses

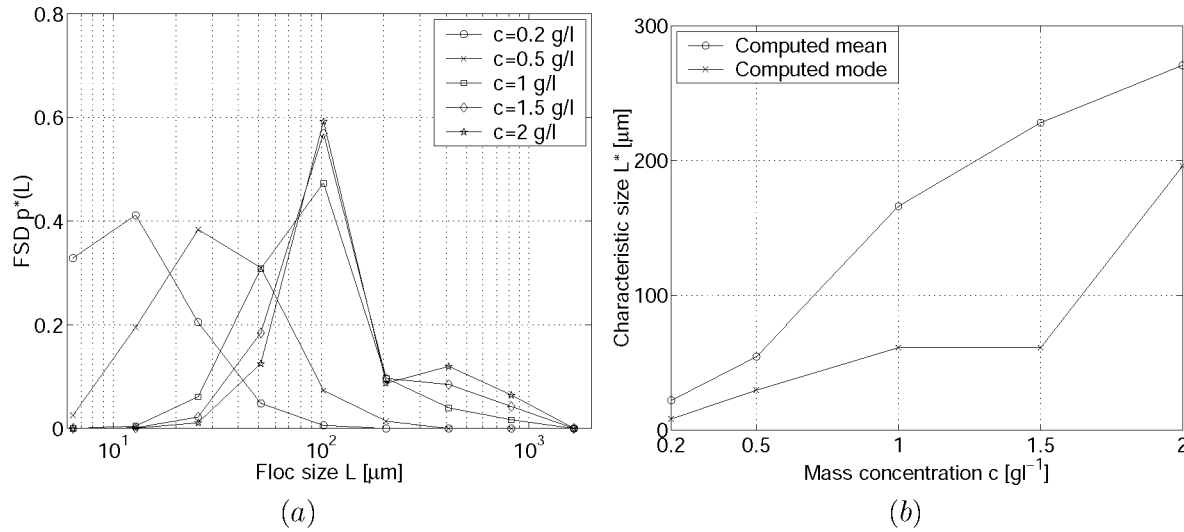


Figure 7.3: (a) representation of the steady state FSDs for sediment mass concentrations $c = \{0.2, 0.5, 1, 1.5, 2\} \text{ g l}^{-1}$ and shear rate $G = 10 \text{ s}^{-1}$. (b) representation of the mean \bar{L}^* and modal floc size \tilde{L}^* as a function of c .

the mode floc size increases with c until a critical point $c = c^*$, beyond which any further increase of concentration causes the opposite effect, Figure 7.4. Qualitatively, for high shear stresses (say greater than 5 dyne/cm^2), the modal floc size tends, in contrast, to be monotonically decreasing for increasing sediment concentration, Figure 7.4. However, our numerical simulation is run with $G = 10 \text{ s}^{-1}$ which corresponds approximately to a shear stress $10^{-2} \text{ dyne/cm}^2$ in Figure 7.4, and with $c = (0.2, 2) \text{ g l}^{-1}$. For these specific values of concentration and shear stresses, the increasing mode in our simulations appears to follow the behaviour depicted qualitatively in Figure 7.4. This comparison with Dyer's relationship between G , c and \tilde{L} strengthens the validity of the model in the prediction of flocculation for a wide variety of sediment concentrations.

7.5.3 Effect of shear rate G

In analogy to the investigation in Section 7.5.2, the behaviour of the model is now investigated with respect to the turbulent shear rate G . Qualitatively, two behaviours are expected corresponding respectively to *unlimited* ($t_r > t_f$) and *limited* ($t_r < t_f$) residence time t_r of the suspension in the turbulence field¹, with t_f the flocculation time (Van Leussen,

¹Within this context, the expressions "unlimited" and "limited" residence time correspond to steady state and non-equilibrium floc size distribution respectively, Chapters 3 and 5.

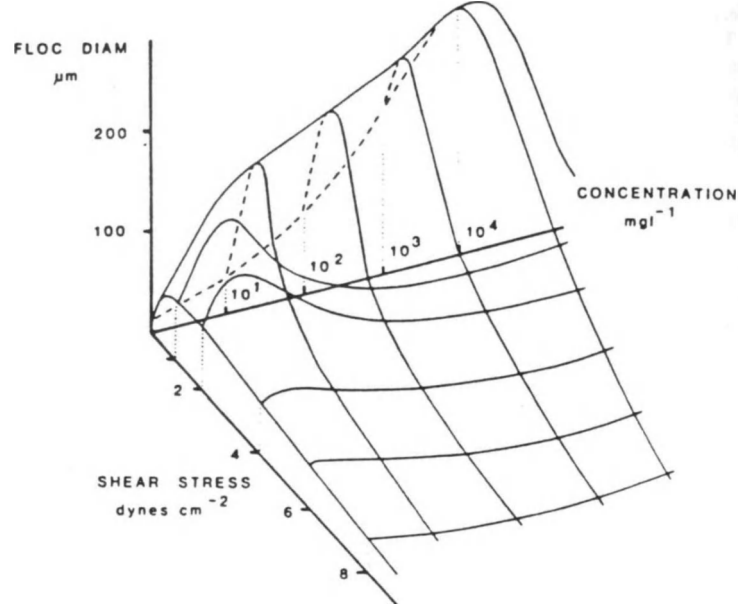


Figure 7.4: Conceptual representation of the modal floc size as a function of concentration and shear stress (Dyer, 1989).

1994; Dyer, 1989). In the first case (unlimited - steady state), the modal floc size \tilde{L} is a monotonically decreasing function of G . In the second case (limited - non-equilibrium), the mode \tilde{L} is a function of G with a maximum at a certain $G = G^*$. Said G^* corresponds to a point of departure between the non-equilibrium (for $G < G^*$) and the steady state (for $G > G^*$) floc size distributions. The shear rate G^* can be also interpreted as an "optimal" flocculation reaction for a given residence time, *i.e.* the residence time $t_r = t_f$. This is well represented in Figure 2.4. It is therefore interesting to analyse the extent to which the population balance in Eq. (7.1) is capable to reproduce this response of the FSD to different forcing G . To this end, the model is set as in Table 7.1, but it is run for shear rates $G = \{5, 10, 20, 40, 80, 160\} \text{ s}^{-1}$ for both unlimited and limited residence time t_r , with arbitrary $t_r = 0.3 \text{ h}$, Table 7.2.

Shear rate	G	$[\text{s}^{-1}]$	5	10	20	40	80	160
Residence time ^(a)			$t_r > t_f$	$t_r > t_f$	$t_r > t_f$	$t_r > t_f$	$t_r > t_f$	$t_r > t_f$
State			SS	SS	SS	SS	SS	SS
Residence time ^(a)			$t_r < t_f$	$t_r < t_f$	$t_r < t_f$	$t_r > t_f$	$t_r > t_f$	$t_r > t_f$
State			NE	NE	NE	SS	SS	SS

^(a) $t_r > t_f$ corresponds to unlimited residence time and steady state, $t_r < t_f$ corresponds to limited residence time and non-equilibrium state.

Table 7.2: Setup of the runs for unlimited and limited residence time for shear rates $G = \{5, 10, 20, 40, 80, 160\} \text{ s}^{-1}$. NE and SS indicate non-equilibrium and steady state respectively.

The results of the computation for unlimited residence time are given in Figure 7.5 (a) where the FSDs show a progressive left-skewed shape for increasing G . This is expected from the theory as the number N_{Agg} of aggregation events scales as $N_{Agg} \propto G$, while the number N_{Bre} of breakup events scales as $N_{Bre} \propto G^{3/2}$. The shape of the FSDs appears

non-monotonic with one maximum at an intermediate floc size for $G < 80 \text{ s}^{-1}$, whereas the shape becomes monotonically decreasing for $G > 80 \text{ s}^{-1}$. The results for limited residence time are shown in Figure 7.5 (b), where the shape of the FSDs is monotonically decreasing for $G < 10 \text{ s}^{-1}$ and $G > 80 \text{ s}^{-1}$, and non-monotonic with one maximum for $10 < G < 80 \text{ s}^{-1}$.

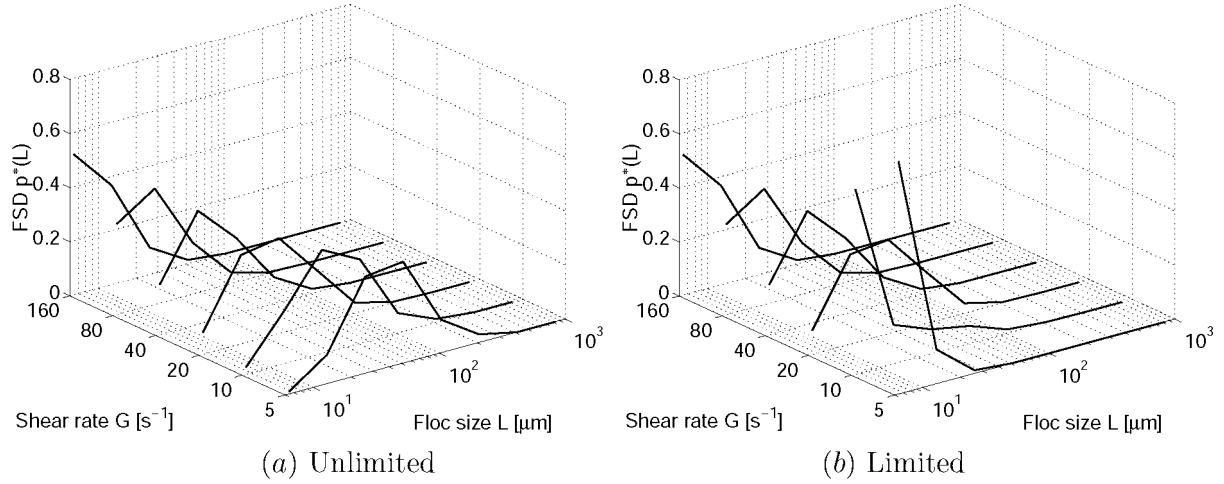


Figure 7.5: Representation of the steady state FSDs as a function of shear rates $G = \{5, 10, 20, 40, 80, 160\} \text{ s}^{-1}$ for (a) unlimited and (b) limited residence time.

Next to the shape of the FSDs, we infer that the mean \bar{L}^* and mode \tilde{L}^* floc size change significantly with G , showing two different behaviours. For unlimited residence time ($t > t_r$) both mean and mode are monotonically decreasing functions of the shear rate G , Figure 7.6 (a) and (b). For limited residence time ($t < t_r$) both mean and mode have a maximum for a given $G = G^*$, as already mentioned. The curves for limited residence time meet the curves for unlimited residence time at $G \approx G^*$, with $G^* \approx 20 \text{ s}^{-1}$. This behaviour of bifurcation is predicted by the theory, and the numerical results follow the schematic drawing in Figure 2.4.

The mode \tilde{L} and mean floc size \bar{L} of the experimental data and numerical simulations are compared in Figure 7.6 for $t_r > t_f$, *i.e.* for the steady state FSDs and for both the calibration (FSDs for $G = \{10, 40\} \text{ s}^{-1}$) and validation set (FSD for $G = \{5, 20\} \text{ s}^{-1}$). The model tends to overestimate the mean size \bar{L} for $G < G^* \approx 20 \text{ s}^{-1}$, and underestimate \bar{L} for $G > G^* \approx 20 \text{ s}^{-1}$, Figure 7.6. This means that the the model is either likely to overestimate aggregation or underestimate breakup for $G < G^*$. In the first case, this may be related to a too high collision frequency. In the second case, this can be either related to the breakup distribution function $\gamma_{i,j}$ that redistributes fragmenting flocs into too large aggregates, or to a breakup rate $B_i^{(s)}$ too small.

From these analyses we infer that, qualitatively, the behaviour of the model with varying G meets the experimental experience and theoretical analysis of flocculation. The floc size distribution is predicted with relative errors $0.2 < \text{Err} < 0.4$, and the shape of the computed FSD meets the experimental and theoretical ones as well.

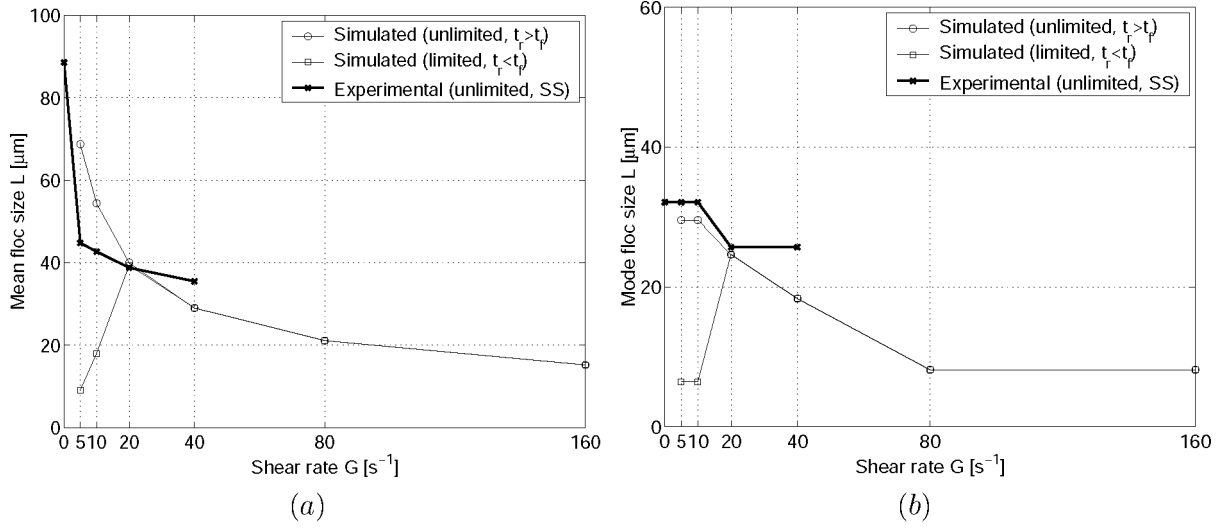


Figure 7.6: (a) relationship of experimental and simulated mean floc size \bar{L} with shear rate G . (b) relationship of experimental and simulated mode \tilde{L} and \tilde{L}^* with shear rate G .

7.6 Sensitivity analysis

The sensitivity of the model to different parameters is investigated in this section. Table 7.3 summarises the model input and settings of all simulations performed (different initial conditions $n_k(t = 0)$, collision efficiencies $\alpha_{i,j}$, breakup distribution functions $\gamma_{i,j}$ and capacity dimensions d_0).

Sensitivity to			Initial distribution	Collision efficiency	Breakup distr. function	Capacity dimension
Shear rate	G	$[\text{s}^{-1}]$	10	10	10	10
Mass concentration	c	$[\text{g l}^{-1}]$	0.5	0.5	0.5	0.5
Initial distribution	n_k		k=1 Uniform	$k = 1$	$k = 1$	$k = 1$
Collision efficiency	$\alpha_{i,j}$		α_{opt}	Eq. (2.5) Eq. (2.6) α_{opt}	α_{opt}	α_{opt}
Breakup distribution function	γ_{ij}		Binomial	Binomial	Binomial Binary Ternary	Binomial
Capacity dimension	d_0		δl^γ	δl^γ	δl^γ	$1.7 \div 2.3$ δl^γ

Table 7.3: Table of numerical simulations carried out for the sensitivity analysis of the population balance in Eq. (7.1), with $E = E_{opt}$, and $\Delta t = 0.5$ s.

7.6.1 Initial conditions

The sensitivity of the model of Eq. (7.1) to initial conditions is investigated through an example of the stability of the solution by comparison of computed FSDs $p^*(L)$ at steady state. The first simulation is run with an initial peak in class $k = 1$, *i.e.* primary particles only. The second is run with initially uniformly distributed concentration $n_k(t = 0)$, and the last is run with an initial peak at large floc sizes belonging to class $k = N_p = 10^4$.

The results in Figure 7.7 show that the system converges to a stable solution. The three cases have been chosen such as to let the population evolve from the most different initial conditions; the results in Figure 7.7 give confidence that the solutions found are effectively stable. This, however, does not prove that the system possesses a single solution; the nonlinearity and complicatedness of the population balance in Eq. (7.1) does not allow an analytical study of the solution. Therefore we cannot exclude other solutions for different values of α_{opt} and E_{opt} and, maybe, other aggregation and breakup mechanisms. This should be subject of further research.

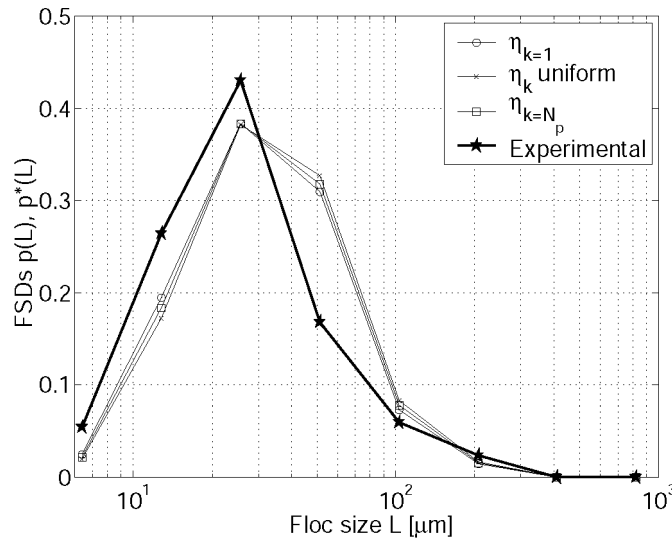


Figure 7.7: Simulated and experimental steady state FSDs $p^*(L)$ and $p(L)$ for different initial conditions $n_k(t = 0)$, and for $G = 10 \text{ s}^{-1}$ and $c = 0.5 \text{ gl}^{-1}$. The model settings are resumed in Table 7.3.

7.6.2 Collision efficiency

The sensitivity of the PBE to the collision efficiency $\alpha_{i,j}$ is investigated by comparing the steady state solution found for three different expressions of $\alpha_{i,j}$: the first is the analytical formulation by Pruppacher & Klett (1978) given in Eq. (2.5); the second is the one proposed by Friedlander (1957) in Eq. (2.6); the last considers $\alpha_{i,j} = \alpha_{opt}$ which was found from calibration in Section 7.4.4.

The results in Figure 7.8 show that the steady state solution is rather sensitive to the collision efficiency $\alpha_{i,j}$. The FSD is monotonically decreasing for the two analytical formulations of $\alpha_{i,j}$, while for $\alpha_{i,j} = \alpha_{opt}$ it is non-monotonic with an intermediate maximum. This discrepancy can be explained as follows: the upper value of the functional expressions of $\alpha_{i,j}$ occurs when two interacting aggregates have identical size L , and it corresponds to $\hat{\alpha}_{i,j} = 0.12$ in Pruppacher & Klett (1978) and $\hat{\alpha}_{i,j} = 0.31$ in Friedlander (1957). The

value of $\alpha_{i,j} = \alpha_{opt} = 0.62$ is much larger than the others, resulting in a higher rate of aggregation and a skewness larger than in the other cases. The FSD with $\alpha_{i,j} = \alpha_{opt}$ is found to be the closest one to the experimental FSD.

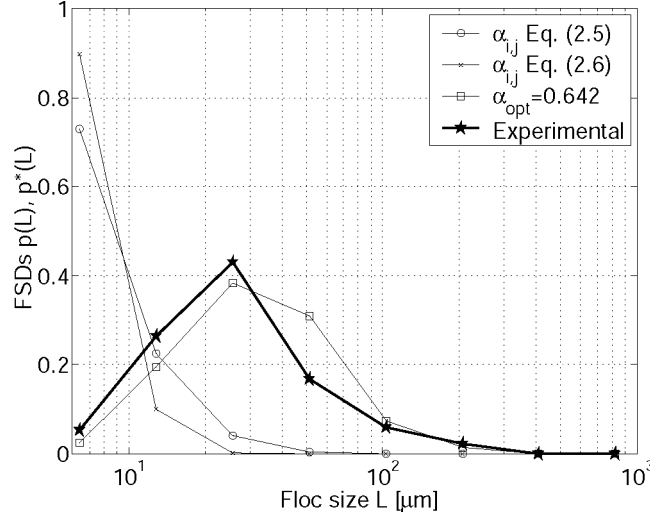


Figure 7.8: Simulated and experimental steady state FSDs $p^*(L)$ and $p(L)$ for different formulations of the collision efficiency $\alpha_{i,j}$, and for $G = 10 \text{ s}^{-1}$ and $c = 0.15 \text{ g l}^{-1}$. The model settings are resumed in Table 7.3.

7.6.3 Breakup distribution function

The sensitivity of the PBE to different breakup distribution functions $\gamma_{i,j}$ is investigated by comparing the steady state solution for binary, ternary and binomial breakup. Binary breakup $\gamma_{i,j}^{(Bin)}$, which is fragmentation of an aggregate with $N_p = j$ primary particles into two aggregates of identical particle number $N_p = i$, is modelled as follows:

$$\gamma_{i,j}^{(Bin)} = \begin{cases} 2 & \text{for } i = j/2, \\ 0 & \text{otherwise,} \end{cases} \quad (7.17)$$

Ternary breakup $\gamma_{i,j}^{(Ter)}$, which is fragmentation into three aggregates, is modelled as follows:

$$\gamma_{i,j}^{(Ter)} = \begin{cases} 1 & \text{for } i = 1/2j, \\ 2 & \text{for } i = 1/4j, \\ 0 & \text{otherwise,} \end{cases} \quad (7.18)$$

where one aggregate has $N_{p,1} = N_p/2$ primary particles of the mother aggregate, while two aggregates have $N_{p,2} = N_{p,3} = N_p/4$ of the mother's. Finally, binomial breakup $\gamma_{i,j}^{(Nom)}$ is already presented in Eq. (7.5). As the total number of daughter flocs is not defined *a priori* in $\gamma_{i,j}^{(Nom)}$, a Monte Carlo extraction of i is applied. Mass conservation is required at each step of the fragmentation process and this process is repeated until $\sum_i \gamma_{i,j} \cdot i = j$.

Figure 7.9 shows the steady state FSDs computed for binary, ternary and binomial breakup distribution functions. These are all non-monotonic, but with different skewness. Binary breakup results in too many large flocs, whereas ternary and binomial breakup replicate the experimental FSD more accurately.

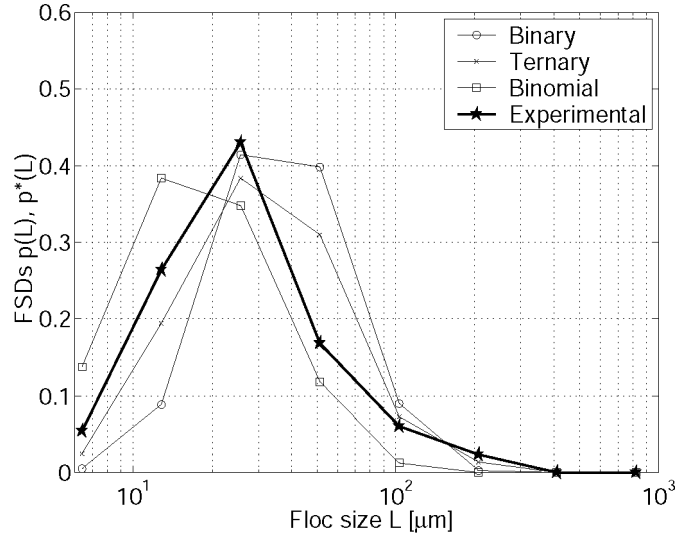


Figure 7.9: Simulated and experimental steady state FSDs $p^*(L)$ and $p(L)$ for different breakup distribution functions $\gamma_{i,j}$, and for $G = 10 \text{ s}^{-1}$ and $c = 0.15 \text{ gl}^{-1}$. The model settings are resumed in Table 7.3.

7.6.4 Capacity dimension

The sensitivity of the solution found by the PBE to different floc's capacity dimension is analysed in this section. Firstly, flocs are described as fully self-similar bodies, *i.e.* with constant capacity dimension d_0 equal to $d_0 = \{1.7, 2, 2.3\}$ and, secondly, as statistically self-similar bodies (*i.e.* multifractals) with $d_0 = \delta \ell^\gamma$.

The sensitivity of the steady state solution to d_0 is shown in Figure 7.10, where we observe that the FSDs $p^*(L)$ computed for $d_0 = \{2, 2.3, \delta \ell^\gamma\}$ compare quite well to each other and to the experimental one. In contrast the FSD computed with $d_0 = 1.7$ appears dramatically right-skewed with respect to all others. This means that either aggregation is

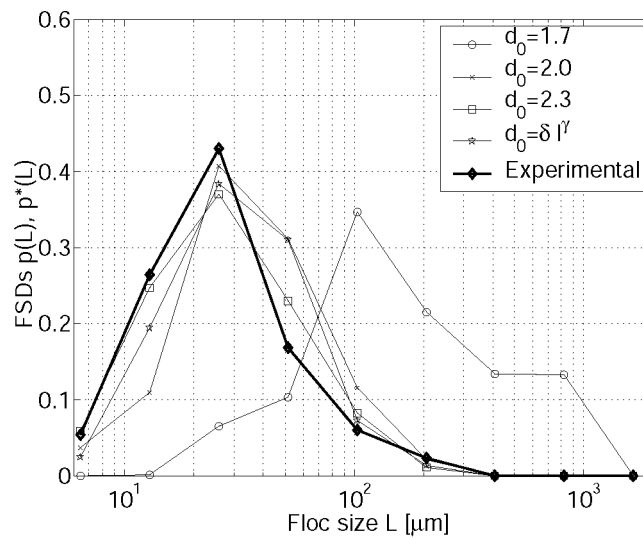


Figure 7.10: Simulated and experimental steady state FSDs $p^*(L)$ and $p(L)$ for different values of capacity dimension d_0 , and for $G = 10 \text{ s}^{-1}$ and $c = 0.15 \text{ gl}^{-1}$. The model settings are resumed in Table 7.3.

overestimated or, *vice versa*, breakup is underestimated. However, the capacity dimension d_0 appears only in the porosity term $[(L_i - L_p)/L_p]^{3-d_0}$ of the breakup frequency function $B_i^{(S)}$ in Eq. (7.4). Physically, this means that flocs with identical size are more likely to disintegrate when d_0 is small, being less compact and more fragile. From this, we would expect $p^*(L)$ to be left-skewed for small d_0 , instead of right-skewed. To better understand this, consider the scaling law $N_p \propto (L/L_p)^{d_0}$. For d_0 decreasing, the number of primary particles N_p within a floc of given size L decreases. However, the total number of primary particles within the system is constant, and proportional to the mass concentration c . This means that a decrease in d_0 is accompanied by an increase of the number concentrations n_k . As a consequence, aggregation can be higher than breakup, as already analysed in the scaling relationship of the numbers N_{Agg} and N_{Bre} of aggregation and breakup events in Section 7.5.2. This, then, would result in larger floc sizes. However, this does not explain the abrupt jump of the FSD with d_0 decreasing to $d_0 = 1.7$, and further research is required to clarify this behaviour.

7.7 Discussion

The numerical simulations analysed in Sections 7.5 and 7.6 allow some more analyses of the overall properties of the model.

7.7.1 Overview of the results

Important characteristics have been observed in the behaviour of the population balance equation proposed in Section 7.2.

Cohesive sediment suspensions are generally characterised, from an engineering point of view, by mass concentration, and by the mean, mode and median floc size. Examining the floc size distributions of our laboratory samples, the probability associated with the mode \tilde{L} appears always in the range $p(\tilde{L}) = 0.4 \div 0.5$, meaning that about half of the populations consist of flocs of size \tilde{L} . The mode \tilde{L} is therefore a useful quantity in characterising the suspended sediment and more useful than the mean floc size, because \bar{L} does not relate to the most frequent floc size \tilde{L} within a population. Models for sediment transport and deposition describe the sediment load with characteristic quantities (mean, mode or median) rather than the floc size distribution. However, the simulations in Sections 7.5 and 7.6 give confidence that the model can be used to predict not only the mean and mode but also the frequencies associated with the full spectrum of floc sizes. In particular, the model seems to replicate flocculation properly in terms of response to different forcing and, qualitatively, to different mass concentrations. Because of this, we are confident that the model may help sediment transport modelers.

The small experimental data set does not allow to explore the properties of the model in a more comprehensive way. For this reason, similar models in the literature are surveyed briefly, and no attempt has been made to reproduce the results with our population balance model. Amongst these, we consider the one by Flesch *et al.* (1999) (FSP-model) applied to polystyrene particles, by Rahmani *et al.* (2004) (RDM-model) applied to asphaltene aggregates, and by Zhang & Li (2003) (ZL-model) applied to latex microspheres. Table 7.4 resumes the characteristics of these models. The structure of these population equations is similar to the one proposed in Eq. (7.1) (deterministic aggregation and stochastic breakup processes), but aggregates are either fully self-similar fractals (FSP- and ZL-models) or

		FSP-model	ZL-model	RDM-model
Collision frequency	$\Lambda_{i,j}$	$\Lambda_{i,j}^{(S)}$	$\Lambda_{i,j}^{(S)} + \Lambda_{i,j}^{(DS)} + \Lambda_{i,j}^{(BM)}$	$\Lambda_{i,j}^{(S)}$
Collision efficiency	α	1	0.8	1
Breakup rate	B_i	$EG^b L_i$	$EG^b L_i$	$EG^b L_i$
Breakup parameter	E	$7 \cdot 10^{-4}$	$7 \cdot 10^{-4}$	$2 \cdot 10^{-5}$
Breakup exponent	b	1.6	1.6	0.61
Breakup distr. function	$\gamma_{i,j}$	Binary Binomial	Binary Ternary Binomial	Binary
Capacity dimension	d_0	2.3	2.2	3
Initial distribution	n_k	From exp.	k=1	From exp.

Table 7.4: Settings of the FSP-, ZL- and RDM-model proposed in the literature.

Euclidian bodies (RDM-model) by virtue of the constancy of d_0 in each model, *i.e.* without the multiscaling geometry observed in Chapter 6. However, these models are structured upon the size L of the aggregates, contrary to Eq. (7.1) which is based on the number of primary particles within a floc. Figure 7.11 (a) shows the experimental floc size distribution found by Oles (1992) with $G = 50 \text{ s}^{-1}$ and the computed FSD obtained with the FSP-model. The computed mode \tilde{L}^* is slightly larger than the experimental one. However, the computed FSD shows a peak in the first class, which is not observed in the experiments by Flesch *et al.* (1999) nor in our experiments or numerical simulations.

Figure 7.11 (b) shows the experimental and computed FSDs obtained with the ZL-model for different shear rates G , showing a decrease of \tilde{L} with increasing G , which is consistent with the results found in Section 7.5.3 and other models. In this case, the simulations fit rather well the experimental data. Finally, Figure 7.11 (c) shows the experimental and computed FSDs obtained with the RDM-model. Here, it is interesting to note that the model gives monotonically decreasing FSDs, with \tilde{L}^* in the range of the primary particle size.

This brief survey shows that the modal floc size can be predicted in some cases, and by some models. The floc size distribution, instead, is more complicated to be reproduced by a population balance equation. The errors Err computed as in Eq. (7.16) gives respectively $Err = 0.389$ for the FSP-model, $Err = 0.748$ for the ZL-model and $Err = 0.526$ for the RDM-model. Considering that the error obtained with the population balance in Eq. (7.1) is $Err \approx 0.30$ for the calibration (Section 7.4.4) and $Err \approx 0.2 \div 0.4$ for the interpolation and extrapolation tests (Section 7.5.1), then we are confident of the quality of the modelling developed and proposed in this chapter.

Analysing these models and the data in Sections 7.5.1, 7.5.2 and 7.5.3 we conclude that the experimental FSDs predominantly show a non-monotonic shape with one maximum. The FSDs computed with our model have a non-monotonic shape in the majority of the cases, except in some cases where it was found monotonically decreasing. The latter can occur for two reasons: (1) specific environmental conditions (very low mass concentration

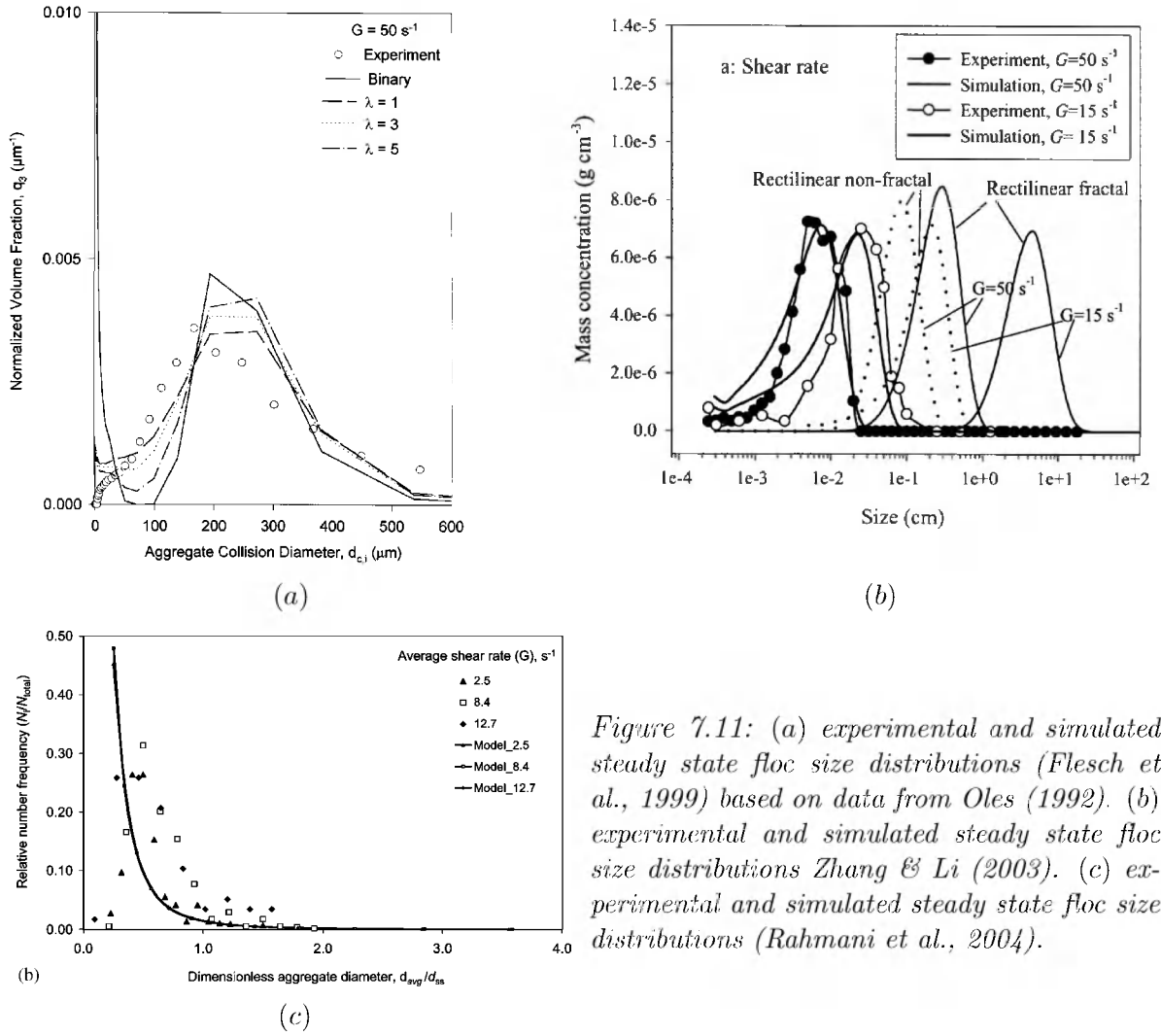


Figure 7.11: (a) experimental and simulated steady state floc size distributions (Flesch et al., 1999) based on data from Oles (1992). (b) experimental and simulated steady state floc size distributions Zhang & Li (2003). (c) experimental and simulated steady state floc size distributions (Rahmani et al., 2004).

- Figure 7.3 (a) - and very high shear rates - Figure 7.5); (2) intrinsic characteristics of the model (functional expressions of the collision efficiency - Figure 7.8). In some other cases, furthermore, the computed FSD is non-monotonic with two maxima (very high sediment concentrations - Figure 7.3 (a) - or in the model by Flesch - Figure 7.11 (a)). The property of monotonicity is fundamental for the proper modelling of the FSD; the following section is therefore dedicated to an analytical and numerical study of this property resulting from a different hypothesis in the modelling.

7.7.2 Mono- and non-monotonicity

Our interest is addressed to the case of monotonically decreasing floc size distributions, possibly originating from the intrinsic structure of the population balance equation. To this end, we introduce a simplified version of the population equation in Section 7.2 and we show the extent to which a particular description of floc structure and processes of aggregation and breakup can effectively induce a systematic (singular) result.

Let us consider the *semi-stochastic* population balance equation described in Section 7.2 in its generalised form of aggregation and breakup, and *quasi self-similar* floc growth. Next consider that aggregation and breakup occur in a fully *symmetric* rather than asymmetric

fashion: two flocs aggregate if and only if they have identical number of primary particles N_p (and size L), and floc breakup releases the two flocs that have formed it. Mass accretion is expressed, in this way, as fully multiplicative. Let us further assume, for simplicity, that the capacity dimension is not ℓ -dependent but constant. In that case, floc growth follows a *fully self-similar* growth path of type $G2$ ($\delta = \text{const} < 3$ and $\gamma = 0$), Section 6.6.3. The simplified population balance equation is:

$$\frac{dn_i}{dt} = \frac{1}{2} \underbrace{\alpha \Lambda_{i-1,i-1}^{(S)} n_{i-1}^2}_{\mathcal{G}_A} - \underbrace{\alpha \Lambda_{i,i}^{(S)} n_i^2}_{\mathcal{L}_A} + \underbrace{2B_{i+1}^{(S)} n_{i+1}}_{\mathcal{G}_B} - \underbrace{B_i^{(S)} n_i}_{\mathcal{L}_B}, \quad (7.19)$$

where the capacity dimension d_0 is considered $d_0 = 2$ for all flocs of any size. The index i refers to the number concentration n_i of aggregates with primary particle number $N_{p,i} = 2^{i-1}$, the collision efficiency is $\alpha = \text{const} \forall i$ and the distribution function for binary breakup in the term \mathcal{G}_B is $\gamma_{i,i-1}^{(Bin)} = 2$. All other terms are as in Section 7.2. Expanding Eq. (7.19) we obtain:

$$\begin{cases} \frac{dn_1}{dt} = 0 - \alpha \Lambda_{1,1}^{(S)} n_1^2 + 2B_2^{(S)} n_2 - 0, \\ \frac{dn_2}{dt} = \frac{1}{2} \alpha \Lambda_{1,1}^{(S)} n_1^2 - \alpha \Lambda_{2,2}^{(S)} n_2^2 + 2B_3^{(S)} n_3 - B_2^{(S)} n_2, \\ \vdots \\ \frac{dn_i}{dt} = \frac{1}{2} \alpha \Lambda_{i-1,i-1}^{(S)} n_{i-1}^2 - \alpha \Lambda_{i,i}^{(S)} n_i^2 + 2B_{i+1}^{(S)} n_{i+1} - B_i^{(S)} n_i, \\ \vdots \\ \frac{dn_{n_c}}{dt} = \frac{1}{2} \alpha \Lambda_{n_c-1,n_c-1}^{(S)} n_{n_c-1}^2 - 0 + 0 - B_{n_c}^{(S)} n_{n_c}. \end{cases} \quad (7.20)$$

At steady state, the system of Eq. 7.20 is such that $dn_i/dt = 0 \forall i \in \{1, \dots, n_c\}$, and considering the balance for n_1 we obtain:

$$\alpha \Lambda_{1,1}^{(S)} n_1^2 = 2B_2^{(S)} n_2. \quad (7.21)$$

Isolating n_1^2 as a function of n_2 , we obtain:

$$n_1^2 = \frac{2B_2^{(S)}}{\alpha \Lambda_{1,1}^{(S)}} n_2,$$

which, upon substitution in the balance of the number concentration n_2 at steady state, gives:

$$\begin{aligned} 0 &= B_2^{(S)} n_2 - \alpha \Lambda_{2,2}^{(S)} n_2^2 + 2B_3^{(S)} n_3 - B_2^{(S)} n_2, \\ \alpha \Lambda_{2,2}^{(S)} n_2^2 &= 2B_3^{(S)} n_3. \end{aligned} \quad (7.22)$$

Eq. (7.22) replicates Eq. (7.21): in practice, at steady state we have the following expression for the number concentration $\{n\}$:

$$n_i = \frac{\alpha \Lambda_{i-1,i-1}^{(S)}}{2B_i^{(S)}} n_{i-1}^2. \quad (7.23)$$

By explicitating terms $\Lambda_{i,i}^{(S)}$ and $B_i^{(S)}$ in Eq. (7.23) we obtain:

$$n_i = \frac{4\alpha G^{-1/2}}{6E\sqrt{\mu/F_y}} \frac{L_{i-1}^3}{\left(\frac{L_i - L_p}{L_p}\right)^{3-d_0} L_i} n_{i-1}^2. \quad (7.24)$$

Similarly to Section 7.2, the size L_i of flocs belonging to class i is computed with the fractal approach:

$$N_{p,i} = 2^{i-1} = (L_i/L_p)^{d_0}. \quad (7.25)$$

where, because of $d_0 = \delta = \text{const}$, we obtain:

$$L_i = L_p 2^{(i-1)/\delta}. \quad (7.26)$$

Substituting Eq. (7.26) into Eq. (7.24) we obtain:

$$n_i = \frac{4\alpha G^{-1/2} L_p^2}{6E \sqrt{\mu/F_y}} \frac{2^{(2i-5)/\delta}}{(2^{(i-1)/\delta} - 1)^{3-\delta}} n_{i-1}^2,$$

which can be re-written, for simplicity, as follows:

$$n_i = X \cdot Y_i \cdot n_{i-1}^2, \quad (7.27)$$

with:

$$X = \frac{4}{6} \frac{\alpha}{E} \frac{G^{-1/2} L_p^2}{\sqrt{\mu/F_y}} \quad \text{and} \quad Y_i = \frac{2^{(2i-5)/\delta}}{(2^{(i-1)/\delta} - 1)^{3-\delta}}.$$

where $X > 0$ always and $Y_i > 0 \forall i \in [2, n_c] \subset \mathbb{N}$. At steady state, the primary particle-based number concentration n_i in each class i is written as a function of the number concentration n_{i-1} of the previous class ($i-1$) in the form of a chain. For this reason, it is possible to write n_i as a function of n_1 as follows:

$$n_i = \left(X^{a(i)} \prod_{k=2}^i Y_k^{b(i,k)} \right) n_1^{c(i)}, \quad (7.28)$$

where:

$$\begin{aligned} a(i) &= 2^{(i-1)} - 1 > 0, \\ b(i, k) &= 2^{(i-k)} > 0, \\ c(i) &= 2^{(i-1)} > 0, \end{aligned}$$

in the range $i \in [2, n_c] \subset \mathbb{N}$. For simplicity, write Eq. (7.28) as follows:

$$n_i = d(i) \cdot n_1^{c(i)}, \quad (7.29)$$

where $d(i)$ is a short-term for the expression in the brackets in Eq. (7.28). The mono- or non-monotonic character of the primary particle-based number concentration n_i can be investigated through the sign of the functions $d(i)$ and $c(i)$. These are both strictly positive quantities. Therefore n_i is a monotonically increasing function $\forall i \in [2, n_c]$. Moreover, the population balance in Eq. (7.19) must satisfy the conservation of primary particles:

$$\sum_{i=1}^{n_c} n_i \cdot 2^{(i-1)} = \text{const}. \quad (7.30)$$

By substituting Eq. (7.29) into Eq. (7.30), we obtain:

$$n_1 + \sum_{i=2}^{n_c} \left(2^{(i-1)} \cdot d(i) \cdot n_1^{c(i)} \right) = \text{const}, \quad (7.31)$$

This equation gives a constraint to the monotonically increasing series n_i in Eq. (7.29). We can expect that the primary particle-based number concentration n_i possesses either a maximum $dn_i/di = 0$ at a given class i^* with $dn_i/di > 0 \forall i < i^*$ and $dn_i/di < 0 \forall i > i^*$, or a monotonically decreasing trend if the constraint causes $dn_i/di = 0$ at $i^* = 1$, hence limiting dn_i/di to negative values $\forall i > 1$.

To put light to this aspect we perform a simple numerical simulation. The population balance in Eq. (7.19) is calibrated with respect to α and E in the same way as in Section 7.4.4, finding $\alpha_{opt} = 1$ and $E_{opt} = 1.44 \cdot 10^{-5}$. Next, a series of runs is carried out to compute to steady state FSD for mass concentrations $c = \{0.2, 0.5, 1, 1.5, 2\} \text{ gl}^{-1}$ and shear rates $G = \{5, 10, 20, 40, 80, 160\} \text{ s}^{-1}$ in order to enable a comparison with Figures 7.3 and 7.5. The results are shown in Figure 7.12 where, in brief, we observe a monotonically decreasing floc size distribution in all cases. Since we have chosen mass concentrations and shear rates that are not extreme, we infer that the nearly invariant monotonic character of the FSDs is due to the chosen formulation of aggregation and breakup processes (*i.e.* fully deterministic) and floc growth (*i.e.* fully self-similar). We infer that the capability of the population balance equation described in Section 7.2 to imitate a non-monotonic floc size distribution depends essentially on asymmetric (rather than symmetric) reactions of aggregation, on stochastic (rather than deterministic) reactions of breakup, and on the quasi self-similar (rather than fully self-similar) growth process of flocs.

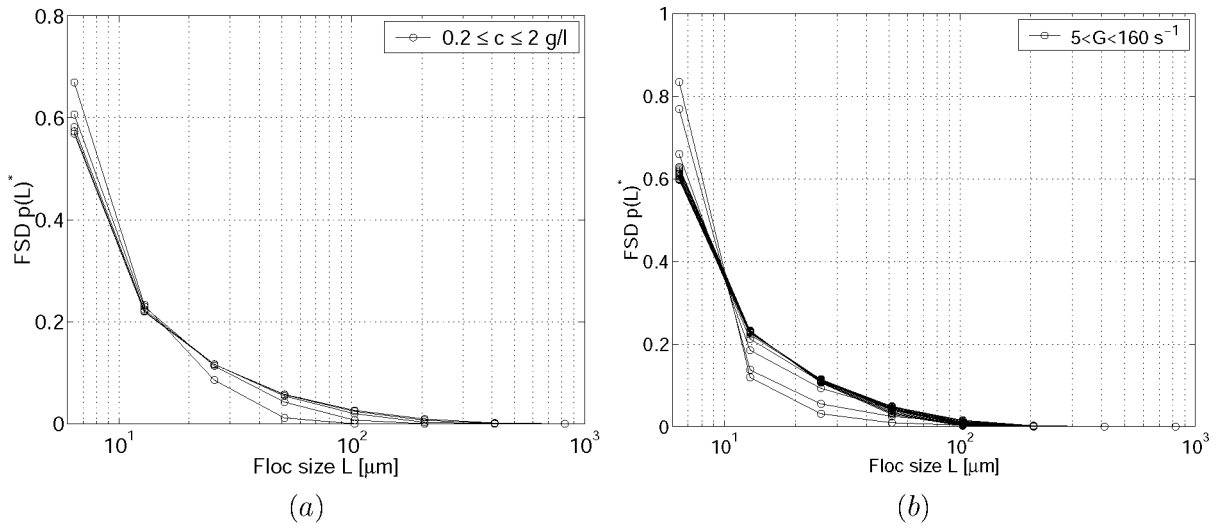


Figure 7.12: Representation of the steady state FSDs $p^*(L)$ computed with the simplified model of Eq. (7.19) for (a) mass concentrations $c = \{0.2, 0.5, 1, 1.5, 2\} \text{ gl}^{-1}$, and (b) shear rates $G = \{5, 10, 20, 40, 80, 160\} \text{ s}^{-1}$.

7.7.3 Self-organised criticality in the population balance equation

The Self-Organised Criticality (SOC) observed in the experimental floc size distributions in Chapter 5 motivates us to analyse whether the model in Eq. (7.1) is able to replicate a power-law distribution $p(r)$ of the rank r in frequency of occurrence. For this reason, a simple experiment is performed: the generalised population balance equation in Eq. (7.1) is run with the settings of Table 7.1 for $G = 40 \text{ s}^{-1}$ and $c = 0.5 \text{ gl}^{-1}$. The resulting FSD $p^*(L)$ is elaborated into the r -ordered probabilities $p(r)$ at times $t = \{0, 0.4, 0.8, 2.8, 3.5\}$

h to detect the presence of a power-law dependence $p(r) \propto r^a$ with exponent $a = -1$. The population equation approaches steady state at time $t \approx 2.2$ h. Therefore the FSDs at times $t = \{0, 0.4, 0.8\}$ s are not at equilibrium, whereas those at times $t = \{2.8, 3.5\}$ h are at steady state. The probabilities $p^*(r)$ are computed for evenly spaced floc size classes, as described in Section 5.5, and the probabilities $p^*(r) < 5 \cdot 10^{-2}$ are neglected also in this case, as they represent a very small share of the flocs.

The r -ordered FSDs $p^*(r)$ given in Figure 7.13 show two features when $p(r) > 5 \cdot 10^{-2}$. The FSDs at non-equilibrium have slope $a < -1$, while the steady state FSDs overlap precisely (as they are at steady state) but they show a slope a slightly larger than -1 . From the analysis of the experimental FSDs in Section 5.5, we argued that a non-equilibrium appears with a power-law sloped as $a > -1$, and that the slope approaches $a = -1$ at steady state. This would imply that the model is more or less able to reach self-organised criticality when the population is at steady state, but is not able to reflect the time evolution of the population towards the criticality point, the state that was experimentally characterised by $a > -1$.

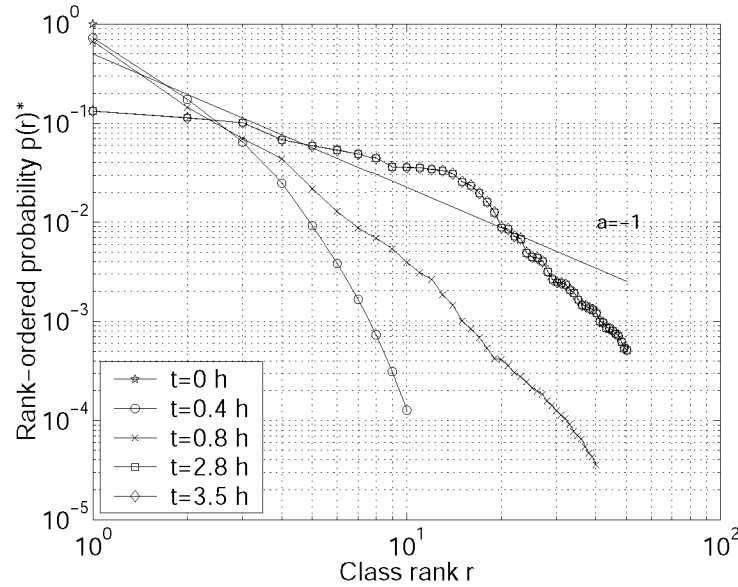


Figure 7.13: Rank-ordered FSDs $p^*(L)$ computed through the model of Eq. (7.1) at times $t = \{0, 0.4, 0.8, 2.8, 3.5\}$ s. The straight line indicates the power-law with exponent $a = -1$ corresponding to SOC.

7.8 Conclusions

The population balance equation proposed in this chapter and its investigation with respect to experimental data allows to draw the following conclusions.

First, the calibration of the parameters of the PBE against laboratory experiments has enabled to simulate the FSD of kaolinite flocs observed in the settling column. The error by the model is relatively small, although the small number of experimental data did not allow a full evaluation. However, the analysis of similar models carried out in Section 7.7.1 has suggested that the results shown in Section 7.5.1 are promising. Further simulations performed in Sections 7.5.2 and 7.5.3, and analysed with respect to established knowledge

of flocculation, have given confidence in the capability of the population balance equation to give realistic results.

Second, the characteristics of the model have been investigated in the sensitivity analysis of Section 7.6, showing that: the solution of the system converges to a steady state FSD; the model should be calibrated with respect to the collision and breakup efficiency; the breakup distribution function can have an impact on the steady state solution, although the breakup mechanisms of flocs remains still unknown; the capacity dimension of the flocs can be either considered constant $d_0 \approx 2$, or expressed as a function of the size according to the quasi self-similar growth path.

Third, the steady state solution shows either a monotonically decreasing or a non-monotonic shape with one maximum (only occasionally with two maxima, for high sediment concentrations). The monotonically decreasing solution of the population balance equation has been investigated by means of a *simplified* population equation, showing that for normal values of mass concentration and turbulence shear (comparable with natural conditions), the system reaches a nearly invariant solution. This is a systematic result possibly caused by fully deterministic and symmetric aggregation and breakup processes and by fully self-similar floc growth. In contrast, the monotonic decreasing solution of the generalised population balance (deterministic asymmetric aggregation, stochastic breakup, and quasi self-similar floc growth) occurred only at high and very high turbulent shear rates. In this case, monotonicity is consistent with experiments and expected from theory. For this reason, the generalised form of the population balance seems more suitable to describe flocculation of cohesive sediment, because it possesses the capability to reproduce FSDs different in shapes.

Fourth, the far-from-equilibrium (statistical stationarity) steady state introduced in Chapter 3 and linked to self-organised criticality in Chapter 5 has not been clearly detected in the numerical results of the population balance equation. In other words, only the steady state solution of the population balance equation shows self-organised criticality, but the time evolution of the r -ordered probabilities of the numerical simulations do not proceed regularly from $a = 0$ towards $a = -1$ as in the experiments. This behaviour leaves an open question which requires to perform more experimental and theoretical research.

Chapter 8

Conclusions and recommendations

Flocculation of cohesive sediment has been investigated along three routes: experimental, analytical and numerical. Various conclusions have been drawn, the detailed description of which has been given in the conclusions of Chapters 5, 6 and 7. For this reason, in this last chapter, the author gives a general and brief overview, together with an indication of applicability and directions for future studies.

8.1 Achievements of the research

The first target attained during this doctoral project is the design and building of the settling column, Chapter 4. This tool for investigating flocculation of cohesive sediment has required expensive and extensive efforts, not only budgetary but also scientific and technical. This facility is in fact unique for the time and length scales involved, for the generation and control of the turbulence field and for the measuring techniques involved. As the full potential of the facility has not been exploited yet, future users of the settling column will give further contributions to the understanding of flocculation.

The second achieved target is the phenomenological description of flocculation on the large length scales, Chapters 3 and 5. A (mono) dispersed population of cohesive particles within a turbulence field represents a system at non-equilibrium. This causes the particles to flocculate yielding flocs with a wide spectrum of sizes and characterised by a mode corresponding to dominant flocs. The floc size distribution displays an evolution during which its shape changes until a far-from-equilibrium steady (*i.e.* statistically stationary) state is reached. However, another representation (r -ordered probability) of the floc size distribution shows that its shape is invariant at any equilibrium, and that a power-law with slope $a = -1$ can be universally used to describe such a state. This slope corresponds to a state of criticality, that the scientific literature identifies with self-organisation. Cohesive sediment is marked by a decrease of spatial entropy and increase of information entropy during flocculation. The former has been inferred (Chapter 3), as no direct measurements are made to investigate this aspect, while the latter is observed in our measurements in the settling column. This allows us to infer that a progressive development of organisation occurs at the expenses of the spatial entropy of the system (decreasing as the system becomes more ordered) and in favour of the information entropy of the floc size distribution (increasing as the population becomes more complex).

The third achieved target is the phenomenological description of the mass-density organisation of the flocs, Chapters 3 and 6. Here, the paradigm of multifractality gives

the spectrum of exponents required to scale floc geometry. Because this spectrum is a continuum, we conclude that real flocs display a complicated network of clusters (and sub-clusters) of primary particles that cannot be simply modelled as fully self-similar, least of all Euclidian. The fact that the fractal dimensions are a *continuum* does not mean that we have to account for an infinity of parameters when modelling floc structure; rather, we observe that one particular fractal dimension (the capacity dimension) changes with floc size during floc growth according to a power-law. This law expresses that flocs do not have a constant fractal dimension and therefore floc growth does not occur in a fully self-similar regime, but in a regime of quasi-self-similarity. This results in the genesis of multifractal flocs; the development of multifractal structures is accompanied by disordered mass-density organisation. In addition, the power-law in its generalised form is capable to reflect other growth processes, that can be involved in other systems, like ballistic deposition, crystal nucleation, viscous fingering and relaxation, or in mixed regimes of growths.

The fourth achievement is the incorporation of both large and small length scales description into a comprehensive phenomenological description of flocculation, Chapter 6. In essence, the large scale tendency of a flocculating system to (self-) organise, showing certain floc size and rank ordered distributions, is directly correlated to the small-scale tendency of the floc structure to become increasingly complex during flocculation.

The fifth achievement is the implementation of the previous issues into a population balance equation, Chapter 7. This is structured in such a way as to describe the stochastic (rather than deterministic) events of aggregation and breakup among flocs of different sizes. However, this is not totally new; the innovation lies in the embedding of the power-law growth of individual flocs in the population balance equation. As the growth process so described is meaningful when considering the primary particles in a floc, the structure of the population equation has been based on the primary particle number rather than the floc size. The coupling of these two aspects has allowed a better description of the interacting units and processes, nonetheless enabling mass conservation in an explicit (and convenient) way, contrary to other continuous and discrete models.

8.2 Application, users and other domains of applicability

Application of the knowledge developed in this thesis can be used in two major contexts in sedimentological sciences: the theoretical/analytical body can be used in the characterisation of suspended matter observed either in the laboratory or *in situ*; the numerical/modelling part, consisting of the population balance equation, can be used to carry out forecasts of the floc size distribution of the suspended matter. To know (or to be able to predict) the floc size distribution of suspensions of cohesive sediment implies to know (or to be able to predict) the settling velocity of sediments, which itself is needed to predict the amount of sediment depositing on the bed. This aspect is of primary importance when studying sedimentation of cohesive sediment in natural waters. Applications are potentially wide: rivers, water basins, lakes, coastal waters, estuaries and harbours are all examples of natural waters in which cohesive sediment can be characterised and modelled.

Users can be from a broad panel of technical/engineering organisations, academics, institutional bodies and governmental agencies directly or indirectly related to water sciences and water management. This applies, for instance, to numerous civil engineering instal-

lations and infrastructures (coastal protection, waste water and water purification plants, hydraulic powers plants, *etc.*), hydrological control (flood prevention, estuaries and river monitoring, *etc.*), and water managers (water supply, hazard/risk management, *etc.*).

The analysis and interpretation of the processes of flocculation is built only partly on the classic approach to cohesive sediments. This thesis presents an original elaboration of (partly) existing knowledge and a new phenomenological description of floc growth and flocculation dynamics. This hampers comparison and validation using existing know-how in sedimentology. As this research is mostly based on concepts borrowed and elaborated from geometry and physics, and both the multifractal description of aggregates and population balance equation describe the evolution of systems of particles regardless of their specific nature (to some extent hidden in the calibration parameters), a number of disciplines different from sedimentology can be users of the present work. Some examples are: meteorological sciences (formation of fogs, droplet dispersions, atmospheric clouds, precipitation, aerosols, *etc.*); chemical/industrial processes (separation, coagulation, condensation, polymerisation and filtering processes). An example of the generalised applicability of one of the results of this research is already appearing within the context of cosmology, as the theory of 2D projections of 3D fractal measures presented in Maggi & Winterwerp (2004a) has been confirmed in a recent work by Sanchez *et al.* (2005) for the observation of the Orion molecular cloud.

8.3 Future improvements

Three directions are suggested here for future improvements in the study of flocculation of cohesive sediment.

First, the observation of the suspended matter in the settling column can be made more accurate if the resolution of the digital camera is higher than that used in our facility. This would allow to reduce the scatter in the characterisation of the geometrical structure of the flocs.

Second, the analysis of self-organisation properties of the suspended matter should be investigated on a wider scale, comprising laboratory data, *in situ* data and numerical simulations. In fact, the geometrical property of the floc size distribution having invariant slope at steady state may be efficiently used to predict short-term changes in the composition of flocs within a population in the real world, hence giving a direct approach to estimate sediment fluxes, with no needs of tracking an extensive time history of the floc size distribution itself.

Third, the capability of the population balance equation should be explored more profoundly, by cross-validating the results with other experiments and, especially, with field data. The data sets analysed in this thesis are the first two series of measurements performed with this settling column. Further evidence or validation of the phenomenology and modelling of flocculation proposed in this thesis can be found only with future experiments in this facility, or by comparisons with other experiments in the field or in the laboratory. This aspect will be very challenging.

Fourth, natural waters always contain biological matter, which is not accounted for in the model. Therefore, a future long-term development of the population balance equation could be the incorporation of biological processes and particles.

8.4 Concluding comment

Some aspects of the dynamics of a population of sediment flocs meet the features of populations studied in other fields of science; this is in essence due to the fact that, in terms of physical description, they consist of units that interact with each other. From this perspective, an abundant number of natural systems can be described by means of interacting units, both in abiotic systems (like atoms, molecules, gases, sediments, smokes, fogs, aerosols, soils, cars, planets, galaxies, *etc.*) and biotic systems (like bacteria, algae, fungi, insects, humans, *etc.*). Whatever the nature of the units and their interactions, these systems can all be referred to as an ensemble of interacting units within an open or closed domain of existence. The most convenient way to underline this common feature is to cite some examples of cosmology, natural sciences and physics.

In the first (cosmology), a number of studies are being carried out to describe the spatial distribution of matter in the universe into galaxies and clusters of galaxies (Pietronero, 1990), hence evoking the particulate nature of the cosmos. Some simple approaches to this issue showed that also galaxies appear with fractal and multifractal mass-density distributions. This was the first example of application of the multifractal spectrum, that was originally developed in mathematics for the study of fractal sets from the theoretical point of view.

In the second example (natural sciences/biology), an approach which goes under the name of autopoiesis (literally translated into "self" - auto - and "production" - poiesis -, Maturana & Varela, 1972) has been developed since the seventies. This refers to the capability of dissipative abiotic and social/community (biotic) systems to produce their own structure, somehow, organising or self-organising. We mention cohesive sediment studied in this thesis as an example of non-living system that shows self-organisation through energy dissipation, and ants communities as counterpart example of biotic systems hierarchically organised, the individuals of which being able to exchange information. Note that both consist of interacting units. A very similar approach was developed more or less contemporary in other disciplines of natural sciences by Bak (1990), who realised the overall tendency of nature to produce certain ordered manifestations over different physical domains, like in the case of sandpile systems (self-organised criticality).

In the third example (numerical physics), a number of scientists, inspired by observations in the real world, started to implement these types of systems consisting of interacting units into simple models based on numerics rather than physics. From here, since some decades ago up to now, a well-developed branch of interdisciplinary science has produced deep knowledge by studying diffusion-limited and cluster-cluster aggregation processes, percolation theory, chaos theory, complexity, *etc.*, hence taking explicitly into account the particulate nature of the systems under investigation.

The fact that an ever-increasing interdisciplinary approach seems to suit better the needs to understand systems of interacting units (see mentioned examples), means that there exist, effectively, common features amongst disparate scientific domains. Striking evidence of this is the increasing number of *laws of invariance* that are being found in nature, and that these laws are, for the majority (if not the totality), *power-laws*. Let us recall the three mentioned examples. Fractality (in cosmology, or anywhere else where fractality can be detected) appears in the form of power-laws. The same applies to self-organised criticality (in natural sciences/biology, and all other disciplines where self-organisation can be detected), where power-laws appear to describe a particular state of critical equilibrium. Finally, the scaling laws describing particulate systems at almost any level (in numerical

physics, and all disciplines correlated to it) appear as power-laws. To the author's knowledge, nobody has come up with a convincing explanation of the fact that power-laws are so common in nature; to his personal opinion, the question is still open. This thesis does not give a contribution to the understanding of these laws of invariance; yet, it provides a further example of the existence of such laws, making them a tool to describe flocculating systems from a phenomenological point of view.

Appendix A

Characterisation and classification of fractal sets

A.1 Characterisation of fractal sets

In this appendix the entropy and disorder functions, and the multifractal spectrum of some simple sets are computed for some illustrative cases to show the possible type of characterisation of the geometrical structure of mud flocs.

Figure A.1 shows the fractals considered for application of the disorder index and multifractal spectrum. All the fractals employed are built in a square frame of 300-by-300 pixels, except fractal $F3$, whose size is 243-by-243 pixels because it is obtained by five multiplicative iterations of an initial element of 3-by-3 pixel size. Fractals $F1$, $F2$ and $F3$ have capacity dimension $d_0^{(F1)} = 2$, $d_0^{(F2)} = 1$ and $d_0^{(F3)} = 1.46$ respectively, where $F1$ and $F2$ are two topologically regular sets, while $F3$ is a typical determinist fractal. $F4$ is a shape with some level of symmetry and determinism. $F5$ and $F6$ are two 2D projected images of kaolinite flocs, embedded in the smallest square of size L and resized to 300-by-300 pixel. The pixel is considered the unit quantity ϵ . Finally, black color means activated pixels, white corresponds to non-activated pixels.

We apply the thermodynamic formalism introduced in Section 3.2.1, with the aim of evaluating the entropy function $S(\epsilon)$ and disorder function $\Upsilon(\epsilon)$ of the sets in Figure A.1. The computation is performed for box sizes $\epsilon = \{5, 10, 50, 100, 300\}$ relative to $F1$, $F2$, $F4$, $F5$ and $F6$, and $\epsilon = \{3, 9, 27, 81, 243\}$ relative to $F3$. We observe in Figure A.2 that the quantity of disorder of $F1$, $F2$ and $F3$ is zero, as they have $S(\epsilon) = 0 \forall \epsilon$. This holds for the Euclidian set $F1$ and $F2$, obviously, and also for $F3$ which, despite being a fractal, is fully recurrent in its structure without irregularities or asymmetries. Analogously, we can also say that $F1$, $F2$ and $F3$ have a very low level of complexity, in that only one pattern can be detected in the ω -covering. Fractals $F4$, $F5$ and $F6$ show, differently, entropy levels that are higher compared to the previous fractals, as the entropy $S(\epsilon) \neq 0$ and $\Upsilon(\epsilon) \neq 0$ with a peak at a given ϵ , Figure A.2. $F4$ possesses some symmetry while $F5$ and $F6$ do not have any regularity or symmetry. The structural organisation of these sets is more complex with respect to the organisation of all the previous fractals, because of the large number of patterns found in the ω -covering of the set.

The multifractal spectrum of the fractals of Figure A.1 has been computed for $q = \{-20, \dots, 20\}$ and for $\epsilon = 100$ pixels. The results are shown in Figures A.3. In particular, $f = \text{const}$ for $F1$, $F2$ and $F3$ in the (f, q) -plane, Figure A.3 (a), corresponding to the value

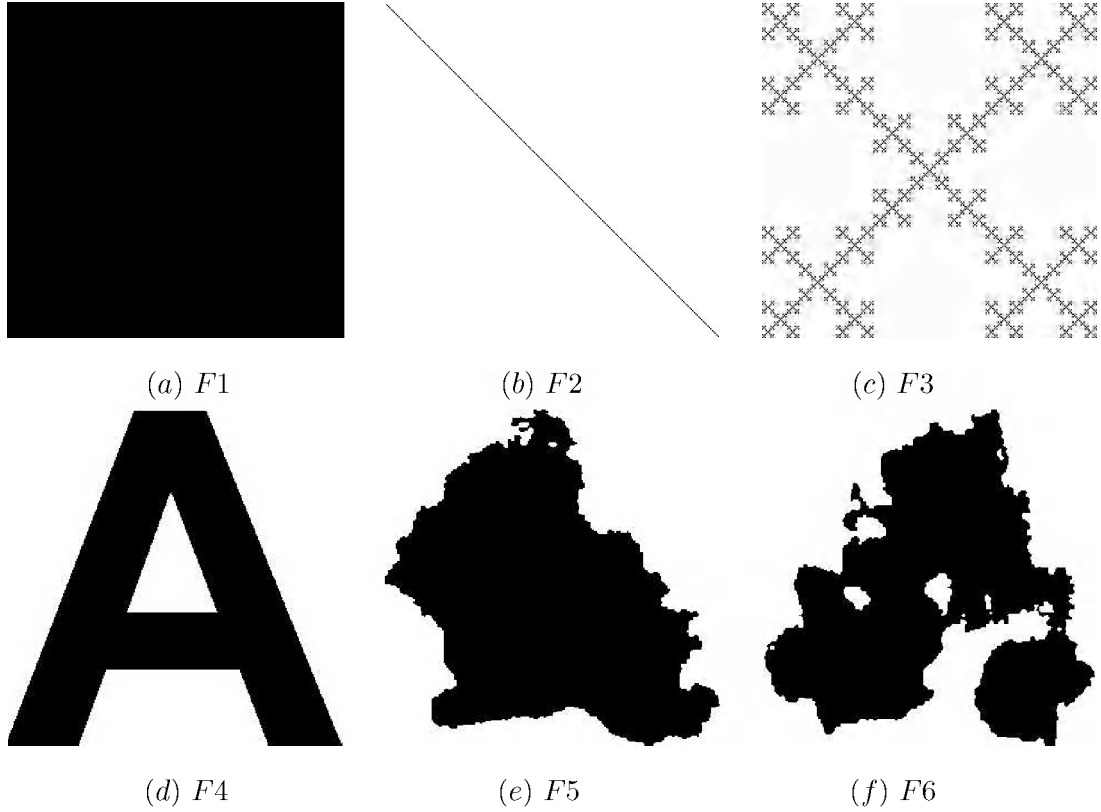


Figure A.1: Fractal sets used to show the application of the disorder and multifractal formalism.

of capacity dimensions of each set, while the multifractal spectrum f is a point in the (f, α) -representation, Figure A.3 (b), meaning that also $\alpha = \text{const} \forall q$, Figure A.3 (c). This is evidence of the fact that $F1$, $F2$ and $F3$ are monofractals. Further, monofractality means that there is a unique scaling in the mass-correlation exponent τ . In fact, $\alpha = d\tau/dq = \text{const}$ means that τ has a constant slope in the (τ, q) -plane. Fractals $F4$, $F5$ and $F6$ show a curved spectrum f both in the (f, q) -plane and in the (f, α) -plane, representing all the fractal dimensions of the set, Figs. A.3 (a) and (b). The singularity strength $\alpha(q) = d\tau/dq \neq \text{const}$ is, in this case, a function of q , Figure A.3 (c). The fact that $F4$, $F5$ and $F6$ show a range of singularity strength α means that each of the q -th $\mu(q, \varepsilon)$ -partitions of the sets possesses a distinct fractal dimensionality. This is evidence of the multifractal nature of $F4$, $F5$ and $F6$. As $\alpha \neq \text{const}$ then $d\alpha/dq \neq 0$, meaning that the mass correlation exponent τ does have a slope $d\tau/dq \neq \text{const}$ with a curvature $d^2\tau/dq^2 \neq 0$. This implies that more than one scaling law is required to describe the mass-density distribution of these sets, Figure A.3 (d).

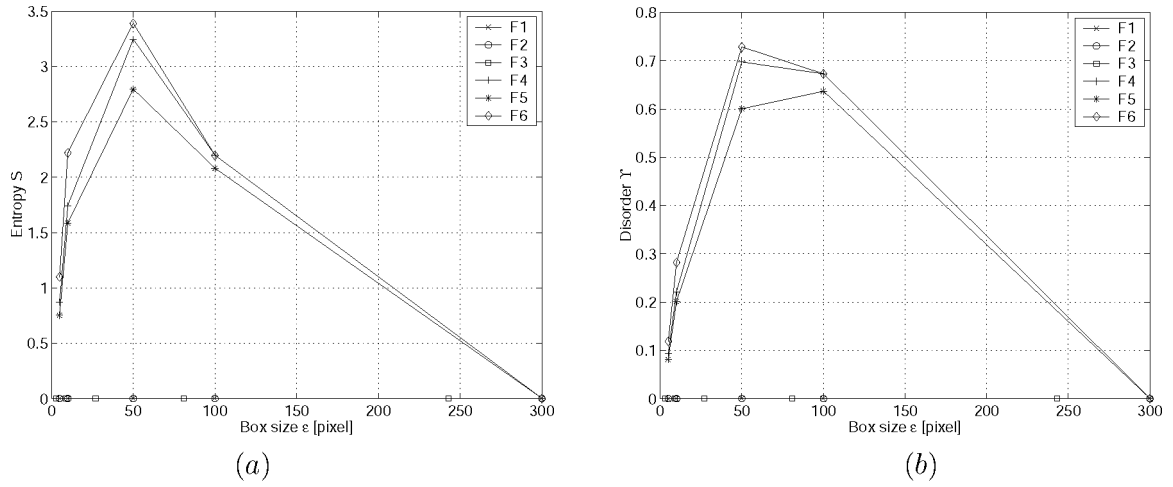


Figure A.2: (a) representation of the entropy function $S(\epsilon)$ and (b) disorder function $\Upsilon(\epsilon)$. In particular, $S' = \sup\{S\}$ at ϵ' and $\Upsilon' = S'/S_{max}$ at ϵ' are the values of entropy and disorder associated to each fractal.

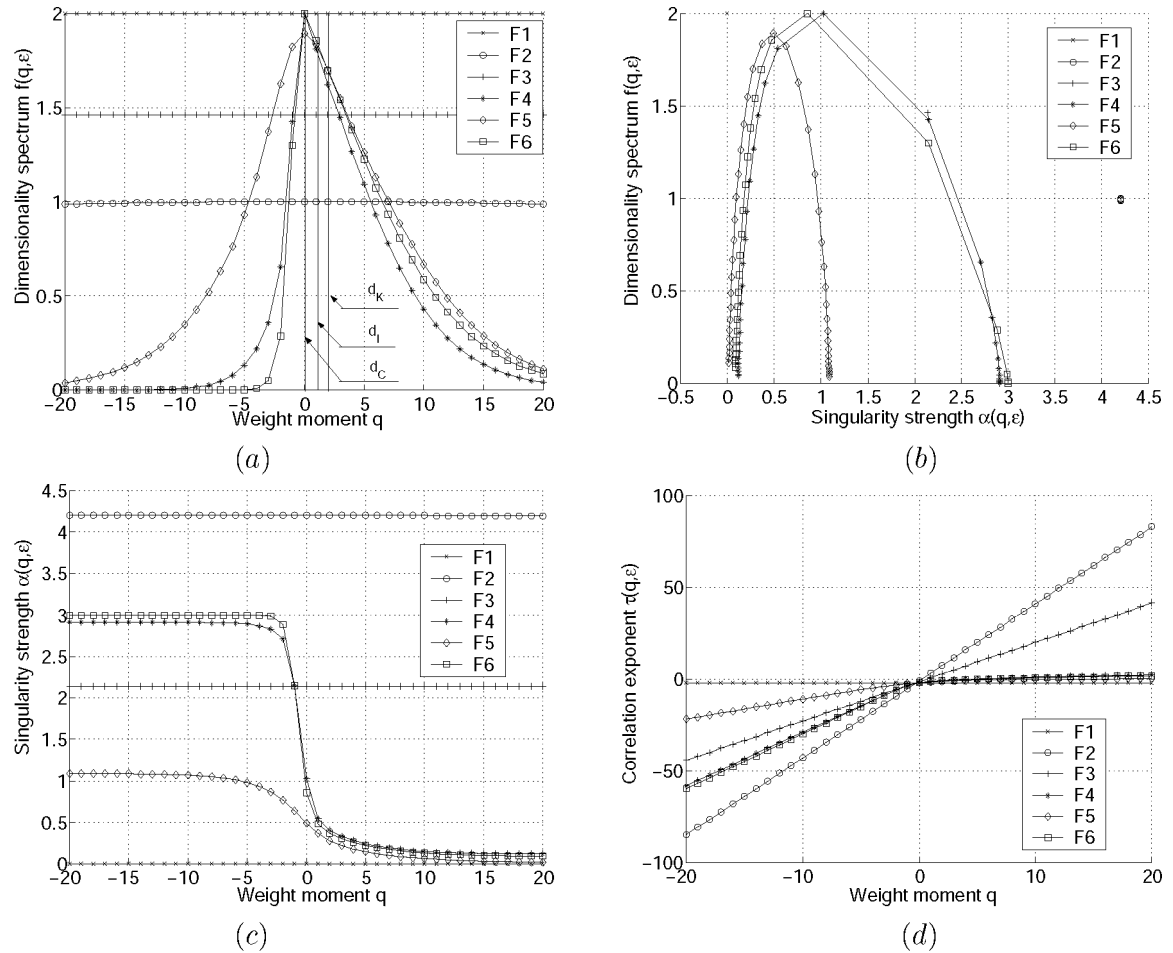


Figure A.3: (a) and (b) multifractal spectrum $f(q)$ respectively as a function of q and $\alpha(q)$, (c) singularity strength $\alpha(q)$ as a function of q and (d) mass-correlation exponent $\tau(q, \epsilon)$ as a function of q .

A.2 Classification of fractal sets

Some features of fractal sets are discussed, in a more general way, to draw a hierarchic tree of classification of fractals, starting from the large-scale down to the small-scale properties.

The fractals represented in Figure A.4 display properties which we use to draw a classification tree. Fractal *E1* in panel (a) is a classic regular (in a sense the simplest) deterministic fractal set obtained by multiplicative steps applied uniformly in space. Fractal *E2* in panel (b) is based on the Cantor set but is built by using two different scales in the initial element (Mach *et al.*, 1995). *E3* is based on the Koch curve but the building algorithm is applied non uniformly in space (Meakin, 1998). Fractal *E4* represents the strange attractor of the chaotic dynamics of the Ikeda equations (Ikeda map) (Ikeda, 1979; Ikeda *et al.*, 1980). *E5* is a random cluster obtained by Monte Carlo simulation of DLA processes (Vicsek, 1992). Finally *E6* is a 2D projection of a real mud floc, obtained by thresholding a gray-scale digital image. These all are essentially fractal sets, but each of them possesses specific properties.

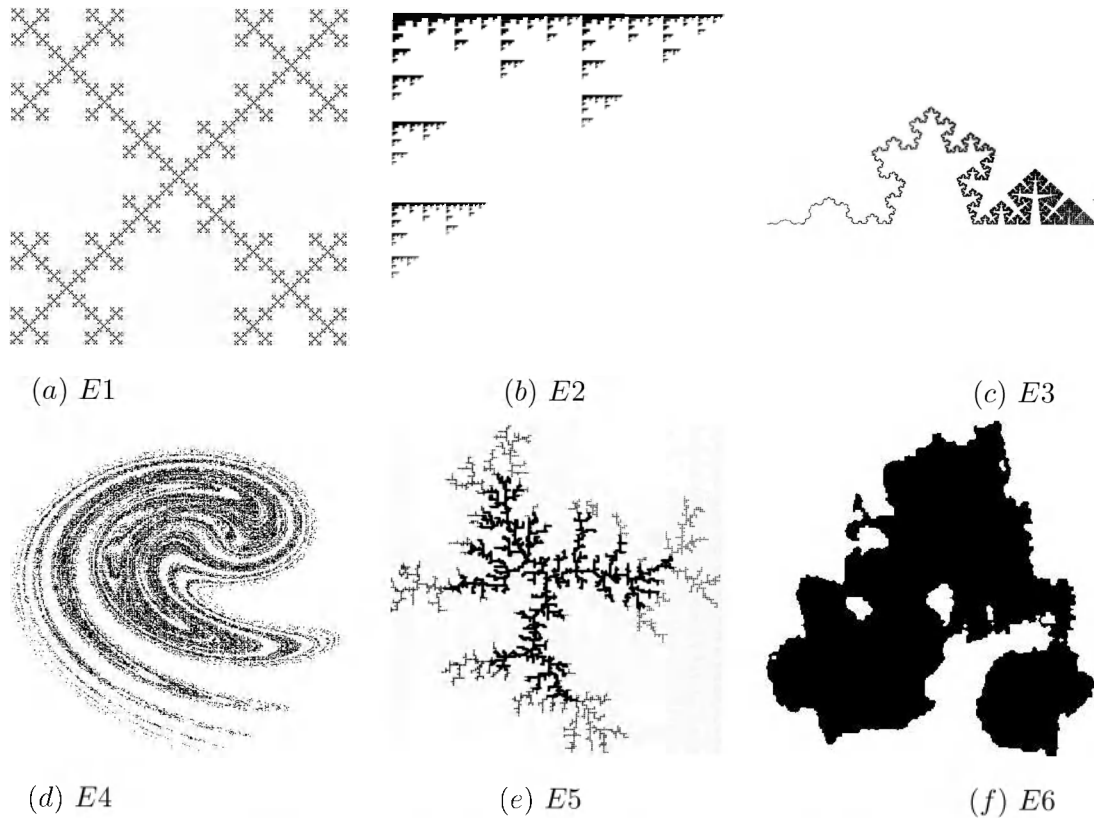


Figure A.4: Fractals used to draw a classification of properties of self-similarity, homogeneity, and mono- and multifractality.

Our classification foresees two main classes of fractals: *artificial* (ART) and *real* (REA), Fig A.5. Fractals *E1-E5* belong to ART-class while *E6* belongs to REA-class. ART-class fractals can be *deterministic* (DET) or *random* (RND). DET-class fractals are those which result from reiterative, known algorithms, or from one or more non-probabilistic equations. Computed random fractals are, instead, obtained by probabilistic equations (Monte Carlo)¹. According to this definition, fractals *E1-E4* belong to DET-class while

¹These are normally associated with real fractals but a distinction has to be made with respect to the

fractal $E5$ belongs to RND-class. The classes defined till now are not referring to the properties of the fractals but to their nature. We consider the *property* of a fractal some feature that can be measured by means of the quantity introduced in Chapter 3, especially by the multifractal spectrum. The properties that we consider in the following steps of the tree are the self-similarity, homogeneity and mono/multifractality.

Self-similarity can be full (FSS) or statistical (SSS). DET-class fractals can be both FSS and SSS. In particular, $E1$ - $E3$ belong to FSS-class, as the building algorithm makes them appear exactly identical at any scale, while fractal $E4$ belongs to SSS-class, because self-similarity is only apparent in chaotic systems. RND-class fractals can be only SSS, by construction, therefore $E5$ belongs to SSS-class. Also real fractals display self-similarity; in some cases this is full (like snow crystals), but most of the cases this is only apparent or full for small ranges of length scales. For this reason, we simply associate SSS properties to REA-class fractals, so that $E6$ belongs to SSS-class.

The second property we explore is *homogeneity*, that is whether the detail of a fractal is homogeneously distributed all over the set, or only to part of it. In this case, FSS-class fractals can be fully homogeneous (FHO) or statistically homogeneous (SHO). Fractals $E1$ and $E2$ belong to FHO-class, by construction, while $E3$ belongs to SHO-class, again by construction. In contrast, SSS-class fractals can be only SHO, as statistical self-similarity itself involves that some regions of the fractal display more detailed structure than others. Consequently $E3$ - $E6$ belong to SHO-class.

The last property is the presence of one (MNO) or more (MLT) scaling laws. FHO-class fractals, being also FSS, present only one scaling law, because they occupy their domain homogeneously and in a fully self-similar way. This means that $E1$ belongs to MNO-class. SHO-class fractals, in contrast to FHO, possess multiscaling behaviour, as $f(q)$ is non-invariant with respect to q , Section 3.2.4. Fractals $E2$ - $E6$ belong, for this reason, to MLT-class.

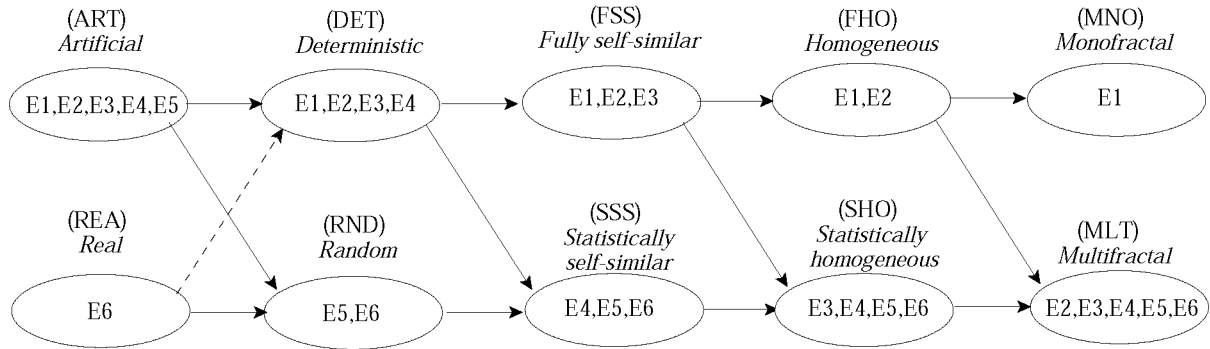


Figure A.5: Hierarchical classification of properties of self-similarity, homogeneity, and mono- and multifractality. The $E1$ - $E6$ labels refer to the sets represented in Figure A.4.

use of the terms. Real fractals often show a complex structure which is the result of a "certain amount" of determinism and a "certain amount" of randomness and for which, however, we do not know the underlying causative rules. Random number generators in digital computing are based on deterministic algorithms. Therefore, simulated random fractals cannot be considered identically to stochastic fractals, but as an approximation.

Appendix B

Detailed description of the column design: computation and experiment

B.1 Determination of the column length

The set $c = \{0.05, 0.25, 1\}$ g/l and $G = \{1, 10, 100\}$ s⁻¹ of concentrations and turbulent shear rates is considered for the numerical computation of the flocculation time scale t_f , equilibrium floc size L_e and settling velocities $w_{se}(c, G)$, Winterwerp (1998). From these quantities, the residence time $t_{rc}(c, G)$ in the column is computed and compared to t_f for establishing the column height H_c , Table B.1.

Turbulent shear rate	G [1/s]	1	1	1	10	10	10	100	100	100
Concentration	c [g/l]	0.05	0.25	1	0.05	0.25	1	0.05	0.25	1
Equilibrium floc size	L_e [m]	5.61E-05	2.65E-04	1.05E-03	2.05E-05	8.64E-05	3.34E-04	9.21E-06	3.01E-05	1.08E-04
Flocculation time	T_f [h]	95.1	19.0	4.8	9.5	1.9	0.48	1.0	0.19	0.05
Settling Velocity	w_{se} [m/s]	2.14E-04	9.54E-04	3.73E-03	8.75E-05	3.22E-04	1.20E-03	4.75E-05	1.21E-04	3.99E-04
Residence time in the column	T_{rc} [h]	5.2	1.2	0.3	12.7	3.5	0.9	23.4	9.1	2.8

Table B.1: Determination of the residence time t_{rc} of the sediment in the settling column, for a column length $H_c = 4$ m.

B.2 Determination of required amount of sediment

This computation is addressed to estimate the total dry sediment mass M_r required for our experiments and the sediment concentration c_s in the storage tank. The quantities M_r and c_s are assessed as a function of c and G :

$$M_{sc} = c \cdot V_c, \quad (\text{B.1})$$

is the suspended sediment mass within the volume V_c of the column. Given the residence time $t_{rc}(c, G)$ in Table B.1, the required sediment supply rate R_r is:

$$R_r(c, G) = \frac{M_{sc}}{t_{rc}(c, G)}, \quad (\text{B.2})$$

from which we estimate the mass $M_r(c, G)$ of dry sediment required for an experiment lasting a total time $t_{exp} = 7$ days:

$$M_r(c, G) = R_r(c, G)t_{exp}. \quad (\text{B.3})$$

Finally, the storage concentration c_s is estimated by:

$$c_s = \frac{M_r}{V_s}, \quad (\text{B.4})$$

for a storage volume $V_s = 100$ l, Table B.2.

Turbulent shear rate	G [1/s]	1	1	1	10	10	10	100	100	100
Concentration	c [g/l]	0.05	0.25	1	0.05	0.25	1	0.05	0.25	1
Suspended mass in the column	M_{sc} [g]	14.1	70.7	282.7	14.1	70.7	282.7	14.1	70.7	282.7
Residence time in the column	T_{rc} [h]	5.2	1.2	0.3	12.7	3.5	0.93	23.4	9.15	2.78
Flux	R_r [g/h]	2.72	60.70	949.18	1.11	20.46	305.19	0.60	7.73	101.55
Required sediment mass	M_r [g]	457	10198	159462	187	3437	51273	101	1298	17060
Storage concentration	c_s [g/l]	4.6	102.0	1594.6	1.9	34.4	512.7	1.0	13.0	170.6

Table B.2: Computation of the total dry sediment mass M_r for an experiment lasting $t_{exp} = 7$ days, and storage concentration c_s for a storage volume $V_s = 100$ l.

B.3 Determination of the buffer volume

The criterion to assess the buffer volume V_b is based on the acceptable level of relative disturbance in concentration $\Delta c/c_d$ due to the application of a pump flow rate $Q^* = Q + \Delta Q$ as a function of V_b , in which the disturbance in flow rate is ΔQ . The noise ΔQ is set at 0.01 and 0.1 times the flow rate $Q = 0.0845$ l/m for a duration $\Delta t = \{1, 10, 100\}$ s. The considered values of V_b are $V_b = \{0.02, 0.05, 0.1, 0.2, 0.5\}$ m³. A conceptual model of the dynamics of the buffer tank is drawn in Figure B.1. The mass and volume balance equations for the dynamics of the buffer are:

$$\begin{cases} V_b \frac{dc}{dt} = Qc_s - Qc - A_c w_{se} c, \\ \frac{dV_b}{dt} = 0, \end{cases} \quad (\text{B.5})$$

where c is the concentration, A_c is the cross-section area of the column, w_{se} the equilibrium settling velocity, and Q is the pump flow rate.

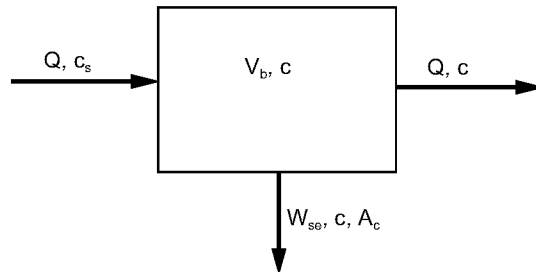


Figure B.1: Conceptual model of the buffer tank.

If we write Eq. (B.5) in a discrete form, we obtain:

$$V_b \frac{\Delta c}{\Delta t} = Q^* c_s - Q^* c_d - A_c w_{se} c_d, \quad (\text{B.6})$$

from which:

$$\frac{\Delta c}{c_d} = \frac{c^* - c_d}{c_d} = \frac{\Delta t}{V_b} \left[Q^* \left(\frac{c_s}{c_d} - 1 \right) - A_c w_{se} \right]. \quad (\text{B.7})$$

The results of the computation of $\Delta c/c_d$ are collected in the Table B.3. The volume V_b suitable with respect to space availability in the climatized room is $V_b \approx 0.1 \text{ m}^3$.

Turbulent shear rate		G [1/s]	1			10			100			
Desired concentration		c _d [kg/m ³]	0.05	0.25	1	0.05	0.25	1	0.05	0.25	1	
Equilibrium settling velocity		w _{se} [m/s]	2.14E-04	9.54E-04	3.73E-03	8.75E-05	3.22E-04	1.20E-03	4.75E-05	1.21E-04	3.99E-04	
Δt = 1 s	ΔQ/Q = 0.01	V _b [m ³]	0.02	7.56E-06	3.37E-05	1.32E-04	3.09E-06	1.14E-05	4.24E-05	1.68E-06	4.29E-06	1.41E-05
		0.05	3.03E-06	1.35E-05	5.27E-05	1.24E-06	4.55E-06	1.70E-05	6.71E-07	1.72E-06	5.64E-06	
		0.1	1.51E-06	6.74E-06	2.64E-05	6.18E-07	2.27E-06	8.48E-06	3.35E-07	8.59E-07	2.82E-06	
		0.2	7.56E-07	3.37E-06	1.32E-05	3.09E-07	1.14E-06	4.24E-06	1.68E-07	4.29E-07	1.41E-06	
		0.5	3.03E-07	1.35E-06	5.27E-06	1.24E-07	4.55E-07	1.70E-06	6.71E-08	1.72E-07	5.64E-07	
	ΔQ/Q = 0.1	V _b [m ³]	0.02	7.56E-05	3.37E-04	1.32E-03	3.09E-05	1.14E-04	4.24E-04	1.68E-05	4.29E-05	1.41E-04
		0.05	3.03E-05	1.35E-04	5.27E-04	1.24E-05	4.55E-05	1.70E-04	6.71E-06	1.72E-05	5.64E-05	
		0.1	1.51E-05	6.74E-05	2.64E-04	6.18E-06	2.27E-05	8.48E-05	3.35E-06	8.59E-06	2.82E-05	
		0.2	7.56E-06	3.37E-05	1.32E-04	3.09E-06	1.14E-05	4.24E-05	1.68E-06	4.29E-06	1.41E-05	
		0.5	3.03E-06	1.35E-05	5.27E-05	1.24E-06	4.55E-06	1.70E-05	6.71E-07	1.72E-06	5.64E-06	
Δt = 10 s	ΔQ/Q = 0.01	V _b [m ³]	0.02	7.56E-05	3.37E-04	1.32E-03	3.09E-05	1.14E-04	4.24E-04	1.68E-05	4.29E-05	1.41E-04
		0.05	3.03E-05	1.35E-04	5.27E-04	1.24E-05	4.55E-05	1.70E-04	6.71E-06	1.72E-05	5.64E-05	
		0.1	1.51E-05	6.74E-05	2.64E-04	6.18E-06	2.27E-05	8.48E-05	3.35E-06	8.59E-06	2.82E-05	
		0.2	7.56E-06	3.37E-05	1.32E-04	3.09E-06	1.14E-05	4.24E-05	1.68E-06	4.29E-06	1.41E-05	
		0.5	3.03E-06	1.35E-05	5.27E-05	1.24E-06	4.55E-06	1.70E-05	6.71E-07	1.72E-06	5.64E-06	
	ΔQ/Q = 0.1	V _b [m ³]	0.02	7.56E-04	3.37E-03	1.32E-02	3.09E-04	1.14E-03	4.24E-03	1.68E-04	4.29E-04	1.41E-03
		0.05	3.03E-04	1.35E-03	5.27E-03	1.24E-04	4.55E-04	1.70E-03	6.71E-05	1.72E-04	5.64E-04	
		0.1	1.51E-04	6.74E-04	2.64E-03	6.18E-05	2.27E-04	8.48E-04	3.35E-05	8.59E-05	2.82E-04	
		0.2	7.56E-05	3.37E-04	1.32E-03	3.09E-05	1.14E-04	4.24E-04	1.68E-05	4.29E-05	1.41E-04	
		0.5	3.03E-05	1.35E-04	5.27E-04	1.24E-05	4.55E-05	1.70E-04	6.71E-06	1.72E-05	5.64E-05	
Δt = 100 s	ΔQ/Q = 0.01	V _b [m ³]	0.02	7.56E-04	3.37E-03	1.32E-02	3.09E-04	1.14E-03	4.24E-03	1.68E-04	4.29E-04	1.41E-03
		0.05	3.03E-04	1.35E-03	5.27E-03	1.24E-04	4.55E-04	1.70E-03	6.71E-05	1.72E-04	5.64E-04	
		0.1	1.51E-04	6.74E-04	2.64E-03	6.18E-05	2.27E-04	8.48E-04	3.35E-05	8.59E-05	2.82E-04	
		0.2	7.56E-05	3.37E-04	1.32E-03	3.09E-05	1.14E-04	4.24E-04	1.68E-05	4.29E-05	1.41E-04	
		0.5	3.03E-05	1.35E-04	5.27E-04	1.24E-05	4.55E-05	1.70E-04	6.71E-06	1.72E-05	5.64E-05	
	ΔQ/Q = 0.1	V _b [m ³]	0.02	7.56E-03	3.37E-02	1.32E-01	3.09E-03	1.14E-02	4.24E-02	1.68E-03	4.29E-03	1.41E-02
		0.05	3.03E-03	1.35E-02	5.27E-02	1.24E-03	4.55E-03	1.70E-02	6.71E-04	1.72E-03	5.64E-03	
		0.1	1.51E-03	6.74E-03	2.64E-02	6.18E-04	2.27E-03	8.48E-03	3.35E-04	8.59E-04	2.82E-03	
		0.2	7.56E-04	3.37E-03	1.32E-02	3.09E-04	1.14E-03	4.24E-03	1.68E-04	4.29E-04	1.41E-03	
		0.5	3.03E-04	1.35E-03	5.27E-03	1.24E-04	4.55E-04	1.70E-03	6.71E-05	1.72E-04	5.64E-04	

Table B.3: Sensitiveness $\Delta c/c_d$ of the buffer tank.

Integrating Eq. (B.5) with respect to time, we obtain the time evolution of $c(t)$:

$$c(t) = \left(c_0 - \frac{Q \cdot c_s}{A_c w_{se} + Q} \right) \cdot e^{-\left(\frac{A_c w_{se} + Q}{V_b} \right) t} + \frac{Q \cdot c_s}{A_c w_{se} + Q}. \quad (\text{B.8})$$

where A_c , w_{se} , c_s , Q , V_s and V_b are known, while c_0 represents the concentration at time $t = 0$. Assuming $c_0 = 0$, Eq. (B.8) becomes:

$$c(t) = \frac{Q \cdot c_s}{A_c w_{se} + Q} \cdot \left[1 - e^{-\left(\frac{A_c w_{se} + Q}{V_b} \right) t} \right]. \quad (\text{B.9})$$

The transition time t_{tb} necessary for the buffer tank to reach a steady state starting from clear water can be assessed from the intercept of the slope at time $t = 0$ of the function of Eq. (B.9) with the desired concentration $c = c_d$. This formulation leads to:

$$t_{tb} = \frac{c_d}{\left| \frac{dc(t)}{dt} \right|_{t=0}} = \frac{c_d}{\left| \frac{d}{dt} \left(\frac{Q \cdot c_s}{A_c w_{se} + Q} \cdot \left[1 - e^{-\left(\frac{A_c w_{se} + Q}{V_b} \right) t} \right] \right) \right|_{t=0}} = \frac{c_d \cdot V_b}{Q \cdot c_s}, \quad (\text{B.10})$$

which depends on c_d for given V_b , Q and c_s given, Table B.4.

Concentration	c	[g/l]	0.05	0.25	1.00
Transition time in the buffer tank	T_{tb}	[h]	0.098	0.490	1.961

Table B.4: Transition time t_{tb} in the buffer tank for a storage concentration $c_s = 10 \text{ kg/m}^3$, pump capacity $Q = 1.42 \cdot 10^{-6} \text{ m}^3/\text{s}$ and $V_b = 100 \text{ l}$.

The residence time T_{rb} is defined by the ratio between the mass present in the buffer tank and mass flux leaving the buffer at equilibrium. This definition leads to the following residence time T_{rb} of sediment in the buffer tank:

$$T_{rb} = \frac{V_b c_d}{Q c_s - Q c_d} = \frac{V_b c_d}{A_c w_{se} c_d} = \frac{V_b}{V_c} t_{rc}, \quad (\text{B.11})$$

The residence time T_{rb} is computed for different concentrations c_d and turbulent shear rates G , Table B.5.

Turbulent shear rate	G	[1/s]	1	1	1	10	10	10	100	100	100
Concentration	c	[g/l]	0.05	0.25	1	0.05	0.25	1	0.05	0.25	1
Residence time in the column	T_{rc}	[h]	5.2	1.2	0.3	12.7	3.5	0.9	23.4	9.1	2.8
Residence time in the buffer tank	T_{tb}	[h]	1.8	0.4	0.1	4.5	1.2	0.3	8.3	3.2	1.0

Table B.5: Estimated residence time T_{rb} in the buffer tank for $V_c = 0.28 \text{ m}^3$ and $V_b = 0.1 \text{ m}^3$.

B.4 Experimental design of the grid

The task of the grid is to produce and control the intensity of a turbulence field by means of axial oscillations. The requirements followed to design the grid were: the grid had to be made of stainless steel and sediment should not adhere to the grid; the turbulence field should be homogeneous and isotropic.

A qualitative evaluation of the rate of oxidation of the metal and the rate of deposition of sediment particles on circular and square cross-section grid elements were carried out, showing that stainless steel was required. Next, qualitative and quantitative experiments were performed with two prototype grids in order to test their dynamical behaviour and turbulence generation. In particular, a rectangular (RG) and triangular (TG) configurations were evaluated, Figure B.2 (a) and (b). These were mounted in a dedicated setup replicating part of the column for a qualitative evaluation of turbulent diffusivity via video recordings, for which polystyrene particles ($2 \div 3 \text{ mm}$ size), sand particles ($0.1 \div 0.4 \text{ mm}$ size) and dye were used as tracers. The prototype grids were inserted in the pipe, and suspended from the top by the oscillating system and stabilised at the bottom against rotation and horizontal oscillation. These grids were 22 cm high and were oscillated with adjustable frequency and amplitude, Figure B.2 (c). This test showed that, although the residence time in the turbulence field was rather short, polystyrene and dye particles were diffused throughout the cross-section of the column within $3 \div 5 \text{ s}$. Particles injected in the core area of the grid showed a fast random diffusion, while particles injected in the neighborhoods of the column-wall were undisturbed, meaning that the grid mixed the fluid weakly in those regions.

This first set of qualitative experiments suggested some simple modifications on the configuration design. The grids RG and TG were modified by adding bars along the

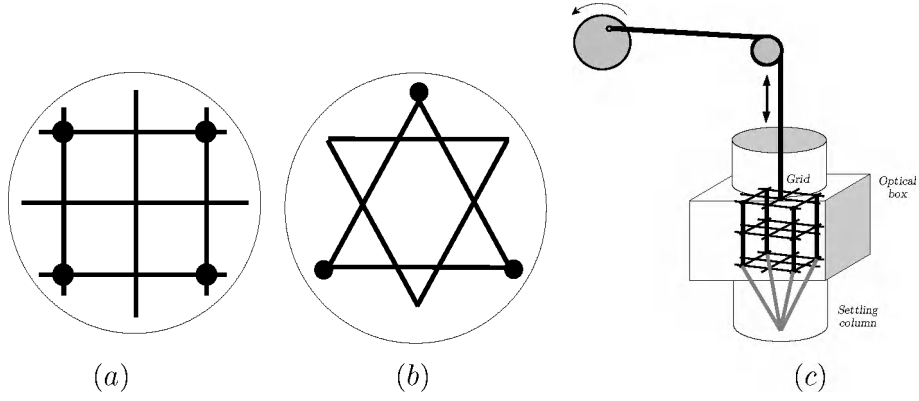


Figure B.2: (a) rectangular configuration *RG* and (b) triangular configuration *TG* tested for the turbulence generation. (c) experimental setup for the qualitative investigation of the diffusion induced by the oscillating grids.

perimeter and in the inner part with the aim of increasing the turbulence generation and reducing the wall effect in part of the settling column, Figure B.3 (a) and (b). The modifications were made only in half structure of the original grids, giving symmetry and preserving sectors of the grid with the original design. Measurements were performed by means of Laser Doppler Anemometry (LDA) to obtain a statistical characterisation of the turbulence, Figure B.3 (c). The particle velocity vectors in the x and y directions were collected at different locations ($L1$, $L2$, etc.) in both the original and modified sides of the grids. From these, the Joint Probability Functions (JPF) were computed.

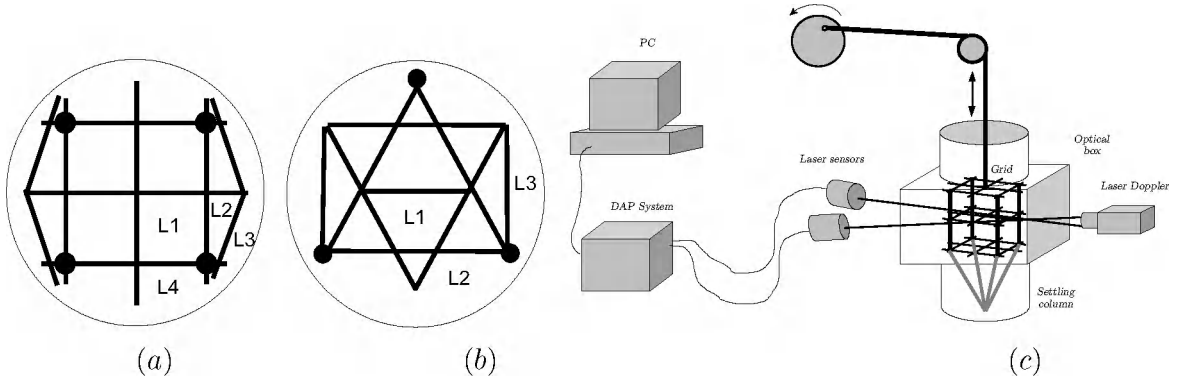


Figure B.3: (a) modified rectangular configuration *MRG* and (b) modified triangular configuration *MTG*. (c) experimental setup for the quantitative investigation of the turbulent motion induced by the oscillating grids.

The modified rectangular prototype MRG showed an appreciable isotropic turbulence field, as the JPFs at locations $L1$, $L2$ and $L3$ were pretty axisymmetric, meaning that no correlation between the x and y components exists, Figure B.4 (a)-(d). The JPF at location $L4$ shows, in contrast, a preferential pattern in the y direction due to the vicinity to the column-wall (about 1.5 cm), but no correlation is visible, meaning that mixing due to *RG* is independent from the direction. However, the variance at $L2$ and $L3$ is higher than at $L1$ and $L4$ because the mesh at these location is smaller, meaning that the turbulence is not fully homogeneous over the cross-section of the column.

The triangular prototype MTG showed a non axisymmetric isoprobability, rather different in shape from location to location, meaning that the mixing process was not uniform

within the cross-section section, Figure B.4 (e)-(g). Furthermore, at location *L1* the velocity vector appears correlated in the *x* and *y* directions. Again, the presence of the column-wall (about 1.5 cm distance) decreases the variance, giving a preferential direction to the velocity vector.

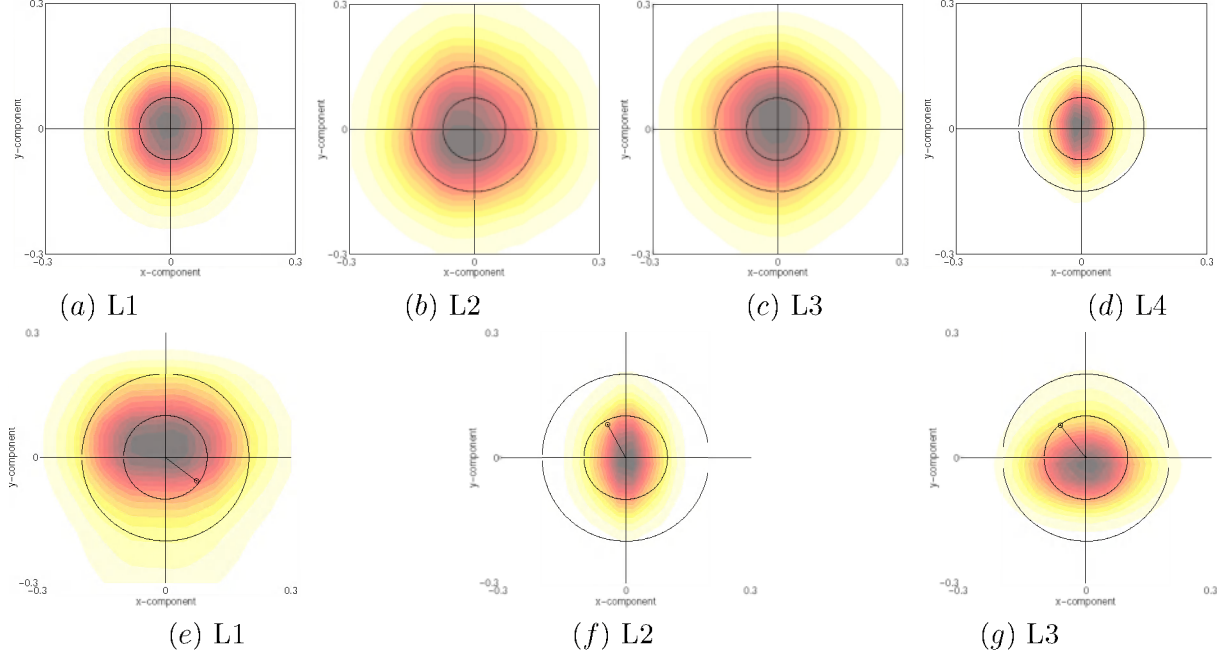


Figure B.4: (a)-(d) JPF of the fluid velocity associated with the grid MRG at the locations represented in Figure B.3 (a). (e)-(g) JPF associated with the grid MTG at the locations represented in Figure B.3 (b).

These results showed that an optimal compromise between hydrodynamical behaviour and manufacturing costs could be attained by using the rectangular grid in its simple configuration, Figure B.2 (a). In fact, the turbulence induced by this grid presented the best geometries (homogeneity and isotropy) and the configuration was much easier to manufacture than other grids. Although turbulence generated by the grid RG is spatially non-homogeneous, flocs diffuse throughout the column during their long residence time, therefore they are subject to statistically homogeneous forcing during their settling.

B.5 Calibration of the grid

The purpose of the calibration of the grid is to determine the relationship between the frequency of oscillation f_g and the rate of turbulent shear G , *i.e.* the turbulence intensity in the column. For isotropic turbulence without mean flow (Nerheim *et al.*, 2002), ε can be retrieved from the Eulerian frequency spectrum of the particle velocity (Tennekes, 1975):

$$\phi(\omega) = a'' \varepsilon^{2/3} u^{2/3} \omega^{-5/3}, \quad (\text{B.12})$$

where ϕ is the energy spectral density function, ω is the frequency, u is the r.m.s. fluctuating velocity and $a'' \approx 1$ is a constant. The 3D particle velocity vectors have been measured in the settling column around the oscillating grid at different grid frequencies f_g by means of a 3D back scatter LDA. These measurements were collected at several locations throughout the cross-section of the column, Figure B.5.

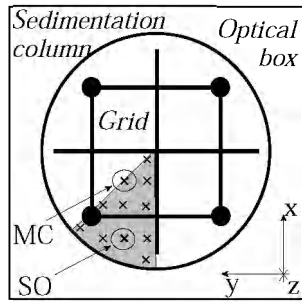


Figure B.5: Sector of the column cross-section where 3D LDA measurements were carried out. The measurements collected in the marked locations are representative for the full cross-section due to symmetry. The results in Figures B.6 are shown only as illustration for the two circled locations MC and SO.

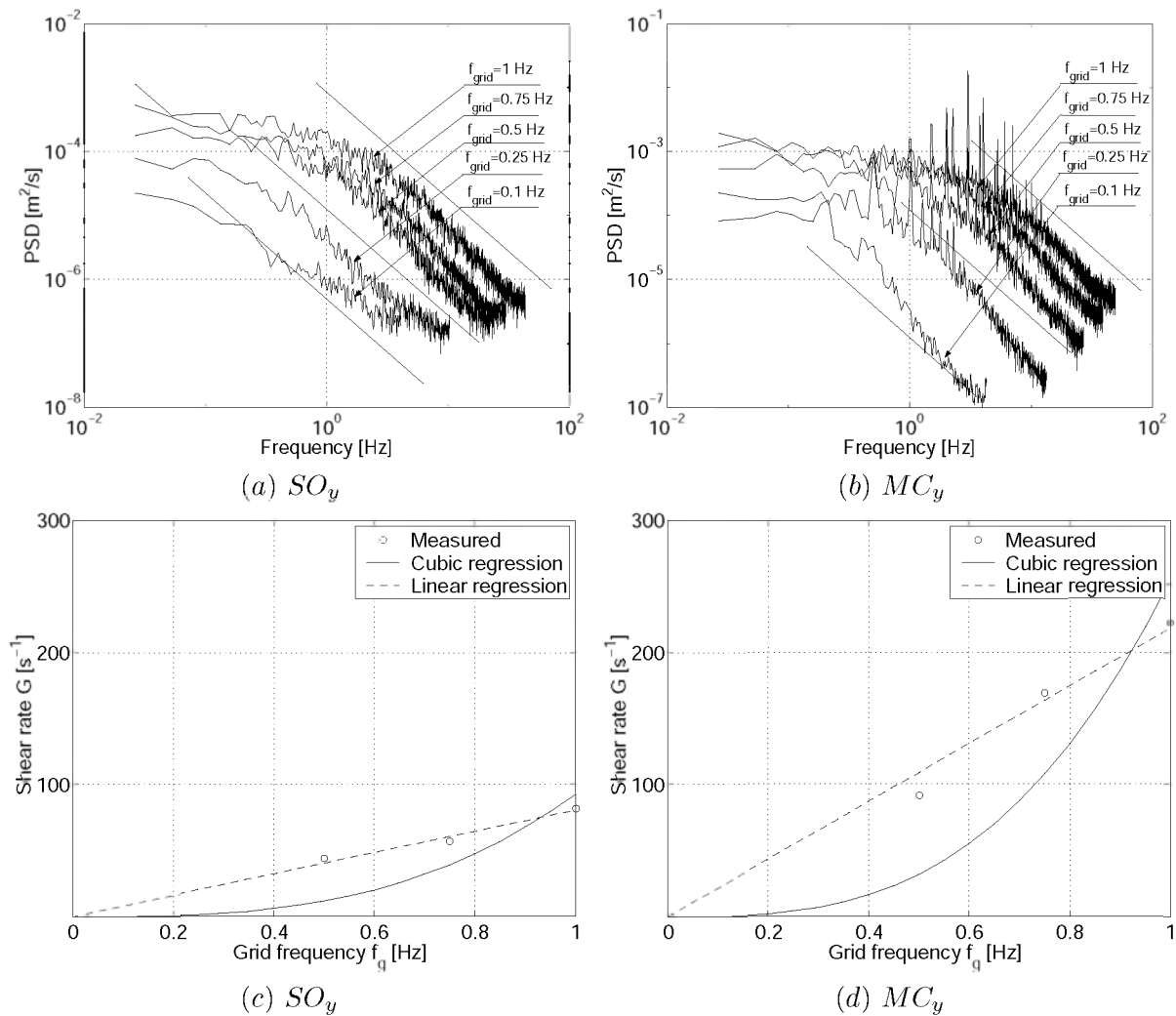


Figure B.6: (a) and (b) examples of energy spectra measured at location SO and MC. (c) and (d) estimated energy dissipation rates at locations SO and MC. Values of G at frequencies $f_g = \{0.1, 0.25\}$ Hz in (c) and (d) are not shown because the corresponding spectra do not show the typical $-5/3$ slope of turbulence. Slopes different from $-5/3$ occurred few times, especially for low f_g -values and when the measuring volume was in the inner part of the grid configuration.

Next, spectra have been computed for each direction at each location, and fitted with a regression line according to the $\omega^{-5/3}$ relationship of the inertial subrange of the spectrum of Eq. (B.12), Figure B.6 (a) and (b). From this, three values of the energy dissipation rates ε_x , ε_y and ε_z are derived. Hence, the average dissipation rate $\bar{\varepsilon} = 1/3(\varepsilon_x + \varepsilon_y + \varepsilon_z)$ was calculated at each location for the grid frequencies $f_g = \{0.1, 0.25, 0.5, 0.75, 1\}$ Hz, and the turbulent shear rate G was computed according to Eq. (2.14) for each f_g , Figure B.6 (c) and (d). The relationship between G and f_g was evaluated in the form of empirical equations in the full range $f_g \in (0, 1]$ Hz. Finally, a map of the turbulent shear rate has been drawn by interpolation, and an area-weighted average has been used to determine the shear rate in the cross-section of the column, Figure B.7 (a) and (b).

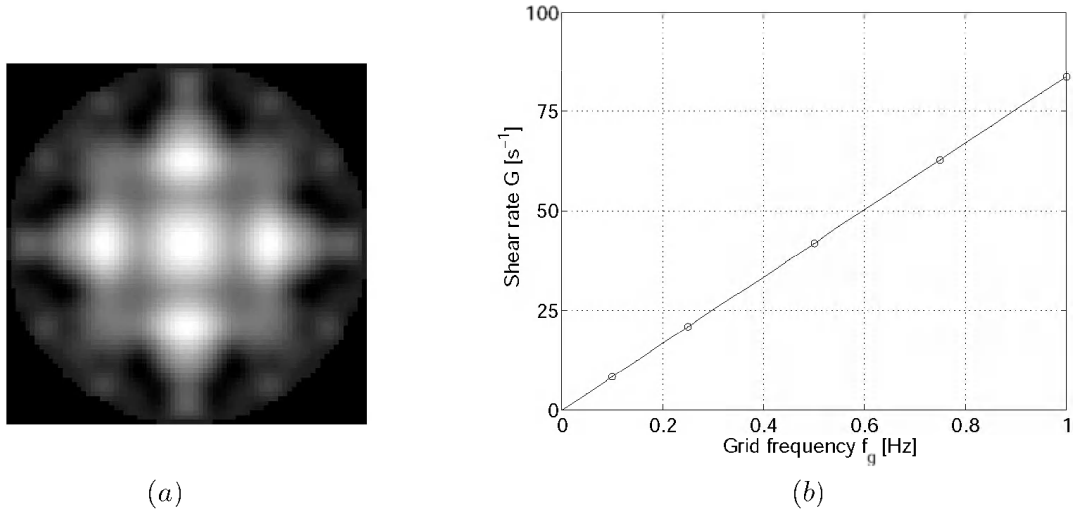


Figure B.7: (a) map of the turbulent shear rate in the cross-section of the column and (b) calibration of G versus f_g .

B.6 Recirculation velocity in the buffer tank

This experiment is aimed at evaluating sediment mixing as a function of the propeller frequency f_p . The experiment was performed by injecting sediment at concentration $c_s = 37.5$ g/l, with pump flow rate $Q_{mud} = 0.127$ l/min in fresh water for frequencies $f_p = \{0.03, 0.08, 0.14, 0.2, 0.25\}$ Hz. The concentration is measured at two locations during the injection, Figure B.8. From the travel distance $d_{s,m} = 0.4$ m between the two measuring points along an average streamline, the recirculation velocity $v_r = d_{s,m}/t_{s,m}$ was assessed, and the travel time $t_{s,m}$ was computed from the horizontal distance between linear regressions of the concentration curves. Figure B.9 (a) shows an example of the measured concentration. The data in Figure B.9 (b) show that v_r increases with f_p . The recirculation velocity v_r for the lowest propeller frequency $f_p = 0.03$ Hz causes the propagation of highly-concentrated clouds of sediment, resulting in a less homogeneous sediment distribution and in a distorted measurement of the travel time. Qualitatively, the propeller frequency $f_p = 0.1$ Hz represents a critical value below which the re-circulating flow is unstable, and above which the mixing dilutes efficiently the suspension at concentration c_s .

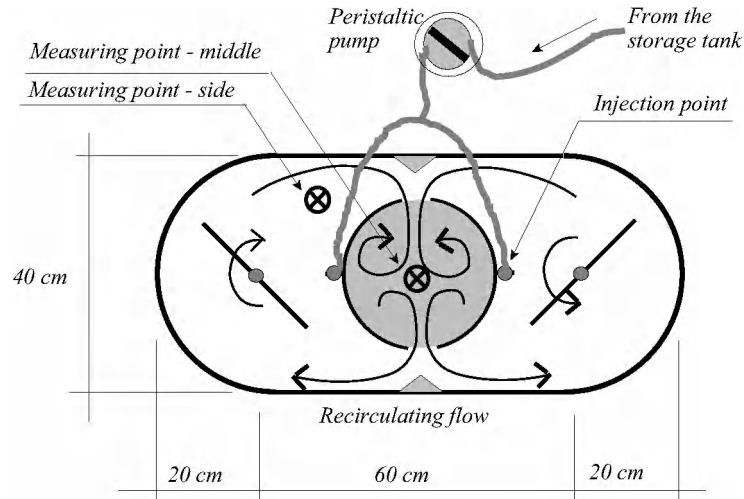


Figure B.8: Setup of the experimental measurements on the buffer tank.

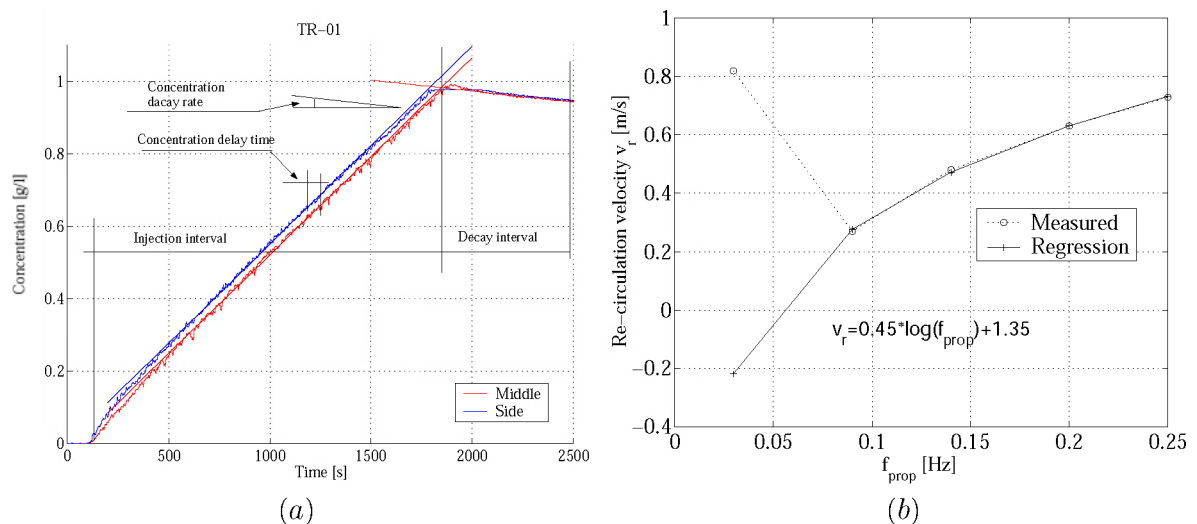


Figure B.9: (a) concentration measured in the middle and side sub-volumes of the buffer tank for $f_p = 0.03$ Hz, and (b) estimation of the travel time $t_{s,m}$.

B.7 Sediment migration from the buffer tank into the column

For this experimental session, the buffer tank was mounted on the bed section, replicating the first part of the column, but without making use of the full facility. Kaolinite was used to track the migration of sediment from the buffer tank into the column. The observations were performed by means of a transparent disk of 25 cm diameter placed about 40 cm below the entering section of the column. Kaolinite was observed to deposit upon this disk homogeneously, showing that the suspension was distributed and mixed properly, with no preferential accumulation points.

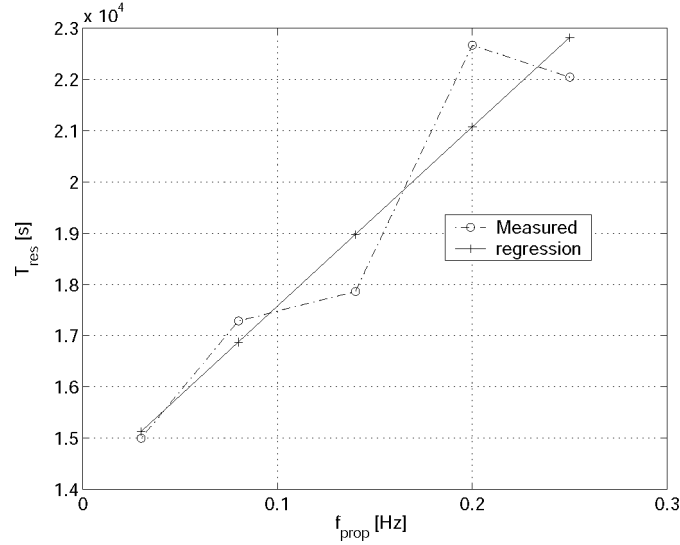


Figure B.10: Measured relaxation time in the buffer tank.

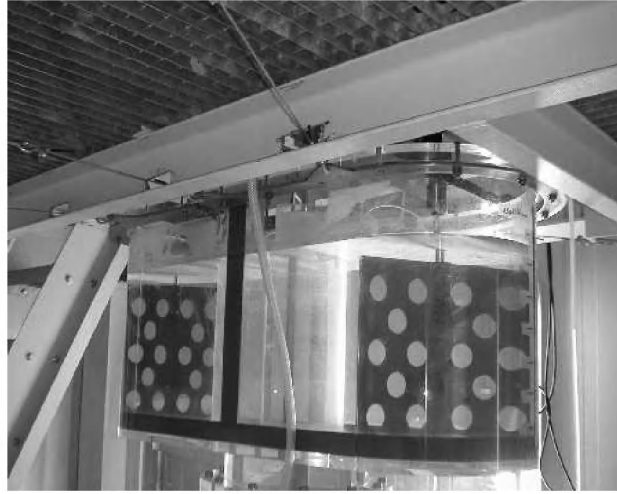
B.8 Relaxation time in the buffer tank

The configuration for this experimental session was the same as the one described in Section B.6. For this experiment, a series of pulses in the form of high rate injections of sediment at $c_s = 37.5$ g/l and $Q = 0.382$ l/min in the buffer tank was applied for a pulse duration $\Delta t = 30$ s at a concentration $c_d \simeq 0.5$ g/l in a testing volume $V_{test} = 0.15$ m³. The concentration decay was recorded in time after stopping the injection, Figure B.9, and the relaxation time t_{rbe} was derived from the intercept of the tangent of the concentration decay at time $t_0 = 0$ for each f_p . Figure B.10 shows that t_{rbe} increased for increasing propeller frequencies f_p .

B.9 Gallery



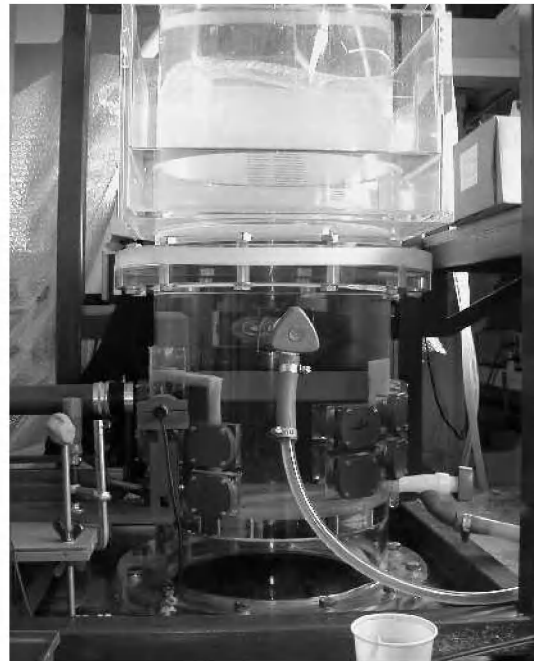
(a)



(b)



(c)



(d)

Figure B.11: (a) storage tank and driving system of the oscillating grid; (b) buffer tank; (c) settling column; (d) measuring section and PIV system.

Appendix C

Projections of compact fractal measures

Evidence of a low accuracy of Eq. (6.1) to compute the 3D capacity dimension $d_0(S_3)$ of a set S_3 from the 2D capacity dimension $d_0(S_2)$ of its projection S_2 is shown by means of correlation analysis in this Appendix. To this end, thirty artificial fractal aggregates $S_3 \subset \mathbb{N}^3$ are generated and projected to obtain the sets $S_2 \subset \mathbb{N}^2$. Next, the preservation of the information of fractality in the perimeter segmentation of the projections S_2 is discussed and an alternative semi-empirical equation to compute $d_0(S_3)$ from S_2 is proposed. Finally, the mentioned semi-empirical equation is validated to DLA and CCA aggregates.

The content of this annex is a synthesis of the works proposed in Maggi & Winterwerp (2004a), to which the reader is referred for a more detailed description.

C.1 Test set

A set of random fractal aggregates $\{S_3\} \subset \mathbb{N}^3$ are generated by means of a simple algorithm which produces self-correlated random structures with known capacity dimension d_0 . This technique is a *static* aggregation algorithm that does not account for diffusion. Starting with a single seed $i = 1$, a second seed $i = 2$ is placed randomly in one of the 3-by-3-by-3 free neighbour locations. Then, one of the existing seeds is chosen randomly from an exponential distribution, and a new seed is attached to it. In this algorithm, recent seeds (large indexes i) have higher probabilities to receive a new seed. This procedure is repeated for 1000 seeds. The capacity dimension $d_0(S_3)$ of the aggregate under construction is tuned by means of the exponent of the exponential distribution. The resulting aggregates $\{S_3\}$ have few open branches, more similar to CCA aggregates than DLA aggregates. The sets $\{S_3\}$ are afterwards projected by $\mathcal{P} : \mathbb{N}^3 \rightarrow \mathbb{N}^2$ along the three Cartesian directions to obtain the projections $\{S_{2,x}^{(j)}\}, \{S_{2,y}^{(j)}\}, \{S_{2,z}^{(j)}\}$, Figure C.1.

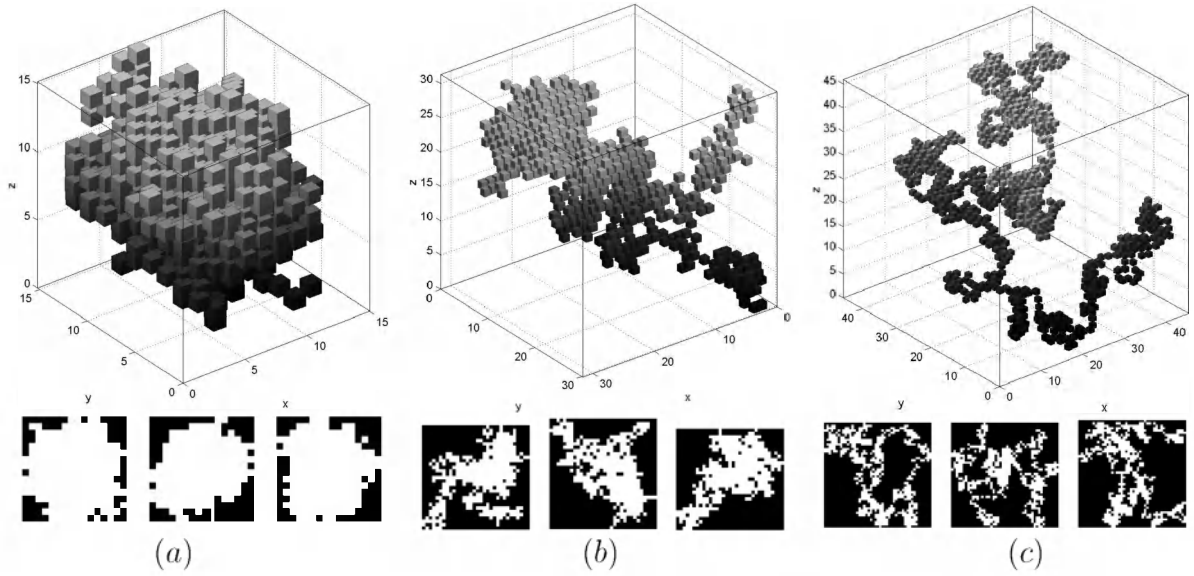


Figure C.1: (a) example of a high-dimensional ($d_0(S_3) = 2.49$) fractal aggregate with massive projections and round-shaped organisation of the primary particles. (b) example of a mid-dimensional ($d_0(S_3) = 2.09$) fractal aggregate. (c) example of a low-dimensional ($d_0(S_3) = 1.81$) fractal aggregate with porous projections and irregular-shaped organisation of the primary particles.

C.2 Correlation analysis between $d_0(S_2)$ and $d_0(S_3)$

The 2D and 3D capacity dimensions $d_0(S_2)$ and $d_0(S_3)$ are computed for each aggregate and each projection as in Eq. (3.11); then, the average 2D capacity dimensions $\overline{d_0(S_2)}$ are further computed as:

$$\overline{d_0(S_2^{(j)})} = \frac{1}{3} \left[d_0(S_{2,x}^{(j)}) + d_0(S_{2,y}^{(j)}) + d_0(S_{2,z}^{(j)}) \right]. \quad (\text{C.1})$$

The relationship between $\overline{d_0(S_2^{(j)})}$ and the known capacity dimension $d_0(S_3^{(j)})$ is given in Figure C.2, where it is shown that the numerical data deviate largely from the theoretical ones obtained from Eq. (6.1). This shows that, for non-homogeneous, finite and closed fractal aggregates, Eq. (6.1) does not enable a direct extraction of $d_0(S_3)$ from S_2 , even for $d_0(S_2) < 2$. This confirms the analytical proof in Hunt & Kaloshin (1997).

C.3 Perimeter of fractal sets

Because of the previous results, we analyse another set belonging to the projection, which appears independent or nearly independent of the transformation: the contour of the projected set S_2 . The contour is a subset of the projection S_2 whose segmentation reflects the roughness of the object in \mathbb{R}^3 , and its perimeter does not represent a capacity of S_2 . Therefore, we investigate to which extent the information of the structure in \mathbb{R}^3 can be found in the contour of the projected set S_2 . The perimeter-based fractal dimension d_P is defined as (Falconer, 1990):

$$d_P = 2 \frac{\log[P]}{\log[A]}, \quad (\text{C.2})$$

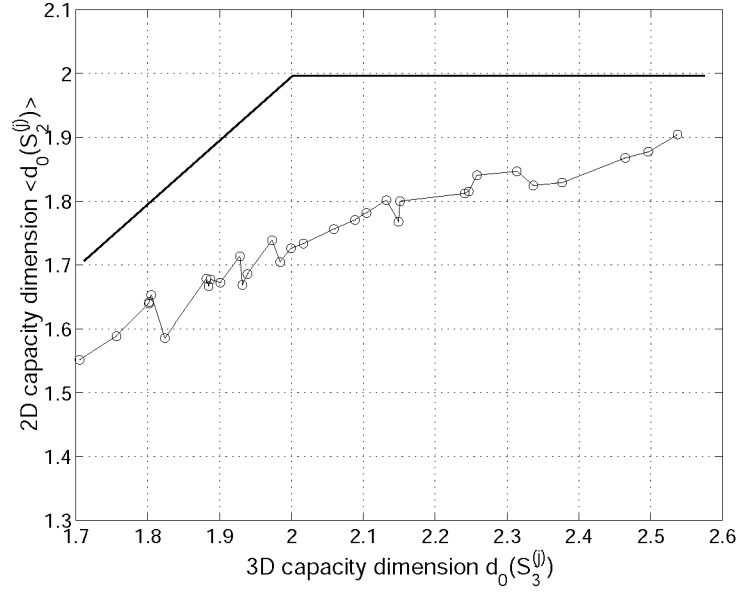


Figure C.2: Relationship between $d_0(S_2^{(j)})$ $d_0(S_3^{(j)})$ according to Eq. (6.1) (solid straight lines) and from numerical analysis.

where P and A represent the perimeter and the area of S_2 ¹. As d_P does not belong to the generalised dimensionality d_q , the theory of projection does not apply to d_P , and therefore it is not subject to the rule of Eq. (6.2). However, d_P still gives information on the fractal structures of aggregates. For this reason, and because of a lack of theoretical work dealing with this problem, we perform a simple correlation analysis between $d_0(S_3^{(j)})$ and $d_P(S_2^{(j)})$.

By means of simple geometry arguments, we compute the values of d_P for the two extreme cases of thin line and massive box projections. Consider an ω -covering of the set S_2 of size L by means of boxes of size ϵ , corresponding to a resolution $\ell = L/\epsilon$. The values of d_P depend on ℓ , as elaborated in the two following cases.

First, consider a projection which becomes a thin line for $\ell \in [1, \infty)$, Figure C.3 (a). In this case $P \equiv A = \ell$ with $\ell \in [1, \infty)$ and, using Eq. (C.2), we obtain:

$$d_P = 2 \frac{\log[P]}{\log[A]} = 2 \frac{\log[\ell]}{\log[\ell]} = 2, \quad \ell \in [1, \infty). \quad (\text{C.3})$$

Second, consider a projection consisting of a massive box for $\ell \in [1, \infty)$, Figure C.3 (b). The perimeter and area are $P = \ell$ and $A = \ell$ for $\ell = 1$, and $P = 4\ell - 4$ and $A = \ell^2$ for $\ell \in [2, \infty)$, from which we write d_P as a function of ℓ :

$$d_P(\ell) = \begin{cases} 2 \frac{\log[\ell]}{\log[\ell]} = 2 & \text{for } \ell = 1, \\ 2 \frac{\log[4\ell-4]}{\log[\ell^2]} = 2 & \text{for } \ell = 2, \\ 2 \frac{\log[4\ell-4]}{\log[\ell^2]} < 2 & \text{for } \ell \in [3, \infty), \end{cases} \quad (\text{C.4})$$

where the cases $\ell = 1$ ($\epsilon = L$) and $\ell = 2$ ($\epsilon = L/2$) represent two trivial solutions for d_P which can be referred to as a pathological effect caused by the low resolution. In contrast,

¹Within our context, A is given by the number of seeds within the projected area and P is given by the number of seeds on the contour.

for $\ell \rightarrow \infty$ ($\epsilon \rightarrow 0$) we obtain the limit:

$$\lim_{\ell \rightarrow \infty} d_P = \lim_{\ell \rightarrow \infty} \frac{\log[4\ell - 4]}{\log[\ell]} = \lim_{\ell \rightarrow \infty} \left(\frac{\log[4]}{\log[\ell]} + \frac{\log[\ell - 1]}{\log[\ell]} \right) = 1, \quad (\text{C.5})$$

which represents an asymptotic case for infinitely high resolutions of fully massive aggregates. The limiting values of d_P are then represented by $d_P = 2$ for line-like projections with $d_0(S_2) = 1$, and $d_P = 1$ for massive projections with $d_0(S_2) = 2$ and infinitely high resolution.

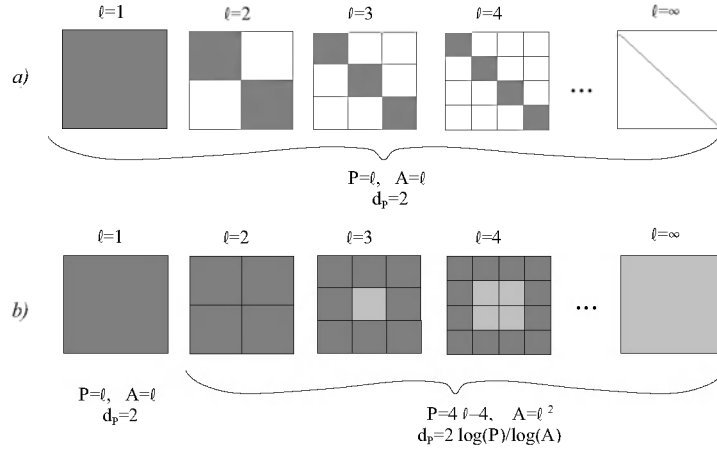


Figure C.3: Geometric representation of the limiting cases of (a) line-like projection and (b) fully massive projection, as functions of the resolution ℓ . Dark gray boxes represent regions of perimeter/area overlapping, while light gray boxes belong to the area solely.

In order to investigate how $d_P(S_2)$ relates to $d_0(S_3)$, we first normalise the projections $\{S_2\}$ with a reference resolution ℓ_r . This is performed by using a magnification factor f_m defined as:

$$f_m = \frac{\ell_r}{\ell},$$

in such a way that:

$$L_m = f_m L, \quad \forall S_2^{(j)}.$$

The average perimeter-based fractal dimension $\overline{d_P(S_2^{(j)})}$ is computed for each aggregate $S_2^{(j)}$ as follows:

$$\overline{d_P(S_2^{(j)})} = \frac{1}{3} \left[d_P(S_{2,x}^{(j)}) + d_P(S_{2,y}^{(j)}) + d_P(S_{2,z}^{(j)}) \right], \quad (\text{C.6})$$

where only the external perimeter is considered, therefore neglecting inner empties. Figure C.4 shows the relationship between $d_P(S_2)$ and $d_0(S_3)$ for $\ell_r = \{16, 256, 1024\}$ pixel. The boundary points Z at $d_0(S_3) = 3$ (massive box) are computed through Eq. (C.4):

$$Z_{16} = (3, z(\ell_r = 16)), \quad Z_{256} = (3, z(\ell_r = 256)), \quad Z_{1024} = (3, z(\ell_r = 1024)), \quad (\text{C.7})$$

where the following notation is applied:

$$z(\ell) = d_P(S_2, \ell) = \frac{\log[4\ell - 4]}{\log[\ell]}. \quad (\text{C.8})$$

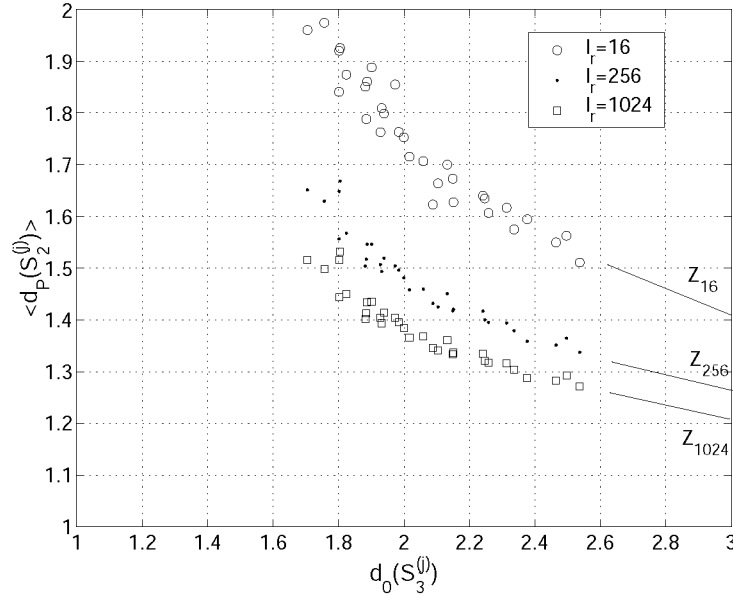


Figure C.4: Representation of the relationship between $d_0(S_3)$ and $d_P(S_2)$ from numerical results.

There are three major features that appear from the results given in Figure C.4. The first is that low-dimensional structures, with a high level of branching at the left-hand side of the plot, possess projections with high values of d_P . In contrast, high-dimensional structures, with massive and round-shaped masses at the right-hand side of the plot, have low values of d_P . The second is that $d_P(S_2)$ does not reach a constant value for $d_0(S_3) > 2$, in contrast to the rule of Eq. (6.1). Rather, a hyperbolic-like correlation does appear in the full range $1 \leq d_0(S_3) \leq 3$. The third is that low resolutions (16 pixels for instance) move the points towards the upper limit $d_P = 2$. An increase in resolution lowers the points asymptotically towards the limit $d_P = 1$, as shown in Eq. (C.5).

C.4 Semi-empirical relation for $d_P(S_2)$ and $d_0(S_3)$

By considering the fully known points Z of Eqs. (C.7) and assuming a function of the form:

$$d_P(S_2) = \frac{a}{[d_0(S_3)]^2} + b, \quad (\text{C.9})$$

we parameterise the results in Figure C.4 by solving the following system:

$$\begin{cases} z(\ell) = \frac{a}{3^2} + b & \text{at } Z = (3, z(\ell)), \\ 2 = \frac{a}{[k(\ell)]^2} + b & \text{at } K = (k(\ell), 2), \end{cases}$$

with $z(\ell)$ defined in Eq. (C.8). The coordinates $k(\ell)$ of the boundary points K at $d_P = 2$ for a given resolution ℓ have been expressed as a function of $z(\ell)$ by fitting the data points in Figure C.4 at the upper limit $d_P = 2$:

$$k(\ell) = k(z(\ell)) = z(\ell)[z(\ell) - 1] + 1. \quad (\text{C.10})$$

which results in:

$$K_{16} = (k(\ell_r = 16), 2), \quad K_{256} = (k(\ell_r = 256), 2), \quad K_{1024} = (k(\ell_r = 1024), 2). \quad (\text{C.11})$$

Hence, the coefficients a and b are:

$$a(\ell) = 9 \left(z(\ell) - \frac{2[k(\ell)]^2 - 9z(\ell)}{[k(\ell)]^2 - 9} \right), \quad b(\ell) = \frac{2[k(\ell)]^2 - 9z(\ell)}{[k(\ell)]^2 - 9}. \quad (\text{C.12})$$

Finally, Eq. (C.9) reads as a function of $d_0(S_3)$ and ℓ as follows:

$$d_P(S_2) = \begin{cases} \frac{a(\ell)}{[d_0(S_3)]^2} + b(\ell) & \text{for } d_0(S_3) > k(z(\ell)), \\ 2 & \text{for } d_0(S_3) \leq k(z(\ell)). \end{cases} \quad (\text{C.13})$$

Figure C.5 shows the numerical results (dots) and the empirical fit (solid curves) obtained from Eq. (C.13) for resolutions $\ell = \{16, 256, 1024\}$ pixels. The fit for $\ell = 16$ pixels is acceptable though not perfect ($R^2 = 0.970$). A better fit is obtained for resolutions $\ell = 256$ pixels ($R^2 = 0.975$) and for $\ell = 1024$ pixel ($R^2 = 0.973$), see Figure C.6. The appreciable alignment of the data point supports the technique here proposed. By inversion of Eq. (C.13), we write:

$$d_0(S_3) = \sqrt{\frac{a(\ell)}{d_P(S_2) - b(\ell)}} \quad \text{for } d_P(S_2) < 2, \quad (\text{C.14})$$

which gives the 3D capacity dimension of the aggregates from the perimeter-based fractal dimension of their projections and the adopted resolution.

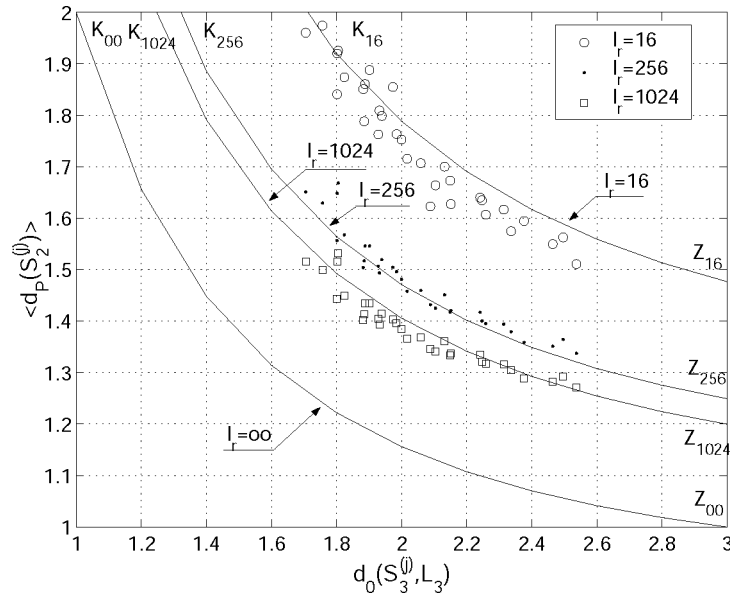


Figure C.5: Representation of the relationship between $d_0(S_3)$ and $d_P(S_2)$ from numerical results (dots) and analytical fitting (solid lines) from Eq. (C.13).

Particularly interesting is the case of infinite resolution $\ell \rightarrow \infty$, for which the coordinates $z(\ell)$ and $k(\ell)$ of the boundary points Z and K in Figure C.5 become:

$$z_\infty = \lim_{\ell \rightarrow \infty} z(\ell) = \lim_{\ell \rightarrow \infty} \frac{\log[4\ell - 4]}{\log[\ell]} = 1, \quad (\text{C.15a})$$

$$k_\infty = \lim_{\ell \rightarrow \infty} k(z(\ell)) = \lim_{\ell \rightarrow \infty} z(\ell)[z(\ell) - 1] + 1 = 1, \quad (\text{C.15b})$$

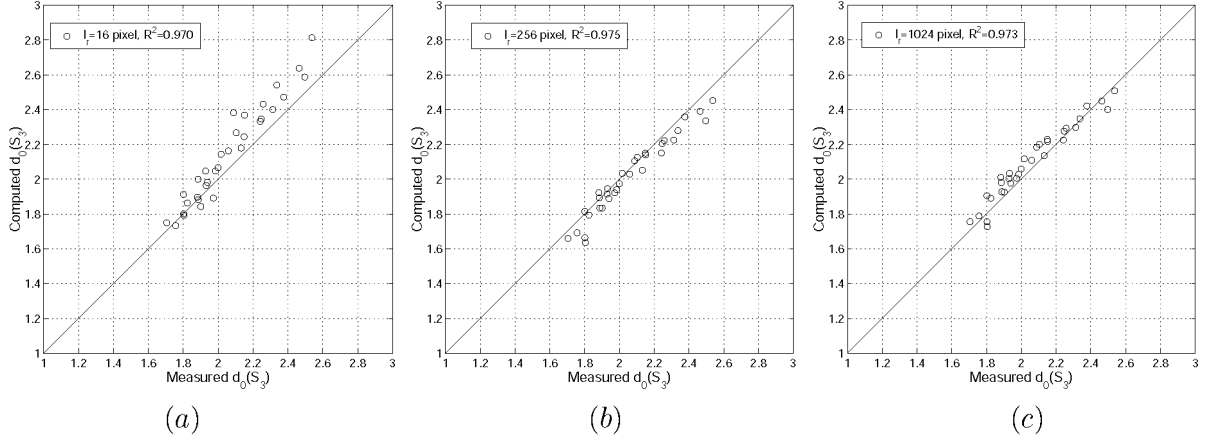


Figure C.6: Comparison of the parameterised values of $d_0(S_3)$ according to Eq. (C.14) versus the measured ones for the tested resolutions $\ell = \{16, 256, 1024\}$ pixels. Also the correlation coefficients R^2 are reported. The data points align along the bisector for exact, full correlation.

and the coefficients in Eqs. (C.12) are consequently:

$$a = \frac{9}{8}, \quad b = \frac{7}{8}. \quad (\text{C.16})$$

Eq. (C.14), in the asymptotic limit $\ell \rightarrow \infty$, is:

$$d_0(S_3) = \sqrt{\frac{9/8}{d_P(S_2)^2 - 7/8}} \quad \text{for} \quad d_P(S_2) < 2, \quad (\text{C.17})$$

that matches the theoretical points $Z = (3, z_\infty)$ and $K = (k_\infty, 2)$ in Figure C.4.

C.5 Validation to DLA and CCA aggregates

Let us consider a compact fractal aggregate S_3 of dimensionless length scale ℓ ; its volume V scales as:

$$V = \ell^{d_0(S_3)}, \quad (\text{C.18})$$

while the area A of its projection $S_2 = \mathcal{P}(S_3)$ scales as:

$$A = \ell^{d_0(S_2)}. \quad (\text{C.19})$$

Under the assumption that ℓ is the length scale for both S_2 and S_3 , the volume V must obey:

$$V \leq A \cdot \ell. \quad (\text{C.20})$$

Substituting Eqs. (C.18) and (C.19) into Eq. (C.20) we obtain $\ell^{d_0(S_3)} \leq \ell^{d_0(S_2)+1}$, which implies:

$$d_0(S_3) \leq d_0(S_2) + 1. \quad (\text{C.21})$$

If we consider a projection $\mathcal{P} : \mathbb{R}^m \rightarrow \mathbb{R}^n$ with $m > n$, then we generalise Eq. (C.21) into the following:

$$d_0(S_m) \leq d_0(S_n) + (m - n), \quad (\text{C.22})$$

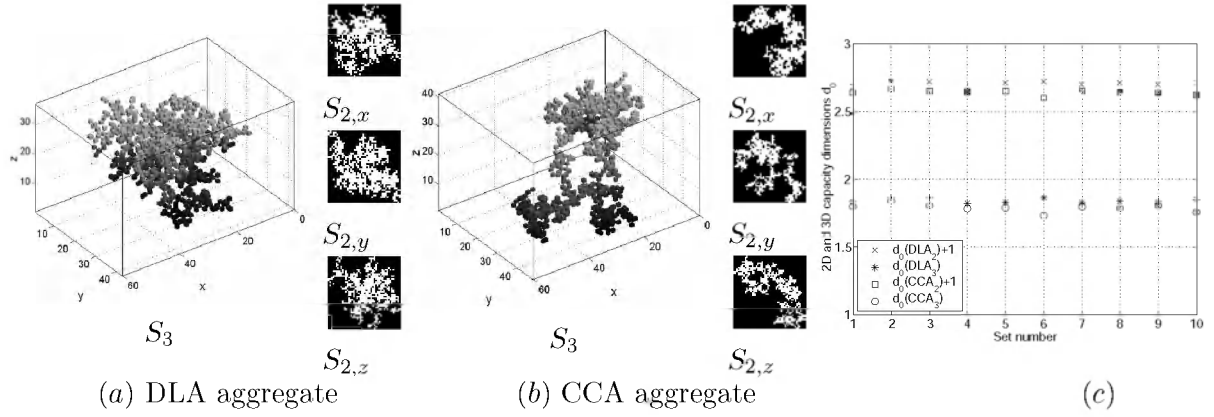


Figure C.7: (a) and (b) examples of 3D DLA and CCA aggregates; their 2D projections are given beside the 3D views. (c) comparisons between $d_0(S_2)$ and $d_0(S_3)$ for DLA and CCA aggregates, where $d_0(S_3)$ is computed as in Eq. (C.14). The data points show that the inequality in Eq. (C.23) is always satisfied.

which holds for compact sets of any embedding dimensions m and n . This inequality gives a geometrical constraint that must be satisfied by any functional relationship between $d_0(S_m)$ and $d_0(S_n)$. Note that $d_0(S_n) = d_0(S_m) - (m - n)$ represents the relationship between the n - and m -dimensional capacity dimensions of an aggregate in \mathbb{R}^m and its cross-section in \mathbb{R}^n (Vicsek, 1992).

Let us consider Eq. (C.17) for the limit case of infinite resolution $\ell \rightarrow \infty$, Section C.4. Upon substitution of Eq. (C.17) into Eq. (C.21) we obtain:

$$d_0(S_3) = \sqrt{\frac{9/8}{d_P(S_2) - 7/8}} \leq d_0(S_2) + 1, \quad (\text{C.23})$$

For fully massive projections, $d_0(S_2) = 2$ and $d_P(S_2) = 1$ (Section C.4) and Eq. (C.23) becomes:

$$\sqrt{\frac{9/8}{1 - 7/8}} = 3 \leq 3,$$

that satisfies the inequality. Analogously, $d_0(S_2) = 1$ and $d_P(S_2) = 2$ for linelike projections, and Eq. (C.23) becomes:

$$\sqrt{\frac{9/8}{2 - 7/8}} = 1 \leq 2,$$

that satisfies the inequality.

To show that the inequality in Eq. (C.23) is satisfied also for $d_0(S_2) \in (1, 2)$ and $d_P(S_2) \in (1, 2)$, a simple numerical simulation is carried out. 10 DLA clusters and 10 CCA clusters of 1000 seeds have been generated according to the algorithms in Vicsek (1992) and Meakin (1998). Next, 2D projections in the three principal directions have been computed similarly to Section C.1; two examples of these aggregates are shown in Figure C.7 (a) and (b).

From these the average $\overline{d_P(S_2)}$ and $\overline{d_0(S_2)}$ are calculated, and used in Eq. (C.23). The results in Figure C.7 (c) show that the inequality in Eq. (C.23) is always satisfied for both DLA and CCA aggregates.

The rationale to use DLA and CCA aggregates is threefold. First, the original derivation of Eq. (C.14) was based on artificial aggregates produced by means of the algorithm described in Section C.1, without considering particle diffusion. Second, DLA and CCA processes (and their combination) are recognised as representative of particle-particle aggregation in colloidal and cohesive suspensions, therefore it is significant to validate Eq. (C.14) on these types of sets. Third, DLA and CCA processes produce aggregates with outlook rather different from one another: for instance, DLA aggregates are featured by radial development of stellar-like branchings, while CCA aggregates display clustered masses connected by bridges, forming (sometimes) closed rings. Fully developed DLA and CCA aggregates usually have different capacity dimensions in \mathbb{R}^3 , $d_0(\text{DLA}_3) \approx 2.5$ and $d_0(\text{CCA}_3) \approx 1.8$ respectively (Vicsek, 1992). However, projections $\mathcal{P} : \mathbb{R}^3 \rightarrow \mathbb{R}^2$ of those aggregates may have similar capacity dimensions $d_0(\mathcal{P}(\text{DLA}_3)) \approx d_0(\mathcal{P}(\text{CCA}_3))$ in \mathbb{R}^2 . This may not allow to discern DLA and CCA aggregates from the capacity of their projections. In contrast, the perimeter-based fractal dimension d_P , being representative of the perimeter segmentation of S_2 rather than its capacity, allows reconstruction of $d_0(S_3)$. A conceptual example is given in Figure C.8, where the two sets B and C have $d_0(B) \equiv d_0(C)$, but such that $d_P(B) \neq d_P(C)$.

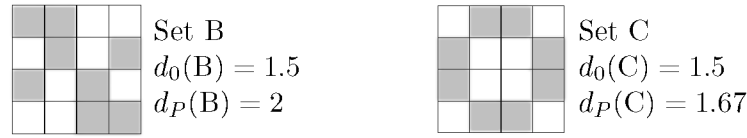


Figure C.8: Examples of sets with identical d_0 and different d_P . Computation of d_P has been done neglecting the inner voids.

The estimated values of $d_0(S_3)$ from $d_P(S_2)$ by means of Eq. (C.14) are shown in Figure C.9 together with those estimated via Eq. (6.1), the latter ones showing a lower accuracy.

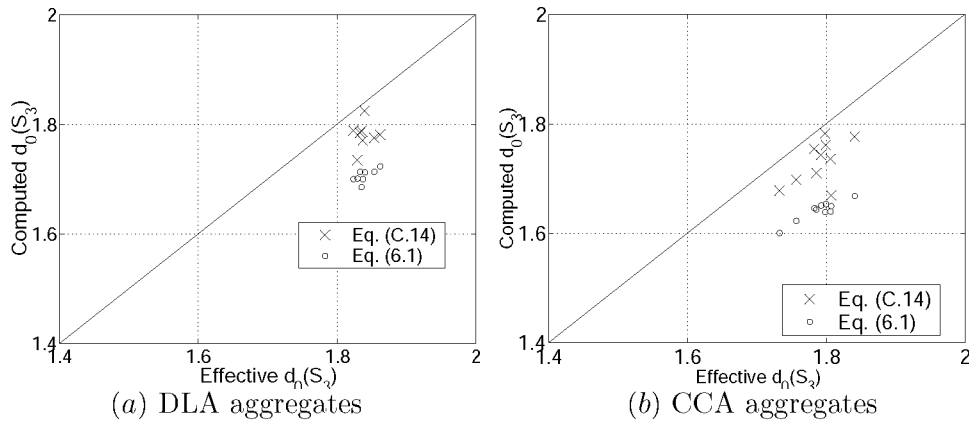


Figure C.9: Comparison between $d_0(S_3)$ evaluated from Eq. (6.1) and Eq. (C.14) for DLA and CCA aggregates.

Bibliography

- Amitrano C. and Coniglio A. (1986). Growth probability distribution in kinetic processes. *Physical Review Letters* 57(8), 1016-1019.
- Ahluwalia R., and Ananthakrishna G. (2001). Power-law statistics for avalanches in a martensitic Transformation. *Physical Review Letters* 86(18), 4076-4079.
- Argyris J., Faust G. and Haase M. (1994). *An exploration of chaos*. John Argyris F.R.S, North-Holland, Amsterdam.
- Auger G. (2004). *The settling column and application to observe flocculation process*. MSc-Thesis, Delft University of Technology, Delft.
- Bache D.H. and Rasool E. (1996). Measurement of the rate of energy dissipation around an oscillating grid by an energy balance approach. *Chemical Engineering Journal* 63, 105-115.
- Badii R. and Politi A. (1997). *Complexity; hierarchical structures and scaling in physics*, Cambridge University Press, Cambridge, UK.
- Balatoni J. and Rényi A. (1956). Remarks on entropy, *Mathematics Institute of the Hungarian Academy of Science* 9, 9-40.
- Bak P., Tang C. and Wiesenfeld K. (1987). Self-organised criticality: An explanation of $1/f$ noise. *Physical Review Letters* 59(4), 381-384.
- Bak P. (1990). Self-organised criticality. *Physica A*(163), 403-409.
- Bak P. (1996). *How nature works; the science of self-organized criticality*. Copernicus Ed, New York.
- Broadway J.D. (1978). Dynamics of growth and breakage of alum floc in presence of fluid shear. *Journal of the Environmental Engineering Division* EE5, 901-915.
- Buchholtz V. and Pöschel T. (1996). Avalanche statistics of sand heaps. *Journal of Statistical Physics* 84, 1373.
- Cai J. and Liu Z.Q. (1998). Thresholding algorithm based on all-pole model. Int. Conf. on Pattern Recognition ICPR98, Australia, 34-36.
- Capra F. (1996). *La rete della vita*. Italian translation (1998), Sansoni Ed., Milano.
- Carlotto M.J. (1997). Histogram analysis using a scale-space approach. *IEEE Trans Pattern Analysis and Machine Intelligence*, PAMI-9, 121-129.
- Casartelli M. and Zerbini M. (2000). Metric features of self-organized criticality states in sandpile models. *Journal of Physics A*(33), 863-872.
- Chakraborti R.K., Gardner K.H., Atkinson J.F. and Benschoten J.E. van (2003). Changes in fractal dimension during aggregation. *Water Research* 37, 873-883.
- Chhabra A. and Jensen R.V. (1989) Direct determination of the $f(\alpha)$ singularity spectrum. *Physical Review Letters* 62(12), 1327-1330.
- Clercx H.J.H. and Schram P.P.J.M (1992). Three particle interactions in suspensions. *Journal of Chemical Physics* 96(4), 3137-3151.
- Collier J.D. and Hooker C.A. (1999). Complexly organised dynamical systems. *Open Systems and Information Dynamics* 6, 241-302.
- De Boer D.H., Stone M. and Lévesque L.M.J. (2000) Fractal dimensions of individual flocs and floc population in streams. *Hydrological Processes* 14, 653-667.

- Dincer I. and Cengel Y.A. (2001). Energy, Entropy and Exergy Concepts and Their Roles in Thermal Engineering. *Entropy* 3, 116-149.
- Dyer K.R. (1989). Sediment processes in estuaries: future research requirements. *Journal of Geophysical Research* 94(c10)-14, 327-332.
- Dobbins W.E. (1944). Effect of Turbulence on Sedimentation, *ASCE Transactions* 109(Paper No. 2218), 629-656.
- Falconer K. (1990). *Fractal geometry; mathematical foundations and applications*. Wiler, Chichester.
- Farley K.J. and Morel F.M.M. (1986). Role of coagulation in the kinetics of sedimentation. *Environmental Science and Technology* 20, 187-195.
- Flesch J.C., Spicer P.T. and Pratsinis S.E. (1999). Laminar and Turbulent Shear-Induced Flocculation of Fractal Aggregates. *American Institute of Chemical Engineers* 45(5), 1114-1124.
- Friedlander S.K (1957). Mass and heat transfer to single spheres and cylinders at low Reynolds number. *American Institute of Chemical Engineers* 3, 43-48.
- Friedlander S.K (1965). The similarity theory of the particle size distribution of the atmospheric aerosols. In: *Aerosols, physical chemistry and application*. K. Spurny Editor, Czechoslovakian Academy of Science, Prague, 115-130.
- Friedlander S.K (1977). *Smoke, Dust and Haze, fundamentals of aerosol behavior*. Wiler, New York.
- Gardner K.H., Theis T.L. and Young T.C. (1998). Colloid aggregation: numerical solution and measurements. *Colloids and Surfaces A* 141, 237-252.
- Gleiser M. and Howell R.C. (2003). Resonant emergence of global and local spatiotemporal order in a nonlinear field model. *Physical Review E* 68, 065203-1.
- Gmachowski L. (1996). Hydrodynamics of Aggregated Media, *Journal of Colloidal and Interface Science* 178(1), 88-86.
- Grassberger P. and Procaccia I. (1983). Characterization of strange attractors. *Physical Review Letters* 50(5), 346-349.
- Guo R. and Pandit S.M. (1998). Automatic threshold selection based on histogram modes and a discriminant criterion. *Machine Vision and Applications* 10, 331-338.
- Gutenberg N. and Richter C.F. (1949). *Seismic of the Earth*. Princeton University Press, Princeton, NJ.
- Halsey T.C., Meakin P. and Procaccia I. (1986a). Scaling structure of the surface layer of Diffusion-Limited Aggregates. *Physical Review Letters* 56(8), 854-857.
- Halsey T.C., Jensen M.H., Kadanoff L.P., Procaccia I. and Shraiman B.I. (1986b). Fractal measures and their singularities: The characterization of strange sets. *Physical Review Letters* 33(2), 1141-1151.
- Hamaker H.C. (1937). The London-van der Waals' attraction between spheroid particles. *Physica* 4, 1058.
- Hentschel H.G.E. and Procaccia I. (1983). The infinite number of generalized dimensions of fractals and strange attractors. *Physica* 8(D), 435-444.
- Hentschel H.G.E., Popescu M.N. and Family F. (2004). Diffusion-limited aggregation with power-law pinning. *Physical Review E* 69, 011403-1.
- Hermanowicz S.W. (2004). Energy and Entropy: Towards the Definition of Physical Sustainability. Submitted to *Environmental Science and Technology*.
- Higashitani K and Iimura K. (1998). Two-dimensional simulation of the breakup Process of Aggregation in Shear and Elongational Flows. *Journal of Colloid and Interface Science* 204, 320-327.

- Higashitani K, Iimura K. and Sanda H. (2001). Simulation of deformation and breakup of large aggregates in flows of viscous fluids. *Chemical Engineering Science* 56, 2927-2938.
- Hunt J.R. (1980). Prediction of Oceanic Particle size distribution from coagulation and sedimentation mechanisms. *Advances in Chemistry* 189 - *Particle in Water*, M.D. Kavanaugh and J.T. Kieke Editors, *American Chemical Society*, 243-257.
- Hunt B.R. and Kaloshin V.Y. (1997). How projections affect the dimension spectrum of fractal measures. *Nonlinearity* 10, 1031-1046.
- Ikeda K. (1979). Multiple-valued stationary state and its instability of the transmitted light by a ring cavity system. *Optics Communications* 30(2), 257-261.
- Ikeda K., Daido H. and Akimoto O. (1980). Optical turbulence: Chaotic Behavior of Transmitted Light from a Ring Cavity. *Physical Review Letters* 45(9), 709-712.
- Jeffrey D.J. (1982). Aggregation and break-up of clay flocs in turbulent flow. *Advances in Colloid and Interface Science* 17, 213-218.
- Jouan R. (2004). *The settling column*, Msc-Thesis Delft University of Technology.
- Kay J. (2002). On Complexity Theory, Exergy and Industrial Ecology: Some Implications for Construction Ecology. In Kibert C. Sendzimir J. Editors, Guy B., *Construction Ecology: Nature as a Basis for Green Buildings*, Spon Press, 72-107.
- Kramer E.M. and Lobkovsky A.E. (1996). Universal power law in the noise from crumpled elastic sheet. *Physical Review E* 53(2), 1465-1469.
- Kranenburg C. (1994). On the fractal structure of cohesive sediment aggregates. *Continental and Shelf Science* 39, 451-460.
- Krishnappan B.C. (1989). Modelling of settling and flocculation of fine sediments in still water. *Canadian Journal of Civil Engineering* 17, 763-770.
- Krishnappan B.C. (1991). Modelling of cohesive sediment transport. International symposium on "The transport of suspended sediments and its mathematical modelling", Florence, Italy.
- Krone R.B. (1963). A study of rheologic properties of estuarial sediments. Tech. Bul. 7, *USAE Comm. on Tidal Hydr.*, Vicksburg, MS.
- Lee S.-I, Seo I.-S, Koopman B. (1997). Effect of mean velocity gradient and mixing time on particle removal in seawater induced flocculation. *Water, Air and Soil Pollution* 78, 179-188.
- Lehtinen K.E.J. and Zachariah M.R. (2001). Self-preserving theory for the volume distribution of particles undergoing Brownian coagulation. *Journal of Colloid and Interface Science* 242, 314-318.
- Lick W. and Lick J. (1988). On the aggregation and disaggregation of fine-grained sediments. *Journal of Great Lakes Research* 14(4), 514-523.
- Lick W., Huang H. and Jepsen R. (1993). Flocculation of Fine-Grained Sediments due to Differential Settling. *Journal of Geophysical Research* 98(C6)-10, 279-288.
- Mach J., Mas F. and Sagues F. (1995). Two representations in multifractal analysis, *Journal of Physics* 28, 5607-5622.
- Maggi F. (2002). *Flocculation of cohesive sediment: literature survey*. Report No. 1-02, Delft University of Technology.
- Maggi F. (2002). *Survey of the numerical characterisation of 2-D complex clusters*. Report No. 4-02, Delft University of Technology.
- Maggi F., Winterwerp J.C., Fontijn H.L., van Kesteren W.G.M. and Cornelisse J.M. (2002). A settling column for turbulence-induced flocculation of cohesive sediments. *Proceedings of HMEM2002 Conference*, Estes Park, Colorado, CO.
- Maggi F. and Winterwerp J.C. (2003). Mud flocs - Part 1 - Efficient thresholding method for image analysis. *Journal of Hydrology*, accepted for publication.
- Maggi F., Manning A.J. and Winterwerp J.C. (2003). Mud flocs - Part 2 - On the characterisation of floc geometry and floc dynamics. *Journal of Hydrology*, accepted for publication.

- Maggi F. and Winterwerp J.C. (2003). An experimental study into the evolution of the size distribution of kaolinite flocs. Proceedings of the 7th INTERCOH conference, Gloucester Point, VA, USA.
- Maggi F. and Winterwerp J.C. (2004). Method for computing the three-dimensional capacity dimension from two-dimensional projections of fractal aggregates. *Physical Review E* 69, 011405.
- Maggi F. and Winterwerp J.C. (2004). Geometric characterisation of kaolinite flocs. Proceedings of the 9th International Symposium on River Sedimentation (ISRS), Yichang, China.
- Manning A.J. and Dyer K.R. (1999). Observation of the size, settling velocity and effective density of flocs and their fractal dimension. *Journal of Sea Research* 41, 87-95.
- Manning A.J. and Dyer K.R. (2002). The use of optics for the in situ determination of flocculated mud characteristics. *Journal of Optics A* 4, S71-S81.
- McAnally W. (1999). *Aggregation and deposition of estuarine fine sediment*. Ph.D. Thesis, University of Florida, FL.
- Maturana H.R. and Varela F.J. (1972). *Autopoiesis and cognition*. Cohen R.S. and Wartofsky M.W. Editors, Dordrecht, Holland.
- McCave I.N. (1984). Size spectra and aggregation of suspended particles in the deep ocean. *Deep-Sea Research* 31(4), 329-352.
- Meakin P. (1998). *Fractals, Scaling and Growth Far From Equilibrium*. Cambridge University Press, Cambridge.
- Mehta A.J. (1991). Review notes on cohesive sediments erosion. *Coastal Sediments*, Kraus N.C., Gingerich K.J., Kriebel D.L. Editors, ASCE, 40-53.
- Mehta A.J. and Partheniades E. (1975). An investigation of the depositional properties of flocculates fine sediments. *Journal of Hydraulic Research* 13(4), 361-381.
- Mietta F. (2004). *A new population balance equation for aggregation and breakup of suspended cohesive sediment flocs*. Msc-thesis, Delft University of Technology, Delft, Netherlands, and Politecnico di Milano, Milano, Italy.
- Mikes D., Verney R., Lafite R., Belorgey M. (2002). Controlling factors in estuarine flocculation processes. Experimental results with material from the Seine Estuary. *Journal of Coastal Research* SI 41, 82-89.
- Nerheim S., Stiansen J.E. and Svendsen H. (2002). Grid-generated turbulence in a mesocosm experiment. *Hydrobiologia* 484, 61-74.
- Nicolis G. and Prigogine I. (1974). *Self-organisation in non equilibrium systems*. Wiley J. and Sons Edit.
- Novak M.M. (2004). *Paradigms of complexity: fractals and structures in the sciences*. Singapore, World Scientific.
- Olami Z., Feder H.J.S. and Christensen K. (1992). Self-organized criticality in a continuous, nonconservative cellular automaton modeling earthquakes. *Physical Review Letters* 68, 1244-1247.
- Oles V. (1992). Shear-induced aggregation and breakup of polystyrene latex particles. *Journal of Colloid Interface Science* 154, 351.
- Olivo J.C. (1994). Automatic threshold selection using the wavelet transform. *Graphical Models and Image Processing* 56, 205-218.
- O'Melia C. (1980). Aquasols: the behaviour of small particles in aquatic systems. *ES&T* 14(9), 1052-1060.
- O'Melia C. (1986). The influence of coagulation and sedimentation on the fate of particles, associated pollutants, and nutrients in lakes. *Chemical proceeding*, 207-224.
- Pandya J.D. and Spielman L.A. (1982). Floc breakup in turbulent flocculation processes. *Journal of Colloid Interface Science* (90), 517-531.

- Parker D.S., ASCE A.M., Kaufman W.J., ASCE M., Jemkins D. (1972). Floc breakup in turbulent flocculation processes. *Journal of Sanitary Engineering Division* SA 1, 79-99.
- Partheniades E. (1971). Erosion and deposition of cohesive sediments. *River Mechanics* CO, 25.1-25.91.
- Pietronero L. (1990). Theory of fractal growth. *Physica A* 163, 316-324.
- Press W.H. (1999). *Numerical Recipes in Fortran 77*. Cambridge University Press, Cambridge, UK.
- Pruppacher H.R. and Klett J.D. (1978). The microphysics of clouds and precipitation. Riedel, Dordrecht.
- Rahmani N.H.G., Dabros T. and Masliyah J.H. (2004). Evolution of asphaltene floc size distribution in organic solvents under shear. *Chemical Engineering Science* 59, 685-697.
- Ramesh N., Yoo J.H. and Sethi I.K. (1995). Thresholding based on histogram approximation. *IEEE Trans System, Man and IEEE Proc. Vis. Image, Signal Proc.* 142(5), 271-279.
- Rouse H. (1938). Experiments on the mechanics of sediment suspension. *Proceedings of the 5th. Intern. Cong. For Applied Mech.*, 550-554.
- Rosenfeld A. and De la Torre P. (1983). Histogram concavity analysis as an aid in threshold selection. *IEEE Trans System, Man and Cybernetics* SMC-13, 231-235.
- Saffman P.G. and Turner J.S. (1956). On the collision of drops in turbulent clouds. *Journal of Fluid Mechanics* 1, 16-30.
- Sánchez N., Alfaro E.J. and Perez E. (2005). The fractal dimension of projected clouds. *The Astrophysical Journal* 625, 849-856.
- Schumann T.E.W. (1940). Theoretical aspects of the size distribution of fog droplets. *Quart. J. Roy. Meteor Soc.* 66, 195-207.
- Serra T. and Casamitjana X. (1998a). Effect of the Shear and Volume Fraction on the Aggregation and Break-up of particle. *American Institute of Chemical Engineers* 44(8), 1724-1730.
- Serra T. and Casamitjana X. (1998b). Structure of the Aggregates During the Process of Aggregation and Break-up Under a Shear Flow. *Journal of Colloid and Interface Science* 206, 505-511.
- Sezan M.I. (1985). A peak detection algorithm and its application to histogram-based image data reduction. *Graphical Models and Image Processing* 29, 47-59.
- Shannon C. (1948). *Bell Systems Tech. J.* 27, 379-423; 27, 623-656.
- Shiner J.S. (2000). Self-organized criticality: self-organized complexity? The disorder and "simple complexities" of power law distributions. *Open Systems and Information Dynamics* 7, 131-137.
- Smoluchowsky M. (1917). Versuch einer Mathematischen Theorie der Koagulations-kinetik Kolloid Lösungen. *Zeitschrift für Physikalische Chemie* 92, 129-168 (Leipzig, in German).
- Snyder R.E. and Ball R.C. (1994). Self-organized criticality in computer models of settling powders. *Physical Review E* 49(1), 104-109.
- Spicer P.T. and Pratsinis S.E. (1996). Coagulation and fragmentation: Universal steady-state particle-size distribution. *American Institute of Chemical Engineers* 42(6), 612-1620.
- Spicer P.T. and Pratsinis S.E. (1996). Shear-induced flocculation: the evolution of floc structure and shape of the size distribution at steady state. *Water Research* 30, 1049-1056.
- Spicer P.T., Pratsinis S.E. and Trennepohl M.D. (1996). Coagulation and fragmentation: the Variation of Shear rate and time lag for attainment of steady state. *Ind. Eng. Chem. Res.* 35, 3074-3080.
- Sreenivasan K.R. (1984). On the scaling of the turbulence energy-dissipation rate. *Physics of Fluids* 27(5), 1048-1051.
- Stanley H.E. and Barabási A.L. (1995). *Fractal concepts in surface growth*. Cambridge University Press, Cambridge (UK).

- Stolzenbach K.D. and Elimelech M. (1993). The effect of particle density on collision between sinking particles: implications for particle aggregation in the ocean. *Deep-Sea Research I* 41(3), 469-483.
- Stone M. and Krishnappan B.G. (2003). Floc morphology and size distributions of cohesive sediment in steady flow. *Water Research* 37, 2739-2747.
- Takayasu H., Nishikawa I. and Tasaki H. (1988). Power-law mass distribution of aggregation systems with injection. *Physical Review A* 37(8), 3110-3117.
- Takayasu H., Nishikawa I. and Tasaki H. (1988). *Universal power law observed in an exponentially growing particle system*, Phys. Rev. A 46, 782-786.
- Tennekes H. and Lumley J.L. (1973). *A first course in turbulence*. The MIT Press.
- Tennekes H. (1973). Eulerian and Lagrangian time microscales in isotropic turbulence. *Journal of Fluid Mechanics* 67, 561-567.
- Thomas D.N., Judd S.J. and Fawcett N. (1999). Flocculation modelling: A review. *Water Research* 33(7), 1579-1592.
- Tsai C.-H. and Hwang S.-C. (1995). Flocculation of Sediment from the Tanshui River Estuary. *Mar. Freshwater Research* 46, 383-392.
- Turner M.J., Blackledge J.M. and Andrews P.R. (1998). *Fractal geometry in digital imaging*. AP San Diego, California (CA).
- Valioulis I.A. (1983). Particle collisions and coalescence in fluids. Report KH-R-44, CIT.
- Van Ledden M. (2003). *Sand-mud segregation in estuaries and tidal basins*. Ph.D. Thesis, Delft University of Technology.
- Van Leussen W. (1994). *Estuarine Macroflocs*. Ph.D. Thesis, University of Utrecht.
- Vane L.M. and Zang G.M. (1997). Effect of aqueous phase properties on clay particle zeta potential and electro-osmotic permeability: Implications for electro-kinetic soil remediation processes. *Journal of Hazardous Materials* 55, 1-22.
- Vicsek T. (1992). *Fractal growth phenomena*. World Scientific, Singapore.
- Zhang J.-J. and Li X.-Y. (1992). Modeling Particle-Size Distribution Dynamics in a Flocculation System. *American Institute of Chemical Engineers* 49(7), 1870-1882.
- Wells M.L. and Goldberg E.D. (1993). Colloid aggregation in seawater. *Marine Chemistry* 41, 353-358.
- Wiesner M.R. (1992). Kinetics of aggregate formation in rapid mix. *Water Research* 26(3), 379-387.
- Winterwerp J.C. (1998). A simple model for turbulence induced flocculation of cohesive sediment. *Journal of Hydraulic Engineering Research* 36(3), 309-326.
- Winterwerp J.C. (1999). *On the dynamics of high-concentrated mud suspensions*. Ph.D. Thesis, Delft University of Technology.
- Winterwerp J.C. (2002). On the flocculation and settling velocity of estuarine mud. *Cont. Shelf Res.* 22, 1339-1360.
- Winterwerp J.C. and Kesteren W.G.M. van (2004). *Introduction to the physics of cohesive sediment in the marine environment*. T. van Loon Ed., Elsevier, Amsterdam.
- Wittel F., Kun F., Herrmann H.J. and Kröplin B.H. (2004). Fragmentation of shells. *Physical Review Letters* 93(3), 035504.
- Yukselen Y. and Kaya A. (2003). Zeta potential of kaolinite in the presence of alkali, alkaline earth and hydrolyzable metal ions. *Water, Air and Soil Pollution* 145, 155-168.

List of symbols

a	Exponent in the SOC formalism	L [L]	Floc size
c [ML ⁻³]	Sediment concentration in the buffer tank	L_p [L]	Primary particle size
c_d [ML ⁻³]	Desired sediment concentration	M_f [M]	Floc mass
c_s [ML ⁻³]	Sediment concentration in the storage tank	N_p	Number of primary particles in a floc
d_0	Capacity dimension (d_C)	P	Dimensionless floc perimeter
d_1	Information dimension (d_I)	S	Entropy function
d_2	Correlation dimension (d_K)	S'	Specific entropy
d_E	Embedding (Euclidian) dimension	S'_{max}	Maximum specific entropy
d_f	Indefinite fractal dimension	T [°C]	Temperature
d_p	Perimeter-based fractal dimension	V_b [L ³]	Buffer volume
d_q	Generalised dimensionality	V_c [L ³]	Settling column volume
f	Multifractal spectrum	α	Singularity strength
f_g [T ⁻¹]	Grid frequency	$\alpha_{i,j}$	Collision efficiency
f_p [T ⁻¹]	Propeller frequency	γ	Distance form self-similarity
ℓ	Dimensionless floc size	$\gamma_{i,j}$	Breakup distribution function
n_i [L ⁻³]	Aggregate number concentration	γ_{τ_d}	Autocorrelation function
s [ppt]	Water salinity	δ	Capacity dimension of the primary particle
t [T]	Time	ε [L ² T ⁻³]	Energy dissipation rate
t_{dyn} [T]	Dynamic transition time of the column	ϵ [L]	Pixel size, box size of the ω -covering
t_f [T]	Flocculation time scale	η_k [L]	Kolmogorov length scale
t_{rb} [T]	Residence time in the buffer tank	κ	Probability of nonlinear breakup
t_{rbe} [T]	Experimental relaxation time in the buffer tank	λ [L]	Taylor microscale
t_{rc} [T]	Residence time in the settling column	μ [ML ⁻¹ T ⁻¹]	Water dynamic viscosity
t_{sta} [T]	Static transition time of the column	ν [L ² T ⁻¹]	Water kinematic viscosity
w [LT ⁻¹]	Settling velocity	ρ_s [ML ⁻³]	Sediment density
A	Dimensionless floc area	ρ_w [ML ⁻³]	Water density
A_g [L]	Maximum grid stroke	ρ_{τ_d}	Normalised autocorrelation function
B [L ⁻³]	Breakup frequency function	τ	Mass-correlation exponent
E	Breakup efficiency	τ_d [T]	Correlation time lag
F_y [Pa]	Floc strength	τ_k [T]	Kolmogorov time scale
G [T ⁻¹]	Turbulent shear rate	v_k [LT ⁻¹]	Kolmogorov velocity scale
H [L]	Total interparticle distance	ϕ [L ³]	Volumetric concentration
H_c [L]	Column height	$\Lambda_{i,j}$ [L ³ T ⁻¹]	Collision rate
K [JK ⁻¹]	Boltzmann constant	Ω	Generalised set
		Υ	Disorder function
		Υ'	Disorder index

List of acronyms

2D	Two-dimension/-al
3D	Three-dimension/-al
CCA	Cluster-Cluster Aggregation
DLA	Diffusion-Limited Aggregation
FSD	Floc Size Distribution
LDA	Laser Doppler Anemometry
NE	Non-equilibrium
OSLIM	Optical Silt Measuring probe
PIV	Particle Image Velocimetry
SOC	Self-Organised Criticality
SPM	Suspended Particle Matter
SS	Steady State

Acknowledgments

When I started to work on my doctoral research I was confident I could have done all myself: well, I was definitely wrong. On the one hand, I found myself able to come up with plenty of ideas to design the components of the column, to imagine how it could have worked better with this or that other solution, to think about the elaboration of all the data therein collected, *etc.* In the same way, I also found myself capable to address my curiosity to disparate disciplines of science to find ideas to describe the processes involved in flocculation, to elaborate a theoretical framework of it, and describe flocculation from a different perspective, perhaps out of the classic approach by sedimentologists. On the other hand, this wandering around the sciences could not have been synthesised into a coherent work without the guidance and directions of Jurjen and Han. Jurjen Battjes, in particular, has been able to make me follow the main path while allowing me to explore the topic departing a bit from the track, and he has given me confidence to find the proper way to bring this work to an end, contributing to my scientific maturity.

However, Jurjen and Han are not the only persons to whom I am grateful. Several Msc-students have been instrumental in finalising this research: Dalia dal Corso has taken part in planning and performing the first experiment, Remi Jouan has contributed in developing and optimising the recording system in the column (Chapter 4), Guillaume Auger has worked in the column to prepare and carry out the second experiment (Chapter 4), and Francesca Mietta has implemented part of the population balance equation (Chapter 7).

I want to express my thanks to the technical staff of the Laboratory, because without them I could not have realised and used the column: Harry Fontijn, Arie den Toom, Fred van der Brugge, Karel de Bruin, Jaap van Duin and Michiel van der Meer. I also mention the financial support from the BEO programme of Delft University of Technology.

Finally, there are many other people I like to thank: my colleagues PhD-students, especially my office mates Ankie Bruens and Petra Dankers, and some persons who I have spent plenty of time talking with, with no limits of topics: Fabiana Maccarini, Cecilia Iacono, Andrea D'ariano, Claudia Giarrusso, Silvia Bolens, Federica Fiamingo, Elisa Aldrighetti, Otti Kievits, Alessandra Crosato and Erik Mosselman.

Curriculum Vitae

Federico Maggi was born in Vercelli, Italy, on January the 15th 1974. From 1988 to 1993 he attended the Lyceum "Amedeo Avogadro" in Vercelli, achieving his high school diploma. From 1993 to 1999 he studied at "Polytechnic of Turin", achieving his Master degree in Civil Engineering. Finally, from 2000 to 2005 he joined Delft University of Technology, working in the Section of Environmental Fluid Dynamics as PhD candidate.

